

# Analysis of the Smoothed Particle Hydrodynamics method for free-surface flows

by

Areti Kiara

Submitted to the Department of Mechanical Engineering  
in partial fulfillment of the requirements for the degree of

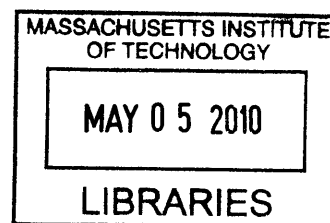
Doctor of Philosophy

at the

MASSACHUSETTS INSTITUTE OF TECHNOLOGY

February 2010

**ARCHIVES**



© Massachusetts Institute of Technology 2010. All rights reserved.

Handwritten signature of Areti Kiara.

Author .....  
Department of Mechanical Engineering  
January 29, 2010

Certified by .....  
Dick K.P. Yue  
Philip J. Solondz Professor of Engineering  
Professor of Mechanical and Ocean Engineering, MIT  
Thesis Supervisor

Accepted by .....  
David E. Hardt  
Ralph E. and Eloise F. Cross Professor of Mechanical Engineering  
Chairman, Committee on Graduate Students



# **Analysis of the Smoothed Particle Hydrodynamics method for free-surface flows**

by

Areti Kiara

Submitted to the Department of Mechanical Engineering  
on January 29, 2010, in partial fulfillment of the  
requirements for the degree of  
Doctor of Philosophy

## **Abstract**

Smoothed Particle Hydrodynamics (SPH) is a simple and attractive meshless Lagrangian particle method with applications in many fields such as astrophysics, hydrodynamics, magnetohydrodynamics, gas explosions, and granular flows that has demonstrated ability to simulate highly non-linear free-surface flows including wave overturning, jets, and the formation of spray and droplets. Despite the increasing popularity and promise of the method, SPH has a number of key issues that must be overcome before the method can realize its full potential in scientific and engineering applications: it is of low order, requires a high degree of tuning, and is inherently unstable. Additionally, there exists little analytic basis or fundamental understanding of the method to guide the many ad-hoc tuning and empirical fixes.

The objective of this thesis is to perform an analytical and numerical investigation of the SPH method for free-surface flows. To this end, we perform a quantitative, unified analysis of the numerical method and the physics it captures, and we assess the method's consistency, stability, and convergence. It is shown that SPH introduces spurious solutions dominant in the dynamics of the solution making quantities such as velocity and pressure essentially unusable without filtering. It is also shown that the method is consistent inside the domain but imposes spurious, leading order, dynamic free-surface boundary conditions which alter the flow and further permit the introduction of spurious solutions. We further extend the analysis to address the effects of different empirical SPH treatments introduced in the literature, classifying these respectively as accuracy, consistency, or stability treatments, and characterizing their effectiveness. Based on the findings of the analysis, we eliminate the tuneable and empirical nature of the method by providing rational guidelines for the usage and effects of the relevant SPH treatments. Finally, we propose a modified SPH method that maintains the key features of SPH and significantly reduces spurious errors present in current SPH implementations.

This thesis is among the first to provide a unified systematic analysis of the SPH method, shedding insight into the many proposed variations and fixes, and informs and guides new rational improvements to the method. This work lays the foundation

for the development of SPH as a valuable engineering tool in the study of violent free-surface flows.

Thesis Supervisor: Dick K.P. Yue

Title: Philip J. Solondz Professor of Engineering

Professor of Mechanical and Ocean Engineering, MIT

*σε εσένα Ανούλα μου,*



## Acknowledgments

Completing this thesis has been my odyssey, a life-changing journey. My acknowledgments to those who helped me towards my destination are heartfelt. Words have never been my allies and I have come to realize that I will never be able to adequately thank those that I am most grateful to.

First and foremost, I would like to thank Professor Dick K.P. Yue. He has been my thesis supervisor, coach and teacher. He has supported me academically and financially, guided me in this research with unique patience and remarkable insight, coached me to evolve on many levels, all the while accepting my temperament. He is the reason I initiated and completed this PhD. It is my great fortune to be his student.

I would also like to thank my thesis committee member Dr. Kelli Hendrickson. She guided me, as a mentor and a friend, from my first days at MIT. She has equipped me with many valuable tools, from teaching me programming to how to give comprehensive presentations. With her clear, rational thinking she has assisted me throughout this research project in its entirety.

I am thankful to my thesis committee member Professor Michael S. Triantafyllou, for helping me come to MIT and for his rational and insightful comments during the thesis meetings.

I would also like to acknowledge my thesis committee member Professor George Karniadakis for paying close attention to my research, strongly encouraging me and giving me invaluable comments and suggestions.

I am grateful to Professor Lian Shen for guiding my approach towards research in my early years at MIT, for his invaluable help in my preparation for the PhD qualifying exams, and for his tireless help in the consistency analysis. I am also thankful to Dr. Yuming Liu for many things, and in particular for his unprecedented patience in teaching me the fundamentals of stability analysis.

At this point I want to acknowledge the Office of Naval Research for funding the various research projects that have led to this dissertation.

I would like to thank all the people in the VFRL for making the lab the wonderful place it is. Special thanks go to lab administrators Dr. Guangyu Wu, Dr. Benjamin Connell, Dr. George Papaioannou, and Hongmei Yan, for their help and friendship.

I would like to acknowledge Mrs. Vefa (Jennifer) for our late night conversations and tell her that she is always in my thoughts.

I am indebted to Leslie Regan and Maria Brennan for their support, their constant encouragement and for helping me focus on my research: they always took care of everything else!

I am also indebted to Mary Thompson, for proofreading this entire manuscript.

In a more personal level, I would also like to thank my undergraduate advisor at the NTUA, Professor Constantine Memos, for his support and friendship. I will always be grateful to Giorgos Tsotsonis for believing in me and making it possible for me to come to MIT. I want to thank the entire "M" company in Boston for many pleasant times spent together, and especially Dr. Andrea Adamo for being my friend.

A heartfelt thank you to my best friend Konstantinos Gouras for teaching me the true values in life. He is always in my heart.

I want to acknowledge those who became my family over the last ten years. Professor Yue for being, silently, more than a father during challenging personal times. Kelli, for having the patience to become my friend. Dr. Sunwoong Lee for *all* that he has given me, for his support, and for his references and numerous arguments on the weak compressibility assumption.

I want to thank my family in Greece, my parents and siblings, and especially my youngest sister Violeta, my father for teaching me never to give up, and my mother for exposing me to her unique perspective of the world, for her encouragement to continue what I had started, and for her coming when most needed.

And last, but not in any way least, Ana-Maria: the beautiful ballerina who gave me back my smile. *All my love goes with you...*





# Contents

<b>1</b>	<b>Introduction</b>	<b>37</b>
1.1	Motivation . . . . .	37
1.2	Thesis scope . . . . .	42
1.3	Thesis structure . . . . .	42
<b>2</b>	<b>Linear analysis of a main SPH algorithm, MA-SPH, for free-surface flows</b>	<b>45</b>
2.1	Introduction . . . . .	45
2.2	Definition of MA-SPH . . . . .	47
2.2.1	Problem statement . . . . .	47
2.2.2	Spatial discretization . . . . .	50
2.2.3	Boundary conditions . . . . .	53
2.2.4	Temporal evolution . . . . .	54
2.3	Framework for the analysis of MA-SPH for free-surface flows . . . . .	55
2.4	Linear analysis of weakly compressible free-surface flows . . . . .	61
2.4.1	Statement, solution and discussion in continuous space . . . . .	62
2.4.2	Discussion on discretization and numerical verification . . . . .	85
2.4.3	Projection of weakly compressible free-surface flows in deep water on to a divergence-free space with modal decomposition . . . . .	100
2.5	Consistency analysis of Kernel Interpolation in MA-SPH for free-surface flows . . . . .	111
2.5.1	Definition of Kernel Interpolation . . . . .	111

2.5.2	Uniform and randomly distributed unbounded particle distribution . . . . .	113
2.5.3	Definition of unbounded smoothly advected particle distribution . . . . .	121
2.5.4	Density in unbounded smoothly advected particle distribution	122
2.5.5	Consistency of Kernel Interpolation technique in unbounded smoothly advected particle distribution. The numerical significance of the SPH density . . . . .	127
2.5.6	Implicit dynamic free-surface boundary condition . . . . .	131
2.6	Linear stability analysis of MA-SPH in semi-infinite domain . . . . .	137
2.6.1	Linear von Neumann stability analysis . . . . .	138
2.6.2	Continuous model . . . . .	139
2.6.3	Semi-discrete algorithm . . . . .	156
2.6.4	Fully-discrete algorithm . . . . .	168
2.6.5	Discussion on the linear stability of MA-SPH with advanced density formulation . . . . .	177
2.7	Conclusions . . . . .	179
<b>3</b>	<b>Analysis of existing treatments for MA-SPH</b>	<b>183</b>
3.1	Introduction . . . . .	183
3.2	Accuracy treatments . . . . .	184
3.2.1	Temporal filtering of pressure measurements . . . . .	185
3.2.2	Spatial averaging of pressure measurements . . . . .	187
3.3	Consistency treatments . . . . .	189
3.3.1	Alternative spatial derivative computation techniques . . . . .	189
3.3.2	Different discrete forms of the equations of motion . . . . .	197
3.4	Stability treatments . . . . .	200
3.4.1	Classification and framework . . . . .	201
3.4.2	XSPH . . . . .	206
3.4.3	Initial dumping . . . . .	207

3.4.4	Artificial viscosity . . . . .	212
3.4.5	Tensile instability treatment . . . . .	216
3.4.6	Density re-initialization schemes . . . . .	217
3.5	Conclusions . . . . .	221
<b>4</b>	<b>Rational development of convergent SPH methods</b>	<b>223</b>
4.1	Introduction . . . . .	223
4.2	A higher-order hSPH scheme with Moving Least Squares . . . . .	226
4.2.1	Governing Equations . . . . .	227
4.2.2	Spatial discretization . . . . .	230
4.2.3	Regularization . . . . .	232
4.2.4	Non-dimensionalization . . . . .	233
4.2.5	Numerical simulations of deep-water Airy waves with hSPH . . . . .	234
4.3	A stable modified SPH, mSPH, scheme with Kernel Interpolation . . . . .	252
4.3.1	Governing Equations . . . . .	253
4.3.2	Spatial discretization . . . . .	257
4.3.3	Boundary conditions . . . . .	258
4.3.4	Hydrostatic initial conditions . . . . .	259
4.3.5	Temporal integration . . . . .	260
4.3.6	Regularization . . . . .	261
4.3.7	An <i>a posteriori</i> error metric . . . . .	263
4.3.8	Numerical simulation of standard SPH dam-break benchmark with mSPH . . . . .	265
4.4	Discussion . . . . .	296
4.5	Conclusions . . . . .	298
<b>5</b>	<b>Conclusions</b>	<b>299</b>
5.1	Thesis contributions . . . . .	299
5.2	Perspectives on the SPH approach . . . . .	302
5.3	Future work . . . . .	304

# List of Figures

2-1	Weakly compressible, gravity free-surface flow. Problem statement. . .	48
2-2	Classification of major uncertainties and probable sources of error in (a) general SPH for applications in compressible, unbounded flows [5, 7] and (b) problem specific SPH for applications in incompressible, free- surface hydrodynamic flows in the presence of gravity [30]. . . . .	57
2-3	Framework of analysis in SPH. . . . .	60
2-4	Graphic solution to the dispersion relation for weakly compressible free-surface gravity waves in shallow water for $a = \kappa/\delta = [5, 10, 100]$ and constant $\epsilon = 10^{-3}$ . Shows that $f_2$ is practically a constant and equal to $1/\epsilon$ in agreement with (2.43). Depth decaying profiles. . . .	70
2-5	Close up of Figure 2-4 to verify Eq. (2.44). Depth decaying profiles. .	71
2-6	Graphic solution to the dispersion relation for weakly compressible free-surface gravity waves in deep water for constant $a = \kappa/\delta = 5$ and $\epsilon = [0.5, 1, 10, 100]$ . Shows the behavior of $f_2$ as $\epsilon$ increases, in agreement with (2.46) and (2.47). Depth decaying profiles. . . . .	73
2-7	Horizontal velocity comparisons of incompressible and $10^{th}$ acoustic modes for three different speeds of sound $c = [1, 2, 5]$ , given equal unit free-surface displacement. Linear plane progressive free-surface with horizontal wavenumber $\kappa = 2\pi$ and water depth $H \rightarrow -\infty$ . . . . .	82
2-8	Vertical velocity comparisons of incompressible and $10^{th}$ acoustic modes for three different speeds of sound $c = [1, 2, 5]$ , given equal unit free- surface displacement. Linear plane progressive free-surface with hori- zontal wavenumber $\kappa = 2\pi$ and water depth $H \rightarrow -\infty$ . . . . .	83

2-9	Dynamic pressure comparisons of incompressible and $10^{th}$ acoustic modes for three different speeds of sound $c = [1, 2, 5]$ , given equal unit free-surface displacement. Linear plane progressive free-surface with horizontal wavenumber $\kappa = 2\pi$ and water depth $H \rightarrow -\infty$ . . . . .	84
2-10	Kinematics and dynamics with respect to time at selected particles along a cross-section at $x = L$ . SPH simulation of linear depth decaying (Airy) wave with $\kappa A = 0.0006$ . Top left, vertical particle position. Top middle, horizontal velocity. Top right, horizontal acceleration. Bottom left, dynamic pressure. Bottom middle, vertical velocity. Bottom right, vertical acceleration. Dimensionless speed of sound $\beta = 10$ and kernel bandwidth $h = 0.01$ . . . . .	89
2-11	Kinematics and dynamics with respect to time at selected particles along a cross-section at $x = L$ . SPH simulation of linear depth decaying (Airy) wave with $\kappa A = 0.006$ . Top left, vertical particle position. Top middle, horizontal velocity. Top right, horizontal acceleration. Bottom left, dynamic pressure. Bottom middle, vertical velocity. Bottom right, vertical acceleration. Dimensionless speed of sound $\beta = 10$ and kernel bandwidth $h = 0.01$ . . . . .	90
2-12	FFT of horizontal (top) and vertical (bottom) accelerations in SPH simulation of linear depth decaying (Airy) wave with $\kappa A = 0.0006$ . Dimensionless speed of sound $\beta = 10$ and kernel bandwidth $h = 0.01$ . Expected cut-off period $T_{66} = 0.001$ . . . . .	92
2-13	In color. Plane progressive wave, $20^{th}$ acoustic mode. Coloring based on initial horizontal velocity field. Wave slope $\kappa A = 0.0006$ , vertical wavenumber $\nu_{20} = \frac{41\pi}{2}$ , theoretical period $T_{20} = 0.03$ . . . . .	93
2-14	Kinematics and dynamics with respect to time at selected particles along a cross-section at $x = L$ . SPH simulation of linear depth oscillatory wave with $n = 0$ , $\kappa A = 0.0006$ , $h = 0.01$ . Top left, vertical particle position. Top middle, horizontal velocity. Top right, horizontal acceleration. Bottom left, dynamic pressure. Bottom middle, vertical velocity. Bottom right, vertical acceleration. . . . .	94

2-15	Kinematics and dynamics with respect to time at selected particles along a cross-section at $x = L$ . SPH simulation of linear depth oscillatory wave with $n = 10$ , $\kappa A = 0.0006$ , $h = 0.01$ . Top left, vertical particle position. Top middle, horizontal velocity. Top right, horizontal acceleration. Bottom left, dynamic pressure. Bottom middle, vertical velocity. Bottom right, vertical acceleration. . . . .	95
2-16	Kinematics and dynamics with respect to time at selected particles along a cross-section at $x = L$ . SPH simulation of linear depth oscillatory wave with $n = 15$ , $\kappa A = 0.0006$ , $h = 0.01$ . Top left, vertical particle position. Top middle, horizontal velocity. Top right, horizontal acceleration. Bottom left, dynamic pressure. Bottom middle, vertical velocity. Bottom right, vertical acceleration. . . . .	96
2-17	Kinematics and dynamics with respect to time at selected particles along a cross-section at $x = L$ . SPH simulation of linear depth oscillatory wave with $n = 20$ , $\kappa A = 0.0006$ , $h = 0.01$ . Top left, vertical particle position. Top middle, horizontal velocity. Top right, horizontal acceleration. Bottom left, dynamic pressure. Bottom middle, vertical velocity. Bottom right, vertical acceleration. . . . .	97
2-18	Kinematics and dynamics with respect to time at selected particles along a cross-section at $x = L$ . SPH simulation ( $h = 0.01$ ) of linear depth oscillatory wave with $n = 40$ , $\kappa A = 0.0006$ . Top left, vertical particle position. Top middle, horizontal velocity. Top right, horizontal acceleration. Bottom left, dynamic pressure. Bottom middle, vertical velocity. Bottom right, vertical acceleration. . . . .	98
2-19	FFT of horizontal (top) and vertical (bottom) accelerations in SPH simulation of $n = 20^{th}$ acoustic mode, $\kappa A = 0.0006$ . Dimensionless speed of sound $\beta = 10$ and kernel bandwidth $h = 0.01$ . Expected $T_{20} = 0.03$ . . . . .	99

2-20	Verification of orthogonality relation (2.91) for $m = -1, n = 0, \dots, 50$ . Deep water assumption, $\kappa H = 2\pi$ . The integral for each mode is of the order of $10^{-6}$ . . . . .	105
2-21	Computation of $\overline{\Phi_{-1}}$ from (2.86) in deep water for a noisy solution $\Phi = 2\Phi_{-1} + \Phi_n, n = 0, \dots, 50$ . The horizontal wavelength is chosen $\kappa = 2\pi/H$ . The error between the reconstructed solution $\overline{\Phi_{-1}}$ and the incompressible solution $2\Phi_{-1}$ is of the order of $10^{-4}$ . Deep water assumption, $\kappa H = 2\pi$ . . . . .	106
2-22	Initial noisy solution $f = f_{-1} + f_{20} + f_u$ , where $f_{-1}$ denotes the unit amplitude incompressible solution, $f_{20}$ denotes the unite amplitude $20^{th}$ acoustic mode and $f_u$ is an unstable mode, i.e., wavenumber larger than $k$ . Top: Computation of orthogonality relation (2.91) for $m = 20,$ $n = 0, \dots, 30$ . Bottom: Comparison between initial noisy solution $f(y)$ (thin solid line), smooth solution from (2.86) (dashed line) and smooth with instability reduction solution (thick solid line) along the depth. Deep water assumption, $kH = 2\pi$ . . . . .	107
2-23	Initial noisy solution $f = f_{-1} + f_{20} + f_u$ , where $f_{-1}$ denotes the unit amplitude incompressible solution, $f_{20}$ denotes the unite amplitude $20^{th}$ acoustic mode and $f_u$ is an unstable mode, i.e., wavenumber larger than $k$ . Top: Computation of orthogonality relation (2.91) for $m = 20,$ $n = 0, \dots, 30$ . Bottom: Comparison between initial noisy solution $f(y)$ (thin solid line), smooth solution from (2.86) (dashed line) and smooth with instability reduction solution (thick solid line) along the depth. Deep water assumption, $kH = 10\pi$ . . . . .	108
2-24	Example grid configuration for the computation of the artificial dy- namic free-surface boundary condition in MA-SPH due to the Ker- nel Interpolation incompleteness near the free-surface. The discrete momentum equation and conservation of mass are computed on the free-surface particle 0. Uniform grid of spacing $h$ in each direction. . .	132

2-25	SPH simulation of a hydrostatic case. Absolute horizontal accelerations along different depths. Water depth $H = 1$ , dimensionless speed of sound $\beta = 40$ . . . . .	148
2-26	SPH simulation of a hydrostatic case. Absolute vertical accelerations along different depths. Water depth $H = 1$ , dimensionless speed of sound $\beta = 40$ . . . . .	149
2-27	SPH simulation of a hydrostatic case. Absolute time rate of change of total pressure along different depths. Water depth $H = 1$ , dimensionless speed of sound $\beta = 40$ . . . . .	150
2-28	SPH simulation of a hydrostatic case. Growth of initial pressure perturbation $p(\vec{x}, 0) = qe^{2\pi(ix + \frac{y}{25h})}$ along different depths. Simulation parameters $c = 20$ , $h = 0.02$ . Expected growth rate $\lambda_e = 48.5$ , obtained $\lambda_o = 48$ . . . . .	151
2-29	SPH simulation of a hydrostatic case. Growth of initial pressure perturbation $p(\vec{x}, 0) = qe^{2\pi(ix + \frac{y}{25h})}$ along different depths. Simulation parameters $c = 20$ , $h = 0.01$ . Expected growth rate $\lambda_e = 109$ , obtained $\lambda_o = 114$ . . . . .	152
2-30	SPH simulation of a hydrostatic case, imposing zero-pressure free-surface fitting. Growth of absolute horizontal accelerations (top left), absolute vertical accelerations (top right) and dynamic pressure (bottom) at selected particles along a vertical cross section. Periodic horizontal boundary conditions and water depth $H = 1$ . . . . .	153
2-31	Simulation of a weakly compressible hydrostatic case. Computation of spatial derivatives with Moving Least Squares. Growth of absolute horizontal accelerations (top left), absolute vertical accelerations (top right) and dynamic pressure (bottom) at selected particles along a vertical cross section. Periodic horizontal boundary conditions and water depth $H = 1$ . . . . .	154

2-32	Simulation of a weakly compressible hydrostatic case. Computation of spatial derivatives with Moving Least Squares. Imposing zero-pressure free-surface fitting. Growth of absolute horizontal accelerations (top left), absolute vertical accelerations (top right) and dynamic pressure (bottom) at selected particles along a vertical cross section. Periodic horizontal boundary conditions and water depth $H = 1$ . . . . .	155
2-33	Unstable growth rates of the fully-discrete mSPH algorithm with fourth order Runge-Kutta as a function of the dimensionless perturbation wavenumber $kh$ . Thin solid line $\mu_c = 1$ , dashed line $\mu_c = 0.8$ , dash-dot line $\mu_c = 0.5$ , thick solid line $\mu_c = 0.1$ . . . . .	176
2-34	Summary of the analysis framework. . . . .	181
3-1	Maximum amplitude of the eigenvalues of the amplification matrix $ \lambda  = \max  \lambda_1, \lambda_2 $ for MA-SPH with ID treatment and modified Predictor-Corrector temporal integration scheme. The amplitude of $ \lambda $ is given as function of the Courant condition $\mu_c = \delta t d/h$ for three values of $\zeta = 1 + 0.5\Gamma\delta t = [1, 1.005, 1.025]$ . Sinusoidal disturbances are assumed.	209
3-2	Maximum amplitude of the eigenvalues of the amplification matrix $ \lambda  = \max  \lambda_1, \lambda_2 $ for MA-SPH with ID treatment and modified Predictor-Corrector temporal integration scheme. The amplitude of $ \lambda $ is given as function of $\mu^* = \delta t d \sinh \mu h/h$ for three values of $\zeta = 1 + 0.5\Gamma\delta t = [1, 1.005, 1.025]$ . Exponential disturbances are assumed. . . . .	210
4-1	Horizontal velocity at depths $[0, -h]$ for $h = 1/16$ . Dashed line theory, thin solid line hSPH method with re-initialization with instability removal and flow field reconstruction every 15 time steps, thick solid line hSPH without re-initialization. . . . .	235
4-2	Vertical velocity at depths $[0, -h]$ for $h = 1/16$ . Dashed line theory, thin solid line hSPH method with re-initialization with instability removal and flow field reconstruction every 15 time steps, thick solid line hSPH without instability removal. . . . .	236

4-3	Pressure at depths $[0, -h]$ for $h = 1/16$ . Dashed line theory, thin solid line hSPH method with re-initialization with instability removal and flow field reconstruction every 15 time steps, thick solid line hSPH without instability removal. . . . .	237
4-4	Horizontal accelerations at depths $[0, -h]$ for $h = 1/16$ . Dashed line theory, thin solid line hSPH method with re-initialization with instability removal and flow field reconstruction every 15 time steps, thick solid line hSPH without instability removal. . . . .	238
4-5	Vertical accelerations at depths $[0, -h]$ for $h = 1/16$ . Dashed line theory, thin solid line hSPH method with re-initialization with instability removal and flow field reconstruction every 15 time steps, thick solid hSPH without instability removal. . . . .	239
4-6	Horizontal velocity at depths $[0, -3h, -6h]$ for $h = 1/16$ . Dashed line theory, solid line hSPH method with re-initialization with instability removal and flow field reconstruction when $\int_{\mathcal{V}} v \geq a_{\ell}/10$ . . . . .	240
4-7	Vertical velocity at depths $[0, -3h, -6h]$ for $h = 1/16$ . Dashed line theory, solid line hSPH method with re-initialization with instability removal and flow field reconstruction when $\int_{\mathcal{V}} v \geq a_{\ell}/10$ . . . . .	241
4-8	Horizontal accelerations at depths $[0, -3h, -6h]$ for $h = 1/16$ . Dashed line theory, solid line hSPH method with re-initialization with instability removal and flow field reconstruction when $\int_{\mathcal{V}} v \geq a_{\ell}/10$ . . . . .	242
4-9	Vertical accelerations at depths $[0, -3h, -6h]$ for $h = 1/16$ . Dashed line theory, solid line hSPH method with re-initialization with instability removal and flow field reconstruction when $\int_{\mathcal{V}} v \geq a_{\ell}/10$ . . . . .	243
4-10	Time rate of pressure change at depths $[0, -3h, -6h]$ for $h = 1/16$ . Dashed line theory, solid line hSPH method with re-initialization with instability removal and flow field reconstruction when $\int_{\mathcal{V}} v \geq a_{\ell}/10$ . . . . .	244

4-11	Simulation of an Airy wave with hSPH method with re-initialization with instability removal and flow field reconstruction every 15 time steps. Horizontal velocity at depths $[0, -h]$ for $h = 1/16$ (top) and $h = 1/32$ (bottom). . . . .	245
4-12	Simulation of an Airy wave with hSPH method with re-initialization with instability removal and flow field reconstruction every 15 time steps. Vertical velocity at depths $[0, -h]$ for $h = 1/16$ (top) and $h = 1/32$ (bottom). . . . .	246
4-13	Simulation of an Airy wave with hSPH method with re-initialization with instability removal and flow field reconstruction every 15 time steps. Dynamic pressure at depths $[0, -h]$ for $h = 1/16$ (top) and $h = 1/32$ (bottom). . . . .	247
4-14	Simulation of an Airy wave with hSPH method with re-initialization with instability removal and flow field reconstruction every 15 time steps. Horizontal acceleration at depths $[0, -h]$ for $h = 1/16$ (top) and $h = 1/32$ (bottom). . . . .	248
4-15	Simulation of an Airy wave with hSPH method with re-initialization with instability removal and flow field reconstruction every 15 time steps. Vertical acceleration at depths $[0, -h]$ for $h = 1/16$ (top) and $h = 1/32$ (bottom). . . . .	249
4-16	Free-surface evolution of a plane progressive wave with steepness $kA = 0.06$ . comparison between linear theory (solid line) and hSPH method with re-initialization with instability removal and flow field reconstruction every 15 time steps (dashed line). . . . .	250
4-17	Free-surface evolution of a plane progressive wave with steepness $kA = 0.25$ . comparison between linear theory (solid line) and hSPH method with re-initialization with instability removal and flow field reconstruction every 15 time steps (dashed line). . . . .	251
4-18	Minimum number of time steps for smoothing to achieve stability. Thin solid line $\mu_c = 1$ , dashed line $\mu_c = 0.8$ , dash-dot line $\mu_c = 0.5$ . . . . .	263

- 4-19 Initial conditions for the standard SPH dam-break benchmark, described in [55]. The kernel bandwidth is  $h = 0.025m$ , the particle spacing is  $dx = 0.75h$ . The domain dimensions are  $L_d = 5.36m$ ,  $L_w = 1.2m$ , and  $H_w = 0.6m$ . . . . . 265
- 4-20 In color. Comparison of time evolving snapshots of the horizontal velocity field of (a) MA-SPH MLS density re-initialization, (b) mSPH with no smoothing, and (c) mSPH with smoothing every  $n = 5$  time steps. The artificial speed of sound is  $c = 26.46m/s$ , the kernel bandwidth is  $h = 0.025$ , the particle spacing is  $dx = 0.75h$  and the Courant condition  $\mu_c = 0.8$  for all simulations. Time increases from top to bottom. It is emphasized that all three simulations are initialized with the same initial conditions, employ identical spatial and temporal discretization parameters, the contour levels use the same coloring schemes, *no* filtering or post-processing has been employed in any of the results, and finally no other treatments have been employed other than those described. . . . . 266
- 4-21 In color. Comparison of time evolving snapshots of the horizontal velocity field of (a) MA-SPH MLS density re-initialization, (b) mSPH with no smoothing, and (c) mSPH with smoothing every  $n = 5$  time steps. The artificial speed of sound is  $c = 26.46m/s$ , the kernel bandwidth is  $h = 0.025$ , the particle spacing is  $dx = 0.75h$  and the Courant condition  $\mu_c = 0.8$  for all simulations. Time increases from top to bottom. It is emphasized that all three simulations are initialized with the same initial conditions, employ identical spatial and temporal discretization parameters, the contour levels use the same coloring schemes, *no* filtering or post-processing has been employed in any of the results, and finally no other treatments have been employed other than those described. . . . . 267

4-22 In color. Comparison of time evolving snapshots of the horizontal velocity field of (a) MA-SPH MLS density re-initialization, (b) mSPH with no smoothing, and (c) mSPH with smoothing every  $n = 5$  time steps. The artificial speed of sound is  $c = 26.46m/s$ , the kernel bandwidth is  $h = 0.025$ , the particle spacing is  $dx = 0.75h$  and the Courant condition  $\mu_c = 0.8$  for all simulations. Time increases from top to bottom. It is emphasized that all three simulations are initialized with the same initial conditions, employ identical spatial and temporal discretization parameters, the contour levels use the same coloring schemes, *no* filtering or post-processing has been employed in any of the results, and finally no other treatments have been employed other than those described. . . . . 268

4-23 In color. Comparison of time evolving snapshots of the horizontal velocity field of (a) MA-SPH MLS density re-initialization, (b) mSPH with no smoothing, and (c) mSPH with smoothing every  $n = 5$  time steps. The artificial speed of sound is  $c = 26.46m/s$ , the kernel bandwidth is  $h = 0.025$ , the particle spacing is  $dx = 0.75h$  and the Courant condition  $\mu_c = 0.8$  for all simulations. Time increases from top to bottom. It is emphasized that all three simulations are initialized with the same initial conditions, employ identical spatial and temporal discretization parameters, the contour levels use the same coloring schemes, *no* filtering or post-processing has been employed in any of the results, and finally no other treatments have been employed other than those described. . . . . 269

4-24 In color. Comparison of time evolving snapshots of the horizontal velocity field of (a) MA-SPH MLS density re-initialization, (b) mSPH with no smoothing, and (c) mSPH with smoothing every  $n = 5$  time steps. The artificial speed of sound is  $c = 26.46m/s$ , the kernel bandwidth is  $h = 0.025$ , the particle spacing is  $dx = 0.75h$  and the Courant condition  $\mu_c = 0.8$  for all simulations. Time increases from top to bottom. It is emphasized that all three simulations are initialized with the same initial conditions, employ identical spatial and temporal discretization parameters, the contour levels use the same coloring schemes, *no* filtering or post-processing has been employed in any of the results, and finally no other treatments have been employed other than those described. . . . . 270

4-25 In color. Comparison of time evolving snapshots of the vertical velocity field of (left column) MA-SPH MLS density re-initialization, (middle column) mSPH with no smoothing, and (right column) mSPH with smoothing every  $n = 5$  time steps. The artificial speed of sound is  $c = 26.46m/s$ , the kernel bandwidth is  $h = 0.025$ , the particle spacing is  $dx = 0.75h$  and the Courant condition  $\mu_c = 0.8$  for all simulations. Time increases from top to bottom. It is emphasized that all three simulations are initialized with the same initial conditions, employ identical spatial and temporal discretization parameters, the contour levels use the same coloring schemes, *no* filtering or post-processing has been employed in any of the results, and finally no other treatments have been employed other than those described. . . . . 271

- 4-26 In color. Comparison of time evolving snapshots of the vertical velocity field of (left column) MA-SPH MLS density re-initialization, (middle column) mSPH with no smoothing, and (right column) mSPH with smoothing every  $n = 5$  time steps. The artificial speed of sound is  $c = 26.46m/s$ , the kernel bandwidth is  $h = 0.025$ , the particle spacing is  $dx = 0.75h$  and the Courant condition  $\mu_c = 0.8$  for all simulations. Time increases from top to bottom. It is emphasized that all three simulations are initialized with the same initial conditions, employ identical spatial and temporal discretization parameters, the contour levels use the same coloring schemes, *no* filtering or post-processing has been employed in any of the results, and finally no other treatments have been employed other than those described. . . . . 272
- 4-27 In color. Comparison of time evolving snapshots of the vertical velocity field of (left column) MA-SPH MLS density re-initialization, (middle column) mSPH with no smoothing, and (right column) mSPH with smoothing every  $n = 5$  time steps. The artificial speed of sound is  $c = 26.46m/s$ , the kernel bandwidth is  $h = 0.025$ , the particle spacing is  $dx = 0.75h$  and the Courant condition  $\mu_c = 0.8$  for all simulations. Time increases from top to bottom. It is emphasized that all three simulations are initialized with the same initial conditions, employ identical spatial and temporal discretization parameters, the contour levels use the same coloring schemes, *no* filtering or post-processing has been employed in any of the results, and finally no other treatments have been employed other than those described. . . . . 273

4-28 In color. Comparison of time evolving snapshots of the vertical velocity field of (left column) MA-SPH MLS density re-initialization. (middle column) mSPH with no smoothing, and (right column) mSPH with smoothing every  $n = 5$  time steps. The artificial speed of sound is  $c = 26.46m/s$ , the kernel bandwidth is  $h = 0.025$ , the particle spacing is  $dx = 0.75h$  and the Courant condition  $\mu_c = 0.8$  for all simulations. Time increases from top to bottom. It is emphasized that all three simulations are initialized with the same initial conditions, employ identical spatial and temporal discretization parameters, the contour levels use the same coloring schemes, *no* filtering or post-processing has been employed in any of the results, and finally no other treatments have been employed other than those described. . . . . 274

4-29 In color. Comparison of time evolving snapshots of the vertical velocity field of (left column) MA-SPH MLS density re-initialization. (middle column) mSPH with no smoothing, and (right column) mSPH with smoothing every  $n = 5$  time steps. The artificial speed of sound is  $c = 26.46m/s$ , the kernel bandwidth is  $h = 0.025$ , the particle spacing is  $dx = 0.75h$  and the Courant condition  $\mu_c = 0.8$  for all simulations. Time increases from top to bottom. It is emphasized that all three simulations are initialized with the same initial conditions, employ identical spatial and temporal discretization parameters, the contour levels use the same coloring schemes, *no* filtering or post-processing has been employed in any of the results, and finally no other treatments have been employed other than those described. . . . . 275

- 4-30 In color. Comparison of time evolving snapshots of the horizontal accelerations of (a) MA-SPH with MLS density re-initialization, (b) mSPH with no smoothing, and (c) mSPH with smoothing every  $n = 5$  time steps. The artificial speed of sound is  $c = 26.46m/s$ , the kernel bandwidth is  $h = 0.025$ , the particle spacing is  $dx = 0.75h$  and the Courant condition  $\mu_c = 0.8$  for all simulations. Time increases from top to bottom. It is emphasized that all three simulations are initialized with the same initial conditions, employ identical spatial and temporal discretization parameters, the contour levels use the same coloring schemes, *no* filtering or post-processing has been employed in any of the results, and finally no other treatments have been employed other than those described. . . . . 276
- 4-31 In color. Comparison of time evolving snapshots of the horizontal accelerations of (a) MA-SPH with MLS density re-initialization, (b) mSPH with no smoothing, and (c) mSPH with smoothing every  $n = 5$  time steps. The artificial speed of sound is  $c = 26.46m/s$ , the kernel bandwidth is  $h = 0.025$ , the particle spacing is  $dx = 0.75h$  and the Courant condition  $\mu_c = 0.8$  for all simulations. Time increases from top to bottom. It is emphasized that all three simulations are initialized with the same initial conditions, employ identical spatial and temporal discretization parameters, the contour levels use the same coloring schemes, *no* filtering or post-processing has been employed in any of the results, and finally no other treatments have been employed other than those described. . . . . 277

4-32 In color. Comparison of time evolving snapshots of the horizontal accelerations of (a) MA-SPH with MLS density re-initialization, (b) mSPH with no smoothing, and (c) mSPH with smoothing every  $n = 5$  time steps. The artificial speed of sound is  $c = 26.46m/s$ , the kernel bandwidth is  $h = 0.025$ , the particle spacing is  $dx = 0.75h$  and the Courant condition  $\mu_c = 0.8$  for all simulations. Time increases from top to bottom. It is emphasized that all three simulations are initialized with the same initial conditions, employ identical spatial and temporal discretization parameters, the contour levels use the same coloring schemes, *no* filtering or post-processing has been employed in any of the results, and finally no other treatments have been employed other than those described. . . . . 278

4-33 In color. Comparison of time evolving snapshots of the horizontal accelerations of (a) MA-SPH with MLS density re-initialization, (b) mSPH with no smoothing, and (c) mSPH with smoothing every  $n = 5$  time steps. The artificial speed of sound is  $c = 26.46m/s$ , the kernel bandwidth is  $h = 0.025$ , the particle spacing is  $dx = 0.75h$  and the Courant condition  $\mu_c = 0.8$  for all simulations. Time increases from top to bottom. It is emphasized that all three simulations are initialized with the same initial conditions, employ identical spatial and temporal discretization parameters, the contour levels use the same coloring schemes, *no* filtering or post-processing has been employed in any of the results, and finally no other treatments have been employed other than those described. . . . . 279

- 4-34 In color. Comparison of time evolving snapshots of the horizontal accelerations of (a) MA-SPH with MLS density re-initialization, (b) mSPH with no smoothing, and (c) mSPH with smoothing every  $n = 5$  time steps. The artificial speed of sound is  $c = 26.46m/s$ , the kernel bandwidth is  $h = 0.025$ , the particle spacing is  $dx = 0.75h$  and the Courant condition  $\mu_c = 0.8$  for all simulations. Time increases from top to bottom. It is emphasized that all three simulations are initialized with the same initial conditions, employ identical spatial and temporal discretization parameters, the contour levels use the same coloring schemes, *no* filtering or post-processing has been employed in any of the results, and finally no other treatments have been employed other than those described. . . . . 280
- 4-35 In color. Comparison of time evolving snapshots of the vertical accelerations of (a) MA-SPH with MLS density re-initialization, (b) mSPH with no smoothing, and (c) mSPH with smoothing every  $n = 5$  time steps. The artificial speed of sound is  $c = 26.46m/s$ , the kernel bandwidth is  $h = 0.025$ , the particle spacing is  $dx = 0.75h$  and the Courant condition  $\mu_c = 0.8$  for all simulations. Time increases from top to bottom. It is emphasized that all three simulations are initialized with the same initial conditions, employ identical spatial and temporal discretization parameters, the contour levels use the same coloring schemes, *no* filtering or post-processing has been employed in any of the results, and finally no other treatments have been employed other than those described. . . . . 281

- 4-36 In color. Comparison of time evolving snapshots of the vertical accelerations of (a) MA-SPH with MLS density re-initialization, (b) mSPH with no smoothing, and (c) mSPH with smoothing every  $n = 5$  time steps. The artificial speed of sound is  $c = 26.46m/s$ , the kernel bandwidth is  $h = 0.025$ , the particle spacing is  $dx = 0.75h$  and the Courant condition  $\mu_c = 0.8$  for all simulations. Time increases from top to bottom. It is emphasized that all three simulations are initialized with the same initial conditions, employ identical spatial and temporal discretization parameters, the contour levels use the same coloring schemes, *no* filtering or post-processing has been employed in any of the results, and finally no other treatments have been employed other than those described. . . . . 282
- 4-37 In color. Comparison of time evolving snapshots of the vertical accelerations of (a) MA-SPH with MLS density re-initialization, (b) mSPH with no smoothing, and (c) mSPH with smoothing every  $n = 5$  time steps. The artificial speed of sound is  $c = 26.46m/s$ , the kernel bandwidth is  $h = 0.025$ , the particle spacing is  $dx = 0.75h$  and the Courant condition  $\mu_c = 0.8$  for all simulations. Time increases from top to bottom. It is emphasized that all three simulations are initialized with the same initial conditions, employ identical spatial and temporal discretization parameters, the contour levels use the same coloring schemes, *no* filtering or post-processing has been employed in any of the results, and finally no other treatments have been employed other than those described. . . . . 283

- 4-38 In color. Comparison of time evolving snapshots of the vertical accelerations of (a) MA-SPH with MLS density re-initialization, (b) mSPH with no smoothing, and (c) mSPH with smoothing every  $n = 5$  time steps. The artificial speed of sound is  $c = 26.46m/s$ , the kernel bandwidth is  $h = 0.025$ , the particle spacing is  $dx = 0.75h$  and the Courant condition  $\mu_c = 0.8$  for all simulations. Time increases from top to bottom. It is emphasized that all three simulations are initialized with the same initial conditions, employ identical spatial and temporal discretization parameters, the contour levels use the same coloring schemes, *no* filtering or post-processing has been employed in any of the results, and finally no other treatments have been employed other than those described. . . . . 284
- 4-39 In color. Comparison of time evolving snapshots of the vertical accelerations of (a) MA-SPH with MLS density re-initialization, (b) mSPH with no smoothing, and (c) mSPH with smoothing every  $n = 5$  time steps. The artificial speed of sound is  $c = 26.46m/s$ , the kernel bandwidth is  $h = 0.025$ , the particle spacing is  $dx = 0.75h$  and the Courant condition  $\mu_c = 0.8$  for all simulations. Time increases from top to bottom. It is emphasized that all three simulations are initialized with the same initial conditions, employ identical spatial and temporal discretization parameters, the contour levels use the same coloring schemes, *no* filtering or post-processing has been employed in any of the results, and finally no other treatments have been employed other than those described. . . . . 285

- 4-40 In color. Comparison of time evolving snapshots of the pressure field of (a) MA-SPH with MLS density re-initialization, (b) mSPH with no smoothing, and (c) mSPH with smoothing every  $n = 5$  time steps. The artificial speed of sound is  $c = 26.46m/s$ , the kernel bandwidth is  $h = 0.025$ , the particle spacing is  $dx = 0.75h$  and the Courant condition  $\mu_c = 0.8$  for all simulations. Time increases from top to bottom. It is emphasized that all three simulations are initialized with the same initial conditions, employ identical spatial and temporal discretization parameters, the contour levels use the same coloring schemes, *no* filtering or post-processing has been employed in any of the results, and finally no other treatments have been employed other than those described. . . . . 286
- 4-41 In color. Comparison of time evolving snapshots of the pressure field of (a) MA-SPH with MLS density re-initialization, (b) mSPH with no smoothing, and (c) mSPH with smoothing every  $n = 5$  time steps. The artificial speed of sound is  $c = 26.46m/s$ , the kernel bandwidth is  $h = 0.025$ , the particle spacing is  $dx = 0.75h$  and the Courant condition  $\mu_c = 0.8$  for all simulations. Time increases from top to bottom. It is emphasized that all three simulations are initialized with the same initial conditions, employ identical spatial and temporal discretization parameters, the contour levels use the same coloring schemes, *no* filtering or post-processing has been employed in any of the results, and finally no other treatments have been employed other than those described. . . . . 287

4-42 In color. Comparison of time evolving snapshots of the pressure field of (a) MA-SPH with MLS density re-initialization, (b) mSPH with no smoothing, and (c) mSPH with smoothing every  $n = 5$  time steps. The artificial speed of sound is  $c = 26.46m/s$ , the kernel bandwidth is  $h = 0.025$ , the particle spacing is  $dx = 0.75h$  and the Courant condition  $\mu_c = 0.8$  for all simulations. Time increases from top to bottom. It is emphasized that all three simulations are initialized with the same initial conditions, employ identical spatial and temporal discretization parameters, the contour levels use the same coloring schemes, *no* filtering or post-processing has been employed in any of the results, and finally no other treatments have been employed other than those described. . . . . 288

4-43 In color. Comparison of time evolving snapshots of the pressure field of (a) MA-SPH with MLS density re-initialization, (b) mSPH with no smoothing, and (c) mSPH with smoothing every  $n = 5$  time steps. The artificial speed of sound is  $c = 26.46m/s$ , the kernel bandwidth is  $h = 0.025$ , the particle spacing is  $dx = 0.75h$  and the Courant condition  $\mu_c = 0.8$  for all simulations. Time increases from top to bottom. It is emphasized that all three simulations are initialized with the same initial conditions, employ identical spatial and temporal discretization parameters, the contour levels use the same coloring schemes, *no* filtering or post-processing has been employed in any of the results, and finally no other treatments have been employed other than those described. . . . . 289

- 4-44 In color. Comparison of time evolving snapshots of the pressure field of (a) MA-SPH with MLS density re-initialization, (b) mSPH with no smoothing, and (c) mSPH with smoothing every  $n = 5$  time steps. The artificial speed of sound is  $c = 26.46m/s$ , the kernel bandwidth is  $h = 0.025$ , the particle spacing is  $dx = 0.75h$  and the Courant condition  $\mu_c = 0.8$  for all simulations. Time increases from top to bottom. It is emphasized that all three simulations are initialized with the same initial conditions, employ identical spatial and temporal discretization parameters, the contour levels use the same coloring schemes, *no* filtering or post-processing has been employed in any of the results, and finally no other treatments have been employed other than those described. . . . . 290
- 4-45 Comparisons of the evolution of  $Q(t)$  in an mSPH dam-break simulation without smoothing (red line) and with smoothing every  $n$  time steps for a constant Courant condition  $\mu = 0.8$  for all simulations. Smoothing periods  $n = [5, 10, 15, 20, 30, 50, 100]$ . . . . . 292
- 4-46 Comparison of free-surface elevation of the standard SPH dam-break benchmark with experimental results of [55] (black line) and mSPH simulation results without smoothing (red line) and with smoothing every  $n$  time steps for a constant Courant condition  $\mu = 0.8$  for all simulations. Smoothing periods  $n = [0, 5, 10, 15, 20, 30, 50, 100]$ . . . . . 293
- 4-47 Comparison of *unfiltered* wall impact pressures of the standard SPH dam-break benchmark with experimental results of [55] (black line) and mSPH simulation results with smoothing every  $n$  time steps for a constant Courant condition  $\mu = 0.8$  for all simulations. Smoothing periods  $n = [1, 2, 5]$ . . . . . 294

4-48 Comparison of *unfiltered* wall impact pressures of the standard SPH dam-break benchmark with experimental results of [55] (black line) and mSPH simulation results without smoothing (red line) and with smoothing every  $n$  time steps for a constant Courant condition  $\mu = 0.8$  for all simulations. Smoothing periods  $n = [0, 5, 10, 20]$ . It is pointed out that the mSPH simulation results without smoothing (red line) seem like a solid line due to the significant HFO of amplitude  $6 \cdot 10^4$  (not shown). . . . . 295

# List of Tables

2.1	Summary of kinematics and dynamics for incompressible and acoustic modes given a unit amplitude velocity potential. . . . .	78
2.2	Summary of the kinematics and dynamics for incompressible and high frequency acoustic modes, given a unit amplitude free-surface displacement. . . . .	79
2.3	Summary of the kinematics and dynamics for incompressible and high frequency acoustic modes, given a unit amplitude dynamic pressure. . . . .	80
2.4	Unstable growth rates . . . . .	178
3.1	MA-SPH linearized evolution equations for infinitesimal disturbances. Both direct and advanced density algorithms are considered. The disturbances are expanded into both oscillatory and exponentially decaying modes. The base flow is assumed to be uniform, the particles are lying in a uniform grid of spacing $h$ and their mass is $m = \rho_j h$ . . . . .	205
3.2	Classification and summary of effects of selected existing semi-empirical treatments to MA-SPH. . . . .	221

# Chapter 1

## Introduction

### 1.1 Motivation

There is strong engineering and scientific interest in studying violent free-surface flows, since such flows yield the highest hydrodynamic loads on marine structures and vehicles [16], play a dominant role in the evolution of coastlines [11], and enhance gas, heat and energy transfer between the ocean and the atmosphere [31].

However, violent free-surface flows remain poorly understood, as they are highly non-linear, transient, multi-scale, two-phase processes, involving multiply connected regions of air and water, rendering them practically intractable to mathematical analysis. In addition, they are of low experimental repeatability, highly oscillatory due to the air compressibility, and with unknown spatial and temporal scaling [16, 28, 31].

Advances in modern computers are establishing numerical methods as indispensable tools in the study of hydrodynamics. The existing numerical methods for the simulation of macro-scale free-surface flows are well established [22, 23]. In contrast, numerical methods for the simulation of complex meso-scale phenomena, such as wave overturning, jet spray, and droplet formations, and evolution of multiply connected regions of air and water, are an active area of research. Development of such meso-scale simulation methods is of significance importance in understanding meso-scale phenomena and eventually complementing the macro-scale methods in the simulation of larger-scale violent free-surface flows.

The main requirement for these meso-scale simulation methods is robustness in simulating free-surfaces of arbitrary complexity, which is a key property of meshless methods. Among existing meshless methods, the mature numerical simulation method Smoothed Particle Hydrodynamics (SPH) [5, 7] has proven over the past three decades that it can simulate robustly multi-scaled free-surfaces of arbitrary complexity. In addition, it is remarkably simple to program and highly efficient [42]. For these reasons SPH is of increasing popularity (Annual International SPHERIC Workshops, 2006-2010), and is used for violent meso-scale simulations across many different disciplines [42], including astrophysics, hydrodynamics, magnetohydrodynamics, gas explosions, and granular flows.

SPH was initially developed for the simulation of polytropic stellar models, i.e., unbounded, compressible flows due to inviscid pressure gradients, as well as gravitational, rotational and magnetic body forces [5, 7]. In SPH the domain is discretized into a set of  $N$  Lagrangian fluid particles, which carry their own time-constant mass  $m$  and time-evolving field properties, such as position  $\mathbf{x}$ , velocity  $\mathbf{u}$  and density  $\rho$ . The uniqueness of SPH is that the density  $\rho_a$  of a Lagrangian particle  $a$  is computed by convolving the mass of neighboring particles  $b$  with a smooth, distance Kernel function  $W$  without the use of grids, i.e.,  $\rho_a = \sum_b m_b W_{ab}$ . The technique is called Kernel Interpolation and is further extended to compute the gradient of a field property  $\nabla f_a$  at the Lagrangian particle  $a$  (collocation point) by convolving the values of the function at neighboring particles  $b$  with the derivative of the Kernel function, i.e.,  $\widehat{\nabla} f_a = \sum_b f_b \frac{m_b}{\rho_b} \nabla W_{ab}$ . The position  $\mathbf{x}_a$  and velocity  $\mathbf{u}_a$  of particle  $a$  are computed by integrating in time the inviscid Euler momentum equations. Explicit constitutive relations are used to compute the gravitational, rotational, and magnetic body forces that appear in the Euler momentum equations, while their corresponding gradients at each Lagrangian particle  $a$  are computed with the Kernel Interpolation technique.

In summary, the SPH algorithm described in [5, 7] is explicit, of order  $N$  computation count, and very simple to code. In addition, even though it was initially regarded as a Monte Carlo integration method with expected first order convergence, the numerical applications demonstrated second order convergence. Without appro-

priately explaining the second order convergence of Kernel Interpolation [25], SPH was extended to numerous, more complex physical models.

In particular, SPH is extended to incompressible, free-surface hydrodynamic flows in [14], demonstrating robustness in simulating highly non-linear, complex free-surfaces. To maintain the simplicity of the initial SPH algorithm for astrophysical flows [5, 7], the author in [14] makes three fundamental assumptions. In the first assumption, it introduces an *artificial* speed of sound and an *artificial* Equation of State to decouple the pressure from the velocity and maintain the explicit nature of the algorithm. The effect of this first simplification in the accuracy of the simulated physics is still poorly understood [1, 2].

As a reference, it is noted here that the established incompressible Navier-Stokes solvers include [22, 23]: (a) pressure correction methods, where a Poisson equation for the pressure is formulated and solved for, requiring knowledge of the free-surface position and matrix inversion; (b) vortex methods that eliminate pressure and solve for the vorticity  $\omega$ ; and (c) the artificial compressibility methods where first an artificial Equation of State is added, transforming the problem to hyperbolic, and next the system is iterated in a pseudo-time until incompressibility is obtained. In that sense, the introduction of an *artificial* Equation of State can be regarded as a special non-iterative case of the artificial compressibility methods.

In the second assumption, the author extends the computation of derivatives with Kernel Interpolation to free-surface particles, where it is known that Kernel Interpolation diverges [51]. The method does not explicitly track, define, or employ any special treatment on the free-surface, essentially imposing an unknown artificial dynamic free-surface boundary condition [21].

In the third assumption, the author models the no-flux boundary conditions with tunable, highly-sensitive to the parameters, Lennard-Jones molecular-type potential forces. Even though more physical boundary condition have since been developed [13, 41, 48], this assumption established the empirical nature of SPH, where several problem-dependant, tunable, and semi-empirical treatments are developed to address issues manifested in simulations.

In summary, SPH is an attractive, meso-scale simulation method that has demonstrated the ability to capture free-surfaces of arbitrary complexity with a simple and robust algorithm [42]. The simplicity and robustness of SPH for free-surface flows are due to (a) the weak compressibility assumption and (b) the assumption that the Kernel Interpolation can be employed without any modifications on the free-surface. The coupling of these two assumptions introduces a set of coupled, unknown errors that firstly result in a series of accuracy, consistency and stability issues, and secondly render the analysis of the SPH method for free-surface flows challenging since it requires a unified approach that accounts for the interaction between the modeling and discretization errors. Up to now, no unified analysis on SPH existed, for example, the accuracy errors due to the weak compressibility assumption have not been appropriately analyzed, the flow properties are ignored in the consistency analysis of the Kernel Interpolation, and the stability analysis is informed by the properties of weakly compressible free-surface flows.

A brief sketch of the existing accuracy, consistency and stability analysis is given here. Regarding the accuracy of the method, it is a well established fact that the SPH dynamic results are plagued by spurious, leading order, high frequency oscillations, rendering them practically unusable without filtering [2, 13, 20, 32, 33, 34, 36, 39]. To the author's knowledge the only reference on the relation of the weak compressibility assumption to these spurious high frequency oscillations is made in [1, 2]. However, no further analysis is attempted in understanding their physics, origins and growth mechanisms in discrete space.

The existing consistency analysis of Kernel Interpolation for prescribed particle distributions is extensive and proves consistency inside the domain of a uniform particle distribution, e.g., [29, 52], and divergence in the presence of boundaries and random particle distributions, e.g., [52]. Numerical findings, however, indicate that SPH is convergent even though the particle distributions eventually become distorted. The seeming discrepancy between the analysis and the numerical results indicates that the behavior of Kernel Interpolation in an SPH simulation is not yet understood. The issue is only mentioned in [25] and addressed in [17]. The, unfortunately not widely

referenced, work of [17] presents the only analysis that points towards the right direction, but is limited to one-dimensional problems without obvious extensions to higher dimensions, and does not relate the consistency properties to the flow properties. Therefore, because the existing consistency analysis of Kernel Interpolation in non-uniform particle distributions is limited, there is uncertainty on the consistency behavior of Kernel Interpolation in an SPH simulation where the particles eventually depart from their initial prescribed configuration.

Lastly, it is a well established fact that SPH is unstable. The existing stability analysis determines that a general SPH algorithm suffers from a tensile instability due to the spatial discretization technique [17, 40, 44, 53]. In [26] a tensile instability treatment is suggested, which does not seem to have any significant effect for the free-surface flows of interest [3, 26], indicating that there must be problem-specific properties in the stability of weakly compressible free-surface flows. In addition, the stability analysis does not distinguish between the continuous model, semi-discrete and fully-discrete algorithms. Therefore, (a) the finding that the spatial discretization technique is responsible for the tensile instability should not be conclusive, (b) the properties of different temporal integration schemes have not been studied, and (c) the analysis does not account for the Courant conditions. In short, the existing stability analysis is not sufficiently identifying the sources of instability in the free-surface flows of interest.

Due to the lack of a known, unified, and conclusive analysis of the method, and in agreement with the initial approach of [14], several semi-empirical treatments have been developed to alleviate the accuracy, consistency, and stability issues in SPH. These existing treatments, in general, introduce tunable parameters further adding to the uncertainty currently associated to the method. Representative examples of semi-empirical existing treatments include the addition of small terms on the right hand sides of the governing equations, such as XSPH [24], Artificial Viscosity [30], stability treatments [26, 37], density re-initialization schemes [1, 48], and local, post-processing filtering of the pressure results [20, 32, 33, 34, 36, 39]. The current State-of-the-Art SPH codes, such as SPHysics, include choices on the majority of the existing

semi-empirical treatments making a numerical analysis of the State-of-the-Art SPH method seemingly intractable and very difficult to distinguish in the simulation results between the actual physics modeled and the effects of the numerical treatments.

Therefore, despite its attractiveness, SPH in its current form lacks a conclusive analysis and has a number of key issues that must be overcome before the method can realize its full potential in applications for the prediction of violent free-surface flows.

## 1.2 Thesis scope

The scope of this thesis is threefold. First, it defines a main SPH algorithm, MA-SPH, which is free of existing semi-empirical treatments, and performs a detailed and thorough numerical analysis on MA-SPH. This analysis allows us to clearly identify the key issues, the sources of error, and the first quantitative error estimates in an SPH simulation. Second, based on the findings of the analysis, this thesis defines a rational approach towards analyzing the effects of the existing treatments by classifying them with respect to the issues they address and by analyzing them only within this context. Third, based on the findings of the analysis and the insight gained from the rationale of the existing treatments, this thesis proposes convergent SPH schemes for the simulation of violent free-surface flows.

The importance of this work is twofold: firstly, it removes the uncertainty currently associated with the SPH, providing a unified framework for a rational analysis of the method for incompressible free-surface flows; and secondly, and most importantly, it provides the foundation for the development of SPH as a valuable engineering tool in the study of violent free-surface flows.

## 1.3 Thesis structure

The thesis is structured into four chapters.

In Chapter 2, a main SPH algorithm is defined. First, the weak compressibility

assumption is validated for continuous, linear, plane-progressive free-surface waves. It is shown that in continuous space, in addition to the incompressible solution, the method admits a set of high frequency oscillatory acoustic modes. Next, the consistency of Kernel Interpolation is considered in (a) uniform, (b) highly distorted, and (c) smoothly advected particle distributions, proving the consistency of Kernel Interpolation in a SPH simulation, where the particles have been smoothly advected from their initial configuration, for the first time. In addition, the implicit dynamic free-surface boundary condition due to the incompleteness of the Kernel Interpolation near the free-surface is determined as a function of the free-surface gradient. Finally, the stability of the continuous, semi-discrete, and fully-discrete schemes are considered determining that SPH is unconditionally unstable in the presence of (a) a free-surface and (b) non-zero base density gradients, which is a generalization of the tensile instability and specifically for the free-surface flows of interest the base density distribution reduces to hydrostatic.

In Chapter 3, several existing semi-empirical treatments are considered. They are classified as accuracy, consistency, and stability treatments and then briefly analyzed within the context of the issue they address. The considered accuracy treatments are local, post-processing techniques of the pressure results. The effective ones are those considering temporal filtering. The considered consistency treatments are shown to increase accuracy but are found to be less robust than Kernel Interpolation in numerical simulations of highly distorted flows. Finally, the findings of the stability treatments indicate that even though the weakly compressible SPH model is inherently unstable for free-surface flows, numerical regularization is possible.

In Chapter 4, based on the findings of Chapters 2 and 3, we propose and validate two rational approaches towards constructing convergent SPH schemes. The first is an approach directing towards stable, low order, modified SPH schemes, and the second approach is directing towards stable, higher order, weakly compressible schemes.

Finally, Chapter 5 summarizes the findings of the analysis and provides suggestions for future work.



## Chapter 2

# Linear analysis of a main SPH algorithm, MA-SPH, for free-surface flows

### 2.1 Introduction

Smoothed Particle Hydrodynamics has two key features. The first feature is a weak compressibility assumption in the continuous model that makes the algorithm explicit, efficient and simple. The second feature is the Kernel Interpolation technique for the estimation of spatial derivatives on discrete Lagrangian particles that allows for the method to be entirely meshless and robust. Despite their attractiveness these two key features of SPH introduce major issues and uncertainties with respect to the accuracy, consistency, and stability of the method. Accuracy issues are most evident in the dynamics that are plagued by large amplitude high frequency oscillations. Consistency issues arise as the Lagrangian particles depart from the initial uniform distribution or approach the free-surface. Stability issues eventually manifest in all long-time SPH simulations [21]. The known, existing analysis on SPH deals only with consistency and stability and is neither complete or conclusive: first, the findings of the consistency analysis differ from numerical findings, and second, the conclusions

from the stability analysis do not help remove the method's instabilities.

In detail, the existing consistency analysis shows that SPH is a low order method [18, 27, 51] that diverges near the boundaries [51]. Yet, convergence has been demonstrated in numerical applications [1]. However, the literature on addressing this discrepancy between the analysis and the numerical findings, by accounting for the motion of the particles, is limited [17, 25, 40]. To address the uncertainty currently associated with the consistency of SPH researchers employ alternative known consistent schemes [18] which however affect the robustness of SPH. It is therefore of great importance to perform a conclusive consistency analysis of the method.

The existing stability analysis identifies a so-called tensile instability dominant in solid and gas dynamics [17, 40, 44, 53]. The instability is defined in terms of both numerical and physical quantities. Treatments suggested in [18, 26, 37] do not seem to address stability issues in the simulations of free-surface flows [3, 48]. Given that the instability of the method is largely mentioned [48] and that up to now SPH cannot even simulate a hydrostatic case [21] it is imperative to perform a complete and conclusive stability analysis of the method.

This chapter presents a unified and detailed analysis of the accuracy, consistency, and stability of the SPH main algorithm both in its continuous and discrete form. First, a main algorithm is defined in section 2.2. Then the framework of the analysis is detailed in section 2.3. The accuracy errors due to the first key feature of SPH, the weak compressibility assumption, are detailed in continuous space and their behavior in discrete space is discussed in section 2.4. Next, in section 2.5 the consistency of the second key feature of SPH, the Kernel Interpolation technique, is analyzed in discrete space for bounded and unbounded particle distributions considering three types of distributions, regular, random, and smoothly advected. Finally, a stability analysis of the method is performed in section 2.6 on the continuous, semi-discrete algorithm and fully-discrete algorithm with alternative temporal integration schemes, for two different formulations of the algorithm.

## 2.2 Definition of MA-SPH

The term Smoothed Particle Hydrodynamics (SPH) has evolved to refer to a somewhat general group of meshless Lagrangian Navier-Stokes numerical simulation methods. Various different combinations of meshless methods for derivative estimation in discrete space employing different pressure solvers coupled with different stability and accuracy treatments are often called SPH. For example, derivative estimation techniques include Kernel Interpolation, Moving Least Squares and Corrected Kernels. Pressure solvers are, for example, non-iterative artificial compressibility, pressure correction. Typical SPH stability and accuracy treatments are described by the addition of terms on the right hand side of the evolution equations (e.g., artificial viscosity and velocity smoothing) or the use of density re-initialization schemes. The above methods are often referred to with self-explanatory acronyms followed by SPH, for example, I-SPH (incompressible pressure correction solver), MLSPH (Moving Least Squares for derivative estimation [18]), XSPH (for smoothed velocity treatment [24]).

To perform an analysis of the method for gravity free-surface flows, first a canonical wave problem and second a reference form of the SPH algorithm need to be defined. For the canonical problem, linear gravity free-surface waves in a semi-infinite domain are chosen. The Lagrangian weakly compressible Euler solver that employs Kernel Interpolation for the computation of spatial derivatives [30] is chosen as the Main Algorithm, referred to hereafter as MA-SPH or simply MA. The effects of the developed treatments are studied separately in Chapter 3. This section details the assumptions and definitions that will be used throughout this chapter.

### 2.2.1 Problem statement

**Domain** Assume a two-dimensional Cartesian coordinate system  $\vec{x} = (x, y)$ , with  $y$  pointing vertically upwards. Consider an undisturbed fluid domain infinite in the horizontal direction  $x$  and bounded in the vertical direction  $y \in [-H, 0]$ . Let  $\eta = \eta(x, t)$  denote the location of the free-surface, where  $\eta = y = 0$  denotes the location of the undisturbed free-surface  $\partial_{\text{fs}}$ . Further, let  $y = -H$  denote the location of the

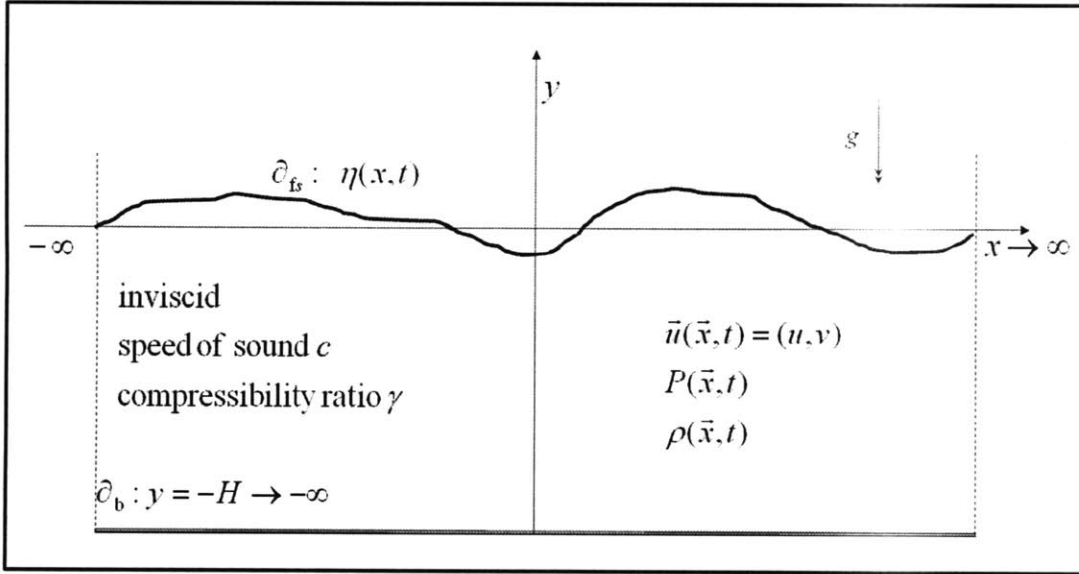


Figure 2-1: Weakly compressible, gravity free-surface flow. Problem statement.

**Unknowns** Let  $t > 0$  denote time. Assume a flow where  $\vec{u}(\vec{x}, t) = (u, v)$ ,  $P(\vec{x}, t)$  and  $\rho(\vec{x}, t)$  denote the unknown fluid velocity, pressure and density respectively at  $(\vec{x}, t)$ .

**Definitions and assumptions** Let  $\vec{g} = -g\hat{j}$ ,  $\rho_f$  and  $P_o$  denote the gravitational acceleration, the undisturbed fluid density and pressure at the free-surface, respectively. Let the bottom be impermeable and located at  $y = -H$ .

If the flow is assumed to be inviscid and incompressible the governing equations are the momentum Euler equations and the continuity equation. In the latter system the velocity and pressure are coupled. Typically, in numerical simulations this translates to the solution of a Poisson equation for the pressure, which involves the inversion of a matrix and implies free-surface tracking. If the flow is assumed to be isothermal and weakly compressible with a known speed of sound  $c$  and a compressibility ratio  $\gamma$ , then it is described by the Euler equation for the momentum, the conservation of mass for the density, and a constitutive Equation of State that relates pressure and

density fluctuations through  $c$  and  $\gamma$ . The numerical simulation of such flow can be explicit, it is simpler to program and more efficient. In [30] it is argued, based on dimensional analysis, that any incompressible flow can be modeled in a numerical simulation as weakly compressible with an error of order  $O(1/c^2)$  as long as the Mach number is small  $\mathcal{M} \equiv \frac{|\vec{u}|_{max}}{c} \ll 1$ , significantly simplifying the computational cost and complexity. Based on the latter argument, [30] suggests modeling incompressible flows as weakly compressible introducing a modeling error of order  $O(1/c^2)$ . The latter assumption, referred to as the weak compressibility assumption, is a key feature of SPH and is revisited in detail in section 2.4. It must be emphasized that  $c$  need not be the actual speed of sound in water. In fact, it is desirable that  $c$  is chosen to be as small as possible, e.g.,  $c \sim 10|\vec{u}|_{max}$  for numerical efficiency determined by a Courant condition. In the same manner an artificial Equation of State can be employed.

Denoting  $\frac{d}{dt}$  as the total or material derivative, i.e.,  $\frac{d}{dt} \equiv \frac{\partial}{\partial t} + \vec{u} \cdot \nabla$ , the governing equations for this weakly compressible flow are:

$$\frac{d\vec{u}}{dt} = -\frac{1}{\rho}\nabla P - \vec{g} \quad (2.1)$$

$$\frac{d\rho}{dt} = -\rho\nabla \cdot \vec{u} \quad (2.2)$$

No simple, analytic Equation of State (EoS) that relates the thermodynamic (total) pressure to the fluid density is known for water. However, for isothermal water flows two EoS are predominantly used within the context of SPH. The first, employed in the majority of SPH literature [3, 4, 30] is the Tait EoS for ideal gases:

$$P = c^2 \rho_f \left[ \left( \frac{\rho}{\rho_f} \right)^\gamma - 1 \right] \quad (2.3)$$

where the fluid is assumed to have a compressibility ratio  $\gamma$ , with a typical value of  $\gamma = 7$ .

The second follows the traditional fluid dynamics approach, [38, 46] relating

changes in pressure to changes in density with an equation of the form

$$dP = c^2 d\rho. \quad (2.4)$$

It can be shown that (2.3) and (2.4) are equivalent to leading order under the weak compressibility assumption, i.e., small density fluctuations. Namely, let the normalized density fluctuations be denoted as  $r \equiv \frac{\rho - \rho_f}{\rho_f} \ll 1$ . Therefore  $\rho = \rho_f(1 + r)$  and  $d\rho = \rho_f dr$ . Differentiating (2.3) obtains

$$\begin{aligned} dP &= c^2 \rho_f d \left[ \left( \frac{\rho}{\rho_f} \right)^\gamma - 1 \right] \\ &= c^2 \left( \frac{\rho}{\rho_f} \right)^{\gamma-1} d\rho \\ &= c^2 \rho_f (1 + r)^{\gamma-1} dr. \end{aligned}$$

Since  $\gamma > 1$  and  $r \ll 1$  it is valid to use Taylor Series Expansion about  $r = 0$ :

$$(1 + r)^{\gamma-1} dr \cong (1 + (\gamma - 1)r + O(r^2)) dr \cong dr + O(r^2).$$

Therefore,

$$dP = c^2 \rho_f d \left[ \left( \frac{\rho}{\rho_f} \right)^\gamma - 1 \right] \cong c^2 \rho_f dr = c^2 d\rho.$$

Both formulations of the Equation of State (2.3) and (2.4) are used hereafter. However, since all analysis in the following sections is linear, the results obtained are valid for both formulations of the EoS. The governing equations (2.1), (2.2) and the EoS (2.4) describe the continuous form of the main SPH algorithm and are referred to hereafter CMA-SPH.

### 2.2.2 Spatial discretization

In Lagrangian methods, like SPH, the evolution of a set of discrete fluid particles is followed in time. The flow is discretized into  $N \gg 1$  fluid particles, with each particle

$a$  carrying its own constant mass  $m_a$ . Let the center of mass of particle  $a$  be initially located at  $\vec{x}_a^0 = \vec{x}_a(t=0)$  and at time  $t$  be located at  $\vec{x}_a(t)$ . Let  $\rho_a(t)$ ,  $P_a(t)$ , and  $\vec{u}_a(t)$  denote the density, pressure and fluid velocity at  $\vec{x}_a(t)$ . Finally, let  $\forall_a(t) = m_a/\rho_a(t)$  denote the volume of particle  $a$ . From the governing equations (2.1), (2.2) and the EoS (2.4) the equations of motion for the position, velocity, density and pressure for each particle  $a$  become:

$$\frac{d\vec{x}_a}{dt} = \vec{u}_a \quad (2.5)$$

$$\frac{d\vec{u}_a}{dt} = -\frac{1}{\rho_a} \nabla P|_a - \vec{g} \quad (2.6)$$

$$\frac{d\rho_a}{dt} = -\rho_a \nabla \cdot \vec{u}|_a \quad (2.7)$$

$$P_a = c^2 d\rho_a. \quad (2.8)$$

Given that  $\frac{1}{\rho} \nabla P = \nabla \frac{P}{\rho} + \frac{P}{\rho^2} \nabla \rho$  the velocity equation (2.6) can also be written as:

$$\frac{d\vec{u}_a}{dt} = -\left( \nabla \frac{P}{\rho} + \frac{P}{\rho^2} \nabla \rho \right) \Big|_a - \vec{g}. \quad (2.9)$$

In order to compute the momentum and density rate of change and evolve the flow in time the terms  $\nabla P|_a$  and  $\nabla \cdot \vec{u}|_a$  must be computed in discrete space at each particle location. In MA-SPH this is achieved with the usage of the Kernel Interpolation technique, hereafter referred to as KI, without the usage of any underlying grid. To define KI, assume a smooth function  $f(\vec{x})$ , such that  $f_a = f(\vec{x}_a)$  and  $\nabla f_a = \nabla f|_{\vec{x}_a}$ . Let  $h$  be a measure of the average fluid particle volume  $\forall$ , such that  $h^2 \sim O(\forall)$ . Let  $W(\vec{x}; h)$  denote a known, analytic Kernel function that is (i) sufficiently smooth, (ii) normalized, and (iii) scales as  $O(\forall)$ , so that in the limit  $h \rightarrow 0$ , the Kernel function  $W$  behaves as a delta function. Further, let  $W$  have compact support of  $O(h)$  and hence refer to  $h$  as the Kernel bandwidth. Finally, define  $\nabla W_{ba} \equiv \nabla W|_{(\vec{x}_b - \vec{x}_a; h)}$  and

$$\widehat{\nabla} f_a \equiv \sum_{b=1}^N f_b \frac{m_b}{\rho_b} \nabla W_{ba}. \quad (2.10)$$

For the case of equi-spaced particles it has been shown that  $\widehat{\nabla}f_a \cong \nabla f_a + O(h^\ell)$  where  $\ell$  is determined by the shape of  $W$  [29]. This statement will be discussed in great detail in section 2.5 and will be extended to non equi-spaced particles. However, for now, it suffices to state that the gradient  $\nabla f_a$  can be computed with accuracy  $O(h^\ell)$  given the values of  $f_b$  at known discrete particles  $b$  within the neighborhood of  $a$  and the known, calculable weight  $\nabla W_{ba}$ . Therefore, the derivatives appearing in (2.6) and (2.7) are approximated in discrete space from (2.10) given the values of  $f$  at neighboring points  $b$ . Namely,

$$\frac{d\vec{x}_a}{dt} = \vec{u}_a \quad (2.11)$$

$$\frac{d\vec{u}_a}{dt} = -\frac{1}{\rho_a} \sum_b^N P_b \frac{m_b}{\rho_b} \nabla W_{ba} - \vec{g} \quad (2.12)$$

$$\frac{d\rho_a}{dt} = -\rho_a \sum_b^N \frac{m_b}{\rho_b} \vec{u}_b \cdot \nabla W_{ba} \quad (2.13)$$

$$P_a = c^2 d\rho_a. \quad (2.14)$$

The alternative form of the Euler equation (2.9) in discrete space becomes

$$\frac{d\vec{u}_a}{dt} = -\sum_b^N m_b \left( \frac{P_b}{\rho_b^2} + \frac{P_a}{\rho_a^2} \right) \nabla W_{ba} - \vec{g}. \quad (2.15)$$

Both forms of the Euler equations (2.12) and (2.15) are generally equivalent inside the domain, but differ on the implementation of the dynamic free-surface boundary conditions. Therefore, this analysis considers either one of the two forms and can be easily extended to the omitted form. It is noted that in practice it is argued that (2.15) conserves global momentum exactly [27] and as a result most simulations in the literature employ (2.15).

Finally, it is noted that generally in the absence of a free-surface, the density is computed from:

$$\rho_a = \sum_b m_b W_{ab} \quad (2.16)$$

It is shown that (2.13) is simply the time rate of change of (2.16) and therefore the

two expressions are in general equivalent. However, they *may* result in different simulation results due to (a) differences in the consistency of Kernel Interpolation when used for interpolation and differentiation, (b) errors due to the temporal integration scheme, and (c) differences in the stability behavior. Assuming that differences in stability behavior are the leading order difference between (2.13) and (2.16), both expressions are considered in the stability analysis of the semi-discrete and fully-discrete algorithms. Notation-wise, when the MA-SPH governing equations are (2.11), (2.13), and (2.12) or (2.15) the algorithm is referred to as MA-SPH with advanced density formulation and when the MA-SPH governing equations are (2.11), (2.16), and (2.12) or (2.15) the algorithm is referred to as MA-SPH with direct density formulation.

### 2.2.3 Boundary conditions

The boundary conditions for an inviscid free-surface flow governed by (2.1) and (2.2) are (i) the no flux on impermeable boundaries  $\vec{u} \cdot \hat{n} = 0$ , where  $\hat{n}$  denotes the surface boundary normal, (ii) the zero pressure  $P(x, y = \eta, t) = 0$  dynamic free-surface boundary condition, and (iii) the continuity of the free-surface  $\dot{y}_{\text{fs}} = \frac{d\eta(x,t)}{dt}$  kinematic free-surface boundary condition.

In MA-SPH the sole boundary condition explicitly implemented is no-flux on the impermeable boundaries, i.e.,  $\vec{u}_a \cdot \hat{n}_{ib} \rightarrow 0$  as  $a \rightarrow \partial_{ib}$  and  $\hat{n}_{ib}$  denotes the surface boundary normal. In practice this is achieved either with tunable Lennard-Jones potential forces [30], or with ghost particles, mirrored with respect to the boundary [3] or with fixed boundary particles [48]. Only the ghost particle approach is considered in this thesis.

The kinematic free-surface boundary condition is satisfied automatically in MA-SPH as in all Lagrangian methods:

$$\frac{dy_a}{dt} = \frac{d\eta}{dt} \text{ for } a \in \partial_{\text{fs}}. \quad (2.17)$$

Finally, the dynamic free-surface boundary condition of  $P_a = 0$  for  $a \in \partial_{\text{fs}}$  is not imposed on the free-surface in MA-SPH when KI is used near the boundaries.

Instead, KI implicitly imposes a leading order spurious dynamic free-surface boundary condition discussed in detail in section 2.5.6.

## 2.2.4 Temporal evolution

The final component of MA-SPH concerns the evolution of (2.11) - (2.15) in time. Let  $q_a^n = [\vec{x}_a^n, \vec{u}_a^n, \rho_a^n, P_a^n]$  be the known position, velocity, density and pressure respectively at time  $t^n$  at particle  $a$ . Further, let  $Q_a^n = [\vec{V}_a^n, \vec{A}_a^n, R_a^n]$  denote the corresponding velocity, acceleration and time rate of change of density as given by (2.11) - (2.15). The quantity  $q_a^n$  is advanced to the next time step  $t^{n+1} = t^n + \delta t$  with an appropriate temporal integration scheme of the form:

$$q_a^{n+1} = q_a^n + Q_a^n \delta t.$$

The schemes most often used and considered are Forward Euler, Predictor-Corrector, modified Predictor-Corrector and fourth order Runge-Kutta . Given a time step size  $\delta t = \mu_c \frac{h}{c}$  the accuracy of the above integration schemes is  $O(\delta t^{m_2})$  where  $m_2 = 1, 2, 4$  respectively. The value of  $\mu_c$  is determined by a Courant condition computed in section 2.6.4.

## 2.3 Framework for the analysis of MA-SPH for free-surface flows

The SPH method is a Lagrangian method with three attractive key features: it is simple, efficient and meshless. The SPH method is first introduced in [5, 7] for the simulation of unbounded, compressible astrophysical flows described by a set of explicit governing and constitutive equations. In discrete space the flow is simulated by a set of  $N$  Lagrangian particles, which carry their own mass and field properties, eliminating the need to compute non-linear advection terms. Because the governing equations describing the evolution of the field properties are explicit, the method is simple and efficient. The uniqueness of SPH is the usage of the Kernel Interpolation technique for the estimation of the density (2.16) and for the estimation of the spatial derivatives (2.10) that appear in the governing equations, rendering the method entirely meshless.

The consistency of Kernel Interpolation was assumed to be similar to the consistency of Monte Carlo integration methods and of order  $N^{-4/7}$ . However, numerical simulation results showed higher convergence of  $N^{-1}$  [5], indicating that this initial approach towards the consistency analysis of Kernel Interpolations is insufficient. Given that the properties of Kernel Interpolation in non-uniform particle distributions are not completely understood [25], Kernel Interpolation introduces two uncertainties. The first uncertainty is whether the density obtained by (2.16) is numerical or physical. The second uncertainty is whether the discrete algorithm is consistent with the continuous model or not. To add to the above uncertainties, existing stability analysis [17, 40, 44, 53] indicates that oscillatory modes in SPH exhibit a tensile instability. In summary, SPH in its most general form, has three attractive key features: it is simple, efficient and meshless but has two major drawbacks: it is unstable and lacks of a conclusive consistency analysis. SPH has been extended to numerous more complex physical problems [42], with the aforementioned drawbacks pending.

In particular in [30] SPH is used for the simulation of incompressible, free-surface hydrodynamic flows. To maintain the key features of the method the author in [30]

makes three non-trivial approximations. The first is related to the continuous model and is the introduction of an *artificial* Equation of State and an *artificial* speed of sound to decouple the velocity from the pressure and maintain the explicit nature of the algorithm. This is referenced as the weak compressibility assumption and its effects on the simulated physics are poorly understood [1, 2]. The second approximation is numerical and involves employing Kernel Interpolation for the computation of gradients near a free-surface, even though it is known that in this case Kernel Interpolation diverges [51] affecting the enforced free-surface boundary condition [21]. The third approximation is again numerical and involves the introduction of an empirical and tunable Lennard-Jones potential force to model no-flux boundary conditions. The effects of this third approximation on the simulated physics have not been studied, but instead research is directed towards employing more physical no-flux boundary conditions [1, 13, 41, 48]. To add to the uncertainties introduced by these three approximations it is noted that compressible flows in the presence of a free-surface develop unstable depth decaying modes [43] in addition to the already studied unstable oscillatory modes [17, 40, 44, 53]. Therefore, in employing SPH for the simulation of free-surface hydrodynamic flows, further non-trivial uncertainties are introduced, in addition to the existing stability and consistency issues present in a general astrophysical SPH simulation. To this point, in an SPH simulation for free-surface flows, the numerical and modeling errors are coupled, no quantitative error analysis exists and as a consequence it is unclear which are the leading sources of error and their scaling.

Figure 2-2 summarizes the major issues and probable sources of error as well as some numerical observations in: (a) a general SPH formulation for applications in compressible, unbounded flows [5, 7] and (b) a problem specific SPH formulation for applications in incompressible, free-surface hydrodynamic flows in the presence of gravity [30]. The usefulness of Figure 2-2 in the analysis of SPH for free-surface hydrodynamic flows is significant, since it classifies the probable sources of error and therefore guides the framework towards the rational analysis of the method.

Figure 2-3 summarizes the framework of the analysis, which focuses on SPH for

	(a) SPH for compressible unbounded flows	(b) SPH for incompressible, free-surface hydrodynamic flows
<b>Accuracy of the continuous model</b> (§ 2.4)		What is the effect of introducing <i>artificial</i> EoS with an <i>artificial</i> speed of sound, in the simulated kinematics and dynamics?
<b>Consistency of Kernel Interpolation</b> (§ 2.5)	The numerics and physics are coupled, is the particle density numerical or physical?	
	What happens when the particles depart from the initial uniform distribution? Does the fully-discrete algorithm remain consistent to the continuous model as the particles move?	
		What are the appropriate solid boundary conditions? What free-surface conditions are actually implemented?
<b>Stability</b> (§ 2.6)	What are the stability properties of the continuous model, semi-discrete algorithm, fully-discrete algorithm?	
	What is the stability of oscillatory modes with a uniform and a non-uniform base density.	What is the stability of oscillatory and depth decaying modes with a hydrostatic base density?

Figure 2-2: Classification of major uncertainties and probable sources of error in (a) general SPH for applications in compressible, unbounded flows [5, 7] and (b) problem specific SPH for applications in incompressible, free-surface hydrodynamic flows in the presence of gravity [30].

free-surface flows, addressing as well the subset of issues present in simulations of compressible, unbounded flows. The analysis is clearly divided into three sections: accuracy, consistency and stability. The analysis and findings of these sections are not independent and must not be considered independently. The first section deals with the accuracy of the weak compressibility assumption. It validates the weak compressibility assumption in the continuous space by comparing a weakly compressible to an incompressible flow in the presence of linear free-surface gravity waves based on the *existing* analysis of [8, 9, 54, 46]. The findings determine that the weakly compressible and incompressible flow are consistent to leading order, provided that the compressible flow is free of spurious acoustic modes. These findings are extended to discrete space employing the findings of the other two sections which (a) verify the presence of inconsistent boundary conditions that can generate spurious acoustic modes and (b) determine that these spurious acoustic modes are unstable. The second section deals with the consistency of Kernel Interpolation for the interpolation of the density and the spatial differentiation of a smooth function in the discrete space during an MA-SPH simulation, both inside the domain and close to the free-surface. For completeness the existing knowledge on uniform and entirely random particle distributions are first revisited. Then the analysis is extended by accounting for the flow properties, where it is assumed that the particles are advected from an initial uniform distribution by a smooth velocity field, in which case the density is proven to be a physical quantity and the algorithm is shown to be consistent with the continuous model. The free-surface boundary condition implemented by the incomplete Kernel Interpolation is considered with respect to the continuous model and shown to depend on the free-surface shape and considered as the main source of generation of the spurious acoustic modes. Lastly, the third section deals with the stability analysis. It considers the continuous model, the semi-discrete algorithm as well as the fully discrete algorithm, using information obtained from the accuracy and consistency sections. The stability of both possible modes is considered (depth decaying and depth oscillatory) in both the absence and presence of base density gradients. For the fully-discrete algorithm different standard temporal integration schemes are

considered, and the stability is determined in terms of the Courant condition.

<b>Accuracy, validation of the weak compressibility assumption for incompressible, linear, plane progressive, free-surface gravity waves (§ 2.4)</b>
<p>Analysis in continuous space (§2.4.1)</p> <ol style="list-style-type: none"> <li>1. Verification of the existence and consistency of the incompressible-like solution</li> <li>2. Identification of the spurious high frequency acoustic solutions that dominate the dynamics</li> </ol>
<p>Discussion regarding extension to discrete space to sketch the expected behavior of the spurious, numerical high frequency acoustic solutions (§2.4.2)</p> <ol style="list-style-type: none"> <li>3. Identification of their source from the inconsistent boundary conditions, initial conditions and noise</li> <li>4. Growth and characteristics to be determined from fully-discrete stability analysis</li> <li>5. Maximum cut-off frequency to be determined from spatial and temporal discretization</li> </ol>
<b>Consistency analysis of Kernel Interpolation in an SPH simulation (§ 2.5)</b>
<p>Consistency analysis of Kernel Interpolation in unbounded domain</p> <ol style="list-style-type: none"> <li>1. Prescribed uniform and random particle distribution <ol style="list-style-type: none"> <li>1.1 Consistency of interpolation and differentiation (§2.5.2)</li> </ol> </li> <li>2. Smoothly advected particle distributions (§2.5.3)</li> <li>3. <ol style="list-style-type: none"> <li>2.1 Particle density (§ 2.5.4)</li> <li>2.2 Numerical significance of the particle density in ensuring the consistency of interpolation and differentiation with Kernel Interpolation (§ 2.5.5)</li> </ol> </li> </ol>
<p>Consistency analysis of Kernel Interpolation in the presence of a free-surface (§ 2.5.6)</p> <ol style="list-style-type: none"> <li>1. Implicit dynamic free-surface boundary condition</li> </ol>
<b>Stability analysis of continuous model, semi-discrete and fully-discrete algorithms (§ 2.6)</b>
<ol style="list-style-type: none"> <li>1. Analysis in terms of modes: depth oscillatory and depth decaying modes</li> <li>2. Assumptions on base density distribution: uniform, smooth non-uniform, hydrostatic</li> <li>3. Temporal integration schemes <ol style="list-style-type: none"> <li>3.1 Forward Euler, modified Predictor Corrector, fourth order Runge-Kutta</li> <li>3.2 Effect of Courant condition for each scheme</li> </ol> </li> </ol>

Figure 2-3: Framework of analysis in SPH.

## 2.4 Linear analysis of weakly compressible free-surface flows

Employing MA-SPH for the simulation of free-surface water waves is based on the assumption that the difference between an incompressible flow and a corresponding isothermal, weakly compressible flow is of  $O(1/c^2)$ , where  $c$  is the speed of sound in the fluid and is a measure of the compressibility of the fluid. This section is dedicated to the validation of this assumption for an Airy wave, i.e., small amplitude, periodic, inviscid, gravity, free-surface wave. The choice of an Airy wave is justified for two reasons: firstly, because the Airy wave is the building block for small amplitude free-surface flows, and secondly, there already exists in the literature a *validated* analysis of the continuous main SPH model (CMA-SPH) for Airy waves, given appropriate choice of parameters, initial, and boundary conditions [8, 46].

In Pidduck [8, 9] it was suggested that the water compressibility be taken into account to resolve the instantaneity paradox in the well-known Cauchy-Poisson problem. Pidduck described the water flow as isothermal and weakly compressible just as it appears in CMA-SPH. A linear analysis was performed verifying that the weakly compressible model captures the depth decaying incompressible solution to leading order with accuracy of order  $O(1/c^2)$ . However, it was shown that given appropriate initial and boundary conditions, the weak compressibility assumption also permits an infinite set of essentially non-attenuating high-frequency depth oscillatory acoustic modes that depend on  $c$  and the water depth. The linear analysis appearing in Pidduck was later employed by [54] in a discussion on whether gravity waves can generate microseisms on a deep water sea-bed. In order to determine the origins of microseisms and quantify their magnitude in deep-water, Longuet-Higgins -in a seminal work [46]-extended the linear isothermal, weakly compressible analysis for gravity waves to account for second order effects. It was shown that higher order solutions can only be depth oscillatory. Areas of predominance of the depth oscillatory behavior were determined and results were verified through observations.

In the discrete MA-SPH simulations these acoustic modes are referred to as spuri-

ous high frequency oscillations (HFO) [2, 15]. The HFO are generated by initial and boundary conditions, numerical round-off errors, and non-linear interactions. The HFO are predominant in the dynamics of the MA-SPH solution. Attempts to remove them (without information from the analysis) led to the generation of the SPH accuracy treatments involving traditional spatial or temporal filtering [6, 19, 20, 32, 33, 49], and suggestions for alternative formulations of the Equation of State [14]. Understanding the nature and behavior of the high frequency oscillations in MA-SPH is essential both for the validation of the weak compressibility assumption as well as for the development of effective treatments for the removal of the spurious high frequency oscillations, and the improvement of the accuracy of the method.

This section follows the linear analysis described in [46], omitting second order effects. It is noted that although the derivation between [8] and [46] is slightly different, the leading order problem determined in both formulations is identical. The approach is as follows: a weakly compressible velocity potential  $\Phi$  is assumed, and the problem defined in section 2.2 is re-formulated into an initial boundary value problem for  $\Phi$  alone, which is further linearized with respect to the wave amplitude. Vertical profiles for the weakly compressible velocity potential are obtained and the solution is compared to a corresponding incompressible one. Next, the expected behavior in discrete space is discussed and verified numerically. Finally, a projection of weakly compressible free-surface flows in deep-water onto a divergence-free space is suggested through an appropriate modal decomposition.

## 2.4.1 Statement, solution and discussion in continuous space

### 2.4.1.1 Statement

Assume a two-dimensional Cartesian coordinate system  $\vec{x} = (x, y)$ , with  $y$  pointing vertically upwards. Consider an undisturbed fluid domain infinite in the horizontal direction  $x$  and bounded in the vertical direction  $y \in [-H, 0]$ , where  $y = 0$  denotes the location of the undisturbed free-surface  $\partial_{\text{fs}}$  and  $y = -H$  denote the location of

the flat bottom  $\partial_b$ , Fig. 2-1. Let  $t > 0$  denote time. Assume a flow periodic in the horizontal direction with wavelength  $\lambda$ . Let  $\vec{u}(\vec{x}, t) = (u, v)$ ,  $P(\vec{x}, t)$  and  $\rho(\vec{x}, t)$  denote the unknown fluid velocity, pressure and density respectively at  $(\vec{x}, t)$ . Finally, let  $\eta(x, t)$  denote the unknown free-surface displacement such that  $y = \eta$  describes  $\partial_{fs}$ . The gravitational acceleration and speed of sound in the fluid are  $\vec{g} = -g\hat{j}$  and  $c$  respectively. It is assumed that  $c$  is constant. The fluid density and pressure at the free-surface are  $\rho_f$  and  $P_o$ , respectively. Density fluctuations are considered, by definition, to be small. For this analysis it is assumed that the flow is slow, inviscid, irrotational, weakly compressible and isothermal. Thus, a scalar velocity potential  $\Phi(\vec{x}, t)$  such that  $\nabla\Phi \equiv \vec{u}$  can be defined.

Following [46], where it is assumed that the free-surface can be decomposed into Fourier modes and a single mode  $\eta = Ae^{i(\kappa x - \omega t)}$  is considered, the equations of motion (2.1) and (2.2) are expressed in terms of the velocity potential  $\Phi$  and integrated into a single scalar equation:

$$\frac{\partial\Phi}{\partial t} + \frac{1}{2}|\nabla\Phi|^2 + gy = -\mathbf{P} \quad (2.18)$$

where

$$\mathbf{P} = \int_{\rho}^{\rho_f} \frac{dP}{\rho} = c^2 \ln \frac{\rho}{\rho_f}. \quad (2.19)$$

Using the linear EoS (2.4) and (2.19), mass conservation (2.2) can now be re-written as

$$\nabla^2\Phi = -\frac{d \ln \rho}{dt} = -\frac{1}{c^2} \frac{d\mathbf{P}}{dt} \quad (2.20)$$

It can be easily seen that  $\mathbf{P}$  can be eliminated by taking the total derivative of (2.18) and substituting in (2.20). After some algebra and dropping higher order terms with respect to  $\Phi \sim \kappa A$ , where  $\kappa A$  is the wave slope, the linearized governing equation for  $\Phi$  becomes:

$$\frac{\partial^2\Phi}{\partial t^2} - c^2\nabla^2\Phi + g\frac{\partial\Phi}{\partial y} = 0 \quad (2.21)$$

It is pointed out here that (2.21) is also the leading order governing equation for

$\Phi$  even when the density is assumed constant in the equation of motion (2.1), i.e.,

$$\frac{d\vec{u}}{dt} = -\frac{1}{\rho_f} \nabla P - \vec{g}.$$

To conclude, the formulation of the initial boundary value problem for the velocity potential  $\Phi$  the initial and boundary conditions need to be stated. A no-flux sea-bed boundary condition is prescribed:

$$\frac{\partial \Phi(x, y = -H, t)}{\partial y} = 0 \text{ on } y = -H \quad (2.22)$$

The dynamic free-surface boundary condition is constant pressure along the free-surface (i.e.,  $P(x, y = \eta, t) = 0$ ) and the kinematic free-surface boundary condition is continuity of the free-surface  $\eta$  (i.e.,  $\frac{d\eta}{dt} = \frac{\partial \phi}{\partial y} \Big|_{(x, y = \eta, t)}$ ). After eliminating  $\eta$  from the dynamic free-surface boundary condition and kinematic free-surface boundary condition and linearizing with respect to the wave slope yields

$$\nabla^2 \Phi(x, y = 0, t) = 0 \text{ on } y = 0 \quad (2.23)$$

The domain in the horizontal direction is considered to be infinite, so the linear solutions in  $x$  will be periodic. The long-time solution is sought, therefore no initial conditions are required.

#### 2.4.1.2 Velocity potential formulation and general solution

The linearized problem for  $\Phi$  is described by the governing equation (2.21), subject to the boundary conditions (2.23) and (2.22). The problem is linear with constant coefficients, therefore separation of variables can be employed to reduce the problem to a set of ordinary differential equations in  $x$ ,  $y$ , and  $t$ . In addition, since the domain is infinite in  $x$ , consider one Fourier mode of a horizontally propagating wave of wavelength  $\lambda$ , wavenumber  $\kappa = \frac{2\pi}{\lambda}$ , and a real, unknown real frequency  $\omega$ . The

velocity potential therefore takes the form:

$$\Phi = \phi(y)e^{i(\kappa x - \omega t)}. \quad (2.24)$$

It is understood and therefore omitted that it is only the real part of (2.24) that is of interest. The problem therefore reduces to determining  $\phi(y)$  and  $\omega$ . Substituting (2.24) into the governing equation (2.21), eliminating  $e^{i(\kappa x - \omega t)}$  and denoting  $\phi' \equiv \frac{\partial \phi}{\partial y}$  we obtain:

$$\begin{aligned} -\omega^2 \phi - c^2(-\kappa^2 \phi + \phi'') + g\phi' &= 0 \rightarrow \\ \phi'' - 2\delta\phi' + (\sigma^2 - \kappa^2)\phi &= 0 \end{aligned} \quad (2.25)$$

Here  $\delta$  is the Pidduck wavenumber [8] defined as:

$$\delta \equiv \frac{g}{2c^2} \quad (2.26)$$

and

$$\sigma = \frac{\omega}{c}. \quad (2.27)$$

In a similar manner, the boundary conditions for  $\phi$  (2.22) and (2.23) become:

$$\phi'' - \kappa^2 \phi = 0 \text{ on } y = 0 \quad (2.28)$$

$$\phi' = 0 \text{ on } y = -H. \quad (2.29)$$

The boundary value problem for  $\phi$  is therefore described by the governing equation (2.25) subject to the boundary conditions (2.28) and (2.29). To solve assume a solution of the form  $\phi(y) \propto e^{\mathbf{m}y}$ . Substituting into (2.25) and eliminating  $e^{\mathbf{m}y}$  yields the characteristic polynomial for  $\mathbf{m}$ :

$$\mathbf{m}^2 - 2\delta\mathbf{m} + (\sigma^2 - \kappa^2) = 0. \quad (2.30)$$

The roots are  $\mathbf{m} = \delta \pm \sqrt{\Delta}$ , where the determinant  $\Delta$  is equal to  $\Delta = (\delta^2 + \kappa^2 -$

$\sigma^2$ ). Emphasizing that  $\sigma$  is still unknown the determinant can be either positive or negative, in which case  $\mathbf{m}$  is either real or imaginary, respectively. The following solutions are given for the cases  $\Delta \leq 0$ :

$$\mu^2 \equiv \delta^2 + \kappa^2 - \sigma^2 \text{ for } \Delta > 0 \quad (2.31)$$

$$(i\nu)^2 \equiv \delta^2 + \kappa^2 - \sigma^2 \text{ for } \Delta < 0 \quad (2.32)$$

It should be noted that by definition both  $\mu$  and  $\nu$  are real. Second,  $\mu$  ( $\Delta > 0$ ) corresponds to depth decaying profiles and  $\nu$  ( $\Delta < 0$ ) corresponds to depth oscillatory profiles. Each case will be considered separately.

### 2.4.1.3 Depth decaying profiles

For the case  $\Delta > 0$  and by the assumption that both  $\mu$  and  $\omega$  are real, the following can be written:

$$\begin{aligned} \mu^2 &\equiv \delta^2 + \kappa^2 - \sigma^2 > 0 \rightarrow \\ \sigma^2 &= \kappa^2 + \delta^2 - \mu^2 > 0. \end{aligned} \quad (2.33)$$

Given  $\phi(y) \propto e^{(\delta \pm \sqrt{\Delta})y}$ , the most general form for  $\phi$  reads:

$$\phi(y) = e^{\delta y} [A \sinh \mu y + B \cosh \mu y]. \quad (2.34)$$

For reference, the first and second derivatives of  $\phi$  are:

$$\phi' = e^{\delta y} [(A\delta + B\mu) \sinh \mu y + (A\mu + B\delta) \cosh \mu y] \quad (2.35)$$

$$\phi'' = e^{\delta y} [(A\delta^2 + A\mu^2 + 2B\delta\mu) \sinh \mu y + (2A\delta\mu + B\delta^2 + B\mu^2) \cosh \mu y] \quad (2.36)$$

The solution to (2.25) can now be obtained from the boundary conditions (2.28) and

(2.29):

$$\begin{aligned}\phi''|_{y=0} - \kappa^2 \phi|_{y=0} &= 0 \rightarrow \\ 2A\delta\mu + B(\mu^2 + \delta^2 - \kappa^2) &= 0\end{aligned}\quad (2.37)$$

$$\begin{aligned}\phi'|_{y=-H} &= 0 \rightarrow \\ -(A\delta + B\mu) \sinh \mu H + (A\mu + B\delta) \cosh \mu H &= 0\end{aligned}\quad (2.38)$$

Eq. (2.33), (2.37) and (2.38) now represent an eigenvalue problem, for the unknowns  $A$ ,  $B$ ,  $\mu$ , and  $\omega$ . Eliminating  $A$  and  $B$  from (2.37) and (2.38) the following relation for  $\mu$  is obtained:

$$\mu H \coth \mu H = \delta H \frac{\kappa^2 - \delta^2 + \mu^2}{\kappa^2 + \delta^2 - \mu^2}. \quad (2.39)$$

Eq. (2.39) along with (2.31) are the dispersion relations for  $\mu$  and  $\omega$  that depend on  $\kappa$ ,  $\delta$ , and  $H$ . It can be readily observed that (2.39) is an even function and thus assuming  $\mu > 0$  does not affect the generality of the solution. It must be noted that (2.39) has no known analytic solution. The solution of (2.39) determines both the number of admissible eigenmodes as well as their eigenvalues. To obtain this solution, the equation will be transformed into a simpler form and two cases for the values of  $\kappa$ ,  $\delta$ , and  $H$  will be considered. Once the number of roots is determined, approximate solutions are derived.

In detail, consider the following two definitions and the single one to one transformation:

$$\begin{cases} \alpha &\equiv \frac{\kappa}{\delta} \\ \epsilon &\equiv \delta H \text{ implying } \epsilon\alpha = \kappa H, \text{ and} \\ y &\equiv \frac{\mu^2 - \delta^2}{\kappa^2} \end{cases} \quad (2.40)$$

To satisfy the assumption that  $0 < \mu < \sqrt{\kappa^2 + \delta^2}$  from the quadratic equation for  $\mu$  (2.31) and also ensure  $\kappa^2 - \delta^2 + \mu^2 > 0$ , it can be easily shown that  $y$  must satisfy

$$y \in [y_o, 1), \text{ where } y_o = \max(-1, -\frac{1}{\alpha^2}). \quad (2.41)$$

Putting everything together (2.39) transforms to

$$\sqrt{1 + \alpha^2 y} \coth(\epsilon \sqrt{1 + \alpha^2 y}) = \frac{1 + y}{1 - y}. \quad (2.42)$$

Given  $\alpha$  and  $\epsilon$  the solution can be found graphically at the intersection(s) of the following two curves

$$f_1(y) \equiv \frac{1 + y}{1 - y} \text{ and } f_2(y) \equiv \sqrt{1 + \alpha^2 y} \coth(\epsilon \sqrt{1 + \alpha^2 y})$$

The following can be determined:

1. Curve  $f_1$  depends only on  $y$ . In the region  $[y_o, 1)$   $f_1$  is monotonically increasing from  $f_1(y_o) = \max(0, \frac{\alpha^2 - 1}{\alpha^2 + 1})$  to  $+\infty$  with  $f_1(0) = 1$ .
2. Curve  $f_2$  depends on  $y$ ,  $\epsilon$ , and  $\alpha$ . The main assumption is that  $\alpha^2 \gg 1 \rightarrow \alpha \gtrsim 5$ . Physically this means that the horizontal wavenumber  $\kappa$  is larger than  $\gtrsim 5\delta$ . In water this is satisfied for the majority of gravity waves as the speed of sound in water  $c_w \simeq 1500\text{m/sec}$  and  $g = 10\text{m/sec}^2$  obtains  $\delta_w \simeq 2.2 \cdot 10^{-6}\text{m}^{-1}$  corresponding to a wavelength  $\lambda_w \simeq 2,800\text{km}$ . Thus it is deduced that the inequality holds for waves shorter than  $\sim 500\text{km}$ .

Inversely, for the minimum numerical wavenumber  $\kappa = \frac{2\pi}{L}$  (where  $L$  is the maximum resolved wavelength),  $\kappa \gtrsim 5\delta$  as long as the speed of sound  $c$  is such that

$$\alpha \gtrsim 5 \rightarrow \frac{\kappa}{\delta} \gtrsim 5 \rightarrow \frac{2c^2\kappa}{g} \gtrsim 5 \rightarrow c \gtrsim 0.6\sqrt{gL}.$$

Assuming  $\alpha^2 \gg 1$  it is evident that  $-y_o = \frac{1}{\alpha^2} \ll 1$ . Therefore, employing Taylor Series Expansion on  $f_2(y)$  it is shown that

$$0 \leq \epsilon \sqrt{1 + \alpha^2 y} \leq \epsilon \sqrt{1 + \alpha^2} \simeq \epsilon \alpha (1 + 1/2\alpha^2) \text{ since } \alpha^2 \gg 1.$$

The eigenvalue problem (2.42) is considered for two extreme cases: deep and shallow water with respect to the horizontal wavenumber  $\kappa$ . For shallow water with respect

to  $\kappa$  or  $\epsilon\alpha \ll 1 \rightarrow \kappa H \ll 1$  the following is obtained. Since for  $y \in [y_o, 1)$  it is  $\epsilon\sqrt{1+\alpha^2 y} \leq \epsilon\alpha(1+1/2\alpha^2) \ll 1$  it follows that  $\coth \epsilon\sqrt{1+\alpha^2 y} \simeq 1/\epsilon\sqrt{1+\alpha^2 y}$  and therefore  $f_2$  behaves as a constant:

$$f_2 \simeq \frac{1}{\epsilon}. \quad (2.43)$$

Further it is  $\epsilon\alpha \ll 1 \rightarrow \epsilon \ll \frac{1}{\alpha}$  and therefore it follows that  $\frac{1}{\epsilon} \gg 1$  and the curves  $f_1$  and  $f_2$  will intersect only once at  $y_1 \sim 1$ . To determine  $y_1$  up to order  $\epsilon$  the values of  $f_1(y_1) = f_2(y_1)$  are equated.

$$\frac{1+y_1}{1-y_1} = \frac{1}{\epsilon} \rightarrow y_1 = 1 - \frac{2\epsilon}{1+\epsilon} \stackrel{\text{TSE}}{\simeq} 1 - 2\epsilon. \quad (2.44)$$

Transforming back to the original variable  $\mu$  shows that in shallow water with respect to  $\kappa$  and for  $\kappa \ll \delta$  the vertical wavenumber for the velocity profile is unique and up to leading order given by

$$\mu^2 \simeq \kappa^2(1 - 2\delta H) + \delta^2. \quad (2.45)$$

The last relation satisfies  $\mu^2 < \kappa^2 + \delta^2$  and upon substitution can be shown to satisfy (2.39) with accuracy  $O(\epsilon)$ .

For deep water with respect to  $\kappa$  or  $\epsilon\alpha \gg 1 \rightarrow \kappa H \gg 1$ , the following is obtained. Recalling the assumption  $\frac{1}{\alpha^2} \ll 1$ , for the case  $y_o \ll 1$  (i.e.,  $y_o = -\frac{1}{\alpha^2}$ ) it can be shown either by l'Hôpital's rule, or by Taylor Series Expansion that

$$f_2(y_o) = \frac{1}{\epsilon}. \quad (2.46)$$

For  $y \sim 1$ , it is by assumption  $\epsilon\sqrt{1+\alpha^2 y} \gg 1$  and therefore  $\coth \epsilon\sqrt{1+\alpha^2 y} \simeq 1$ . Thus there exists a region where

$$f_2(y) \simeq \sqrt{1+\alpha^2 y}.$$

Further, differentiating  $f_1$  and  $f_2$  with respect to  $y$ , it is found that  $f_1', f_2' > 0$ , i.e., both functions are monotonically increasing. Thus,  $f_1 \in [\frac{\alpha^2-1}{\alpha^2+1}, \infty)$  and  $f_2 \in [\frac{1}{\epsilon}, \sqrt{1+\alpha^2}]$ .

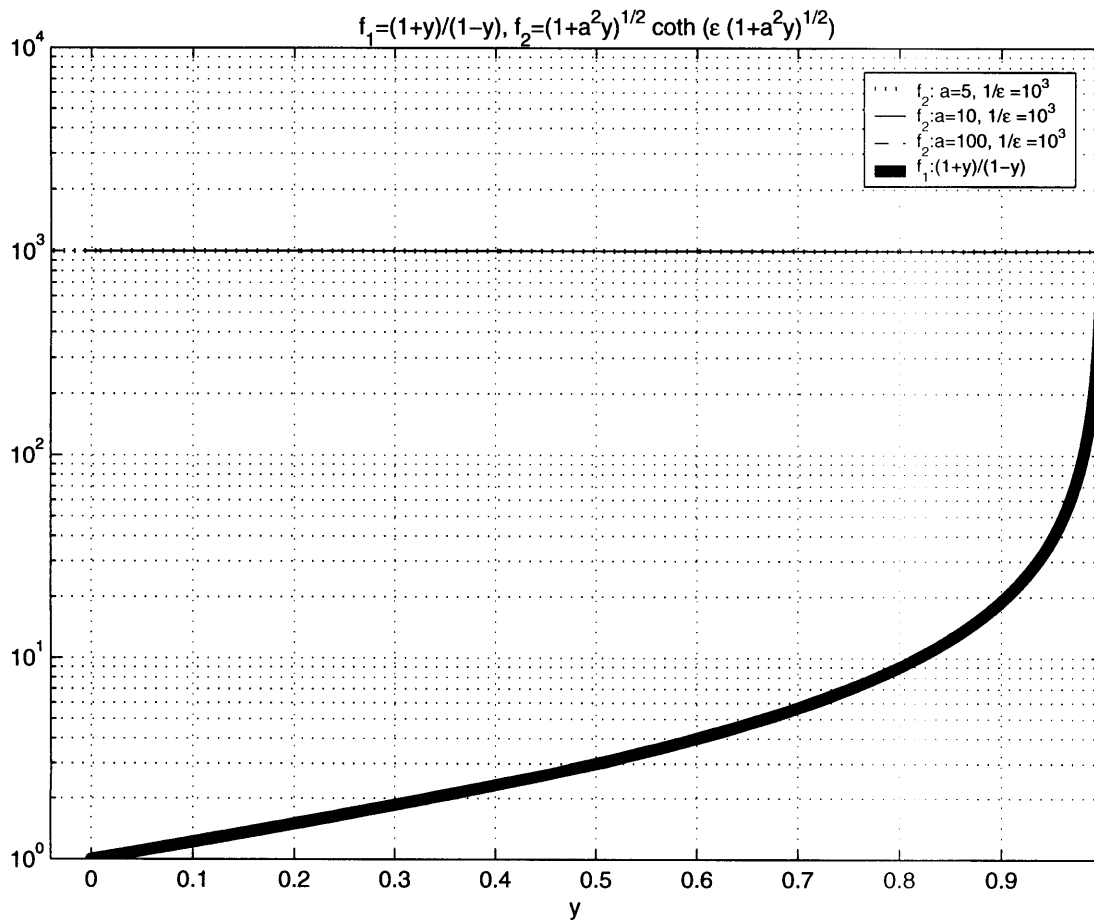


Figure 2-4: Graphic solution to the dispersion relation for weakly compressible free-surface gravity waves in shallow water for  $a = \kappa/\delta = [5, 10, 100]$  and constant  $\epsilon = 10^{-3}$ . Shows that  $f_2$  is practically a constant and equal to  $1/\epsilon$  in agreement with (2.43). Depth decaying profiles.

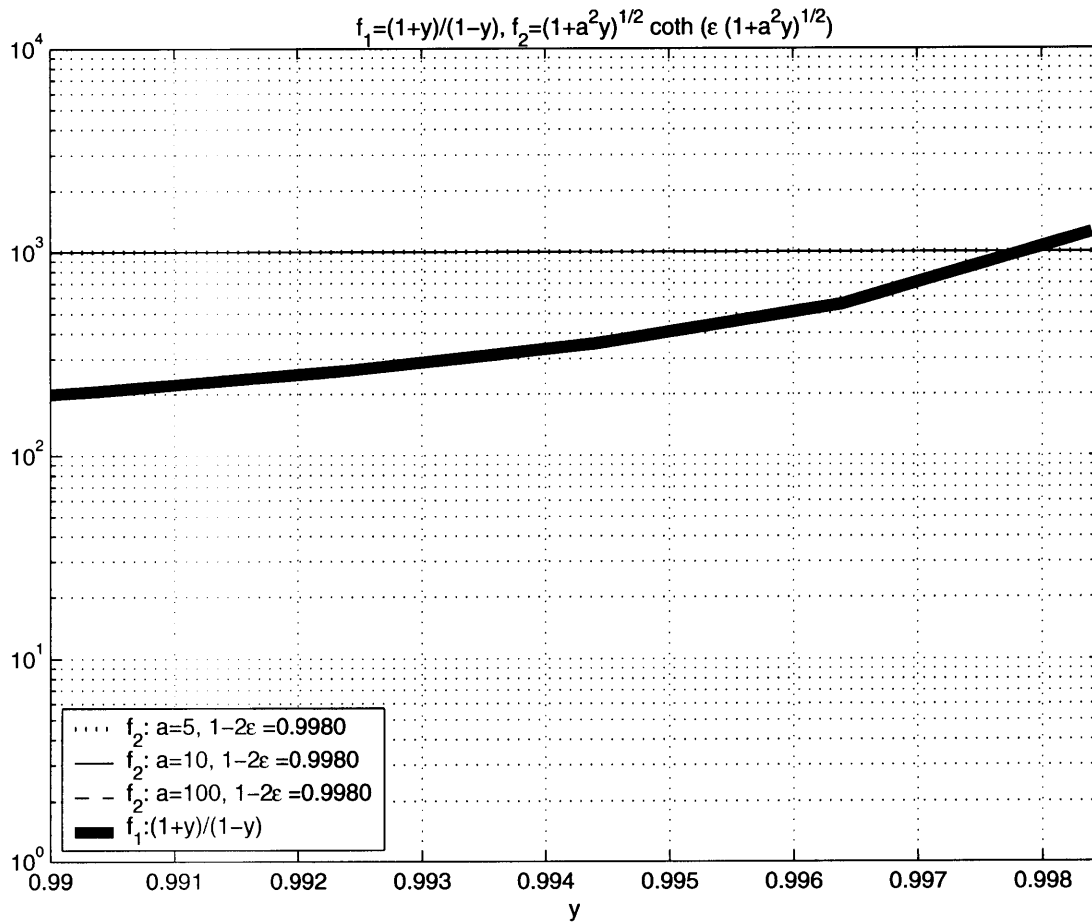


Figure 2-5: Close up of Figure 2-4 to verify Eq. (2.44). Depth decaying profiles.

Also  $f_1'' > 0$  while  $f_2'' < 0$  therefore the functions may intersect at most twice: once close to 1 and once close to  $y_o$  given appropriate value of  $\epsilon$ . For  $\epsilon \gg 1$  it can be seen by inspection that  $f_1$  and  $f_2$  will intersect on  $y = 0$  where  $f_1(0) = 1$  and  $f_2(0) = \coth \epsilon \simeq 1$ . As  $\epsilon$  decreases the intersection between  $f_1$  and  $f_2$  moves towards  $y_o$ . Let  $\epsilon_o$  denote the value of  $\epsilon$  for which the two curves will intersect at  $y = y_o = -\frac{1}{\alpha^2}$ . It is

$$\frac{1 - \frac{1}{\alpha^2}}{1 + \frac{1}{\alpha^2}} = \frac{1}{\epsilon_o} \rightarrow \epsilon_o = 1 + \frac{2}{\alpha^2 - 1} > 1.$$

Therefore, for  $\epsilon < \epsilon_o$  the two curves will intersect only once at  $y_1$  close to 1:

$$\begin{aligned} \frac{1 + y_1}{1 - y_1} &= \sqrt{1 + \alpha^2 y_1} \rightarrow \\ \alpha^2 y^2 - 2\alpha^2 y + \alpha^2 - 4 &= 0 \xrightarrow{\Delta=16\alpha^2} \\ y_{1,2} &= 1 \pm \frac{2}{\alpha} \xrightarrow{y < 1} \\ y_1 &= 1 - \frac{2}{\alpha}. \end{aligned} \tag{2.47}$$

Transforming back to the original variable  $\mu = \sqrt{\kappa^2 y + \delta^2}$  reveals that in deep water, the depth decaying vertical velocity potential profile can admit either (i) a single solution with wavenumber  $\mu = \kappa - \delta$  when  $\epsilon = \delta H < \epsilon_o$ , or (ii) two solutions with wavenumbers  $\mu = \delta$  and  $\mu = \kappa - \delta$  respectively when  $\epsilon = \delta H \geq \epsilon_o$ .

Recalling that the desired result for deep water is depth decaying waves it is of interest to eliminate the additional solution  $\mu = \delta$ . Therefore, the value of  $\epsilon_o$  provides a lower bound on the choice of the speed of sound for the numerical simulation given the water depth  $H$ . In other words, the speed of sound must be chosen so that it satisfies for all simulated waves  $\epsilon_o < \frac{\alpha^2 + 1}{\alpha^2 - 1}$ , or equivalently  $\delta^2 - \frac{\kappa^2 H}{2} \delta + \frac{\kappa^2}{2} > 0$ .

With the eigenmodes and eigenvalues understood the vertical velocity potential profile can now be obtained. Once it is ensured that (2.39) has a unique solution for  $\mu$  that is equivalent to the incompressible solution  $\kappa$  up to order  $\delta$ , from (2.37) it can be shown that:

$$\frac{B}{A} \simeq 1. \tag{2.48}$$

The corresponding velocity potential  $\Phi$  in deep water reduces to the incompressible

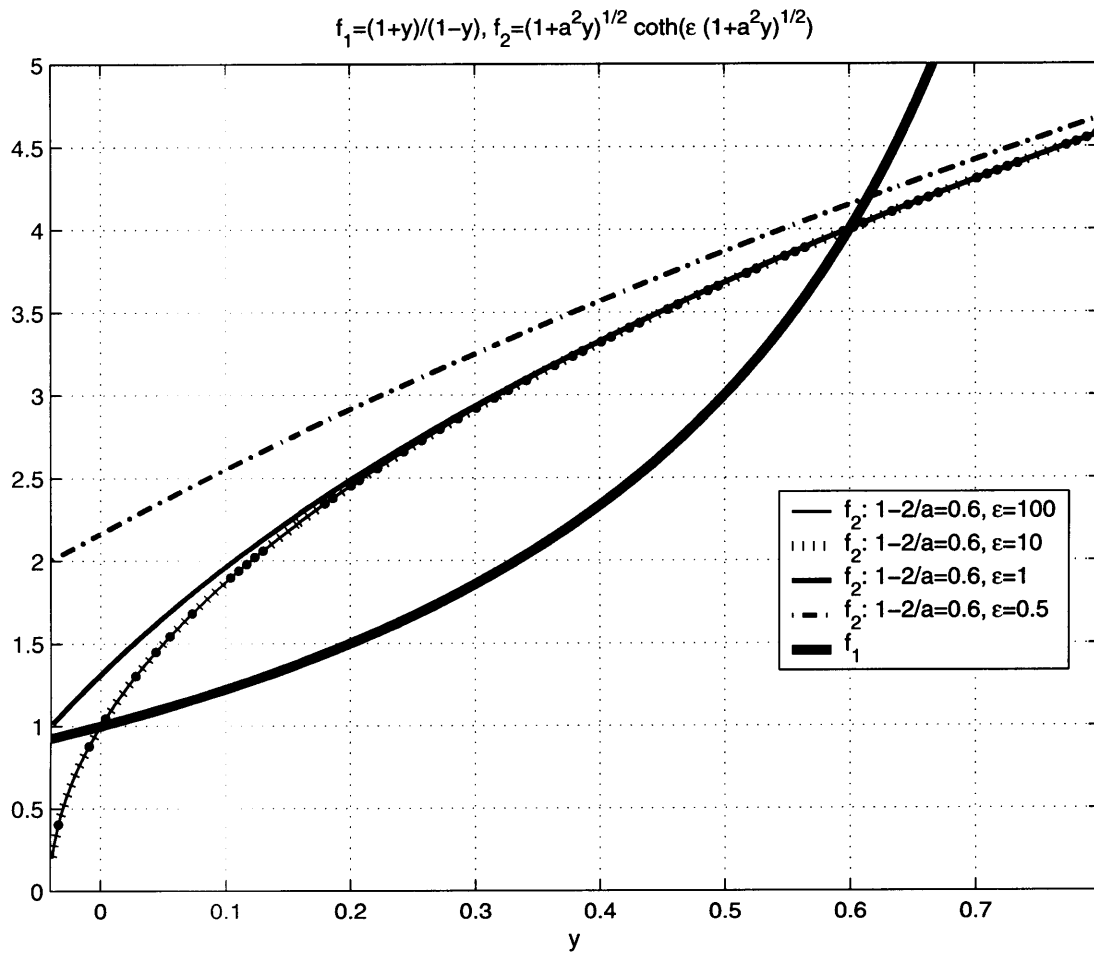


Figure 2-6: Graphic solution to the dispersion relation for weakly compressible free-surface gravity waves in deep water for constant  $a = \kappa/\delta = 5$  and  $\epsilon = [0.5, 1, 10, 100]$ . Shows the behavior of  $f_2$  as  $\epsilon$  increases, in agreement with (2.46) and (2.47). Depth decaying profiles.

solution:

$$\Phi = Ae^{\delta y}(\sinh(\kappa - \delta)y + \cosh(\kappa - \delta)y) = Ae^{\kappa y}, \quad (2.49)$$

where the coefficient  $A$  can be determined from the free-surface profile  $\eta(x)$  through the kinematic free-surface boundary condition  $\frac{d\eta}{dt} = \frac{\partial\phi}{\partial y}$  on  $y = 0$ . Finally, substituting  $\mu = \kappa - \delta$  into (2.31) obtains the wave frequency, which is equal to the corresponding incompressible short-wave frequency:

$$\sigma^2 = 2\kappa\delta \rightarrow \omega = \sqrt{g\kappa}. \quad (2.50)$$

In short, it has been shown that given appropriate choice of the speed of sound, we have essentially obtained the an incompressible Airy wave to order  $\delta \sim 1/c^2$ , verifying to leading order the weak compressibility assumption made in [30].

#### 2.4.1.4 Depth oscillatory profiles

It is recalled that the characteristic polynomial for  $\mathbf{m}$  has a solution for both  $\Delta > 0$  and  $\Delta < 0$ , where  $\Delta = (\delta^2 + \kappa^2 - \sigma^2)$ . For  $\Delta < 0$  and by the assumption that both  $\nu$  and  $\omega$  are real, the following can be written:

$$\begin{aligned} (i\nu)^2 &\equiv \delta^2 + \kappa^2 - \sigma^2 > 0 \rightarrow \\ \sigma^2 &= \kappa^2 + \delta^2 + \nu^2 > 0. \end{aligned} \quad (2.51)$$

Given  $\phi(y) \propto e^{(\delta \pm \sqrt{\Delta})y}$  the most general form for  $\phi$  reads:

$$\phi(y) = e^{\delta y} [C \sin \nu y + D \cos \nu y]. \quad (2.52)$$

For reference, the first and second derivatives of  $\phi$  are:

$$\phi' = e^{\delta y} [(C\delta - D\nu) \sin \nu y + (C\nu + D\delta) \cos \nu y] \quad (2.53)$$

$$\phi'' = e^{\delta y} [(C\delta^2 - C\nu^2 - 2D\delta\nu) \sin \nu y + (2C\delta\nu + D\delta^2 - D\nu^2) \cos \nu y]. \quad (2.54)$$

The solution to (2.25) can now be obtained from the boundary conditions (2.28) and (2.29):

$$\begin{aligned}\phi''|_{y=0} - k^2\phi|_{y=0} &= 0 \rightarrow \\ 2C\delta\nu + D(-\nu^2 + \delta^2 - \kappa^2) &= 0\end{aligned}\quad (2.55)$$

$$\begin{aligned}\phi'|_{y=-H} &= 0 \rightarrow \\ -(C\delta - D\nu)\sin\nu H + (C\nu + D\delta)\cos\nu H &= 0.\end{aligned}\quad (2.56)$$

Eq. (2.52), (2.55) and (2.56) now represent an eigenvalue problem for the unknowns  $C$ ,  $D$ ,  $\nu$ , and  $\omega$ . Eliminating  $C$  and  $D$  from (2.55) and (2.56) the following relation is obtained for  $\nu$ :

$$\nu H \cot \nu H = \delta H \frac{\kappa^2 - \delta^2 - \nu^2}{\kappa^2 + \delta^2 + \nu^2}. \quad (2.57)$$

Eq. (2.57) along with (2.51) are the dispersion relations for  $\nu$  and  $\omega$  and depend on  $\kappa$  and  $\delta$ . Leading order solutions to (2.57) are easily derived under the assumption that the dimensionless number  $\delta H = gH/2c^2 \ll 1$ . Therefore, knowing that  $|\frac{\kappa^2 - \delta^2 - \nu^2}{\kappa^2 + \delta^2 + \nu^2}| \leq 1$  the dispersion relation (2.57) is simplified to finding the zeroth roots of the  $\cot \nu H$ . Namely,

$$\begin{aligned}\nu H \cot \nu H &= \delta H \frac{\kappa^2 - \delta^2 - \nu^2}{\kappa^2 + \delta^2 + \nu^2} \rightarrow \\ \nu H \cot \nu H &< \delta H \ll 1 \rightarrow \\ \nu H \cot \nu H &\simeq 0 \xrightarrow{\nu H \neq 0} \\ \nu_n H &\simeq \frac{2n+1}{2}\pi, \text{ where } n = 0, 1, \dots\end{aligned}\quad (2.58)$$

The above approximation is more accurate as  $\delta H \rightarrow 0$  and  $n \rightarrow \infty$ . In fact, neglecting the term  $|\frac{\kappa^2 - \delta^2 - \nu_n^2}{\kappa^2 + \delta^2 + \nu_n^2}| < 1$  in (2.57), a first order solution with respect to  $\delta H$  can be derived by considering a Taylor Series Expansion of the cotangent about  $\frac{2n+1}{2}\pi$ .

Letting  $y_n = \nu_n H - \frac{2n+1}{2}\pi$ , it is shown that up to leading order  $\nu_n H$  is given by:

$$\begin{aligned}
y_n \cot y_n &= \delta H \xrightarrow{\text{TSE}} \\
(-1)^{n+1} \left( \frac{\pi}{2} y_n + y_n^2 \right) &= \delta H \rightarrow \\
y_n &= \frac{\pi}{4} \left[ 1 + \sqrt{1 - (-1)^n \frac{16\delta H}{\pi^2}} \right] \rightarrow \\
\nu_n H &\simeq \frac{2n+1}{2}\pi - (-1)^n \frac{2}{\pi} \delta H. \tag{2.59}
\end{aligned}$$

The fact that the above relations neglect  $\kappa$  can be alleviated iteratively by substituting the above result into (2.57). From the first iteration, neglecting terms  $O(\delta H)^2$ , it is

$$\nu_n H = \frac{2n+1}{2}\pi - (-1)^n \frac{2}{\pi} \delta H \frac{1 - k_n^2}{1 + k_n^2}, \tag{2.60}$$

where  $k_n \equiv \frac{2n+1}{2\kappa H}\pi$ . Since  $|\frac{1-k_n^2}{1+k_n^2}| \leq 1$  the above verifies that (2.58) is  $O(\delta H)$ .

Given  $\nu_n$  from (2.58), the vertical velocity potential profile can now be obtained. From (2.55) it can be shown that

$$\frac{D}{C} = \frac{2\delta\nu_n}{\kappa^2 + \nu_n^2 - \delta^2}. \tag{2.61}$$

The corresponding velocity potential  $\Phi_n$  in deep water becomes

$$\Phi_n = C_n e^{\delta y} \left( \sin \nu_n y + \frac{2\delta\nu_n}{\kappa^2 + \nu_n^2 - \delta^2} \cos \nu_n y \right). \tag{2.62}$$

The coefficient  $C_n$  can be determined from the free-surface profile  $\eta(x)$  through the kinematic free-surface boundary condition  $\frac{d\eta}{dt} = \frac{\partial\phi}{\partial y}$  on  $y = 0$ . Finally, substituting (2.58) into (2.51) determines the wave frequency

$$\sigma_n^2 = \kappa^2 + \delta^2 + \nu_n^2 \rightarrow \omega_n = c\sqrt{\kappa^2 + \delta^2 + \nu_n^2}, \tag{2.63}$$

where it can be seen that for  $n \gg 1$  it is

$$\omega_n \simeq n \frac{c\pi}{H}. \quad (2.64)$$

#### 2.4.1.5 Comparison of incompressible and acoustic modes

This section compares the amplitudes of the kinematics and dynamics of the incompressible and acoustic modes. Initially, the following two groups definitions are given:

1. Let the subscript  $-1$  denote deep water incompressible-like quantities. In particular let  $\mathbf{m}_{-1} = \mu = (\kappa - \delta)$  and  $\omega_{-1} \equiv \sqrt{g\kappa}$  denote the incompressible wavenumber and frequency, respectively. Let  $\psi_{-1} \equiv e^{\kappa y}$  and  $\varphi_{-1} \equiv \psi_{-1} e^{i(\kappa x - \omega_{-1} t)}$  denote the incompressible unit amplitude depth decaying vertical velocity potential profile and the normalized velocity potential, respectively. Finally, let  $C_{-1}$  denote the amplitude of the velocity potential such that  $\Phi_{-1} \equiv C_{-1} \varphi_{-1} = C_{-1} \psi_{-1}(y) e^{i(\kappa x - \omega_{-1} t)}$  and  $\phi_{-1}(y) \equiv C_{-1} \psi_{-1}(y)$ .
2. Let the subscript  $n = 0, 1, 2, \dots$  denote depth oscillatory, i.e., acoustic quantities. In particular let  $\mathbf{m}_n = \nu_n = \frac{2n+1}{2} \frac{\pi}{H}$  and  $\omega_n \equiv c \sqrt{\kappa^2 + \delta^2 + \nu_n^2}$  denote the acoustic wavenumber and frequency, respectively. Let  $\psi_n \equiv e^{\delta y} (\sin \nu_n y + s_n \cos \nu_n y)$  and  $\varphi_n \equiv \psi_n e^{i(\kappa x - \omega_n t)}$  denote the acoustic unit amplitude vertical velocity potential profile and the unit amplitude velocity potential, respectively. Noting that  $s_n \equiv \frac{2\delta\nu_n}{\kappa^2 + \nu_n^2 - \delta^2}$ , for  $n \gg 1$  it is  $s_n \rightarrow \frac{2\delta}{\nu_n}$  and therefore for  $\delta H \ll 1 \rightarrow e^{\delta y} \simeq 1$  it is  $\psi_n \simeq \sin \nu_n y + \frac{2\delta}{\nu_n} \cos \nu_n y$ . Finally, let  $C_n$  denote the amplitude of the velocity potential such that  $\Phi_n \equiv C_n \varphi_n = C_n \psi_n(y) e^{i(\kappa x - \omega_n t)}$  and  $\phi_n(y) \equiv C_n \psi_n(y)$ .

Table 2.1 summarizes the kinematics and dynamics for each mode given a unit amplitude velocity potential  $\varphi$ . The horizontal and vertical velocities are  $u = \varphi_x$  and  $v = \varphi_y$  respectively. The dynamic pressure  $P_d^*$  is given by  $P_d^* = \frac{P_d}{\rho} = -\Phi_t$ .

Table 2.2 summarizes the kinematics and dynamics for the incompressible mode and the high frequency acoustic modes, i.e.,  $n \gg 1$  (such that  $\nu_n \gg \kappa \gg \delta$  and  $\delta H \ll 1 \rightarrow e^{\delta y} \simeq 1$ ) given a unit amplitude free-surface displacement  $\eta = e^{i(\kappa x - \omega_n t)}$ .

Table 2.1: Summary of kinematics and dynamics for incompressible and acoustic modes given a unit amplitude velocity potential.

	<b>Incompressible</b>	<b>Acoustic</b>
	<b>mode</b>	<b>modes</b>
	$n = -1$	$n \geq 0$
$\varphi_n$	$e^{\kappa y} e^{i(\kappa x - \omega_{-1} t)}$	$e^{\delta y} (\sin \nu_n y + s_n \cos \nu_n y) e^{i(\kappa x - \omega_n t)}$
$u_n$	$i\kappa e^{\kappa y} e^{i(\kappa x - \omega_{-1} t)}$	$i\kappa e^{\delta y} (\sin \nu_n y + s_n \cos \nu_n y) e^{i(\kappa x - \omega_n t)}$
$v_n$	$\kappa e^{\kappa y} e^{i(\kappa x - \omega_{-1} t)}$	$e^{\delta y} [(\delta - \nu_n s_n) \sin \nu_n y + (\delta s_n + \nu_n) \cos \nu_n y] e^{i(\kappa x - \omega_n t)}$
$P_d^*$	$i\sqrt{g\kappa} e^{\kappa y} e^{i(\kappa x - \omega_{-1} t)}$	$i\omega_n e^{\delta y} (\sin \nu_n y + s_n \cos \nu_n y) e^{i(\kappa x - \omega_n t)}$

The velocity potential is related to the free-surface displacement through the kinematic free-surface boundary condition  $\eta(x, t) = -\frac{1}{g} \Phi_t|_{y=0}$ . By definition, it is  $\Phi_n = C_n \psi_n(y) e^{i(\kappa x - \omega_n t)}$  and therefore the amplitude of the velocity potential  $C_n$  given a unit amplitude free-surface displacement of frequency  $\omega_n$  is given by

$$\begin{aligned}
 \eta_n(x, t) &= -\frac{1}{g} (\Phi_n)_t|_{y=0} \rightarrow \\
 e^{i(\kappa x - \omega_n t)} &= \frac{i\omega_n}{g} C_n \psi_n(0) e^{i(\kappa x - \omega_n t)} \rightarrow \\
 C_n &= -\frac{ig}{\omega_n} \frac{1}{\psi_n(0)}. \tag{2.65}
 \end{aligned}$$

It is emphasized that in this case the free-surface displacement is a unit  $[L]$ , and therefore the units for the velocity potential, the velocity and the dynamic pressure  $P_d^*$  are  $[L^2 T^{-1}]$ ,  $[L T^{-1}]$ , and  $[L^2 T^{-2}]$  respectively.

Finally, Table 2.3 summarizes the free-surface displacement and the kinematics for the incompressible mode and the high frequency acoustic modes given a unit amplitude for the dynamic pressure, i.e.,  $P_d^* = \psi_n(y) e^{i(\kappa x - \omega_n t)}$ . Similarly to Table 2.2 in this case the dynamic pressure  $P_d^*$  is a unit  $[L^2 T^{-2}]$ , and therefore the units for the free-surface displacement, velocity potential and velocity are  $[L]$ ,  $[L^2 T^{-1}]$ , and  $[L T^{-1}]$

Table 2.2: Summary of the kinematics and dynamics for incompressible and high frequency acoustic modes, given a unit amplitude free-surface displacement.

	Incompressible mode	High frequency acoustic modes
	$n = -1$	$n \gg 1$
$\eta$	$e^{i(\kappa x - \omega_{-1} t)}$	$e^{i(\kappa x - \omega_n t)}$
$\psi_n(0)$	1	$s_n = \frac{2\delta}{\nu_n}$
$C_n$	$-i\sqrt{\frac{g}{\kappa}}$	$-ic$
$\varphi_n$	$-i\sqrt{\frac{g}{\kappa}}e^{\kappa y}e^{i(\kappa x - \omega_{-1} t)}$	$-ic(\sin \nu_n y + \frac{2\delta}{\nu_n} \cos \nu_n y)e^{i(\kappa x - \omega_n t)}$
$u_n$	$\sqrt{g\kappa}e^{\kappa y}e^{i(\kappa x - \omega_{-1} t)}$	$c\kappa(\sin \nu_n y + \frac{2\delta}{\nu_n} \cos \nu_n y)e^{i(\kappa x - \omega_n t)}$
$v_n$	$-i\sqrt{g\kappa}e^{\kappa y}e^{i(\kappa x - \omega_{-1} t)}$	$ic(\delta \sin \nu_n y - \nu_n \cos \nu_n y)e^{i(\kappa x - \omega_n t)}$
$P_d^*$	$ge^{\kappa y}e^{i(\kappa x - \omega_{-1} t)}$	$c^2\nu_n(\sin \nu_n y + \frac{2\delta}{\nu_n} \cos \nu_n y)e^{i(\kappa x - \omega_n t)}$

respectively.

From Tables 2.1, 2.2, and 2.3 the following two observations regarding the velocity divergence and velocity ratios are made. First, the Laplacian for the velocity potential of the  $n = -1$  mode, i.e., the incompressible mode, is zero everywhere, as expected. However, the Laplacian of the velocity potential for the acoustic modes, given that  $\delta H \ll 1 \rightarrow e^{\delta y} \simeq 1$ , is approximately:

$$\nabla^2 \varphi_n \simeq (a \sin \nu_n y + b \cos \nu_n y)e^{i(\kappa x - \omega_n t)} \neq 0, \quad (2.66)$$

where  $a = \delta^2 - \nu_n^2 - \kappa^2 - 2\delta\nu_n s_n$  and  $b = \delta^2 s_n - \nu_n^2 s_n - \kappa^2 + 2\delta\nu_n$ .

Second, for the incompressible mode the horizontal and vertical velocities are out of phase in the horizontal direction and of equal amplitude. However, for the acoustic modes the horizontal and vertical velocities are out of phase both in the vertical and horizontal directions and are *not* of equal amplitude. In particular for the high

Table 2.3: Summary of the kinematics and dynamics for incompressible and high frequency acoustic modes, given a unit amplitude dynamic pressure.

	<b>Incompressible mode</b>	<b>High frequency acoustic modes</b>
	$n = -1$	$n \gg 1$
$P_d^*$	$e^{\kappa y} e^{i(\kappa x - \omega_{-1} t)}$	$(\sin \nu_n y + \frac{2\delta}{\nu_n} \cos \nu_n y) e^{i(\kappa x - \omega_n t)}$
$\eta$	$\frac{1}{g} e^{i(\kappa x - \omega_{-1} t)}$	$\frac{1}{c^1 \nu_n} e^{i(\kappa x - \omega_n t)}$
$\varphi_n$	$-i \sqrt{\frac{1}{g\kappa}} e^{\kappa y} e^{i(\kappa x - \omega_{-1} t)}$	$-i \frac{1}{c \nu_n} (\sin \nu_n y + \frac{2\delta}{\nu_n} \cos \nu_n y) e^{i(\kappa x - \omega_n t)}$
$u_n$	$\sqrt{\frac{\kappa}{g}} e^{\kappa y} e^{i(\kappa x - \omega_{-1} t)}$	$\frac{\kappa}{c \nu_n} (\sin \nu_n y + \frac{2\delta}{\nu_n} \cos \nu_n y) e^{i(\kappa x - \omega_n t)}$
$v_n$	$-i \sqrt{\frac{\kappa}{g}} e^{\kappa y} e^{i(\kappa x - \omega_{-1} t)}$	$i \frac{1}{c \nu_n} (\delta \sin \nu_n y - \nu_n \cos \nu_n y) e^{i(\kappa x - \omega_n t)}$

frequency acoustic modes it is

$$u_n \sim i C_n \kappa \sin \nu_n y, \text{ and} \quad (2.67)$$

$$v_n \sim C_n \nu_n \cos \nu_n y. \quad (2.68)$$

Therefore the ratio of the horizontal over the vertical velocities scales as  $\frac{u_n}{v_n} \sim \frac{\kappa}{\nu_n} \simeq \frac{\kappa H}{n\pi}$ . In words, for an acoustic mode  $n \gg 1$ , the amplitude of the vertical velocity increases linearly with  $n$  compared to the corresponding horizontal velocity.

The linear superposition of an incompressible mode and a high frequency acoustic mode is considered. The magnitudes of the incompressible mode and the acoustic mode are compared at a given instant in time. Two example cases are demonstrated. In the first it is assumed that the two modes have equal free-surface displacement amplitudes and the ratios of the kinematic and dynamic amplitudes are computed from Table 2.2. In the second case it is assumed that the pressure coefficients are equal and the ratios of the kinematic and free-surface displacements are computed from Table 2.3.

First it is assumed that the flow field is formed by the linear superposition of a unit amplitude free-surface displacement of incompressible frequency  $\omega_{-1}$  and of a unit amplitude free-surface displacement of an acoustic high frequency  $\omega_n$  with equal horizontal wave lengths, i.e.,

$$\eta = \eta_{-1} + \eta_n, \quad (2.69)$$

where  $n \gg 1$ . From Table 2.2 it is readily observed that the incompressible mode attenuates and practically diminishes for  $\kappa|y| > 2\pi$  while the acoustic mode is practically non-attenuating. Therefore, after a certain depth the only mode that can be observed is the oscillatory one. On the free-surface where the incompressible mode has its maximum value of the horizontal velocity it is

$$\frac{u_{-1}}{u_n} = \frac{\sqrt{g\kappa}}{\frac{g\kappa}{c\nu_n}} = \frac{c\nu_n}{\sqrt{g\kappa}}. \quad (2.70)$$

This means that the incompressible mode dominates for longer waves or higher modes  $n$ . However, for the vertical velocity it is the opposite, i.e.,

$$\frac{v_{-1}}{v_n} = \frac{\sqrt{g\kappa}}{c\nu_n}. \quad (2.71)$$

The dynamic pressures are identically equal at  $y = 0$ , i.e.,

$$\frac{P_{d-1}^*}{P_{dn}^*} = \frac{g}{g} = 1. \quad (2.72)$$

However, at depths where  $|\sin \nu_n y| = 1$  the acoustic dynamic pressure scales as  $c^2 \nu_n$ !

Second, it is assumed that the flow field is formed by the linear superposition of an incompressible mode of unit amplitude dynamic pressure and frequency  $\omega_{-1}$  and of an acoustic mode of unit amplitude dynamic pressure and (high) frequency  $\omega_n$  with equal horizontal wave lengths, i.e.,

$$P_d^* = P_{d-1}^* + P_{dn}^*, \quad (2.73)$$

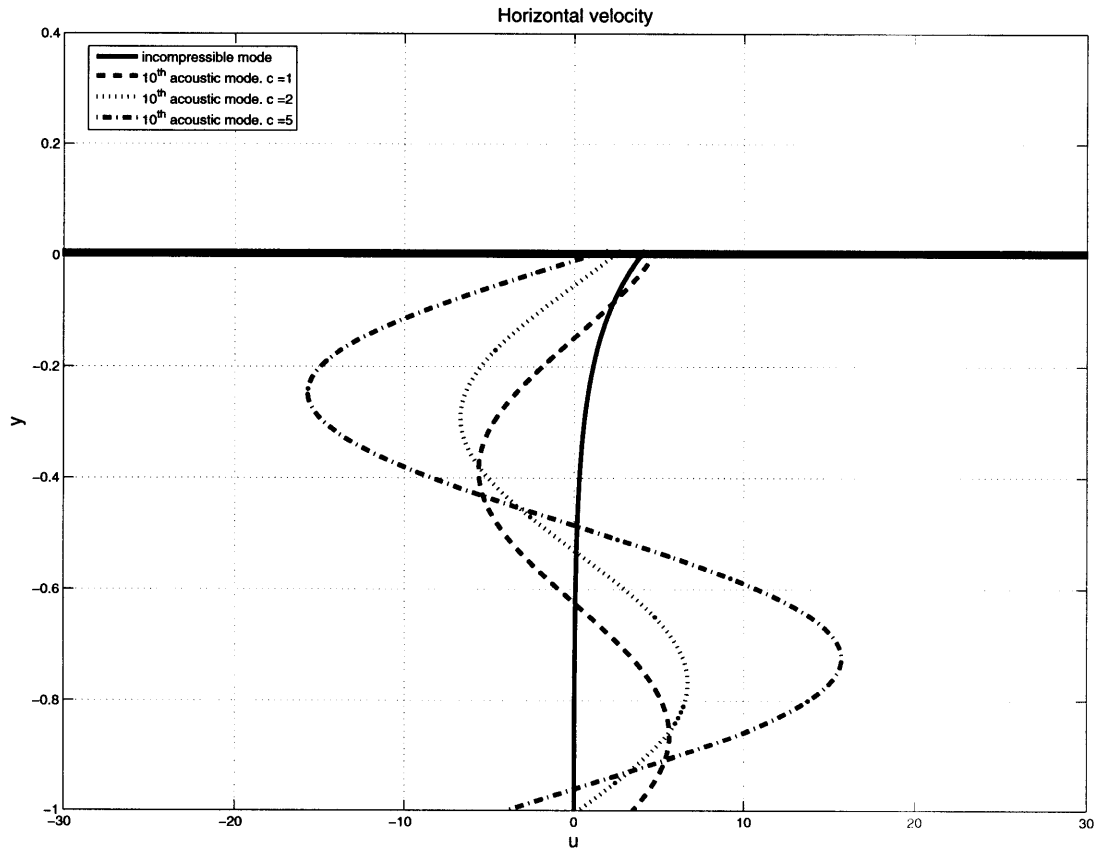


Figure 2-7: Horizontal velocity comparisons of incompressible and  $10^{\text{th}}$  acoustic modes for three different speeds of sound  $c = [1, 2, 5]$ , given equal unit free-surface displacement. Linear plane progressive free-surface with horizontal wavenumber  $\kappa = 2\pi$  and water depth  $H \rightarrow -\infty$ .

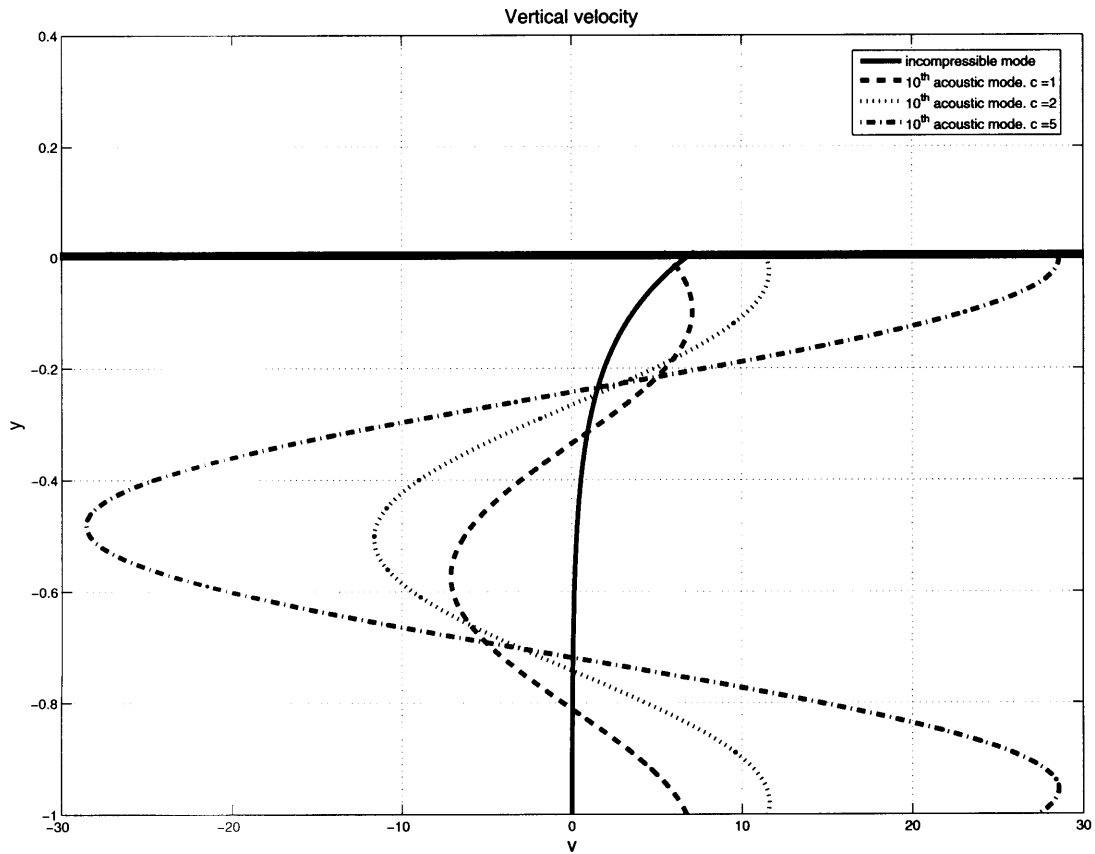


Figure 2-8: Vertical velocity comparisons of incompressible and 10<sup>th</sup> acoustic modes for three different speeds of sound  $c = [1, 2, 5]$ , given equal unit free-surface displacement. Linear plane progressive free-surface with horizontal wavenumber  $\kappa = 2\pi$  and water depth  $H \rightarrow -\infty$ .

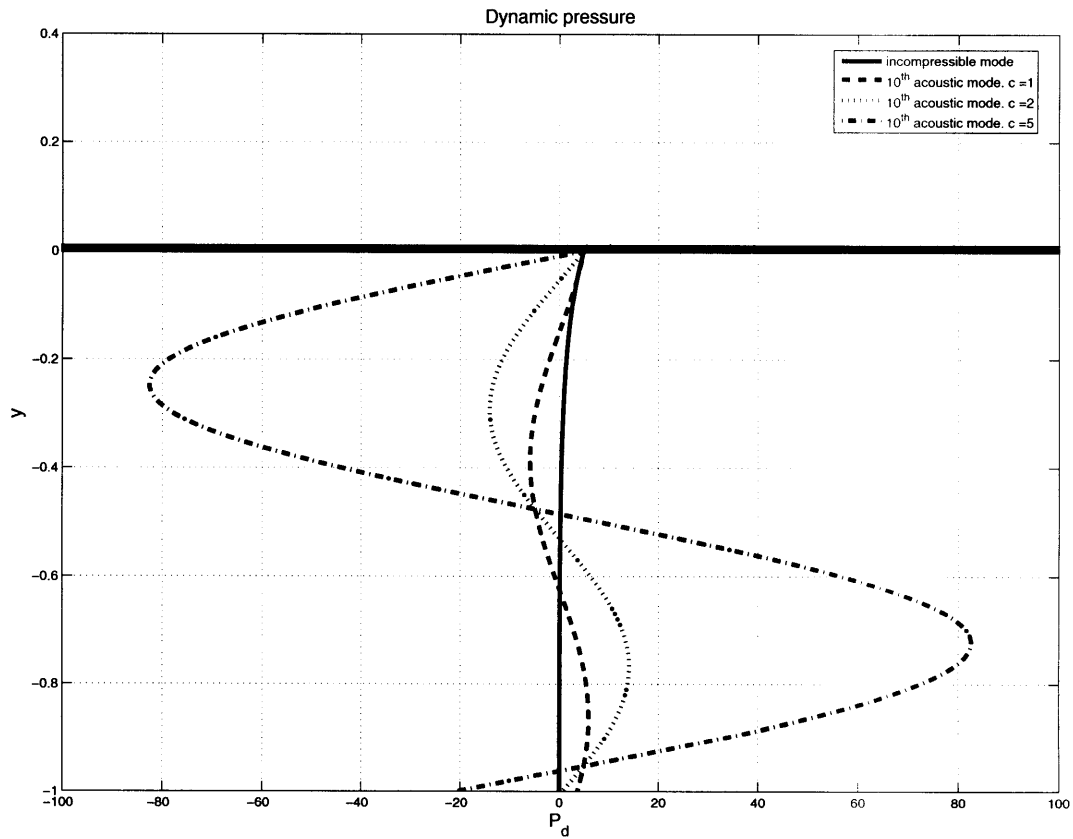


Figure 2-9: Dynamic pressure comparisons of incompressible and 10<sup>th</sup> acoustic modes for three different speeds of sound  $c = [1, 2, 5]$ , given equal unit free-surface displacement. Linear plane progressive free-surface with horizontal wavenumber  $\kappa = 2\pi$  and water depth  $H \rightarrow -\infty$ .

where  $n \gg 1$ . From Table 2.3 it is readily observed that on the free-surface, where the incompressible mode has its maximum dynamic pressure value, it is:

$$\frac{P_{d-1}^*}{P_{dn}^*} = \frac{\nu_n}{2\delta} \gg 1. \quad (2.74)$$

This means that the incompressible mode dominates. However, for depths such that  $\sin \nu_n y \simeq 1$  the dynamic acoustic pressure will be of order one. For the free-surface displacements it is

$$\frac{\eta_{-1}}{\eta_n} = \frac{c^2 \nu_n}{g} = \frac{\nu_n}{2\delta} \gg 1. \quad (2.75)$$

This means that the measured free-surface displacement will be mainly due to the incompressible mode. For the horizontal velocity on the free-surface it is

$$\frac{u_{-1}}{u_n} = \sqrt{\frac{\nu_n^4}{8\delta^3 \kappa}} \gg \gg 1, \quad (2.76)$$

while for the vertical velocity on the free-surface it is

$$\frac{v_{-1}}{v_n} = \sqrt{\frac{\kappa}{2\delta}} \gg 1. \quad (2.77)$$

## 2.4.2 Discussion on discretization and numerical verification

**Discussion on the effects of the discretization** In a MA-SPH numerical simulation for free-surface flows the desired result is only the depth decaying mode. The acoustic depth oscillatory modes, even though they exist in the real continuous world [46], can not be correctly resolved in an MA-SPH simulation and are therefore spurious. The acoustic modes of an MA-SPH simulation are spurious solutions for two reasons. The first reason is that the acoustic modes are (i) spuriously generated by the implicit MA-SPH dynamic free-surface boundary condition, discussed in section 2.5.6, (ii) spuriously generated by numerical round off errors, and (iii) spuriously unstable in an MA-SPH fully-discrete simulation, discussed in section 2.6.4. The second reason is that the acoustic modes depend on the speed of sound (unlike the incompressible

solutions) and therefore are not accurately resolved when an artificial speed of sound is used. In short, the acoustic modes in an MA-SPH simulation for free-surface flows are entirely un-physical, are undesired, and are therefore the leading accuracy error in an MA-SPH simulation.

Given that acoustic modes are the leading accuracy error in MA-SPH simulations, the comparison of the magnitudes of the desired incompressible solution to a spurious acoustic solution at a given instant in time, performed in the previous section 2.4.1.5, is of fundamental importance in the accuracy analysis. The two examples discussed in section 2.4.1.5 are helpful in that they offers a quantitative explanation why and where in MA-SPH simulations the acoustic modes dominate the dynamics (rendering them unusable) all while the displacements are smooth. In particular it is demonstrated that (a) that in deep water a weakly compressible numerical simulation like MA-SPH will contain only the spurious acoustic modes after a certain depth. (b) that if the incompressible and spurious free-surface displacements are of the same amplitude then the spurious pressure will be in general significantly larger than the incompressible one, i.e., the dynamics will be completely corrupted, (c) that if the dynamics of the two modes are of the same amplitude then it is guaranteed that the free-surface displacements will be mainly of the incompressible type, and (c) that close to the free-surface for the horizontal velocity the incompressible mode dominates over high frequency acoustic modes  $n \gg 1$  while for the vertical velocity the high frequency acoustic modes dominate over the incompressible mode.

As a closing, tangential remark, it is pointed out that the maximum acoustic wavenumber that can be resolved in a numerical simulation is determined by the grid size  $h$ :

$$\nu_{max} \leq \frac{\pi}{h}, \quad (2.78)$$

in which case the maximum numerical ‘cut-off’ frequency  $\omega_{max}$  is given by:

$$\omega_{max} = c \sqrt{\kappa^2 + \delta^2 + \left(\frac{\pi}{h}\right)^2} \xrightarrow{h \ll 1} \omega_{max} \simeq \frac{c\pi}{h}. \quad (2.79)$$

The wavenumber of the dominant acoustic mode is

$$\nu_d \leq \frac{\pi}{\alpha h}, \quad (2.80)$$

where  $\alpha$  is determined from the stability properties of the fully-discrete algorithm and the Courant condition  $\mu_c$ . As seen in section 2.6.4 for a fourth order Runge-Kutta temporal integration scheme and a typical Courant condition it is  $\alpha \sim O(5)$ . The value of  $\nu_d$  determines the value of the dominant frequency for the high frequency acoustic modes

$$\omega_{n_d} \simeq c \frac{\pi}{\alpha h}. \quad (2.81)$$

**Numerical verification** The analysis of weakly compressible free-surface flows, section 2.4, indicates the presence of two sets of linearly independent solutions: One that is exponentially depth decaying, hereafter incompressible mode, and an infinite series  $n = 0, 1, 2, \dots$  of depth oscillatory, hereafter acoustic modes. Their existence is verified via an SPH simulation and their behavior is studied. In general, for a given free-surface displacement the magnitude of the dynamics of the depth oscillatory components is larger than those of the depth decaying component and practically constant with depth. Given that the acoustic modes are generated mainly at the free-surface, section 2.5.6, it is expected that the acoustic pressure will dominate the dynamics. This is the main reason that although SPH cannot capture the incompressible wave, the acoustic components can be accurately reproduced.

To show the above we simulate a free-surface flow with MA-SPH and fourth order Runge-Kutta temporal integrator, in a deep water periodic domain of length  $L$ . The flow is initialized first with incompressible Airy waves of two different steepness  $\kappa A$  and then with various single acoustic modes. For all cases the dimensionless speed of sound employed is  $\beta = \frac{c^2}{gH} = 10$  and the Kernel bandwidth  $h = 0.01$ . From the analysis, and given that with MA-SPH we can resolve numerically up to a maximum wavenumber  $\nu_{max} = \frac{2\pi}{6h}$ , we expect that the frequencies present at any MA-SPH simulation should not exceed  $\omega_{max} \cong c\sqrt{k^2 + \nu_{max}^2}$ . Therefore, the cut-off period for

all the simulations is expected to be  $T_{66} = 0.001$ , independent of the wave steepness, or the initial conditions.

First the field is initialized with an incompressible wave solution. Figures 2-10 and 2-11 show the horizontal and vertical kinematics as well as the pressure along the depth at  $x = L$  for  $\kappa A = [0.0006, 0.006]$  for one and two periods respectively. It is noticeable that the accelerations are plagued by high frequency oscillations, i.e., spurious acoustic modes dominating as the water depth increases. This is since, section 2.4.1.5, the  $n$ th acoustic mode particle displacements scale as  $a_l$ , the horizontal and vertical velocities scale as  $a_l\beta$ , and  $a_l\beta n$  respectively and the pressure  $P \propto a_l\beta^2 n$ , is practically constant with depth. Therefore, the acoustic modes dominate the dynamics with increasing depth. As a consequence, the lower  $\kappa A$  the acoustic noise dominates the incompressible solution faster.

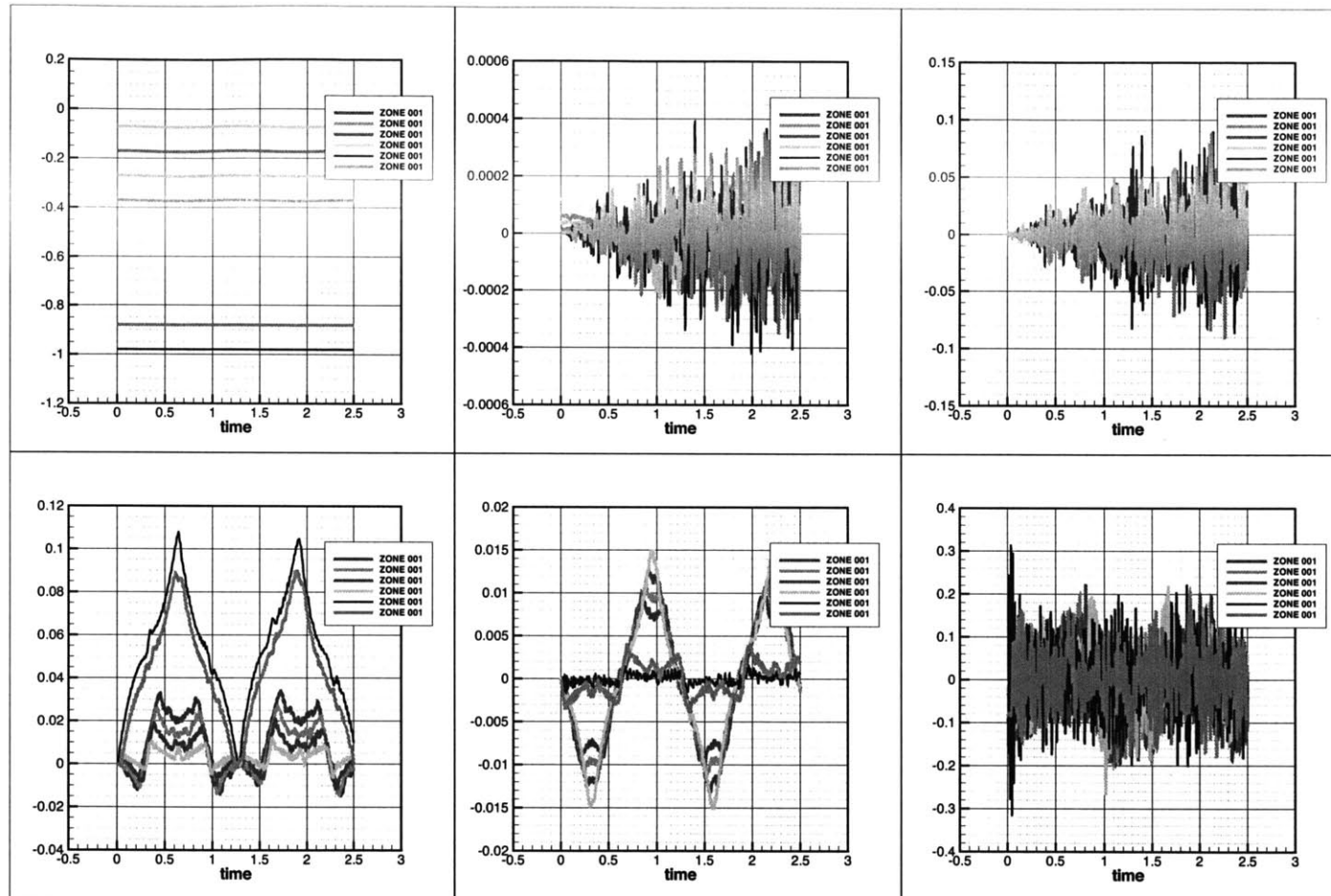


Figure 2-10: Kinematics and dynamics with respect to time at selected particles along a cross-section at  $x = L$ . SPH simulation of linear depth decaying (Airy) wave with  $\kappa A = 0.0006$ . Top left, vertical particle position. Top middle, horizontal velocity. Top right, horizontal acceleration. Bottom left, dynamic pressure. Bottom middle, vertical velocity. Bottom right, vertical acceleration. Dimensionless speed of sound  $\beta = 10$  and kernel bandwidth  $h = 0.01$ .

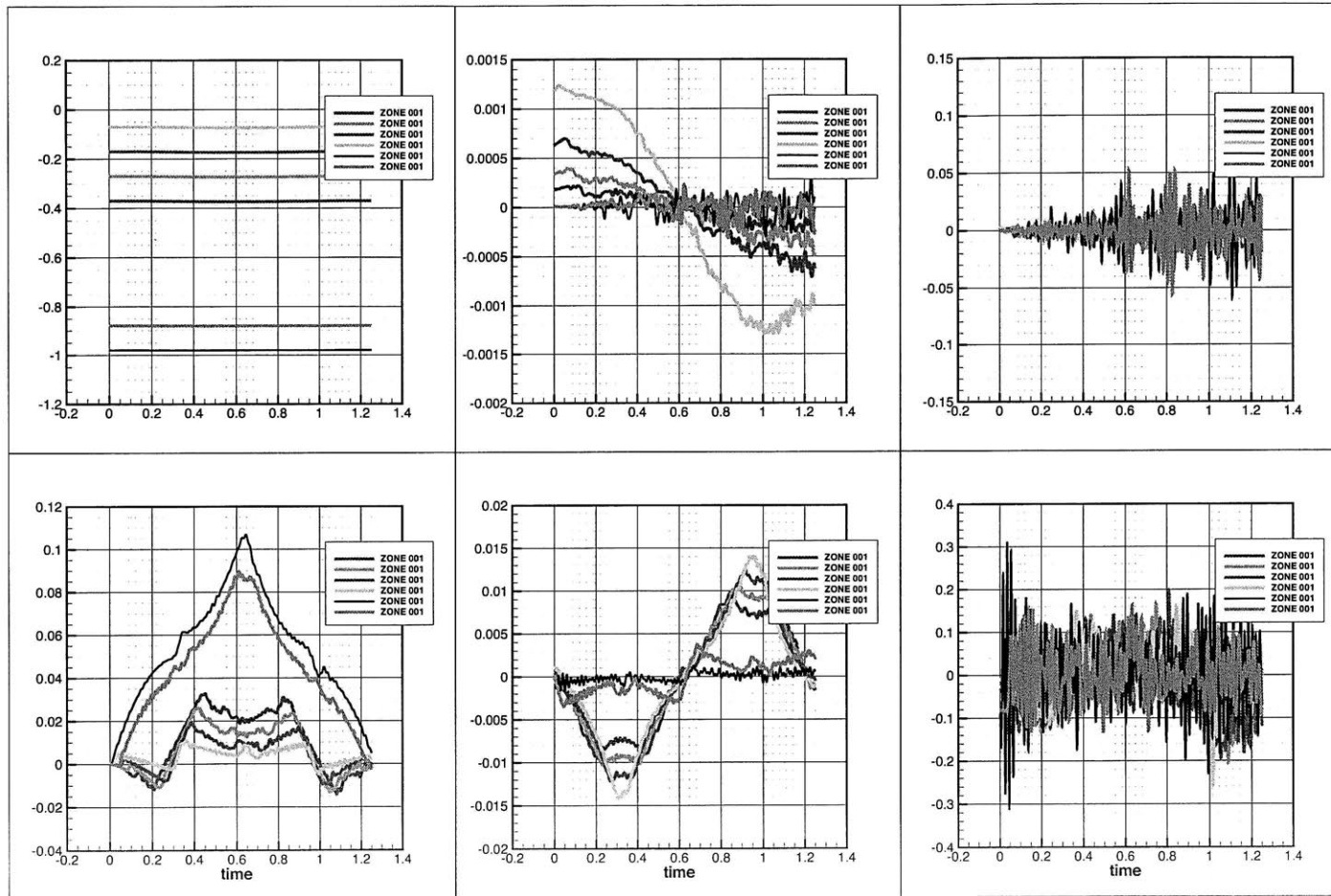


Figure 2-11: Kinematics and dynamics with respect to time at selected particles along a cross-section at  $x = L$ . SPH simulation of linear depth decaying (Airy) wave with  $\kappa A = 0.006$ . Top left, vertical particle position. Top middle, horizontal velocity. Top right, horizontal acceleration. Bottom left, dynamic pressure. Bottom middle, vertical velocity. Bottom right, vertical acceleration. Dimensionless speed of sound  $\beta = 10$  and kernel bandwidth  $h = 0.01$ .

Figure 2-12 shows the Fourier amplitudes of the kinematics of a linear depth decaying Airy wave with  $\kappa A=0.0006$ . The dimensionless speed of sound used is  $\beta = 10$  and kernel bandwidth  $h = 0.01$ . The cut-off period is therefore computed to be  $T_{66} = 0.001$ . The depth oscillatory components are generated predominantly by the spurious dynamic free-surface boundary condition, section 2.5.6. It is shown that the weakly compressible analysis is in agreement with the MA-SPH simulation results. The depth decaying components however, are plagued by spurious acoustic modes, the latter dominating as the water depth increases. The acoustic modes have been accurately predicted by the analysis and their frequencies are better represented in MA-SPH, with increasing accuracy as the mode number increases. A maximum cut-off frequency has been identified based on the speed of sound and maximum resolved wavenumber  $\nu_{max} \simeq \frac{\pi}{6h}$  in the grid spacing.

These numerical examples are useful in that they clearly demonstrate that for each wavenumber  $\kappa$  there will appear one depth decaying mode and  $n = 0, 1, \dots, n_{max}$  depth oscillatory modes. In practice it is expected that the simulated waves will not be monochromatic but rather have  $\ell$  depth decaying modes, resulting into  $\ell \times n$  depth oscillatory modes.

Second, we initialize with various acoustic modes. The dimensionless speed of sound is for all the simulations  $\beta = 10$  and the kernel bandwidth  $h = 0.01$ . The cut-off period is therefore computed to be  $T_{66} = 0.001$ . Numerical noise is expected to dominate predominantly over modes with smaller  $n$ . Figure 2-13 shows the initial horizontal velocity field for  $n=20$ ,  $kA = 0.0006$ . Figures 2-14 to 2-18 show the kinematics and dynamics with respect to time at selected particles along a cross-section at  $x = L$  for  $n = [0, 10, 15, 20, 40]$ , respectively. The wave steepness is for all cases  $\kappa A = 0.0006$ . As expected, the simulations of higher modes are better resolved.

Concluding, these simple numerical test cases verify why generally in existing applications the free-surface displacements are in agreement with experimental results, e.g., [6, 49], while dynamic loads are plagued by large amplitude high frequency oscillations e.g., [1, 2, 14, 15].

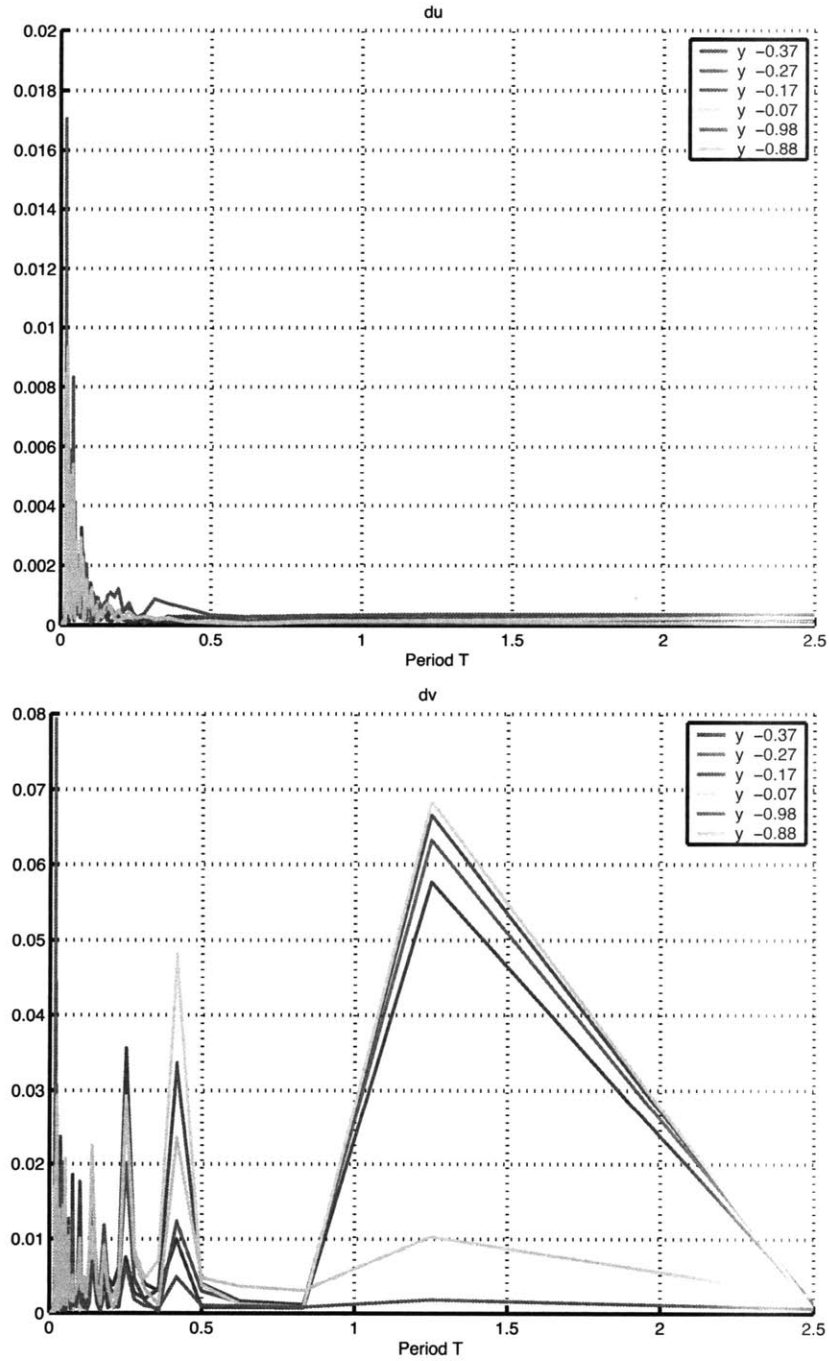


Figure 2-12: FFT of horizontal (top) and vertical (bottom) accelerations in SPH simulation of linear depth decaying (Airy) wave with  $\kappa A=0.0006$ . Dimensionless speed of sound  $\beta = 10$  and kernel bandwidth  $h = 0.01$ . Expected cut-off period  $T_{66} = 0.001$ .

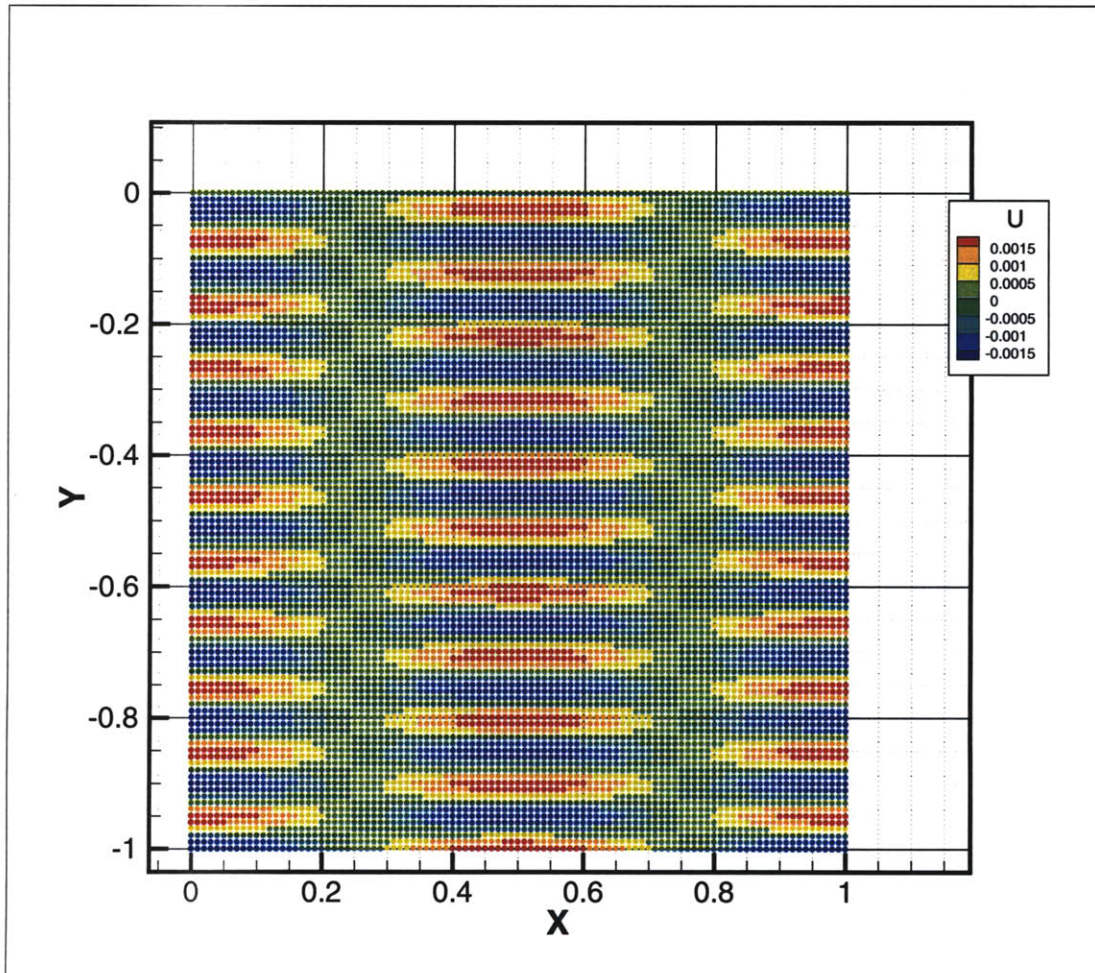


Figure 2-13: In color. Plane progressive wave, 20<sup>th</sup> acoustic mode. Coloring based on initial horizontal velocity field. Wave slope  $\kappa A = 0.0006$ , vertical wavenumber  $\nu_{20} = \frac{41\pi}{2}$ , theoretical period  $T_{20} = 0.03$ .

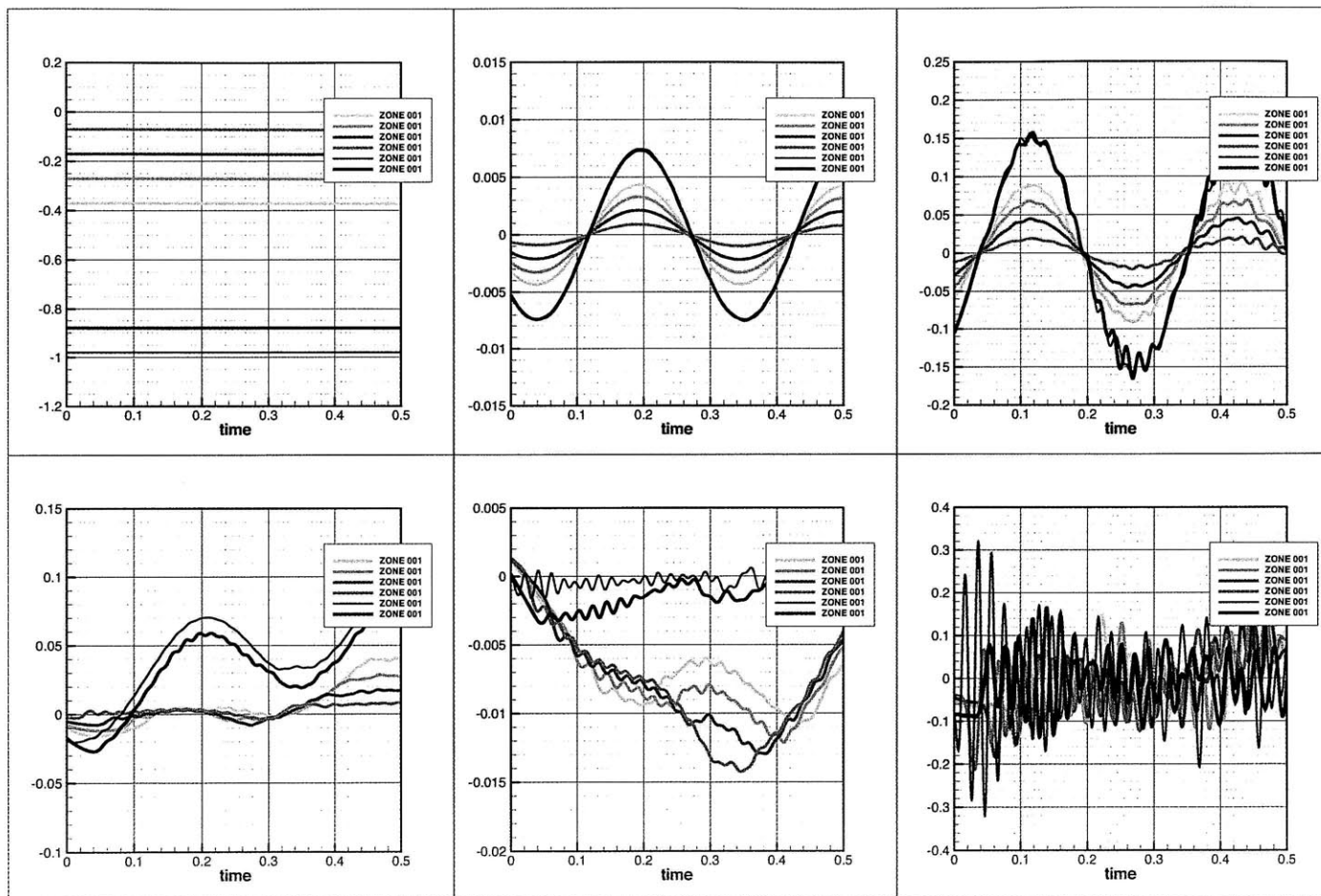


Figure 2-14: Kinematics and dynamics with respect to time at selected particles along a cross-section at  $x = L$ . SPH simulation of linear depth oscillatory wave with  $n = 0$ ,  $\kappa A = 0.0006$ ,  $h = 0.01$ . Top left, vertical particle position. Top middle, horizontal velocity. Top right, horizontal acceleration. Bottom left, dynamic pressure. Bottom middle, vertical velocity. Bottom right, vertical acceleration.

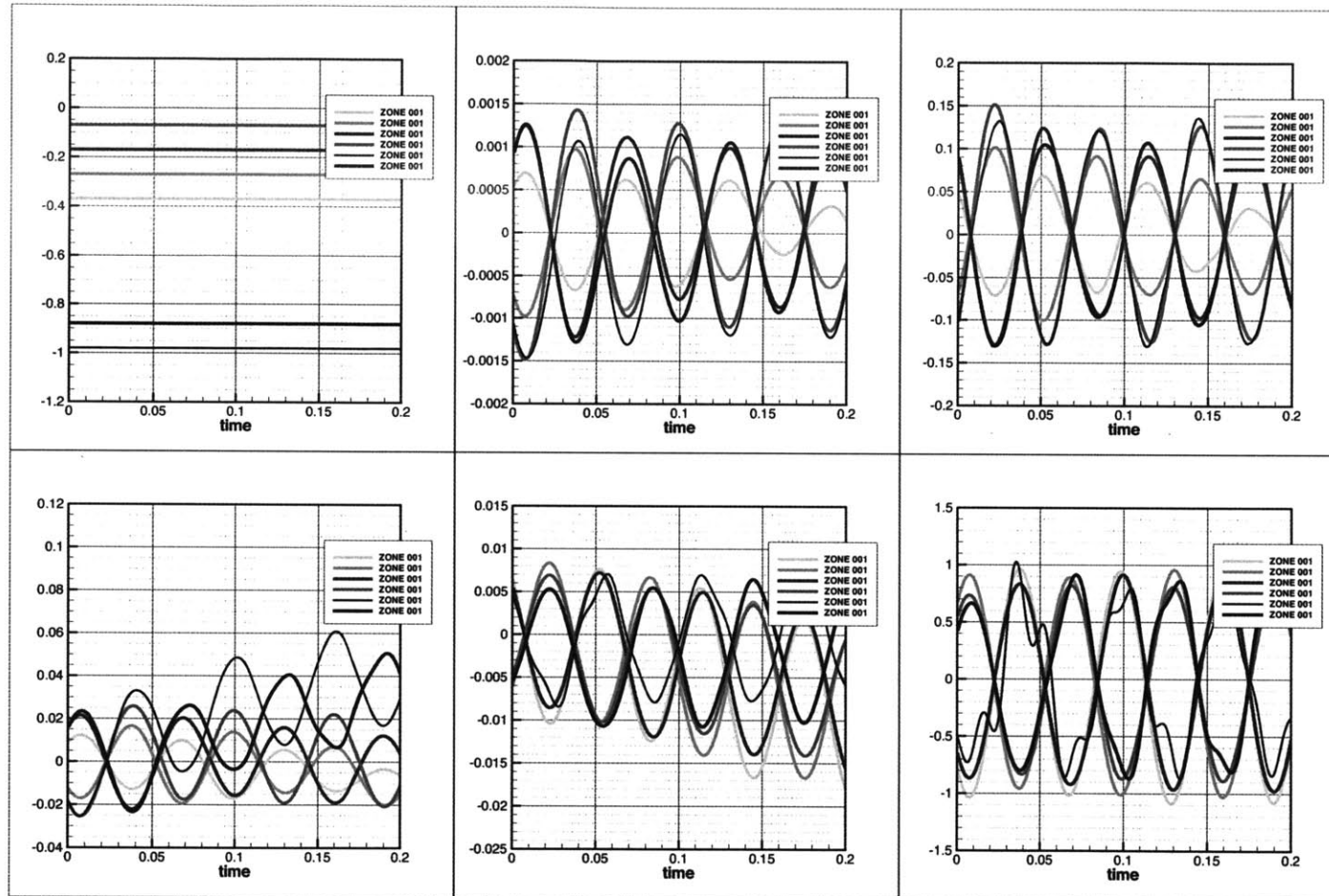


Figure 2-15: Kinematics and dynamics with respect to time at selected particles along a cross-section at  $x = L$ . SPH simulation of linear depth oscillatory wave with  $n = 10$ ,  $\kappa A = 0.0006$ ,  $h = 0.01$ . Top left, vertical particle position. Top middle, horizontal velocity. Top right, horizontal acceleration. Bottom left, dynamic pressure. Bottom middle, vertical velocity. Bottom right, vertical acceleration.

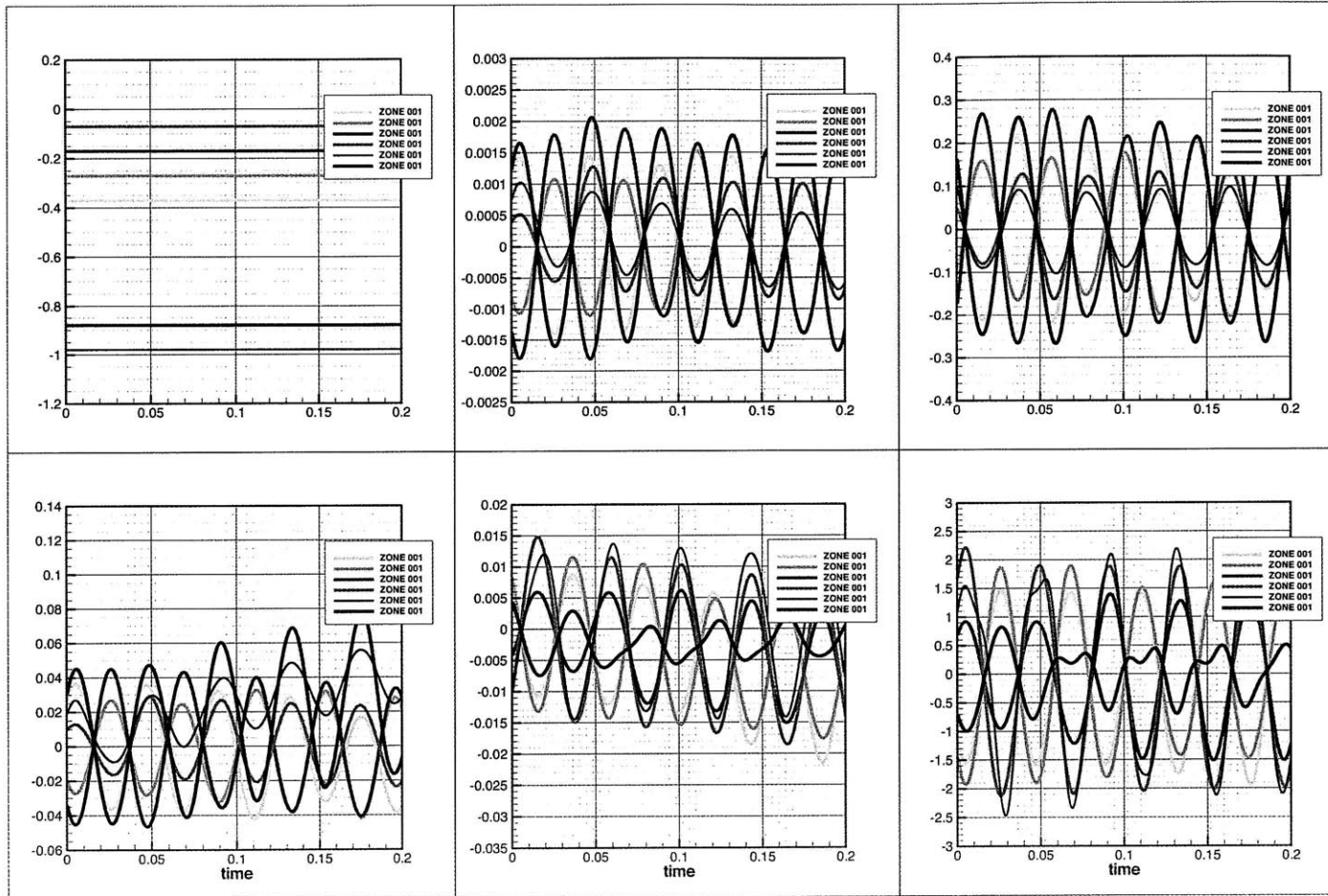


Figure 2-16: Kinematics and dynamics with respect to time at selected particles along a cross-section at  $x = L$ . SPH simulation of linear depth oscillatory wave with  $n = 15$ ,  $\kappa A = 0.0006$ ,  $h = 0.01$ . Top left, vertical particle position. Top middle, horizontal velocity. Top right, horizontal acceleration. Bottom left, dynamic pressure. Bottom middle, vertical velocity. Bottom right, vertical acceleration.

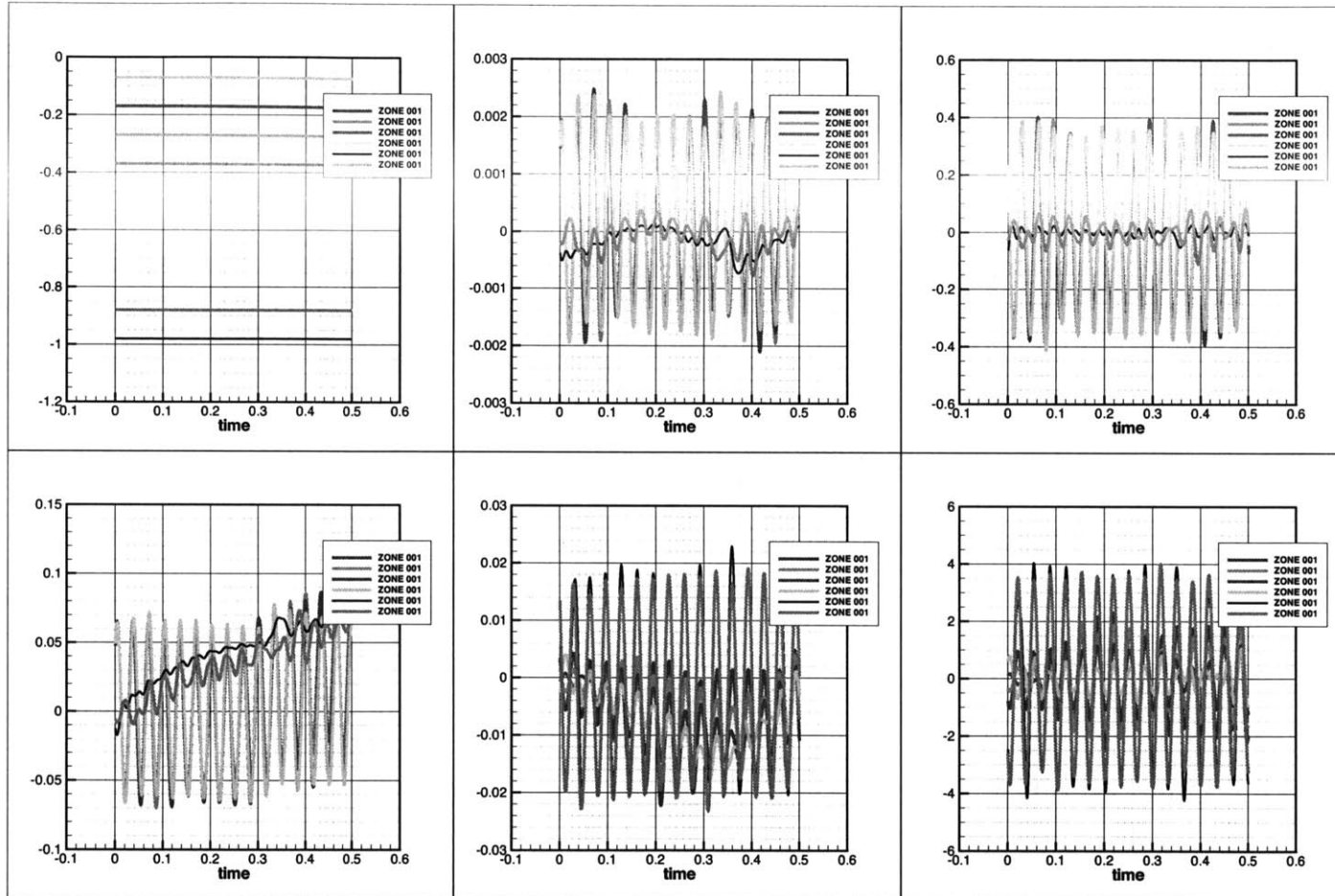


Figure 2-17: Kinematics and dynamics with respect to time at selected particles along a cross-section at  $x = L$ . SPH simulation of linear depth oscillatory wave with  $n = 20$ ,  $\kappa A = 0.0006$ ,  $h = 0.01$ . Top left, vertical particle position. Top middle, horizontal velocity. Top right, horizontal acceleration. Bottom left, dynamic pressure. Bottom middle, vertical velocity. Bottom right, vertical acceleration.

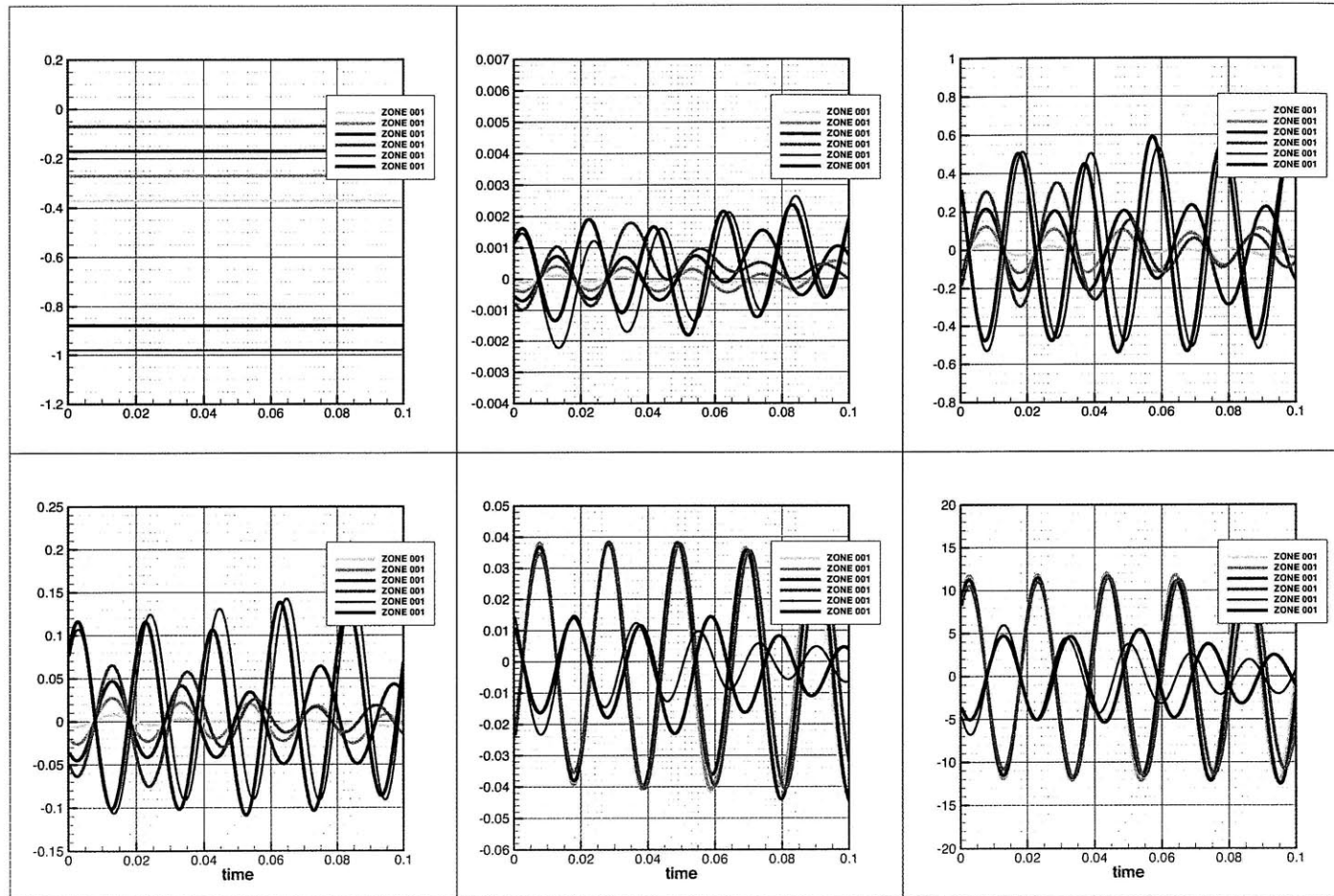


Figure 2-18: Kinematics and dynamics with respect to time at selected particles along a cross-section at  $x = L$ . SPH simulation ( $h = 0.01$ ) of linear depth oscillatory wave with  $n = 40$ ,  $\kappa A = 0.0006$ . Top left, vertical particle position. Top middle, horizontal velocity. Top right, horizontal acceleration. Bottom left, dynamic pressure. Bottom middle, vertical velocity. Bottom right, vertical acceleration.

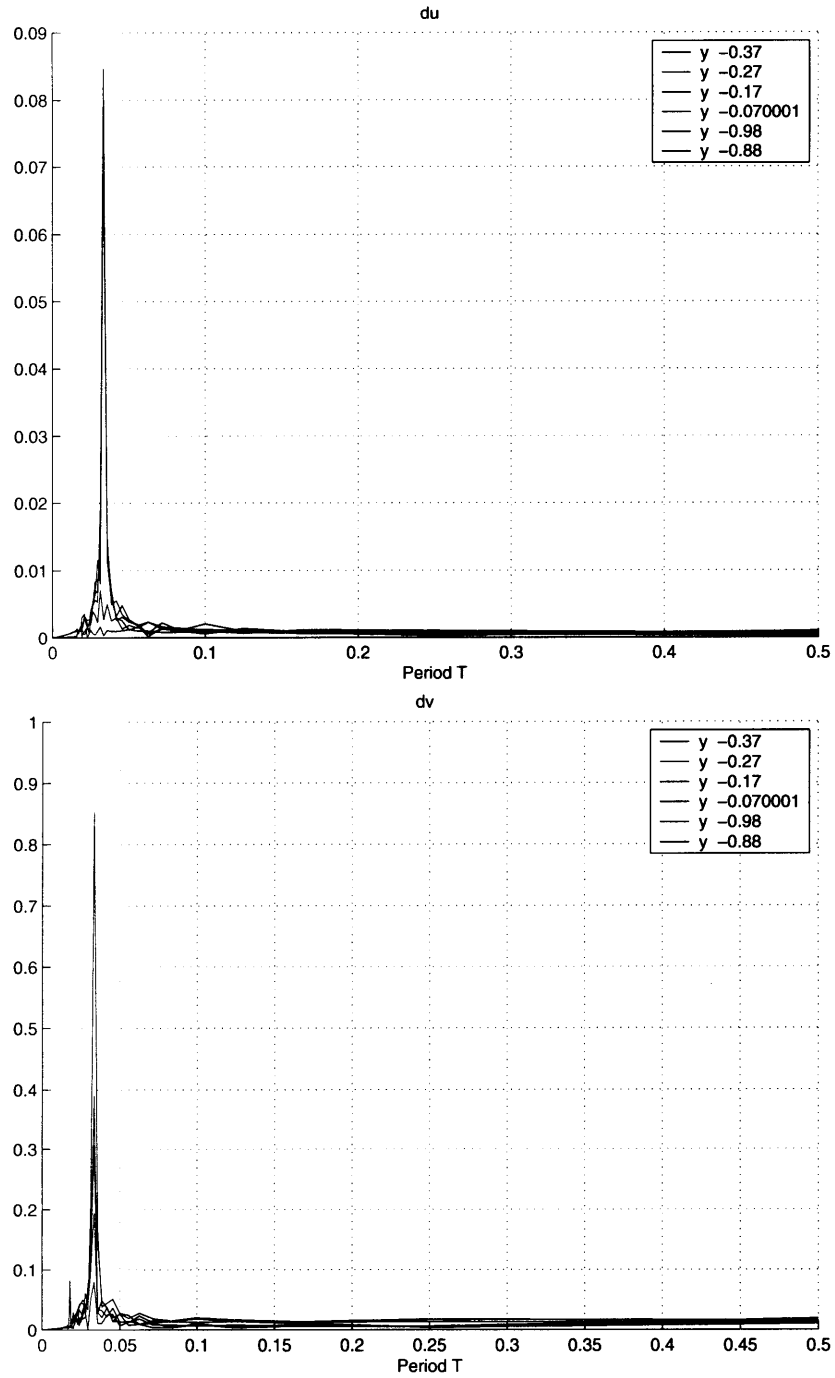


Figure 2-19: FFT of horizontal (top) and vertical (bottom) accelerations in SPH simulation of  $n = 20^{th}$  acoustic mode,  $\kappa A = 0.0006$ . Dimensionless speed of sound  $\beta = 10$  and kernel bandwidth  $h = 0.01$ . Expected  $T_{20} = 0.03$

### 2.4.3 Projection of weakly compressible free-surface flows in deep water on to a divergence-free space with modal decomposition

In section 2.4.1.2 it was demonstrated that the linearized weakly compressible boundary value problem for the velocity potential  $\Phi$  allows for two sets of periodic free-surface gravity waves. The first are depth decaying modes and are consistent up to order  $O(\delta)$ , or equivalently  $O(1/c^2)$ , with the corresponding incompressible modes. The second are high frequency acoustic modes. As discussed in section 2.4.2, in a numerical MA-SPH simulation these acoustic modes are spurious, dominate the dynamics, and are therefore unwanted.

The objective is to decompose the MA-SPH solution field into incompressible depth decaying modes and acoustic depth oscillatory modes, remove the spurious acoustic modes and retain only the incompressible modes. Such decomposition requires the formulation of an orthogonality relation between the incompressible and acoustic modes. Particular care has to be taken in the formulation of the orthogonality relation because the boundary value problem as defined by (2.25) subject to (2.28) and (2.29) is not a typical Sturm-Liouville boundary value problem as the coefficients in the free-surface boundary condition (2.28) contain an eigenvalue.

The approach has as follows. A single horizontal wavenumber is assumed, i.e., single Fourier mode in the horizontal direction. An orthogonality relation is formed for the vertical velocity potential from the governing equation (2.25) and the boundary conditions (2.28) and (2.29). The latter relation is re-written in terms of vertical and horizontal velocities and further simplified to maintain only the incompressible modes. Finally, it is extended to account for arbitrary Fourier modes in the horizontal direction.

**Single horizontal wavenumber** The decomposition for a single, known horizontal wavenumber  $\kappa$  is obtained for a two-dimensional semi-infinite domain described by the Cartesian coordinate system  $[x, y]$ . Let  $y = 0$  denote the position of the free-surface

and  $y = -H \rightarrow -\infty$  the flat sea-bed. Assume a flow in the domain that is described by a velocity potential  $\Phi(x, y, t)$  given by (2.21), i.e.,  $\Phi_{tt} - c^2 \nabla^2 \Phi + g \Phi_y = 0$ , subject to the boundary conditions  $\nabla^2 \Phi(x, 0, t) = 0$  and  $\Phi_y(x, -H, t) = 0$ . Here  $c$  denotes the speed of sound in the fluid and  $g$  the gravitational acceleration. Given that the governing equation for  $\Phi$  is linear and that  $-\infty < x < +\infty$  it can be assumed that  $\Phi = \phi(y)e^{i(\kappa x - \omega t)}$ . Substituting into the governing equation and boundary conditions obtains

$$\phi'' - 2\delta\phi' + (\sigma^2 - \kappa^2)\phi = 0 \quad (2.82)$$

$$\phi'(0) - \frac{\omega^2}{g}\phi(0) = 0 \quad (2.83)$$

$$\phi'(-H) = 0 \text{ where } H \rightarrow \infty. \quad (2.84)$$

As described in sections 2.4.1.3 and 2.4.1.4 the solution can be written in terms of modes  $\psi_n$

$$\begin{aligned} \Phi &= \sum_{n=-1}^{+\infty} \Phi_n = \sum_{n=-1}^{+\infty} a_n \psi_n e^{i(\kappa x - \omega_n t)} \\ &= a_{-1} \underbrace{\psi_{-1}}_{e^{(\kappa-\delta)y}} e^{i(\kappa x - \sqrt{g\kappa}t)} + \sum_{n \geq 0} a_n \underbrace{\psi_n}_{(\sin \nu_n y + c_n \cos \nu_n y)} e^{i(\kappa x - \omega_n t)}, \end{aligned} \quad (2.85)$$

where the subscript  $-1$  denotes the incompressible-like mode and subscripts  $\geq 0$  denote the depth oscillatory modes (section 2.4.1.5). It is recalled, for reference, that the wavenumber and frequency of the acoustic modes are  $\nu_n = \frac{2n+1}{2H}\pi$ ,  $\omega_n = c\sqrt{\kappa^2 + \delta^2 + \nu_n^2}$ . The depth decaying mode can be selected from the total solution employing the following relation

$$\Phi_{-1}(x, y, t) = \frac{\int_{-H}^0 e^{\kappa z} [v(x, z, t) - iu(x, z, t)] dz}{2\kappa \int_{-H}^0 e^{2\kappa z} dz} e^{\kappa y}. \quad (2.86)$$

where by definition  $\nabla \Phi = [u, v]$ . To prove (2.86), first an orthogonality relation for two different modes  $n$  and  $m$  is formulated. In detail, the governing equation (2.82)

is multiplied by  $r(y) = e^{-2\delta y}$  and re-written as

$$(e^{-2\delta y} \phi')' + (\sigma^2 - \kappa^2) e^{-2\delta y} \phi = 0. \quad (2.87)$$

Two modes  $\psi_n$  and  $\psi_m$  that satisfy (2.87) are assumed. Equation (2.87) for  $n$ ,  $m$  is multiplied with  $(\omega_m^2)\psi_m$  and  $(\omega_n^2)\psi_n$  respectively. Subtracting, integrating from  $-H$  to 0 and collecting terms yields

$$\begin{aligned} I &= \int_{-H}^0 \left[ (\omega_m^2 \psi_m) \left( (e^{-2\delta z} \psi_n')' + (\sigma^2 - \kappa^2) \psi_n \right) - \right. \\ &\quad \left. (\omega_n^2 \psi_n) \left( (e^{-2\delta z} \psi_m')' + (\sigma^2 - \kappa^2) \psi_m \right) \right] dz = 0 \rightarrow \\ I &= \underbrace{\int_{-H}^0 \left[ \omega_m^2 \psi_m (e^{-2\delta z} \psi_n')' - \omega_n^2 \psi_n (e^{-2\delta z} \psi_m')' \right] dz}_{I_1} + \\ &\quad (\omega_n^2 - \omega_m^2) \int_{-H}^0 [e^{-2\delta z} \kappa^2 \psi_n \psi_m] dz = 0. \end{aligned} \quad (2.88)$$

The first integral on the right hand-side of (2.88),  $I_1$ , is integrated by parts and the boundary conditions are applied

$$\begin{aligned} I_1 &= \int_{-H}^0 \left[ \omega_m^2 \psi_m (e^{-2\delta z} \psi_n')' - \omega_n^2 \psi_n (e^{-2\delta z} \psi_m')' \right] dz \\ &= e^{-2\delta z} (\omega_m^2 \psi_m \psi_n' - \omega_n^2 \psi_n \psi_m') \Big|_{-H}^0 + (\omega_n^2 - \omega_m^2) \int_{-H}^0 e^{-2\delta z} \psi_n' \psi_m' dz \xrightarrow[\psi(-H)=0]{\psi'(0)=\frac{\omega^2}{g} \psi(0)} \\ &= (\omega_n^2 - \omega_m^2) \int_{-H}^0 e^{-2\delta z} \psi_n' \psi_m' dz. \end{aligned} \quad (2.89)$$

Putting everything together, yields the orthogonality relation

$$\begin{aligned}
I &= 0 \rightarrow \tag{2.90} \\
I_1 + (\omega_n^2 - \omega_m^2) \int_{-H}^0 e^{-2\delta z} \psi'_n \psi'_m dz &= 0 \rightarrow \\
(\omega_n^2 - \omega_m^2) \int_{-H}^0 e^{-2\delta z} \psi'_n \psi'_m dz + (\omega_n^2 - \omega_m^2) \int_{-H}^0 e^{-2\delta z} \kappa^2 \psi_n \psi_m dz &= 0 \rightarrow \\
(\omega_n^2 - \omega_m^2) \underbrace{\int_{-H}^0 e^{-2\delta z} (\psi'_n \psi'_m + \kappa^2 \psi_n \psi_m) dz}_{I_{nm}} &= 0 \rightarrow \\
(\omega_n^2 - \omega_m^2) I_{nm} &= 0 \xrightarrow{\omega_n \neq \omega_m} \\
I_{nm} = \int_{-H}^0 e^{-2\delta z} (\psi'_n \psi'_m + \kappa^2 \psi_n \psi_m) dz &= 0 \text{ for } n \neq m. \tag{2.91}
\end{aligned}$$

Next, it is shown how the orthogonality relation (2.91) can be used to extract the amplitude of a single mode  $n$  from the velocity potential  $\Phi$ , where  $\Phi$  is given in (2.85). Assume the integral  $I_2$

$$\begin{aligned}
I_2 &= \int_{-H}^0 e^{-2\delta y} [\psi'_n \Phi_z + \kappa^2 \psi_n \Phi] dy \xrightarrow{(2.85)} \\
&= \int_{-H}^0 e^{-2\delta z} \left[ \psi'_n \sum_m a_m \psi'_m e^{i(\kappa x - \omega_n t)} + \kappa^2 \psi_n \sum_m a_m \psi_m e^{i(\kappa x - \omega_n t)} \right] dz \\
&= \sum_m a_m e^{i(\kappa x - \omega_n t)} \int_{-H}^0 e^{-2\delta z} [\psi'_n \psi'_m + \kappa^2 \psi_n \psi_m] dz \\
&= \sum_m a_m e^{i(\kappa x - \omega_n t)} I_{nm} \xrightarrow{I_{nm}=0 \text{ for } n \neq m} \\
&= a_n I_{nn} e^{i(\kappa x - \omega_n t)}. \tag{2.92}
\end{aligned}$$

Noting that  $\Phi_x = u \xrightarrow{\Phi \propto e^{i\kappa x}} \kappa \Phi = -iu$  and  $\Phi_y = v$  the following relation can be used to obtain the amplitude of a single mode  $n$  in terms of the velocity components

$$a_n e^{i(\kappa x - \omega_n t)} = \frac{1}{I_{nn}} \int_{-H}^0 e^{-2\delta z} [\psi'_n v - i\kappa \psi_n u] dz. \tag{2.93}$$

Since, it is of interest to remove all the acoustic modes and maintain only the incompressible mode the following filter can be used to obtain the desired incom-

pressible solution:

$$\begin{aligned}
a_n e^{i(\kappa x - \omega_n t)} &= \frac{\int_{-H}^0 e^{(\kappa - 3\delta)z} [(\kappa - \delta)v - i\kappa u] dz}{(2\kappa^2 - 2\kappa\delta + \delta^2) \int_{-H}^0 e^{2(\kappa - 2\delta)z} dz} \xrightarrow{\delta \ll \kappa} \\
&\simeq \frac{\int_{-H}^0 e^{\kappa z} [v - iu] dz}{2\kappa \int_{-H}^0 e^{2\kappa z} dz}.
\end{aligned} \tag{2.94}$$

Equation (2.94) can be further approximated by  $a_n e^{i(\kappa x - \omega_n t)} \simeq \int_{-H}^0 e^{\kappa z} [v - iu] dz$ . However, in a numerical simulation the integrals in (2.94) are computed through a quadrature formula and it is found that it is best if the integration in the denominator is performed numerically as well.

Finally, putting everything together, after the acoustic modes have been filtered out, the *entire*, incompressible flow field can be reconstructed from

$$\bar{\Phi}(x, y, t) = \frac{\int_{-H}^0 e^{\kappa z} [v(x, z, t) - iu(x, z, t)] dz}{2\kappa \int_{-H}^0 e^{2\kappa z} dz} e^{\kappa y}. \tag{2.95}$$

This proves the validity of (2.86). There is an approximation error of order  $O(\delta)$  due to the assumption

$$\psi_{-1} = e^{(\kappa - \delta)y} = e^{\kappa y} e^{-\delta y} = e^{\kappa y} (1 - \delta y) \simeq e^{\kappa y} + O(\delta), \tag{2.96}$$

which is still within our acceptable error bounds regarding the consistency with the incompressible solution.

**Numerical verifications** To validate the model decomposition we consider random time steps in an MA-SPH simulation of a small amplitude Airy wave with  $\kappa H = 2\pi$ . The integral (2.91) is computed for  $n = 0, \dots, 50$  acoustic modes. Note that the  $N$  is bounded by the kernel bandwidth  $h$ . Figure 2-20 shows the magnitude of the integral (2.91) for  $m = -1$ , and  $n = 0, \dots, 50$  in deep water. The horizontal wavelength is chosen  $\kappa = 2\pi/H$ . Figure 2-21 computes the final reconstructed solution  $\bar{\Phi}_{-1}$  from (2.86) in deep water from a noisy solution  $\Phi = 2\Phi_{-1} + \Phi_n$ ,  $n = 0, \dots, 50$ . The horizontal wavelength is chosen  $\kappa = 2\pi/H$ . Figures 2-22 and 2-23 demonstrate

verify the orthogonality relation for an acoustic mode and compare an initial noisy and reconstructed solutions, with respect to the water depth for two different values of  $\kappa H$ .

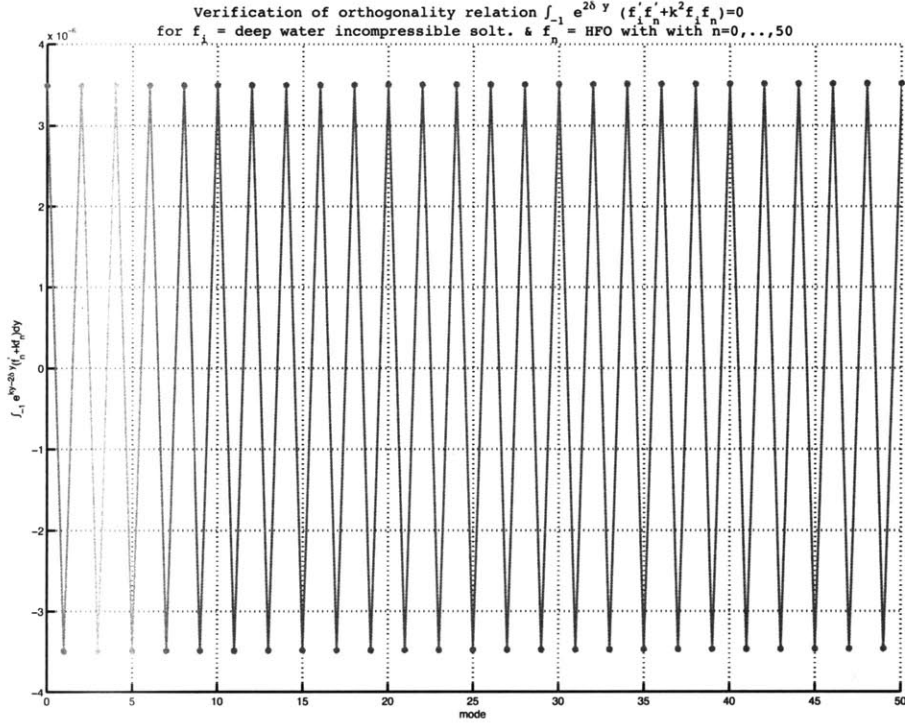


Figure 2-20: Verification of orthogonality relation (2.91) for  $m = -1$ ,  $n = 0, \dots, 50$ . Deep water assumption,  $\kappa H = 2\pi$ . The integral for each mode is of the order of  $10^{-6}$ .

**Multiple horizontal wavenumbers** To extend (2.86) to account for multiple wavenumbers a Fourier decomposition in the horizontal direction is assumed. Namely, it is assumed that the velocity potential at a time instant  $t$  can be decomposed into

$$\Phi(x, y) = \sum_{m=0}^M \sum_{n=-1} a_{m,n} \psi_{m,n}(y) \sin \kappa_m x + b_{m,n} \psi_{m,n}(y) \cos \kappa_m x, \quad (2.97)$$

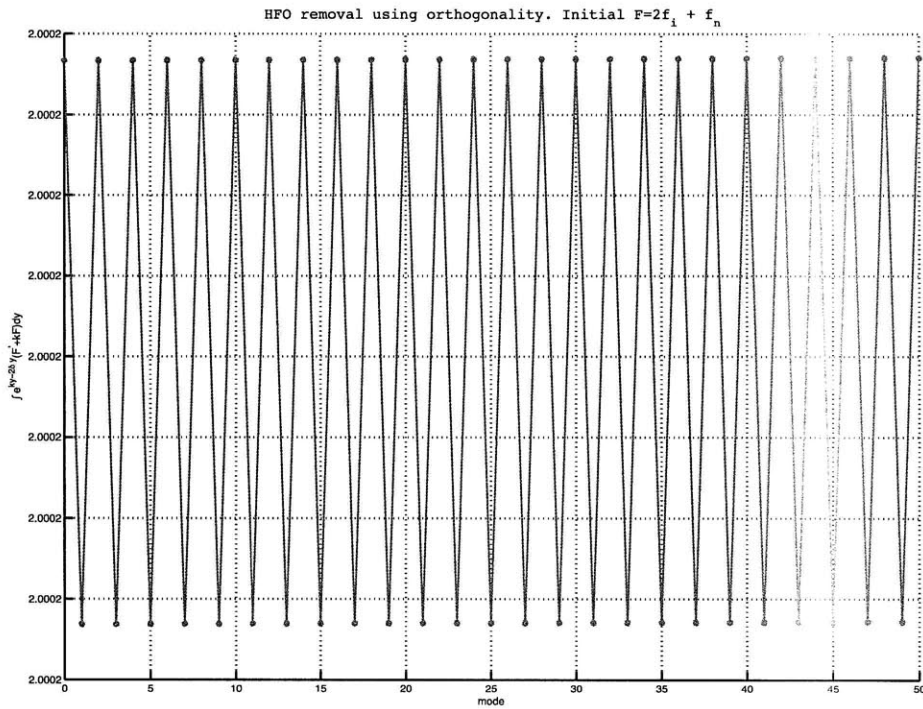


Figure 2-21: Computation of  $\overline{\Phi_{-1}}$  from (2.86) in deep water for a noisy solution  $\Phi = 2\Phi_{-1} + \Phi_n$ ,  $n = 0, \dots, 50$ . The horizontal wavelength is chosen  $\kappa = 2\pi/H$ . The error between the reconstructed solution  $\overline{\Phi_{-1}}$  and the incompressible solution  $2\Phi_{-1}$  is of the order of  $10^{-4}$ . Deep water assumption,  $\kappa H = 2\pi$ .

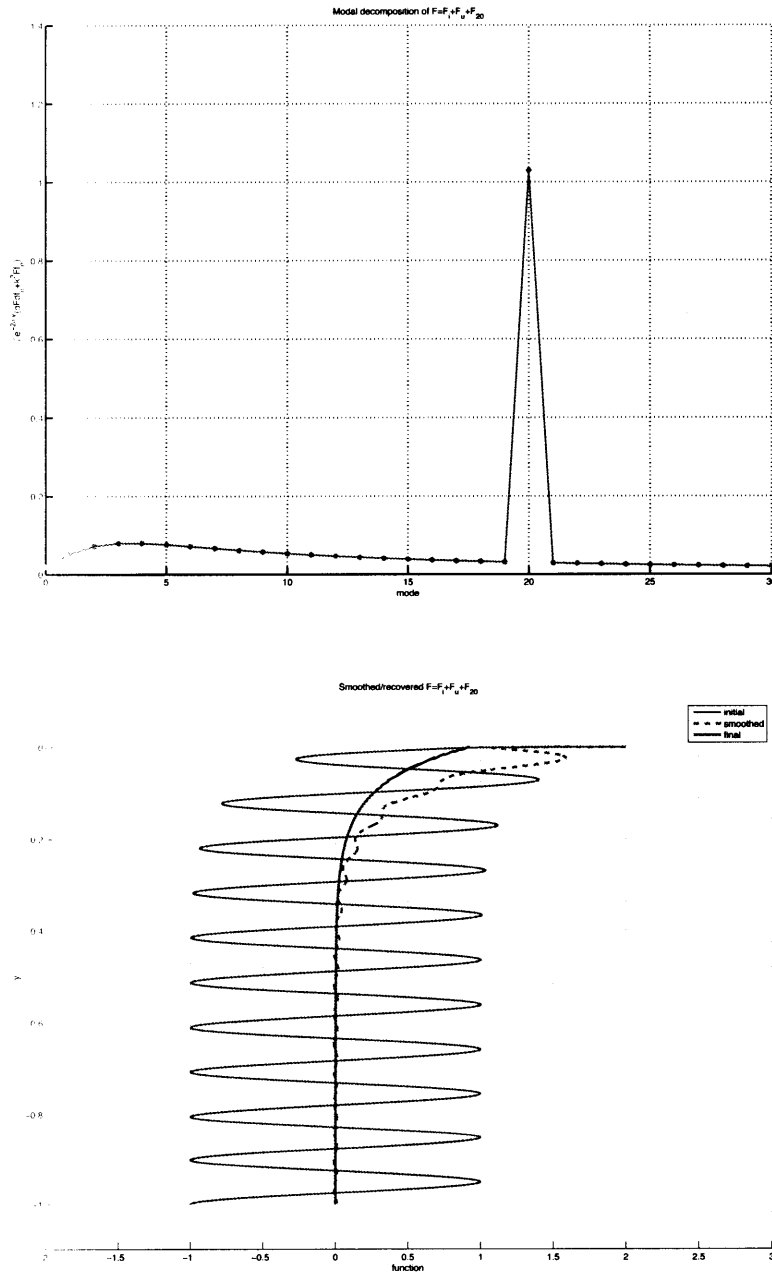


Figure 2-22: Initial noisy solution  $f = f_{-1} + f_{20} + f_u$ , where  $f_{-1}$  denotes the unit amplitude incompressible solution,  $f_{20}$  denotes the unit amplitude  $20^{th}$  acoustic mode and  $f_u$  is an unstable mode, i.e., wavenumber larger than  $k$ . Top: Computation of orthogonality relation (2.91) for  $m = 20$ ,  $n = 0, \dots, 30$ . Bottom: Comparison between initial noisy solution  $f(y)$  (thin solid line), smooth solution from (2.86) (dashed line) and smooth with instability reduction solution (thick solid line) along the depth. Deep water assumption,  $kH = 2\pi$ .

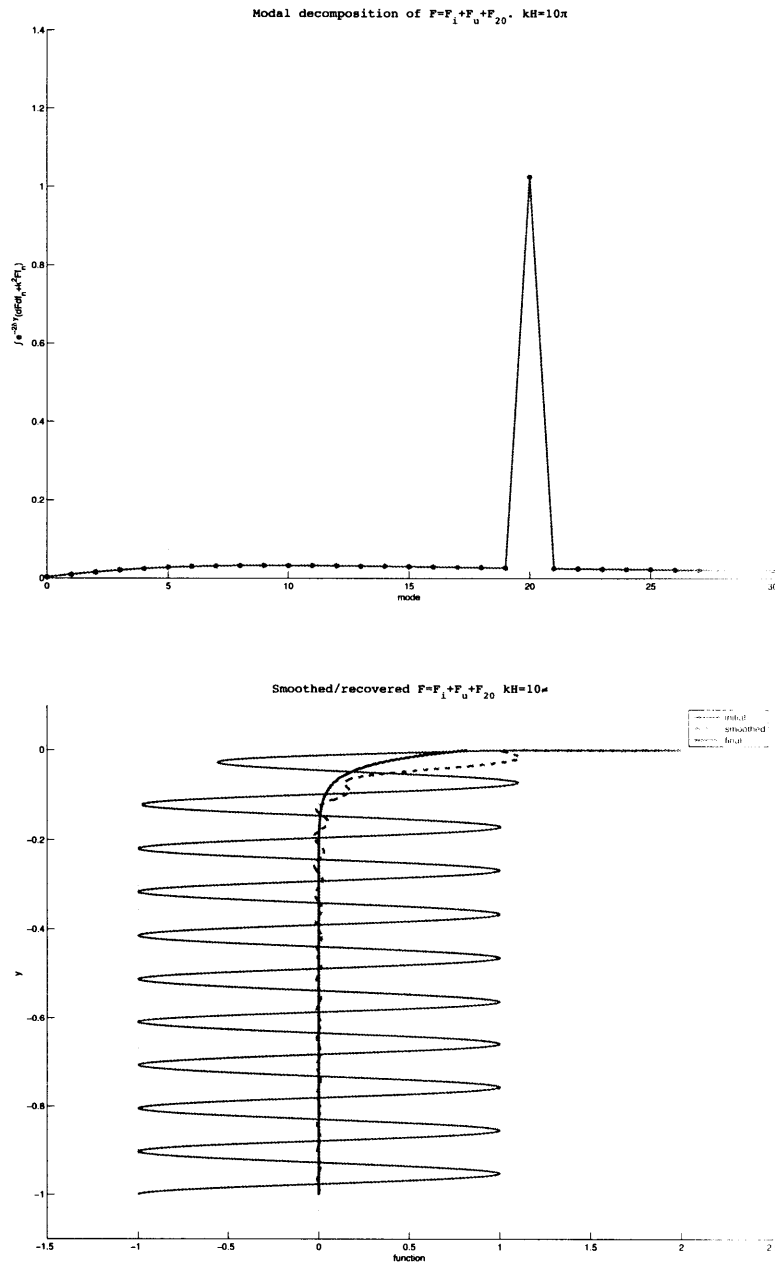


Figure 2-23: Initial noisy solution  $f = f_{-1} + f_{20} + f_u$ , where  $f_{-1}$  denotes the unit amplitude incompressible solution,  $f_{20}$  denotes the unit amplitude  $20^{th}$  acoustic mode and  $f_u$  is an unstable mode, i.e., wavenumber larger than  $k$ . Top: Computation of orthogonality relation (2.91) for  $m = 20$ ,  $n = 0, \dots, 30$ . Bottom: Comparison between initial noisy solution  $f(y)$  (thin solid line), smooth solution from (2.86) (dashed line) and smooth with instability reduction solution (thick solid line) along the depth. Deep water assumption,  $kH = 10\pi$ .

where  $\kappa_m = \frac{2\pi m}{L}$  and it is implied that  $a_{m,n}$  and  $b_{m,n}$  have a parametric time dependence. Given that  $\nabla\Phi = \vec{u}$ , multiplying the velocity components with complex conjugates and integrating over the domain length obtains

$$\int_0^L \Phi_y(\sin \kappa_m x^*) dx^* = \int_0^L v(x^*, y)(\sin \kappa_m x^*) dx^* \xrightarrow[=\frac{L}{2}\delta_{mn}]{\int \sin \kappa_m x \sin \kappa_n x} \frac{L}{2} \sum_{n=-1} a_{m,n} \psi'_{m,n}(y)$$

where  $\delta_{mn}$  is the Kronecker delta. Similarly, the following are also obtained:

$$\int_0^L v(x^*, y)(\cos \kappa_m x^*) dx^* = \frac{L}{2} \sum_{n=-1} b_{m,n} \psi'_{m,n}(y) \quad (2.98)$$

$$\int_0^L u(x^*, y)(\sin \kappa_m x^*) dx^* = -\frac{L}{2} \kappa_m \sum_{n=-1} b_{m,n} \psi_{m,n}(y) \quad (2.99)$$

$$\int_0^L u(x^*, y)(\cos \kappa_m x^*) dx^* = \frac{L}{2} \kappa_m \sum_{n=-1} a_{m,n} \psi_{m,n}(y) \quad (2.100)$$

The simplified orthogonality relation (2.94) becomes

$$\begin{aligned} a_{m,-1} &= \int_{-H}^0 \frac{e^{\kappa_m y^*}}{I_{-1,1,m}} \left[ \sum_n a_{m,n} \psi'_{m,n} + \kappa_m \sum_n a_{m,n} \psi_{m,n} \right] dy^* \\ &= \frac{2}{L} \int_{-H}^0 \frac{e^{\kappa_m y^*}}{I_{-1,1,m}} dy^* \int_0^L dx^* [v \sin \kappa_m x^* + u \cos \kappa_m x^*], \end{aligned} \quad (2.101)$$

and

$$\begin{aligned} b_{m,-1} &= \int_{-H}^0 \frac{e^{\kappa_m y^*}}{I_{-1,1,m}} \left[ \sum_n b_{m,n} \psi'_{m,n} + \kappa_m \sum_n b_{m,n} \psi_{m,n} \right] dy^* \\ &= \frac{2}{L} \int_{-H}^0 \frac{e^{\kappa_m y^*}}{I_{-1,1,m}} dy^* \int_0^L dx^* [v \cos \kappa_m x^* - u \sin \kappa_m x^*]. \end{aligned} \quad (2.102)$$

Finally, the smoothed field is obtained from:

$$\begin{aligned} \bar{\Phi}_M(x, y, t) &= \frac{2}{L} \sum_m^M \left\{ \sin \kappa_m x \int_{-H}^0 \frac{e^{\kappa_m y^*}}{I_{-1,1,m}} dy^* \int_0^L [v \sin \kappa_m x^* + u \cos \kappa_m x^*] dx^* + \right. \\ &\quad \left. + \cos \kappa_m x \int_{-H}^0 \frac{e^{\kappa_m y^*}}{I_{-1,1,m}} dy^* \int_0^L [v \cos \kappa_m x^* - u \sin \kappa_m x^*] dx^* \right\} e^{\kappa_m y}, \end{aligned} \quad (2.103)$$

where it is recalled that  $I_{-1,1,m} = 2\kappa_m \int_{-H}^0 e^{2\kappa_m y^*} dy^*$ . Of course, in practice the integrals are computed for each mode and then the velocities and the dynamic pressure are computed from  $\nabla\Phi = \vec{u}$  and  $\Phi_t + \frac{P_d}{\rho_f} = 0 \xrightarrow{\omega_m^2 = g\kappa_m} P = \rho_f u \sqrt{\frac{g}{\kappa_m}}$ .

Two approaches are considered in obtaining the above smoothed field. In the first approach the field is reconstructed from (2.103) for a small number of horizontal wavenumbers, say  $M = O(5)$ . The volume integrals can be computed either by direct summation on the particle locations, or for higher accuracy, at desired locations through a quadrature scheme. The values of the velocity at the latter quadrature points are computed through MLS interpolation. The approach is of order  $O(N)$ , where  $N$  is the total number of particles, and does not require an underlying grid.

In the second approach, the particle velocities are interpolated along a regular grid of spacing  $[\delta x, \delta y]$ . An FFT is performed along the horizontal direction at each depth  $b\delta y$  to obtain  $a_{m,n}\psi_{m,n}(b\delta y)$ . Then (2.94) is applied along the depth for each mode  $m$  to obtain  $a_{m,-1}$ . Finally, an IFFT is performed to reconstruct the field. A hat filter can be used at this step to maintain desired horizontal wavenumbers. Finally, the smoothed velocities can be either interpolated back to the particle locations, or the regular grid can be considered to indicate updated particle locations. This approach, is still  $O(N)$  and although it appears less attractive because it requires re-gridding. However, it allows the direct removal of the most unstable modes, as will be discussed in the following section, and is thus preferred for numerical simulations. Applications were restricted to small amplitude waves, to avoid re-gridding issues.

## 2.5 Consistency analysis of Kernel Interpolation in MA-SPH for free-surface flows

In MA-SPH the continuous weakly compressible equations of motion (2.5) - (2.8) are integrated numerically over a finite number of discrete Lagrangian fluid particles. The spatial derivatives appearing in the aforementioned equations of motion are computed at each particle position with Kernel Interpolation, as described in (2.11) - (2.14). The particles are advected from the equations of motion and thus are not necessarily expected to be distributed on a structured grid. The major advantage of employing Kernel Interpolation (KI) for the computation of spatial derivatives at each particle position is that it does not require any underlying mesh or structure on the particle positions, rendering MA-SPH as a truly meshless method.

This section deals with the consistency analysis of KI for the estimation of the value of a function and its first derivative at a given particle position in discrete space for uniform, random and smoothly advected particle distributions. First, KI in discrete space is defined in section 2.5.1. Next, the consistency of KI in an unbounded domain is considered. The MA-SPH density is considered for smoothly advected particles that were initially placed on a regular, unbounded grid and consistency of KI for smoothly advected particles is proven. Finally, the presence of a free-surface and its effect on the implemented boundary conditions is studied in section 2.5.6.

### 2.5.1 Definition of Kernel Interpolation

Kernel Interpolation is used to compute the value of a function or its derivatives at a known particle position (collocation point) in discrete space as the convolution of the values of the function at neighboring particles with a known analytic distance function. It does not require the use of grids. KI was introduced and analyzed completely in [29] for the case of equi-spaced particles in an unbounded domain. Later work, presented in [25], in the context of SPH has approached the issue in slightly different manner but without adding further insight.

To define KI first assume a number of one-dimensional particles  $a = -N_l, \dots, -1, 0, 1, \dots, +N_r$  lying along the  $x$  axis. Assume that each particle  $a$  carries its own mass  $m_a$ , density  $\rho_a$ , and volume  $\forall_a \equiv m_a/\rho_a$ . Let the position of the center of mass of particle  $a$  be  $x_a \in (L_l, L_r)$ . Let  $W(x, h)$  denote an analytic, smooth kernel function of  $x$  and the parameter  $h$ , which is defined as the kernel bandwidth with units of length. For now assume that the kernel scales as  $h^{-1}$ , i.e.,  $W \sim h^{-1}$ , that it has compact support, i.e.,  $W = 0$  for  $|x| > \alpha h$ ,  $\alpha \sim O(1)$  and that it is normalized  $\int_{-\infty}^{+\infty} W dx = \int_{-\alpha h}^{+\alpha h} W dx = 1$ . Examples of such kernels include the B-Splines [29], appropriately normalized Gaussians, etc. Finally, consider a sufficiently smooth function  $f(x)$ . KI for the interpolation of the value of the function is defined as:

$$\hat{f}(x_a) \equiv \sum_{b=-N_l}^{+N_r} f(x_b) \frac{m_b}{\rho_b} W(x_a - x_b, h). \quad (2.104)$$

The value of the first derivative is

$$\frac{\hat{d}f}{dx}(x_a) \equiv \sum_{b=-N_l}^{+N_r} f(x_b) \frac{m_b}{\rho_b} \frac{dW}{dx}(x_a - x_b, h). \quad (2.105)$$

To simplify the above expressions denote hereafter  $f_a \equiv f(x_a)$ ,  $f'_a \equiv \frac{df}{dx}(x_a)$ ,  $W_{ab} \equiv W(x_a - x_b, h)$ , and  $W'_{ab} \equiv \frac{dW}{dx}(x_a - x_b, h)$ . To conclude the definition of KI it must be pointed out that the density of each particle may be unknown. Substituting  $f$  with  $\rho$  in (2.104) the following definition is obtained:

$$\rho_a \equiv \sum_{b=-N_l}^{+N_r} \rho_b \frac{m_b}{\rho_b} W_{ab} = \sum_{b=-N_l}^{+N_r} m_b W_{ab}. \quad (2.106)$$

It should be noted that if the mass has units  $[M]$ , the units of the particle density in this case are  $[ML^{-1}]$  and thus the particle volume has units  $[L]$ . This is in agreement with the initial one-dimensional assumption. Equations (2.104) and (2.105) along with (2.106) conclude the definition of KI for the estimation of the value of a function and its first derivative at a particle position, given the values of the function and the relative distances of known neighboring particles. The above three relations are

re-displayed below for ease to the reader

$$\begin{aligned}\rho_a &\equiv \sum_{b=-N_l}^{+N_r} m_b W_{ab} \\ \hat{f}_a &\equiv \sum_{b=-N_l}^{+N_r} \frac{m_b}{\rho_b} f_b W_{ab} \\ \hat{f}'_a &\equiv \sum_{b=-N_l}^{+N_r} \frac{m_b}{\rho_b} f_b W'_{ab}.\end{aligned}$$

In two-dimensions  $[x, y]$  the kernel functions are often defined as radial basis functions. However, higher dimensional kernels can be simply obtained as the tensor products of one-dimensional kernels. For example in two-dimensions it is  $\mathbf{W}(\vec{x}, h) \equiv W(x, h)W(y, h)$ . In this case the units of  $\mathbf{W}$  are  $[L^{-2}]$ . The density has units of  $[ML^{-2}]$  and the volume  $[L^2]$ . In this case if  $g(\vec{x})$  denotes a sufficiently smooth function of  $\vec{x}$  and  $g_a \equiv g(\vec{x}_a)$  then KI is defined as:

$$\rho_a \equiv \sum_{b=-N_l}^{+N_r} m_b \mathbf{W}_{ab} \quad (2.107)$$

$$\hat{g}_a \equiv \sum_{b=-N_l}^{+N_r} \frac{m_b}{\rho_b} g_b \mathbf{W}_{ab} \quad (2.108)$$

$$\hat{\nabla} g_a \equiv \sum_{b=-N_l}^{+N_r} \frac{m_b}{\rho_b} g_b \nabla \mathbf{W}_{ab}, \quad (2.109)$$

where

$$\nabla \mathbf{W}_{ab} = W'(x_a - x_b, h)W(y_a - y_b, h)\hat{i} + W(x_a - x_b, h)W'(y_a - y_b, h)\hat{j}. \quad (2.110)$$

## 2.5.2 Uniform and randomly distributed unbounded particle distribution

Kernel Interpolation is defined in section 2.5.1 for the interpolation of the value of a function and its first derivative at a particle position, given the values of the function

and the relative distances of known neighboring particles. What is of outmost interest is to determine the consistency of KI, i.e., if  $\hat{f} = f + O(h^{\ell_0})$  and  $\hat{f}' = f' + O(h^{\ell_1})$  what are the values of  $\ell_0$  and  $\ell_1$  in an SPH simulation? In order to answer this question several steps need to be taken. First, the unbounded, one-dimensional problem is considered. It is assumed that the particles are equi-spaced. The moments of the kernel are related to the values of  $\ell_0$  and  $\ell_1$ . Next, the density equation is investigated. Assuming that the particles have been advected by the equations of motion (2.11) - (2.14) the consistency of KI is proven inside the domain of an MA-SPH simulation. This section in large follows the approach of [29]. Certain assumptions are made and consistency is demonstrated for the cubic B-Spline. Finally, the results are generalized for any grid and kernel combination.

### 2.5.2.1 Uniform particle distribution

Assume a one-dimensional, infinite, and uniform grid of particles with spacing  $\delta x = h$  with  $x_a = ah$ ,  $a = -\infty, \dots, +\infty$ . Let the mass of particle  $a$  be  $m_a \equiv m = \text{constant}$ . Since the particles are equi-spaced it is reasonable to assume that  $\forall_a = h$  and thus  $\rho_a \equiv \rho_f = m/h = \text{constant}$ . Let  $W(x, h)$  denote a continuous kernel function and let the kernel bandwidth be equal to  $h$ . To simplify the demonstrations all computations will be performed with the most commonly used kernel, i.e., the cubic B-Spline (2.111) and  $h = \delta x$ . Everything can be easily extended to different appropriate kernels and different ratios of  $\delta x/h$  provided that  $\delta x/h \sim O(1)$ , i.e., the kernel has a compact support. The last assumption is an efficiency requirement for numerical simulations.

$$W(x, h) = \frac{2}{h} \begin{cases} \frac{2}{3} + \left(\frac{x}{h}\right) + \frac{1}{2} \left(\frac{x}{h}\right)^2 + \frac{1}{12} \left(\frac{x}{h}\right)^3 & \text{for } -2 \leq \left(\frac{x}{h}\right) \leq -1 \\ \frac{1}{3} - \frac{1}{2} \left(\frac{x}{h}\right)^2 - \frac{1}{4} \left(\frac{x}{h}\right)^3 & \text{for } -1 \leq \left(\frac{x}{h}\right) \leq 0 \\ \frac{1}{3} - \frac{1}{2} \left(\frac{x}{h}\right)^2 + \frac{1}{4} \left(\frac{x}{h}\right)^3 & \text{for } 0 \leq \left(\frac{x}{h}\right) \leq 1 \\ \frac{2}{3} - \left(\frac{x}{h}\right) + \frac{1}{2} \left(\frac{x}{h}\right)^2 - \frac{1}{12} \left(\frac{x}{h}\right)^3 & \text{for } 1 \leq \left(\frac{x}{h}\right) \leq 2 \\ 0 & \text{for } \left|\frac{x}{h}\right| > 2 \end{cases} \quad (2.111)$$

First, the consistency of estimating the value of the function is considered, i.e.,  $\hat{f} = f + O(h^{\ell_0})$ . From (2.111) the values of  $W$  at  $x = [-2h, -h, 0, h, 2h]$  are evaluated

to  $[0, \frac{1}{6h}, \frac{2}{3h}, \frac{1}{6h}, 0]$  respectively. Recalling that  $W_{ab} = W(x_a - x_b, h) = W([(a - b)h], h)$  the next follows

$$\begin{aligned} \sum_{b=-\infty}^{+\infty} \frac{m_b}{\rho_b} W_{ab} &= \sum_{b=a-2}^{a+2} h W_{ab} = h \left( \frac{1}{6h} + \frac{2}{3h} + \frac{1}{6h} \right) = 1 \\ \sum_{b=-\infty}^{+\infty} \frac{m_b}{\rho_b} x_{ba} W_{ab} &= \sum_{b=a-2}^{a+2} h [(b - a)h] W_{ab} = h \left( -h \frac{1}{6h} + 0 + h \frac{1}{6h} \right) = 0 \\ \sum_{b=-\infty}^{+\infty} \frac{m_b}{\rho_b} x_{ba}^2 W_{ab} &= \sum_{b=a-2}^{a+2} h [(b - a)h]^2 W_{ab} = h \left( h^2 \frac{1}{6h} + 0 + h^2 \frac{1}{6h} \right) = \frac{h^2}{3} \end{aligned} \quad (2.112)$$

The consistency of (2.104) is easily proven by taking the Taylor Series Expansion of  $f_b$  about  $x_a$ :

$$\begin{aligned} \hat{f}_a &\equiv \sum_{b=-\infty}^{+\infty} \frac{m_b}{\rho_b} f_b W_{ab} = \sum_b h \left( f_a + x_{ba} f'_a + \frac{x_{ba}^2}{2!} f''_a \right) W_{ab} = \\ &= f_a \sum_b h W_{ab} + f'_a \sum_b h x_{ba} W_{ab} + f''_a \sum_b h \frac{x_{ba}^2}{2!} W_{ab} \stackrel{(2.112)}{=} \\ &= f_a + f'_a \frac{h^2}{6}. \end{aligned} \quad (2.113)$$

Next, the consistency of KI in the estimation the value of the first derivative of a function is considered, i.e.,  $\hat{f}' = f' + O(h^{\ell_1})$ . The first derivative of the cubic B-Spline is:

$$W'(x, h) = \frac{2}{h^2} \begin{cases} 1 + \left(\frac{x}{h}\right) + \frac{1}{4} \left(\frac{x}{h}\right)^2 & \text{for } -2 \leq \left(\frac{x}{h}\right) \leq -1 \\ -\left(\frac{x}{h}\right) - \frac{3}{4} \left(\frac{x}{h}\right)^2 & \text{for } -1 \leq \left(\frac{x}{h}\right) \leq 0 \\ -\left(\frac{x}{h}\right) + \frac{3}{4} \left(\frac{x}{h}\right)^2 & \text{for } 0 \leq \left(\frac{x}{h}\right) \leq 1 \\ -1 + \left(\frac{x}{h}\right) - \frac{1}{4} \left(\frac{x}{h}\right)^2 & \text{for } 1 \leq \left(\frac{x}{h}\right) \leq 2 \\ 0 & \text{for } \left|\frac{x}{h}\right| > 2 \end{cases} \quad (2.114)$$

From (2.114) the values of  $W'$  at  $x = [-2h, -h, 0, h, 2h]$  are  $[0, \frac{1}{2h^2}, 0, \frac{-1}{2h^2}, 0]$ , respec-

tively. The next follows

$$\begin{aligned}
\sum_{b=-\infty}^{+\infty} \frac{m_b}{\rho_b} W'_{ab} &= \sum_{b=a-2}^{a+2} h W'_{ab} = h \left( \frac{-1}{2h^2} + \frac{1}{2h^2} \right) = 0 \\
\sum_{b=-\infty}^{+\infty} \frac{m_b}{\rho_b} x_{ba} W'_{ab} &= \sum_{b=a-2}^{a+2} h [(b-a)h] W'_{ab} = h \left( -h \frac{-1}{2h^2} + h \frac{1}{2h^2} \right) = 1 \\
\sum_{b=-\infty}^{+\infty} \frac{m_b}{\rho_b} x_{ba}^2 W'_{ab} &= \sum_{b=a-2}^{a+2} h [(b-a)h]^2 W'_{ab} = h \left( h^2 \frac{-1}{2h^2} + h^2 \frac{1}{2h^2} \right) = 0 \\
\sum_{b=-\infty}^{+\infty} \frac{m_b}{\rho_b} x_{ba}^3 W'_{ab} &= \sum_{b=a-2}^{a+2} h [(b-a)h]^3 W'_{ab} = h \left( -h^3 \frac{-1}{2h^2} + h^3 \frac{1}{2h^2} \right) = h^2
\end{aligned} \tag{2.115}$$

The consistency of (2.105) is easily proven by taking the Taylor Series Expansion of  $f$  about  $x_a$ :

$$\begin{aligned}
\hat{f}'_a &\equiv \sum_{b=-\infty}^{+\infty} \frac{m_b}{\rho_b} f_b W'_{ab} = \sum_b h \left( f_a + x_{ba} f'_a + \frac{x_{ba}^2}{2!} f''_a + \frac{x_{ba}^3}{3!} f'''_a \right) W'_{ab} = \\
&= f_a \sum_b h W'_{ab} + f'_a \sum_b h x_{ba} W'_{ab} + f''_a \sum_b h \frac{x_{ba}^2}{2!} W'_{ab} + f'''_a \sum_b h \frac{x_{ba}^3}{3!} W'_{ab} \stackrel{(2.115)}{=} \\
&= f'_a + f'''_a \frac{h^2}{6}.
\end{aligned} \tag{2.116}$$

Eq.(2.112) and (2.115) are called consistency conditions. It is evident that any kernel that has been constructed in such a way as to satisfy the appropriate consistency conditions in a given grid will provide a consistent KI in the aforementioned grid.

The previous relations can be easily generalized to any kernel and grid combination. In detail, assume a grid and a kernel whose moments satisfy the following relations for the given grid:

$$\begin{aligned}
\sum_b \frac{m_b}{\rho_b} x_{ba}^m W_{ab} &= \delta_{0,m}^k, \text{ true for all } m = 0, 1, \dots, \ell_0 - 1 \text{ and} \\
\sum_b \frac{m_b}{\rho_b} \frac{x_{ba}^{\ell_0}}{\ell_0!} W_{ab} &= \alpha h^{\ell_0},
\end{aligned} \tag{2.117}$$

where,  $\delta^k$  denotes the Kroenecker delta and no assumptions have been made on the shape of the kernel. By Taylor Series expansion of  $f_b$  about  $x_a$  it can be shown that

$\hat{f}$  is consistent with  $f$  up to  $O(h^{\ell_0})$ :

$$\tilde{f}_a \equiv \sum_b \frac{m_b}{\rho_b} f_b W_{ab} = f_a + \alpha h^{\ell_0} f_a^{(\ell_0)} + \text{h.o.t.} \quad (2.118)$$

In a similar manner, let the first derivative of the kernel satisfy:

$$\begin{aligned} \sum_b \frac{m_b}{\rho_b} x_{ba}^n W'_{ab} &= \delta_{1,n}^k \text{ true for all } n = 0, 1, \dots, \ell_1 \text{ and} \\ \sum_b \frac{m_b}{\rho_b} \frac{x_{ba}^{\ell_1+1}}{(\ell_1+1)!} W'_{ab} &= \beta h^{\ell_1}. \end{aligned} \quad (2.119)$$

By Taylor Series expansion of  $f_b$  about  $x_a$  it can be shown that  $\hat{f}'$  is consistent with  $f'$  up to  $O(h^{\ell_1})$ :

$$\tilde{f}'_a \equiv \sum_b \frac{m_b}{\rho_b} f'_b W'_{ab} = f'_a + \beta h^{\ell_1} f_a^{(\ell_1+1)} + \text{h.o.t.} \quad (2.120)$$

It must be noted that for a kernel to be used for the computation of the value of the first derivative of a function it only needs to satisfy (2.119) and NOT both (2.117) and (2.119).

The previous can be easily extended to higher dimensions simply by taking the tensor products of the kernels in each direction and/or for higher order derivatives by taking appropriate moments.

In summary, the consistency of KI for uniform unbounded grid is reviewed. For a specific grid and kernel combination, in which the moments of the kernel are described by (2.117) it was shown that KI is consistent to order  $O(h^{\ell_0})$  for the estimation of the function at a given particle. Similarly, and not necessarily at the same time, for a specific grid and kernel combination, in which the moments of the kernel are described by (2.119) it is shown that KI is consistent to order  $O(h^{\ell_1})$  for the estimation of the derivative of a function at a given particle. Therefore, it was shown that as  $h \rightarrow 0$  KI converges.

### 2.5.2.2 Transforms in uniform particle distribution

To perform a numerical stability analysis of a spatially discrete scheme the Fourier transforms of the spatial interpolation and/or differentiation scheme must be known. Therefore, for the stability analysis of MA-SPH it is imperative to compute the Fourier transforms corresponding to KI. The latter are also indicative of the consistency of the spatial interpolation and/or differentiation scheme. For this reason the computation of the transforms is considered to be part of the consistency analysis of KI and is thus performed here.

However, for the simulation of free-surface waves with MA-SPH an additional transform of the KI must be performed. As has been discussed in section 2.4 flow quantities in free-surface gravity waves under the linear weak compressibility assumption can be spatially decomposed into two sets of modes in the vertical direction: oscillatory (imaginary wavenumber) or exponential (real wavenumber). Therefore, in the present section two transforms are considered: Fourier and exponential.

Given that higher-dimensional kernels can be simply obtained as the tensor products of one-dimensional kernels, the analysis is performed in one dimension. The cubic B-Spline of compact support  $h$  described in 2.111 is considered.

The approach has as follows. A one-dimensional domain and a smooth function are introduced. The function is expanded in terms of modes that can be either real or imaginary. The KI for the function and its first derivative are given. The modal expansion of the function is substituted and the transforms are obtained.

Namely, assume a one-dimensional, infinite, uniform particle grid. Let the spacing be  $\delta x = h$  with  $x_a = ah$ ,  $a = -\infty, \dots, +\infty$ . Let the mass of particle  $a$  be  $m_a \equiv m = \text{constant}$ . Since the particles are equi-spaced it is reasonable to assume that  $\forall_a = h$  and thus  $\rho_a \equiv \rho_f = m/h = \text{constant}$ . Let  $W(x, h)$  denote a continuous kernel function with kernel bandwidth  $h$ . All computations will be performed with the cubic B-Spline (2.111) but can be easily extended to different appropriate kernels and different ratios of  $\delta x/h$  with  $\delta x/h \sim O(1)$ . The last assumption is essentially an efficiency requirement for numerical simulations.

A sufficiently smooth function  $f(x)$  is considered. Assume the following modal expansion for  $f_b = f(x_b)$ :

$$f_b = f e^{\kappa x_b}, \quad (2.121)$$

where without loss of generality (shifting the origin) it is assumed that  $f \equiv f(0)$ . The wavenumber  $\kappa$  can be either imaginary,  $\kappa \rightarrow ik$ , or real,  $\kappa \rightarrow \mu$ . Substituting the above modal expansion into (2.104) the transform of the function interpolation is obtained.

$$\begin{aligned} \hat{f} &= \sum_b \frac{m_b}{\rho_b} f_b W_b \rightarrow \\ &= \sum_b h f e^{\kappa x_b} W_b \rightarrow \\ &= h f \left( e^{-\kappa h} \frac{1}{6h} + \frac{2}{3h} + e^{\kappa h} \frac{1}{6h} \right) \rightarrow \\ &= f \left[ 1 + \frac{(e^{\kappa h/2} - e^{-\kappa h/2})^2}{6} \right], \end{aligned} \quad (2.122)$$

where  $W_b = W(x_b; h)$  with  $W_{\pm 1} = \frac{1}{6h}$ ,  $W_0 = \frac{2}{3h}$  and 0 elsewhere. For  $\kappa \rightarrow ik$  it is  $\hat{f} = f - \frac{2}{3} \sin^2(kh/2)$ . For  $\kappa \rightarrow \mu$  it is  $\hat{f} = f + \frac{2}{3} \sinh^2(\mu h/2)$ . For small  $|\kappa h| \rightarrow e^{\kappa h} \simeq \kappa h$  it is apparent that  $\hat{f} \simeq f(1 + \frac{\kappa^2}{6} h^2)$ .

In the same manner it can also be obtained that

$$g^* = \sum_b \frac{m_b}{\rho_b} f_b x_b W_b = \frac{h}{3} f \frac{e^{\kappa h} - e^{-\kappa h}}{2}. \quad (2.123)$$

For  $\kappa \rightarrow ik$  it is  $g^* = \frac{h}{3} f \cos kh$ . For  $\kappa \rightarrow \mu$  it is  $g^* = \frac{h}{3} f \cosh \mu h$ . Substituting the

modal expansion into (2.105) the transform of the function differentiation is obtained.

$$\begin{aligned}
\hat{f}' &= \sum_b \frac{m_b}{\rho_b} f_b W'_{-b} \longrightarrow \\
&= -\sum_b h f e^{\kappa x_b} W'_b \longrightarrow \\
&= -h f \left( e^{-\kappa h} \frac{1}{2h^2} + e^{\kappa h} \frac{-1}{2h^2} \right) \longrightarrow \\
&= f \frac{e^{\kappa h} - e^{-\kappa h}}{2h}, \tag{2.124}
\end{aligned}$$

where  $-W'_{-b} = W'_b = \frac{dW}{dx}(x_b; h)$  with  $W'_{\pm 1} = \frac{\mp 1}{2h^2}$  and 0 elsewhere. For  $\kappa \rightarrow ik$  it is  $\hat{f}' = f \frac{i \sin kh}{h}$ . For  $\kappa \rightarrow \mu$  it is  $\hat{f}' = f \frac{\sinh \mu h}{h}$ . For small  $|\kappa h| \rightarrow e^{\kappa h} \simeq \kappa h$  it is apparent that  $\hat{f}' \simeq f \kappa$ .

In the same manner it can also be obtained that:

$$g^{**} = \sum_b \frac{m_b}{\rho_b} f_b x_b W_b = f \frac{e^{\kappa h} + e^{-\kappa h}}{2} \tag{2.125}$$

For  $\kappa \rightarrow ik$  it is  $g^{**} = f \cos kh$ . For  $\kappa \rightarrow \mu$  it is  $g^{**} = \cosh \mu h$ .

### 2.5.2.3 Randomly distorted particle distribution

In general if (2.112) and (2.115) are not satisfied in a particular grid (random, presence of boundaries etc) then *in general* kernel interpolation can diverge. For example let

$$\sum_{b=-\infty}^{+\infty} \frac{m_b}{\rho_b} W_{ab} = \underbrace{\alpha}_{O(1)} \rightarrow \hat{f}_a = \sum_{b=-\infty}^{+\infty} \frac{m_b}{\rho_b} f_b W_{ab} = \alpha f_a + O(f'_a h). \tag{2.126}$$

Then, the function is estimated up to a constant, independently of the grid size and the KI is referred to as incomplete. This situation be easily remedied if the kernel is re-normalized, rendering KI consistent up to order  $O(h)$ . However, in the case of the first derivative it is

$$\sum_{b=-\infty}^{+\infty} \frac{m_b}{\rho_b} W'_{ab} = \underbrace{\beta}_{O(1/h)} \rightarrow \hat{f}'_a = \sum_{b=-\infty}^{+\infty} \frac{m_b}{\rho_b} f_b W'_{ab} = \beta f'_a + O(f'_a) \cong O(f'_a/h). \tag{2.127}$$

Evidently, as  $h \rightarrow 0$  the estimation of the derivative diverges. Remedies similar to that used for the estimation of the function point to Moving Least Squares (MLS) [18] or similar type of methods [50, 51, 52], which are computationally slightly more expensive and less robust.

### 2.5.3 Definition of unbounded smoothly advected particle distribution

In the previous section 2.5.2.1 the approach to the consistency of KI with a kernel of compact support for a given unbounded grid is reviewed. Keeping in mind that the goal is to investigate the consistency of KI in an SPH simulation, the present section defines (for small times) a smoothly advected particle distribution that results from an initial uniform distribution that has been advected from a smooth velocity field described by MA-SPH. First, a set of initially equi-spaced particles is considered. Those are assumed to have been smoothly advected from the MA-SPH governing equations. Then, assumptions are made on their relative motion.

Once again, assume a one-dimensional, infinite, and uniform grid of particles with spacing  $\zeta x = h$ . Each particle  $a$  is initially (time  $t^o = 0$ ) located at  $x_a^o = ah$ , where  $a = -\infty, \dots, +\infty$ . The initial mass of each particle is  $m_a = m = \text{const}$ . The initial density of each particle is  $\rho_a^o \equiv \rho_f = m/h = \text{const}$ . Let  $W(x, h)$  denote the cubic B spline (2.111). Assume that the particles are advected by a sufficiently smooth velocity field. Namely, each particle  $a$  has the flow field velocity at the particle position, i.e.,  $u_a(t) \equiv u(x_a, t)$ . The velocity gradient at the position of particle  $a$  is denoted as  $u'_a \equiv \frac{\partial u}{\partial x}(x_a, t)$ . After time  $t$  the position of particle  $a$  is

$$x_a^t = x_a^o + \int_0^t u_a(x_a^r(\tau), \tau) d\tau \equiv x_a^o + \zeta_a^t. \quad (2.128)$$

At time  $t$  the distance between particles  $a$  and  $b$  is:

$$x_{ab}^t = x_a^t - x_b^t = \underbrace{(a-b)h}_{x_{ab}} + \underbrace{\zeta_a^t - \zeta_b^t}_{\zeta_{ab}^t} = x_{ab} + \zeta_{ab}^t, \quad (2.129)$$

where essentially  $\zeta_{ab}^t$  denotes the relative distance of particles  $a$  and  $b$  at time  $t$  due to a temporally integrated velocity gradient from 0 to  $t$ . Since from here on all quantities will be referred to the same time  $t$ , the superscript  $t$  will be dropped.

## 2.5.4 Density in unbounded smoothly advected particle distribution

Once a smoothly advected distribution has been defined the values of the kernel are computed for the later relative positions and the density (2.106) is estimated in terms of flow field quantities. This allows to ultimately prove the consistency between the two expressions for the density computation (2.106) and (2.13) in the following section 2.5.5.

The density of particle  $a$  given by (2.106) becomes

$$\begin{aligned}\rho_a &= \sum_b m_b W_{ab} \xrightarrow{m_b = \rho_f h} \\ &= \rho_f h \sum W(x_{ab}, h) = \\ &= \rho_f h \sum W(x_{\overline{ab}} + \zeta_{ab}, h).\end{aligned}\tag{2.130}$$

Next,  $W(x_{\overline{ab}} + \zeta_{ab}, h)$  is expanded in Taylor Series about  $\overline{x_{ab}}$ :

$$\begin{aligned}W_{ab} &= W(x_{\overline{ab}} + \zeta_{ab}, h) \\ &\cong \underbrace{W(x_{\overline{ab}}, h)}_{W_{\overline{ab}}} + \frac{\zeta_{ab}}{h} \underbrace{h W'(x_{\overline{ab}}, h)}_{W'_{\overline{ab}}} + O\left(\frac{\zeta_{ab}}{h}\right)^2.\end{aligned}\tag{2.131}$$

It is assumed that for a smooth flow there exists a time  $t$  small enough where it can be assumed that for all particles it is

$$\frac{\zeta_{ab}}{h} \ll 1.\tag{2.132}$$

In detail, from (2.128) and given that  $x_{\overline{ab}} \sim O(h)$  it can be seen that  $\zeta_{ab}$  scales as  $tu_{ab} \sim t(hu')$ . Or, equivalently  $\frac{\zeta_{ab}}{h} \sim tu'$ . Therefore, for a smooth flow there exists a

time  $t$  small enough where the above assumption holds. Substituting the expanded value of  $W_{ab}$  into (2.130) and dropping the higher order terms with respect to  $\frac{\zeta_{ab}}{h}$  the density becomes:

$$\begin{aligned}
\rho_a &\cong \rho_f h \sum_b \left( W_{ab} + \frac{\zeta_{ab}}{h} h W'_{ab} \right) \\
&= \rho_f \left( \sum_b h W_{ab} + \sum_b h \zeta_{ab} W'_{ab} \right) \xrightarrow{(2.112)} \\
&= \rho_f \left( 1 + \sum_b h (\zeta_a - \zeta_b) W'_{ab} \right) \xrightarrow{(2.115)} \\
&= \rho_f \left( 1 - \sum_b h \zeta_b W'_{ab} \right) \xrightarrow{(2.116)} \\
\rho_a &\cong \rho_f (1 - \zeta'_a) + O(h^2 \zeta''', (\zeta^2)'')
\end{aligned} \tag{2.133}$$

In SPH literature it is always accepted that the expression  $\sum_b m_b W_{ab}$  is a measure of the density at particle  $a$  at time  $t$ . Geometric arguments can be easily made for a one-dimensional domain, as in [17, 53], but it is not obvious how the latter can be extended to higher dimensions. The above analysis can be easily extended in any dimension to prove that indeed the density computed by  $\sum_b m_b W_{ab}$  is consistent with the density that satisfies the conservation of mass (2.7) or (2.13). It is recalled that  $\sum_b m_b W_{ab}$  is referred to as the direct density while the density advanced by the temporal integration of mass conservation (2.13) is referred to as the advanced density.

In summary, the consistency relation between the direct and advanced density is investigated with two approaches:

1. Firstly, and most straightforwardly, it is shown that the advanced density is related to the direct density simply by taking the total derivative of the direct

density.

$$\begin{aligned}
\rho_a &= \sum m_b W(x_a - x_b, h) \\
\frac{d\rho_a}{dt} &= \frac{d}{dt} \sum m_b W(x_a - x_b, h) \\
&= \sum \frac{d}{dt} (m_b W(x_a - x_b, h)) \xrightarrow{m=\text{const}} \\
&= \sum m_b \frac{d}{dt} W(x_a - x_b, h) \\
&= \sum m_b \frac{dW_{ab}}{dx} \frac{d(x_a - x_b)}{dt} \\
&= \sum_b (u_a - u_b) W'_{ab} \xrightarrow{(2.115)}
\end{aligned} \tag{2.134}$$

$$\frac{d\rho_a}{dt} = - \sum_b m_b u_b W'_{ab}. \tag{2.135}$$

Therefore, the numerical consistency of the direct and the advanced density is determined by the temporal interpolation scheme, i.e., it should be  $O(\delta t^{\ell_2})$ , where  $\delta t$  is the numerical time stepping.

2. Inversely, the direct density should be consistent to the time integral of the conservation of mass. In (2.133) it is shown that at time  $t$  the density at particle  $a$  is given by:

$$\rho_a \cong \rho_f (1 - \zeta'_a) + O(h^2 \zeta''', (\zeta^2)''). \tag{2.136}$$

From the definition of  $\zeta_a$  at time  $t$ :

$$\begin{aligned}
\zeta_a &\equiv \int_0^t u_a(\tau) d\tau \rightarrow \\
\zeta'_a &= \frac{\partial}{\partial x} \left( \int_0^t u_a(\tau) d\tau \right) \Big|_{x_a(t)} \\
&= \int_0^t d\tau \frac{\partial u_a(\tau)}{\partial x} \Big|_{x_a(t)} = \int_0^t d\tau \frac{\partial u_a(\tau)}{\partial x} \Big|_{x_a^\tau + (x_a^t - x_a^\tau)} \\
&\cong \underbrace{\int_0^t d\tau \frac{\partial u_a(\tau)}{\partial x} \Big|_{x_a^\tau}}_{\mathcal{A}} + \underbrace{\int_0^t d\tau (\zeta_a^t - \zeta_a^\tau) \frac{\partial^2 u_a(\tau)}{\partial x^2} \Big|_{x_a^\tau}}_{\mathcal{B}} + \text{h.o.t.} \quad (2.137)
\end{aligned}$$

The scales  $U$ ,  $L$ ,  $t$  for characteristic velocity, characteristic length scale and elapsed time respectively are introduced. Also, let  $\bar{\zeta}$  denote the characteristic length scale for  $\zeta_a$ . Non-dimensionalizing  $\mathcal{A}$  and  $\mathcal{B}$  in the right hand side of the last equation to compare magnitudes obtains:

$$\mathcal{A} = \int_0^t d\tau \frac{\partial u_a(\tau)}{\partial x} \Big|_{x_a^\tau} \sim t \frac{U}{L}, \text{ and} \quad (2.138)$$

$$\mathcal{B} = \int_0^t d\tau (\zeta_a^t - \zeta_a^\tau) \frac{\partial^2 u_a(\tau)}{\partial x^2} \Big|_{x_a^\tau} \sim t \bar{\zeta} \frac{U}{L^2} = \frac{\bar{\zeta}}{h} \frac{h}{L} \left( t \frac{U}{L} \right). \quad (2.139)$$

By construction, it is  $h/L \ll 1 \sim \varepsilon$ . By assumption, the analysis is conducted for time steps small enough that  $\bar{\zeta}/h \ll 1$ . It can be chosen to be  $\bar{\zeta}/h \sim \varepsilon$  in which case it is

$$\mathcal{B} \sim \varepsilon^2 \mathcal{A}, \quad (2.140)$$

and finally the density  $\rho_a$  at time  $t$  obtains

$$\rho_a^t = \sum_b m_b W_{ab} = \rho_f \left( 1 - \int_0^t d\tau \frac{\partial u_a(\tau)}{\partial x} \Big|_{x_a^\tau} \right) + O(\varepsilon^2). \quad (2.141)$$

From the conservation of mass, following the Boussinesq approximation:

$$\begin{aligned}
\frac{1}{\rho_f} \frac{d\rho_{fa}(\tau)}{d\tau} &= -u'_{fa} = - \left. \frac{\partial u_{fa}(\tau)}{\partial x} \right|_{x_a(\tau)} \xrightarrow{f d\tau} \\
\int_0^t d\tau \frac{1}{\rho_f} \frac{d\rho_{fa}(\tau)}{d\tau} &= - \int_0^t d\tau \left. \frac{\partial u_{fa}(\tau)}{\partial x} \right|_{x_a(\tau)} \\
\frac{1}{\rho_f} (\rho_{fa}) \Big|_0^t &= - \int_0^t d\tau \left. \frac{\partial u_{fa}(\tau)}{\partial x} \right|_{x_a(\tau)} \rightarrow \\
\rho_{fa}^t &= \rho_f \left( 1 - \int_0^t d\tau \left. \frac{\partial u_{fa}(\tau)}{\partial x} \right|_{x_a(\tau)} \right). \tag{2.142}
\end{aligned}$$

Comparing (2.141) and (2.142) reveals that if  $u_{fa} = u_a$  then

$$\rho_a^t = \rho_{fa}^t + O(\varepsilon^2) = \rho_{fa}^t + O(\bar{\zeta}/L). \tag{2.143}$$

The later result is straightforwardly extended to two-dimensions. A final comment should be made here: the initial weak compressibility assumption required that the density fluctuations scaled as the Mach number, i.e.,  $\frac{\delta\rho}{\rho} \sim O(\mathcal{M}^2)$ . For this to be satisfied it should be required that both  $\zeta'_a$  and  $h^2\bar{\zeta}'''$  should be at most  $O(\mathcal{M}^2)$ . It can then be observed that in a domain of length 1, the value of  $\mathcal{M}$  should give an upper bound for the choice of the kernel bandwidth  $h$ , i.e.,  $h \leq \mathcal{M}$ .

Summarizing, a relation for the MA-SPH density of smoothly advected particles in terms of the flow field velocity gradient has been established for both the direct and advanced density formulations. The consistency of the above relation to the continuous equations has also been determined.

### 2.5.5 Consistency of Kernel Interpolation technique in unbounded smoothly advected particle distribution. The numerical significance of the SPH density

The consistency of KI for particles lying on a uniform particle distribution has been long established. However, in an MA-SPH simulation the particles are not uniformly distributed. In fact the key to the success of MA-SPH is that there are no underlying mesh or structure requirements in the particle distribution. Is there any way to determine the consistency of KI in a realistic MA-SPH simulation? In the first SPH papers KI was viewed as a Monte Carlo integration and the consistency of the method was thought to be of order  $N^{-\frac{4}{7}}$ , where  $N$  is the number of particles in the *entire* domain. Numerical results showed that the method did better than that. In [25] Monaghan argued that the improved performance was because in an SPH fluid flow the particles will never become entirely distorted. It is pointed out that in MA-SPH the employed kernels are of compact support and thus analysis that considers kernels of infinite support and argues consistency in terms of  $N$  is out of the context of this thesis. Fulk in [17] showed that KI in one-dimension is consistent up to  $O(h^2, h\Delta x)$ . Fulk's result seemed to bridge the analysis to simulation results, where despite the presence of boundaries and the fact that the particle configuration is eventually distorted, SPH has been shown to be consistent at least up to  $O(h)$ . The aim of this section is twofold: to show the consistency of KI for a smoothly advected particle configuration in terms of  $h$  and the flow properties and to determine the conditions under which KI can deteriorate during the evolution of the flow.

To analyze the consistency of KI in an MA-SPH simulation it must be understood that the Lagrangian particle distribution is not completely random. It initiates from a regular grid (where the interpolation properties are known) and evolves from a smooth velocity field, obtained by the MA-SPH governing equations. The approach therefore is to start following an initially regular grid as it evolves for small times and to expand  $f(x_j^n)$  about  $x_i^n$ , at each time step  $n$ . Following this approach we are able to compute for the first time the consistency of Kernel Interpolation in a particle

distribution that consists of smoothly advected particles, initially placed on a uniform grid.

Once again, assume an infinite, one-dimensional, uniform grid of particles with spacing  $\delta x = h$ . Each particle  $a$  is initially (time  $t^o = 0$ ) located at  $x_a^o = ah$ , where  $a = -\infty, \dots, +\infty$ . The initial mass of each particle is  $m_a = m = \text{const}$ . The initial density of each particle is  $\rho_a^o \equiv \rho_f = m/h = \text{const}$ . Let  $W(x, h)$  denote the cubic B spline (2.111). Assume that the particles are advected by a sufficiently smooth velocity field. Namely, each particle  $a$  has the flow field velocity at the particle position, i.e.,  $u_a(t) \equiv u(x_a, t)$ . The velocity gradient at the position of particle  $a$  is denoted as  $u'_a \equiv \frac{\partial u}{\partial x}(x_a, t)$ . After time  $t$  the position of particle  $a$  is:

$$x_a^t = x_a^o + \int_0^t u_a(x_a^\tau(\tau), \tau) d\tau \equiv x_a^o + \zeta_a^t. \quad (2.144)$$

At time  $t$  the distance between particles  $a$  and  $b$  is:

$$x_{ab}^t = x_a^t - x_b^t = x_{ab}^- + \zeta_{ab}^t. \quad (2.145)$$

Since, from here on, all quantities will be referred to the same time  $t$ , the superscript  $t$  will be dropped. For small enough times the density of particle  $a$  given by (2.133) is:

$$\rho_a \cong \rho_f (1 - \zeta'_a) + O(h^2 \zeta''', (\zeta^2)''). \quad (2.146)$$

Substituting (2.146) for the density into (2.104) for the estimation of the function with KI obtains

$$\begin{aligned} \hat{f}_a &\equiv \sum_b \frac{m_b}{\rho_b} f_b W_{ab} \xrightarrow{m_b = \rho_f h} \\ &\cong \sum_b \frac{\rho_f h}{\rho_f (1 - \zeta'_b)} f_b W(x_{ab}^- + \zeta_{ab}, h) + O(h^2 \zeta''', (\zeta^2)''). \end{aligned} \quad (2.147)$$

Further, by Taylor Series expansion of  $W_{ab}$  about  $W_{ab}^-$  and  $(1 - \zeta'_b)^{-1}$  about 1, the

above expression simplifies to

$$\begin{aligned}\hat{f}_a &\cong \sum_b h(1 + \zeta'_b)(f_a + x_{ba}f'_a + \frac{x_{ba}^2}{2!}f''_a)(W_{ab} + \zeta_{ab}W'_{ab}) + O(h^2\zeta''', (\zeta^2)') \\ &\cong f_a + \frac{h^2}{6}f''_a + O(h^2\zeta''', (\zeta^2)').\end{aligned}\quad (2.148)$$

Similarly, for the estimation of the first derivative

$$\begin{aligned}\hat{f}'_a &\equiv \sum_b \frac{m_b}{\rho_b} f_b W'_{ab} \xrightarrow{m_b = \rho_f h} \\ &\cong \sum_b \frac{\rho_f h}{\rho_f(1 - \zeta'_b)} f_b W'(x_{ab} + \zeta_{ab}, h) + O(h^2\zeta''', (\zeta^2)'') \xrightarrow{\text{TSE}} \\ &\cong \sum_b h(1 + \zeta'_b)(f_a + x_{ba}f'_a + \frac{x_{ba}^2}{2!}f''_a)(W'_{ab} + \zeta_{ab}W''_{ab}) + O(h^2\zeta''', (\zeta^2)'') \\ &\cong f'_a + \frac{h^2}{6}f'''_a + O(h^2\zeta', (\zeta^2)').\end{aligned}\quad (2.149)$$

$$\begin{aligned}&\cong \sum_b h(1 + \zeta'_b)(f_a + x_{ba}f'_a + \frac{x_{ba}^2}{2!}f''_a)(W'_{ab} + \zeta_{ab}W''_{ab}) + O(h^2\zeta''', (\zeta^2)'') \\ &\cong f'_a + \frac{h^2}{6}f'''_a + O(h^2\zeta', (\zeta^2)').\end{aligned}\quad (2.150)$$

Putting everything together, and omitting the subscript  $a$  for brevity it is

$$\sum f_b W_{ab} = f + f'' \frac{h^2}{6} - \left[ f u' + h^2 \left( f' \frac{u''}{3} + f'' \frac{u'}{6} \right) \right] t \quad (2.151)$$

$$\sum \frac{f_b}{\rho_b} W_{ab} = f + f'' \frac{h^2}{6} + f \frac{u'''}{6} h^2 t \quad (2.152)$$

$$\sum f_b W'_{ab} = f' + f''' \frac{h^2}{6} - \left[ f u'' + f' u' + h^2 \left( f'' \frac{3u''}{8} + f''' \frac{u'}{12} \right) \right] t \quad (2.153)$$

$$\sum \frac{m_b}{\rho_b} f_b W'_{ab} = f' + f^{(3)} \frac{h^2}{6} + h^2 \left[ f \frac{u^{(4)}}{6} + f' \frac{u^{(3)}}{2} + f'' \frac{u''}{8} + f^{(3)} \frac{u'}{12} \right] t. \quad (2.154)$$

Thus KI, as defined in (2.104) and (2.105) is consistent up to order  $O(h^2, h^2\zeta') = O(h^2, h^2(f u d\tau)')$  when the density  $\rho$  is computed either directly from (2.106) or advanced from the temporal integration of (2.13). Although, the analysis followed here is different from Fulk [17], the two results can in fact be shown to be in agreement. In [17] it is shown that in one-dimension the error behaves as of order  $O(h^2, h\Delta x)$ , where  $\Delta x \equiv \frac{m}{\rho}$  is a measure of the particle volume. However, from the estimation of the density  $\rho = \rho_f(1 - \zeta')$ . Therefore  $\Delta x = \frac{\rho_f h}{\rho_f(1 - \zeta')} \cong h(1 + \zeta')$  translating the

consistency result to  $O(h^2, h^2\zeta')$ , which is in agreement with the above results. One advantage of the later consistency expression, i.e.,  $O(h^2, h^2\zeta')$ , is that it provides an estimation of the behavior of the kernel interpolation in terms of the flow properties and elapsed time. In addition it shows that if the velocity gradients are maintained small throughout the simulation then the performance of the kernel interpolation is improved. Another advantage of the current analysis is that it can be straightforwardly extended to higher dimensions. In two-dimensions, the density can be shown to be

$$\rho_a \cong \rho_f(1 - \nabla \cdot u), \quad (2.155)$$

in which case, after some algebra, it is again found that KI, as defined in (2.104) and (2.105), is consistent up to order  $O(h^2, h^2\nabla \cdot u)$ .

Finally, from the previous analysis it is understood that the consistency of the Kernel Interpolation depends on the term  $\int \nabla \cdot u dt$ , i.e., the compressibility of the fluid. This means that if SPH simulates the incompressible flow with accuracy  $O(1/c^2)$ , then Kernel Interpolation inside the domain is consistent with  $O(h^2, h^2/c^2) \sim O(h^2)$ .

This is in complete agreement with the SPH simulations of Couette flow, one of the benchmark cases for SPH. Solving the governing equations for Couette flow in the presence of a known pressure gradient gives a measure of the accuracy of KI *only*, since it decouples the compressibility assumption and thus the simulation is free of spurious modes described in section 2.4. In that sense Couette flow provides an excellent demonstration for the consistency of KI in a bounded smoothly advected grid.

Summarizing, consistency relations for KI in smoothly advected grids for the interpolation of a function and the value of its first derivative in both one-dimension and two-dimensions were obtained in terms of the kernel bandwidth and the velocity divergence.

### 2.5.6 Implicit dynamic free-surface boundary condition

The solution to MA-SPH defined by (2.11)-(2.4) depends on the imposed boundary conditions (section 2.2.3). In MA-SPH the free-surface kinematic boundary condition is satisfied exactly, because it is a Lagrangian method. In MA-SPH the pressure-free, dynamic free-surface boundary condition is not explicitly imposed. However, due to the incompleteness of KI near the boundaries, an artificial dynamic free-surface boundary condition is implicitly imposed. Since this artificial dynamic free-surface boundary condition is produced by the incompleteness of the KI near the boundaries it is reasonable to assume that it will depend on the shape of the free-surface. Therefore, long-time solution to MA-SPH with the implicit artificial dynamic free-surface boundary condition are expected to differ from long-time solutions that assume a pressure-free dynamic free-surface boundary condition . Therefore, knowledge of the aforementioned artificial dynamic free-surface boundary condition is fundamental for validation of MA-SPH long-time solutions.

To determine the artificial dynamic free-surface boundary condition in MA-SPH two approaches are considered. First, the value of the artificial dynamic free-surface boundary condition is demonstrated for a free-surface particle on a uniform grid. The KI is performed employing the cubic B-Spline with support equal to the particle spacing. Second, the approach described in [21] is used to generalize the results.

Assume a two-dimensional semi-infinite domain and a Cartesian coordinate system  $\vec{x} = [x, y]$ , with  $x \in (+\infty, -\infty)$  and  $y \in [0, -\infty)$ . The domain is discretized into  $N \rightarrow \infty$  particles positioned on a regular grid of spacing  $\delta x = \delta y = h$ . The particles have volume  $\forall = \delta x \delta y = h^2$  and mass  $m = \rho_f h^2$ . The center of mass of particle  $a$  is located at  $\vec{x}_a = (a_x, a_y)h$  where  $a_x = -\infty, \dots, +\infty$  and  $a_y = -\infty, \dots, -1, 0$ . Each particle  $a$  has velocity  $\vec{u}_a = \vec{u}(\vec{x}_a)$  and pressure  $P_a = P(\vec{x}_a)$ , assumed to be sufficiently smooth.

To determine the artificial dynamic free-surface boundary condition in MA-SPH the equations of motion (2.12) and (2.13) are computed on a free-surface particle. Without loss of generality the particle under consideration is positioned on the origin,

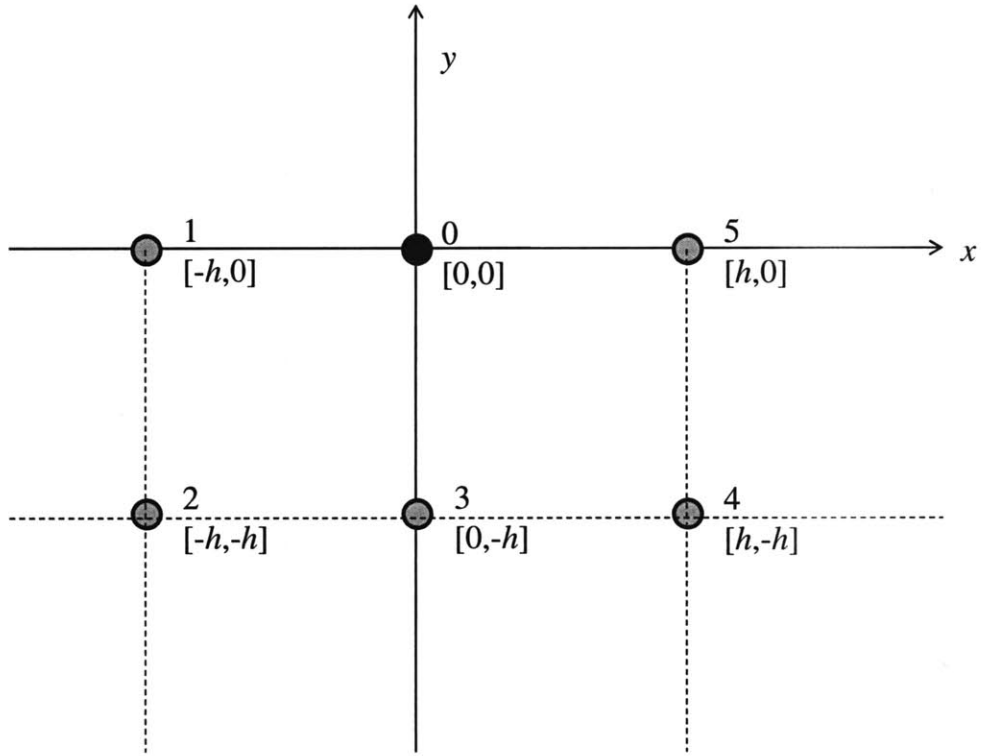


Figure 2-24: Example grid configuration for the computation of the artificial dynamic free-surface boundary condition in MA-SPH due to the Kernel Interpolation incompleteness near the free-surface. The discrete momentum equation and conservation of mass are computed on the free-surface particle 0. Uniform grid of spacing  $h$  in each direction.

Since the velocity and pressure are assumed to be sufficiently smooth, their values at particle  $b$  can be expanded in Taylor Series about the origin:

$$P_b = P + \vec{x}_b \cdot \nabla P$$

$$\vec{u}_b = \vec{u} + (\vec{x}_b \cdot \nabla) \vec{u}$$

where  $P, \vec{u}$  are the values at the origin. Substituting into (2.12) and (2.13) yields

$$\frac{\widehat{d\vec{u}}}{dt} = -\frac{1}{\rho} \sum_b \frac{m_b}{\rho_b} (P + \vec{x} \cdot \nabla P) \nabla w_{0b} - g\hat{j} \quad (2.156)$$

$$\frac{\widehat{d\rho}}{dt} = -\sum_b m_b (\vec{x} \cdot \nabla) \vec{u} \cdot \nabla w_{0b}. \quad (2.157)$$

First, the velocity evolution equation is considered. Recalling that  $m = \rho h^2$  for all particles (2.156) becomes

$$\begin{aligned} \frac{\widehat{d\vec{u}}}{dt} &= -\frac{h^2}{\rho} \sum_b (P + \vec{x}_b \cdot \nabla P) \nabla w_{0b} - g\hat{j} \\ &= -\frac{Ph^2}{\rho} \sum_b \nabla w_{0b} - \frac{h^2}{\rho} \nabla P \cdot \sum_b \vec{x}_b \nabla w_{0b} - g\hat{j} \\ &= -\frac{Ph^2}{\rho} \underbrace{\sum_b \nabla w_{0b}}_{T_1} - \frac{h^2}{\rho} P_x \underbrace{\sum_b x_b \nabla w_{0b}}_{T_2} - \frac{h^2}{\rho} P_y \underbrace{\sum_b y_b \nabla w_{0b}}_{T_3} - g\hat{j}. \end{aligned}$$

Let the kernel be defined as the product of  $w_{0b} = w(0 - \vec{x}_b, h) = W(-x_b, h)W(-y_b, h)$ , where  $W$  denotes the one-dimensional cubic B-Splines. For the particle configuration described in Figure 2-24 only the particles  $a = 0, \dots, 5$  contribute. Upon substitution of the values of the B-Spline (2.111) and its derivative (2.114), the terms  $T_1, T_2$  and  $T_3$  are obtained after some algebra:

$$T_1 = \begin{bmatrix} \sum_0^5 W'(-x_b)W(y_b) \\ \sum_0^5 W(x_b)W'(-y_b) \end{bmatrix} \rightsquigarrow \frac{1}{h^3} \begin{bmatrix} 0 \\ -\frac{1}{2} \end{bmatrix}, \quad (2.158)$$

$$T_2 = \begin{bmatrix} \sum_0^5 x_b W'(-x_b)W(-y_b) \\ \sum_0^5 x_b W(-x_b)W'(-y_b) \end{bmatrix} \rightsquigarrow \frac{1}{h^2} \begin{bmatrix} \frac{5}{6} \\ 0 \end{bmatrix}, \text{ and} \quad (2.159)$$

$$T_3 = \begin{bmatrix} \sum_0^5 y_b W'(-x_b)W(-y_b) \\ \sum_0^5 y_b W(-x_b)W'(-y_b) \end{bmatrix} \rightsquigarrow \frac{1}{h^2} \begin{bmatrix} 0 \\ \frac{1}{2} \end{bmatrix}, \quad (2.160)$$

where  $P_x = \left. \frac{\partial P}{\partial x} \right|_0$  and  $P_y = \left. \frac{\partial P}{\partial y} \right|_0$ . Therefore the computed acceleration at the origin

reduces to

$$\widehat{\frac{d\vec{u}_a}{dt}} = \begin{bmatrix} -\frac{5}{6} \frac{P_x}{\rho} \\ \frac{1}{2} \frac{P}{h\rho} - \frac{1}{2} \frac{P_y}{\rho} - g \end{bmatrix} \xrightarrow{h \rightarrow 0} \begin{bmatrix} 0 \\ \frac{1}{2h} (\frac{P_d}{\rho} - gy) \end{bmatrix}. \quad (2.161)$$

Further, by decomposing the pressure into  $P = -\rho gy + P_d$  where the first term on the right hand side denotes the hydrostatic component and the second term the hydrodynamic, the computed acceleration obtains

$$\widehat{\frac{d\vec{u}}{dt}} = \begin{bmatrix} -\frac{5}{6} \frac{P_{dx}}{\rho} \\ \frac{1}{2} \frac{P_d - hP_{dy}}{h\rho} - \frac{1}{2} g(1 + \frac{y}{h}) \end{bmatrix} = \frac{d\vec{u}_a}{dt} + \begin{bmatrix} \frac{1}{6} \frac{P_{dx}}{\rho} \\ \frac{1}{2} \frac{P_d + hP_{dy}}{h\rho} - \frac{1}{2} g(1 + \frac{y}{h}) \end{bmatrix}. \quad (2.162)$$

Second, the mass conservation is considered. Recalling that  $m = \rho h^2$  for all particles and following the same procedure as with the acceleration. (2.157) after some algebra becomes

$$\begin{aligned} \widehat{\frac{d\vec{\rho}}{dt}} &= -\rho h^2 \left( u_x \underbrace{\sum_0^5 x_b \frac{\partial w}{\partial x}}_{5/6h^2} + u_y \underbrace{\sum_0^5 y_b \frac{\partial w}{\partial x}}_0 + v_x \underbrace{\sum_0^5 x_b \frac{\partial w}{\partial y}}_0 + u_y \underbrace{\sum_0^5 y_b \frac{\partial w}{\partial y}}_{1/2h^2} \right) \\ &= -\rho \left( \frac{5}{6} u_x + \frac{1}{2} v_y \right) \\ &= \frac{d\vec{\rho}}{dt} + \rho \left( \frac{1}{6} u_x + \frac{1}{2} v_y \right). \end{aligned} \quad (2.163)$$

Based on the findings of section 2.5.5, if the particle at the origin is advected by a smooth velocity field, the expressions (2.5.6) and (2.163) remain valid to leading order. It can be observed that the error is most prominent in the  $y$  direction, which is perpendicular to the free-surface.

The expressions (2.5.6) and (2.163) are a very particular choice of a free-surface shape, grid and kernel. Although they are indicative of the error due to the incomplete KI near the free-surface they cannot be of further analytical use. To extend the analysis described in section 2.4 the dynamic free-surface boundary condition should be expressed in terms of the shape of the free-surface or some other flow quantity. The analysis suggested in [21] obtains the equations of motion on the free-surface in terms of integrals instead of sums and incorporates the free-surface normal. The

analysis by [21] investigates only the leading order term, i.e., integral form of  $T1$  in acceleration. The result can be straightforwardly extended to include higher order terms, but it suffices for the present analysis.

Namely in [21] only the velocity evolution equation is considered. Substituting  $m = \rho\mathcal{V}$ , where  $\mathcal{V}$  denotes particle volume and replacing the summations with integrals (2.156) becomes

$$\begin{aligned}\frac{\widetilde{d\vec{u}}}{dt} &= -\frac{1}{\rho} \int_{\mathcal{V}} (P + \vec{x} \cdot \nabla P) \nabla w(\vec{x}) d\mathcal{V} - g\hat{j} \\ &= -\frac{P}{\rho} \int_{\mathcal{V}} \nabla w(\vec{x}) d\mathcal{V} - \frac{\nabla P}{\rho} \cdot \int_{\mathcal{V}} \vec{x} \nabla w(\vec{x}) d\mathcal{V} - g\hat{j} \\ &= -\frac{P}{\rho} \underbrace{\int_{\mathcal{V}} \nabla w(\vec{x}) d\mathcal{V}}_{C_1} - \frac{P_x}{\rho} \int_{\mathcal{V}} x \nabla w(\vec{x}) d\mathcal{V} - \frac{P_y}{\rho} \int_{\mathcal{V}} y \nabla w(\vec{x}) d\mathcal{V} - g\hat{j}. \quad (2.164)\end{aligned}$$

The term  $C_1$  is the leading order term. This is the only term considered in [21] and of interest here. By Green's Theorem,  $C_1$  becomes

$$C_1 = \int_{\mathcal{V}} \nabla w(\vec{x}) d\mathcal{V} = \int_{\partial} w(\vec{x}) \vec{n} dS = \int_{\text{FS}} w(\vec{x}) \vec{n}_{\text{FS}} dS, \quad (2.165)$$

where  $\int_{\partial}$  denotes integration along the boundary and  $\vec{n}$  denotes the boundary normal. Further, it is  $w_{\partial} \neq 0$  only on the free-surface, since it vanishes everywhere else. For the linear waves discussed in section 2.4 the free-surface is  $\eta = \eta(x) = ae^{ikx}$  and  $ak \ll 1$ . Therefore, after dropping terms of  $O((ak)^2)$ , the leading order free-surface normal reduces to

$$\vec{n}_{\text{FS}} = \frac{\nabla \eta}{|\nabla \eta|} = \frac{[\eta_x, 1]}{\sqrt{1 + \eta_x^2}} \simeq [\eta_x, 1]. \quad (2.166)$$

Therefore, the momentum equation on the free-surface becomes to leading order

$$\frac{\widetilde{d\vec{u}}}{dt} = -\frac{P}{\rho} \int_{\text{FS}} w(\vec{x}) \frac{\nabla \eta}{|\nabla \eta|} dS - g \simeq -\frac{P}{\rho} \nabla \eta \underbrace{\int_{\text{FS}} W(x) W(0) dx}_{\alpha/h} - g, \quad (2.167)$$

where it is assumed that  $\nabla \eta$  is practically constant within the support of  $w$ , i.e.,  $kh \ll 1$ . Evidently  $\alpha$  depends only on the choice of kernel. In a uniform grid, for

the cubic B-Spline with  $h$  equal to the particle spacing it is  $\alpha = \frac{2}{3}$ , which differs by a factor of  $\frac{4}{3}$  from (). In either case, what is of interest is the fact that on the free-surface the computed acceleration is given by

$$\frac{\widehat{d\vec{u}}}{dt} = -\alpha \frac{P}{\rho h} \nabla \eta - g \hat{j}. \quad (2.168)$$

It is reasonable to assume that, for a numerical simulation in deep water, the particle spacing is of the same order of magnitude as the free-surface amplitude, i.e.,  $\frac{a}{h} \sim O(1)$ . Given that for the linear gravity waves of consideration it is  $\frac{P}{\rho g} \sim O(a)$  and  $\vec{n}_{\text{FS}} \simeq [\eta_x, 1] \sim [O(ak), O(1)]$ , the horizontal free-surface acceleration scales as

$$\frac{\rho \widehat{du}}{g dt} \sim \alpha \frac{a}{h} ak \sim ak, \quad (2.169)$$

and the vertical direction scales as

$$\frac{\rho \widehat{dv}}{g dt} \sim \alpha \frac{a}{h} \sim \alpha. \quad (2.170)$$

This means, that for a low resolution deep water free-surface gravity wave, the incompleteness of the KI near the free-surface makes the free-surface particles accelerate with a ‘new’ gravitational acceleration. This is equivalent to imposing a vertical hydrostatic-like pressure on the free-surface. Thus the zero-pressure dynamic free-surface boundary condition (2.28), for the  $\Phi = \phi(y)e^{i(\kappa x - \omega t)}$  problem defined in section 2.4, becomes

$$\beta g \phi' - \omega^2 \phi = 0 \text{ on } y = 0 \rightarrow \quad (2.171)$$

$$\phi'' - \kappa^2 \phi = 2\delta(1 - \beta)\phi'. \quad (2.172)$$

The last equation physically means that the free-surface particles have a greater speed of sound than the rest of the fluid domain, i.e., the fluid is ‘stiffer’ near the free-surface.

## 2.6 Linear stability analysis of MA-SPH in semi-infinite domain

The numerical stability analysis of MA-SPH is of fundamental importance, since it determines either the conditions for the scheme's stability or the maximum unstable growth rates of infinitesimal disturbances and thus the scheme's useful computational life.

MA-SPH for free-surface flows first assumes a continuous weakly compressible flow model (CMA-SPH), then obtains its semi-discrete form through KI and finally obtains its fully-discrete form (MA-SPH) through an explicit temporal integration scheme. In order to perform a complete stability analysis that elucidates and allows for improvements on the MA-SPH algorithm, it is essential to perform the analysis starting from the continuous model, proceeding with the semi-discrete algorithm and concluding with the fully-discrete MA-SPH algorithm. In detail, stability analysis of CMA-SPH for both sets of normal modes (section 2.4), i.e., depth decaying and acoustic, reveals that the continuous model is inherently unstable. Next, stability analysis of the semi-discrete scheme reveals how the continuous unstable growth rates are altered by KI. Finally, consideration of the fully-discrete scheme determines the effect of the temporal integration scheme and the significance of the Courant condition, suggesting how to numerically stabilize the inherently unstable continuous model in Chapter 4.

The existing stability analysis of SPH is a characteristic example of the misunderstandings raised when the above order in the analysis is violated. Due to the significant, documented stability issues of MA-SPH, substantial effort has been dedicated to the linear stability analysis of the fully-discrete scheme [17, 26, 44, 53]. All available analysis indicates the presence of a tensile instability that depends on the sign of the product of the pressure and the second derivative of the kernel. The tensile instability does not depend strictly on flow quantities but it is implied that it results from the spatial discretization and can therefore be remedied by the usage of alternative derivative computation techniques [18]. Further, it does not depend either

on the time step size or on the choice of the temporal integration scheme. Therefore, suggesting that all temporal integration schemes are equally stable. As a result, treatments based on the findings of the analysis have not been able to fully remove the instabilities in SPH.

Section 2.6.2 presents a stability analysis of the CMA-SPH where it is confirmed that in the presence of a free-surface the unstable modes can be depth decaying or depth oscillatory [43]. From the analysis of the semi-discrete algorithm, in section 2.6.3, the tensile instability is expressed in terms of the flow quantities and it is shown to depend only on the gradient of the base density distribution. Finally, from the analysis of the fully-discrete scheme for oscillatory disturbances in section 2.6.4, it is found that (a) low order schemes are unstable even in uniform base density distributions, (b) appropriate Courant conditions exist for the analyzed higher order schemes modified Predictor-Corrector and fourth order Runge-Kutta under the assumption of a uniform base density distributions, and (c) fourth order Runge-Kutta is unstable in the presence of a hydrostatic density distribution, but with very small growth rates.

### **2.6.1 Linear von Neumann stability analysis**

The linear von Neumann stability analysis (Von Neumann and Richtmeyer, 1950) performed in this section begins with a definition of the system (semi-infinite domain) and the physical variables that describe the flow. The governing equations for the physical variables are also defined. An initial base flow that satisfies the governing equations is assumed and infinitesimal disturbances are superimposed. The equations that describe the evolution of the aforementioned disturbances are obtained after subtracting the base flow. These equations are linearized by neglecting terms of higher order with respect to the disturbances. Then disturbances are expanded in terms of normal modes. Both real and imaginary wavenumbers are considered. For the semi-discrete analysis, the linearized equations for the disturbances are further simplified by performing the KI summations for the normal modes. For the fully-discrete scheme the temporal integration scheme is chosen. The linearized fully-discrete schemes describing the evolution of the disturbances for both the direct and

advanced density formulations are obtained. These are reduced to a linear system of the form  $q^{n+1} = Aq^n$ , where  $n, n + 1$  denote the values of the vector quantity  $q$  at the time steps  $n$  and  $n + 1$  respectively and  $A$  is the amplification matrix. The system is stable if the magnitude of all the eigenvalues of  $A$  are at most equal to 1, i.e.,  $|\lambda|_{\max} \leq 1$ .

## 2.6.2 Continuous model

First, the stability of the CMA-SPH equivalent linearized velocity potential (section 2.4) is considered inside a two-dimensional domain with zero base flow. Then the linear stability analysis on the CMA-SPH algorithm described by (2.1), (2.2), and (2.4) is performed in one-dimension.

**Velocity potential formulation** Assume a two-dimensional semi-infinite domain and a Cartesian coordinate system  $\vec{x} = [\bar{x}, \bar{y}]$ , with  $\bar{x} \in (+\infty, -\infty)$  and  $\bar{y} \in [0, -\infty)$  where  $\bar{y} = 0$  denotes the location of the free-surface. Let the flow in the domain be described by a velocity potential  $\bar{\Phi}(\bar{x}, \bar{y}, t)$  given by the linear (2.21). Assume an unperturbed state, i.e.,  $\bar{\Phi} = 0$ , and let  $\Phi$  denote an infinitesimal disturbance of the velocity potential. Since  $\bar{\Phi} = 0$  and its governing equation (2.21) is linear, the evolution equation for  $\Phi$  is also given by (2.21). This equation is linear with constant coefficients and thus, separation of variables is assumed. The disturbance is expressed in terms of normal modes: Fourier modes in the horizontal direction and either oscillatory modes (Fourier modes) or depth decaying modes, [43], in the vertical direction. It is investigated under what conditions the time evolution grows exponentially, i.e., the system is unstable. Putting everything together

$$\Phi(\bar{x}, \bar{y}, t) = e^{k\bar{y}} e^{i\kappa\bar{x}} e^{\omega t}, \quad (2.173)$$

where both  $\kappa$  and  $\omega$  are real, and  $\mu$  can be either real or imaginary. Substituting in (2.21) and factoring out  $e^{k\bar{y}}e^{i\kappa\bar{x}}e^{\omega t}$  the characteristic polynomial for  $\omega$  is obtained

$$\frac{\omega^2}{c^2} = (-\kappa^2 + k^2) - 2\delta k. \quad (2.174)$$

Here  $\delta = \frac{g}{2c^2} \ll 1$ , where  $c, g$  are the speed of sound in the medium and the gravitational acceleration respectively.

First, the depth decaying modes, i.e.,  $k \rightarrow \mu$ , where  $\mu$  is real, are considered and obtain

$$\frac{\omega^2}{c^2} = \mu^2 - \kappa^2 - 2\delta\mu > 0 \rightarrow \mu > \kappa. \quad (2.175)$$

This means that any disturbance of wavenumber  $k = \mu > \kappa$  will grow exponentially in time with a growth rate given by

$$\omega = \sqrt{c^2\mu^2 - g\mu - c^2\kappa^2} = c\mu\sqrt{1 - \frac{2\delta}{\mu} - \frac{\kappa^2}{\mu^2}}. \quad (2.176)$$

The growth rate scales linearly with  $c$  and  $\mu$  and is reduced as  $g$  and  $\kappa$  increase. Thus, gravity helps to stabilize the system. The highest growth rate occurs for  $\kappa = 0$ , i.e., an infinitely long wave or everything constant in  $\bar{x}$ . This coincides with the observation in [43] where it was noted that assuming a reduced one dimensional problem is the worst case scenario with respect to the stability of the numerical simulation in a semi-infinite domain.

It is pointed out, that the disturbance  $k = \mu > \kappa$  does not satisfy the physical boundary value problem of zero free-surface pressure and no-flux on the sea-bed. Therefore, such instability is artificial, i.e., it can exist only in the numerical scheme. It is generated by inconsistencies in the numerical implementation of the boundary and initial conditions as well as from numerical round-off errors. For comparison note that for  $\mu = \kappa - \delta$ ,  $\omega$  is imaginary, i.e., the depth decaying modes that satisfy the physical boundary value problem are stable.

Second, depth oscillatory modes, i.e.,  $k \rightarrow i\nu$ , where  $\nu$  is real, are considered and

obtain

$$\frac{\omega^2}{c^2} = -\nu^2 - \kappa^2 - i2\delta\nu \rightarrow \omega \text{ is complex.} \quad (2.177)$$

This means that a disturbance of wavenumber  $k = i\nu$  will grow exponentially in time with growth rate given by

$$w \equiv \Re(\omega) = \Re(\sqrt{-c^2\nu^2 - c^2\kappa^2 - ig\nu}). \quad (2.178)$$

To determine the real part  $w$ , of the complex  $\omega$ , let  $\omega = w + iz$ , where both  $w, z$  are real and non-zero. Then  $\omega^2 = (w + iz)^2 = -c^2\nu^2 - c^2\kappa^2 - ig\nu$ . Equating real and imaginary parts, after some algebra obtains

$$w^2 = \frac{1}{2} \left[ -c^2\nu^2 - c^2\kappa^2 + \sqrt{(c^2\nu^2 + c^2\kappa^2)^2 + g^2\nu^2} \right]. \quad (2.179)$$

The term in the square root can be written as

$$\begin{aligned} \sqrt{(c^2\nu^2 + c^2\kappa^2)^2 + g^2\nu^2} &= (c^2\nu^2 + c^2\kappa^2) \left( 1 + \frac{\overbrace{g^2\nu^2}^{O(\delta^2)}}{(c^2\nu^2 + c^2\kappa^2)^2} \right)^{1/2} \xrightarrow{\text{TSE}} \\ &= (c^2\nu^2 + c^2\kappa^2) \left( 1 + \frac{g^2\nu^2}{2(c^2\nu^2 + c^2\kappa^2)^2} \right). \end{aligned}$$

Putting everything together, the growth rate  $w$  of a disturbance with wavenumber  $i\nu$  is found to be

$$w = \frac{g}{2c^2} \frac{\nu}{\nu^2 + \kappa^2} = \delta \frac{\nu}{\nu^2 + \kappa^2}. \quad (2.180)$$

This growth rate scales linearly with  $g$  and inversely with  $c^2$ ,  $\nu$  and  $\kappa^2$ . Thus for depth oscillatory disturbances gravity de-stabilizes the system. Again, the largest growth rate occurs for  $\kappa = 0$ , i.e., an infinitely long wave or everything constant in  $x$ . Therefore, the stability analysis performed hereafter is one dimensional, keeping in mind that it is a simplification of the described two-dimensional semi-infinite problem.

It is pointed out, that the disturbance  $k = i\nu$  does not satisfy the physical boundary value problem of zero free-surface pressure and no-flux on the sea-bed. Therefore,

such instability is artificial, i.e., it can exist only in the numerical scheme. It is generated by inconsistencies in the numerical implementation of the boundary and initial conditions as well as from numerical round-off errors. For comparison note that for  $k = \delta + i\nu$ ,  $\omega$  is imaginary, i.e., the depth oscillatory modes that satisfy the physical boundary value problem are stable.

As a summary, the velocity potential formulation is unconditionally unstable in the presence of numerically generated depth decaying modes with wavenumber  $\mu > \kappa$  and unstable in the presence of numerically generated purely depth oscillatory modes with wavenumber  $i\nu$ . In the former case gravity stabilizes the system, while in the latter case gravity de-stabilizes the system.

### 2.6.2.1 CMA-SPH

Most typical hydrodynamic SPH simulations, such as the standard dam-break benchmark (SPHERIC 2006), assume a hydrostatic initial condition [3, 48]. For this reason, the present stability analysis first solves the hydrostatic case for the CMA-SPH weakly compressible flow, and then, investigates the stability properties of infinitesimal disturbances superimposed on the hydrostatic case. As discussed, the most unstable condition occurs when the flow is independent of  $\bar{x}$ , therefore hereafter the flow is considered one-dimensional and along the vertical axis.

Let the vertical axis be  $\bar{y} \in [0, -\infty)$  where  $\bar{y} = 0$  denotes the location of the free-surface. Let  $t \geq 0$  denote time and  $g$  the gravitational acceleration. Let  $\rho_f$ ,  $c$  denote the uniform unperturbed fluid density and the uniform speed of sound. Assume a stationary fluid with hydrostatic density  $\bar{\rho}(\bar{y})$  and hydrostatic pressure  $\bar{P}(\bar{y})$ . The governing equations (2.1), (2.2), and (2.4) that describe the hydrostatic CMA-SPH weakly compressible flow reduce to

$$\frac{d\bar{y}}{dt} = 0 \tag{2.181}$$

$$\frac{d\bar{\rho}}{dt} = 0 \tag{2.182}$$

$$\frac{d\bar{v}}{dt} = -\frac{\bar{P}_{\bar{y}}}{\bar{\rho}} - g = 0. \tag{2.183}$$

The last equation (2.183), determines the form of the hydrostatic pressure and density distribution in a weakly compressible fluid, given that the free-surface density is  $\rho_f$ , equivalent to zero-pressure. Namely, the last equation is integrated from 0 to  $\bar{y}$  to obtain

$$\begin{aligned}
-\frac{\bar{P}_{\bar{y}}}{\bar{\rho}} &= g \xrightarrow{dP=c^2 d\rho} \\
-c^2 \frac{\bar{\rho}_{\bar{y}}}{\bar{\rho}} &= g \rightarrow \\
(\ln \bar{\rho})_{\bar{y}} &= -\frac{g}{c^2} \xrightarrow{\int_0^{\bar{y}}} \\
\bar{\rho} &= \rho_f e^{-2\delta\bar{y}}, \text{ where } \delta = \frac{g}{2c^2}. \tag{2.184}
\end{aligned}$$

Next, infinitesimal disturbances  $y$ ,  $v$ ,  $\rho_f r$ , and  $P$  are superimposed on the hydrostatic case in the position, velocity, density and pressure respectively. The governing equations (2.1), (2.2), and (2.4) become

$$\frac{d(\bar{y} + y)}{dt} = v \tag{2.185}$$

$$\frac{dv}{dt} = -\frac{(\bar{P} + P)_{\bar{y}}}{(\bar{\rho} + \rho)} - g \tag{2.186}$$

$$\frac{d(\bar{\rho} + \rho)}{dt} = -(\bar{\rho} + \rho)v_{\bar{y}} \tag{2.187}$$

The total density can be written as

$$\bar{\rho} + \rho_f r = \rho_f (e^{-2\delta y} + r). \tag{2.188}$$

Dropping higher order terms, with respect to the disturbances, the pressure gradient term in the momentum equation (2.186) is expressed as

$$\begin{aligned}
-\frac{(\bar{P} + P)_{\bar{y}}}{(\bar{\rho} + \rho)} &= -c^2 \frac{\rho_f (-2\delta e^{-2\delta y} + r_y)}{\rho_f (e^{-2\delta y} + r)} \xrightarrow[r \ll \delta y, \text{ TSE}]{e^{\delta y} \sim O(1)} \\
&= -c^2 (-2\delta + r_y e^{2\delta y}) (1 - r e^{2\delta y}) \xrightarrow{rrh=\text{h.o.t.}} \\
&= -c^2 (-2\delta + 2\delta r e^{2\delta y} + r_y e^{2\delta y}) \xrightarrow{2c^2 \delta = g} \\
&= g - g r e^{2\delta y} - c^2 r_y e^{2\delta y}. \tag{2.189}
\end{aligned}$$

Similarly, after some algebra the density equation (2.187) simplifies to

$$\frac{dr}{dt} = -e^{-2\delta y} v_y. \quad (2.190)$$

Noting that from Taylor Series Expansion it is  $e^{\pm 2\delta y} \simeq 1 \pm 2\delta y$ , to leading order for the evolution of the disturbances it can be assumed that  $e^{\pm 2\delta y} \simeq 1$ . Substituting into (2.186) and (2.187) the governing equations for the disturbances in position, velocity and density reduce to

$$\begin{aligned} \frac{dy}{dt} &= v \\ \frac{dv}{dt} &= -gr - c^2 r_y \end{aligned} \quad (2.191)$$

$$\frac{dr}{dt} = -v_y. \quad (2.192)$$

Next, the disturbances are assumed to be of the standard form  $e^{kij} e^{i\kappa\bar{x}} e^{\omega t}$ , where both  $\kappa$  and  $\omega$  are real and  $k$  is either depth oscillatory ( $k \rightarrow i\nu$ ) or depth decaying ( $k \rightarrow \mu$ ). Substituting in (2.185), (2.191) and (2.192) the system is written in matrix form as

$$\frac{d}{dt} \begin{bmatrix} y \\ v \\ r \end{bmatrix} = \underbrace{\begin{bmatrix} 0 & 1 & 0 \\ 0 & 0 & -g - c^2 k \\ 0 & -k & 0 \end{bmatrix}}_{\text{Amplification matrix}} \begin{bmatrix} y \\ v \\ r \end{bmatrix}. \quad (2.193)$$

The amplitude of the maximum positive real part of the eigenvalues of the amplification matrix determines the growth rate of the system. For this case, the eigenvalues of the amplification matrix are

$$\omega_{1,2,3} = [0, \pm\sqrt{c^2 k^2 + gk}]. \quad (2.194)$$

For depth decaying components with  $\mu > 0$ , the system is unconditionally unstable with growth rate

$$\omega = \sqrt{c^2 \mu^2 + g\mu}. \quad (2.195)$$

This is slightly worse compared to the stability of the velocity potential formulation (2.176), since now gravity de-stabilizes the system. This result also emphasizes that the hydrostatic base flow must be taken into account in the stability analysis of the fully-discrete systems for the free-surface flows of interest.

For depth oscillatory components it is found that

$$\omega = \sqrt{-c^2\nu^2 - ig\nu}. \quad (2.196)$$

The growth rate is determined by the real part of the term in the square root. Assuming  $\omega = w + iz$  and following the same approach as with the velocity potential formulation, the growth rate  $w$  is found to be

$$w = \frac{\delta}{\nu}, \quad (2.197)$$

in agreement with the velocity potential formulation.

### 2.6.2.2 Numerical verification

The findings of the stability analysis in section 2.6.2.1 indicate that in a fixed, semi-infinite domain there exist unstable depth decaying modes with significant growth rates. The practical implication is that the depth decaying modes of the errors generated mainly at the free-surface and the numerical noise, will eventually terminate the simulation.

To qualitatively verify this result we simulated a hydrostatic case with periodic horizontal boundary conditions employing MA-SPH with fourth order Runge-Kutta temporal integration scheme. The domain is initialized with hydrostatic initial conditions. The evolution of the horizontal accelerations, vertical accelerations, and time rate of pressure change (by definition zero in a hydrostatic case) are recorded at selected particle locations along a vertical cross section (Figures 2-25 to 2-27). It is observed that although the initial perturbations generated by numerical errors, are oscillatory eventually significant instabilities dominate the simulation.

To quantitatively verify the findings of the analysis in section 2.6.2.1, infinitesimal disturbances of known depth decaying wavenumbers are *imposed* as initial conditions in a hydrostatic MA-SPH simulation with periodic horizontal boundary conditions. The evolution of the dynamic pressure (by definition zero in a hydrostatic case) is recorded at selected particle locations along a vertical cross section (Figures 2-28 and 2-29) for two different kernel bandwidths  $h = [0.02, 0.01]$  with equal corresponding initial particle spacings  $dy = [0.02, 0.01]$ . The obtained instability growth rates of the dynamic pressures compare very well to those obtained from the analysis in section 2.6.2.1. It is also observed that in this case the amplitude of the depth decaying modes dominates over the oscillatory modes initially, as well.

To further assess the statements that the depth decaying instabilities (a) are not allowed to develop when the dynamic free-surface boundary condition  $P(x, y = \eta, t) = 0$  is satisfied exactly and (b) are generated predominantly in the free-surface due to the incomplete Kernel Interpolation (section 2.5.6) three more simulations are performed. These three simulations employing MA-SPH with fourth order Runge-Kutta temporal integration schemes, have all periodic horizontal boundary conditions, the water depth is  $H = 1$  are all initialized with hydrostatic initial conditions, and are left to evolve without imposing any perturbations. The perturbations are all generated numerically within the simulation. The evolution of the horizontal accelerations, vertical accelerations, and time rate of pressure change (by definition zero in a hydrostatic case) are recorded at selected particle locations along a vertical cross section.

Each simulation differs in the implementation of the free-surface boundary condition: (i) employs KI but imposes a zero-pressure fitting on the free-surface at each time step, (ii) employs the consistent derivative computation technique MLS (section 3.3.1.1) for the computation of the derivatives to reduce the amplitude of the errors introduced by the artificial dynamic free-surface boundary condition (section 2.5.6), and (iii) employs the consistent derivative computation technique MLS for the computation of the derivatives and imposes a zero-pressure fitting to the free-surface at each time step.

The zero-pressure fitting with Kernel Interpolation, shown in Fig. 2-30 delays

the appearance of the instability, verifying the assumption that the instabilities are generated predominantly by the artificial free-surface dynamic boundary condition with Kernel Interpolation. Figures 2-31 and 2-32 compare the effect of using MLS without and with imposed zero free-surface pressure. Each treatment further delays the appearance and growth rate of the instabilities, but does not remove them. These findings are of essential importance, since in agreement with [43] they verify that this instability cannot be removed by simply increasing the accuracy of the derivative computation technique, since it is inherent to the method and will thus demonstrate itself eventually through any round-off error. It is however, noted that this type of instability manifests itself in periodic or fixed domain and is not expected to plague problems such as the dam-break, at least for a short time.

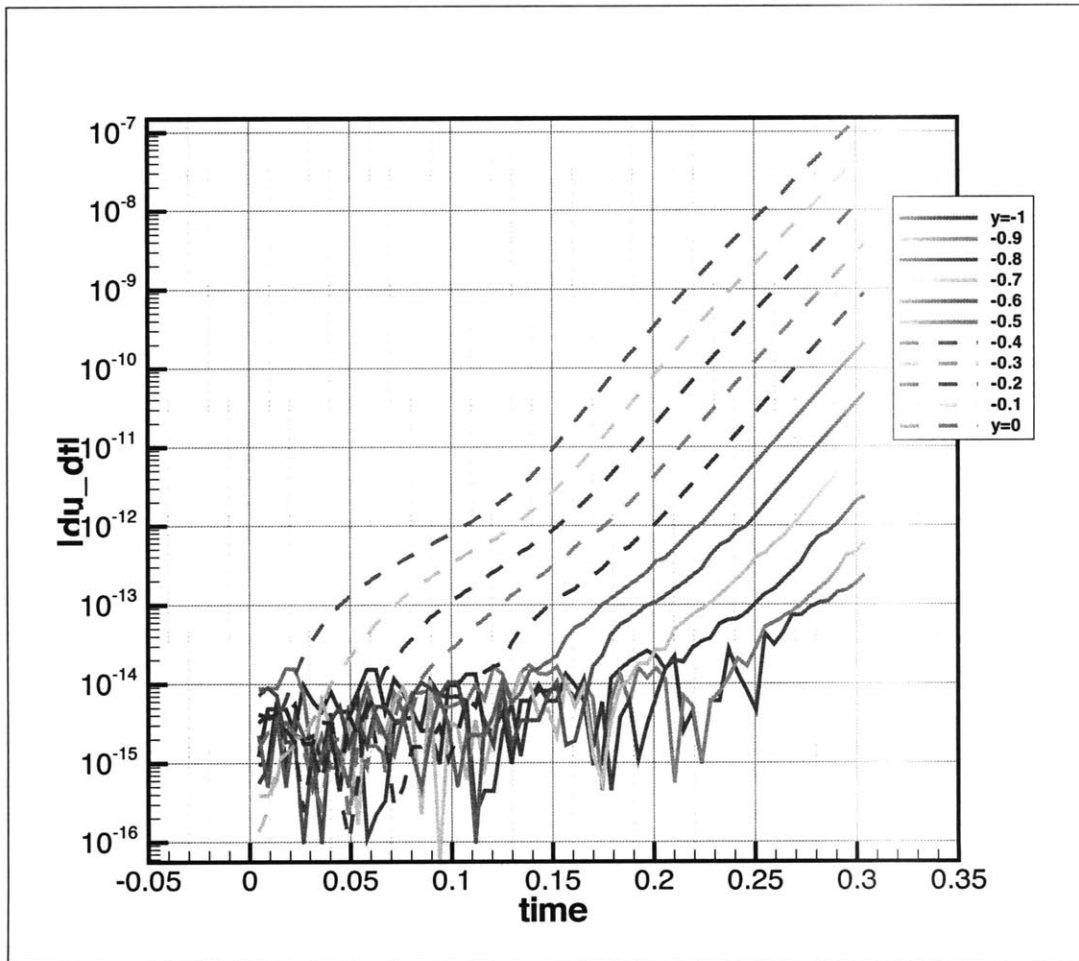


Figure 2-25: SPH simulation of a hydrostatic case. Absolute horizontal accelerations along different depths. Water depth  $H = 1$ , dimensionless speed of sound  $\beta = 40$ .

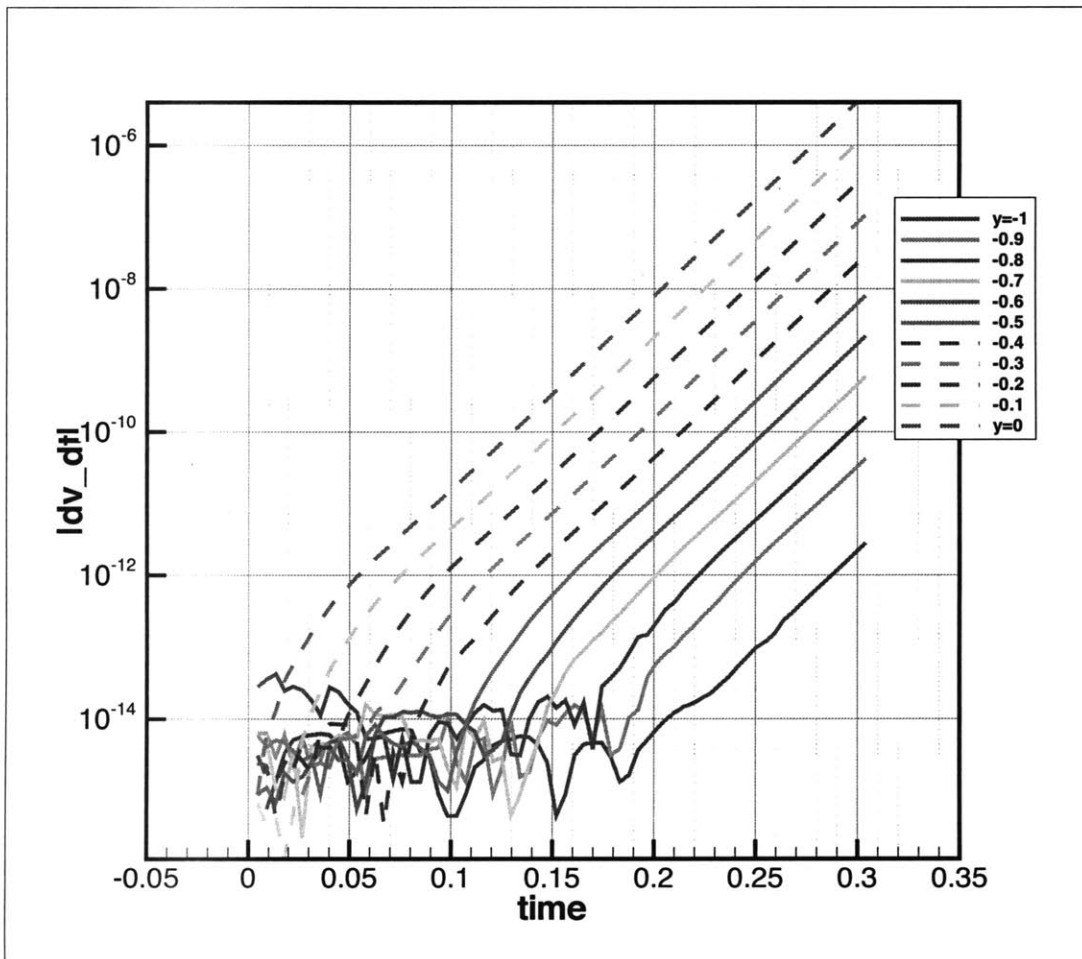


Figure 2-26: SPH simulation of a hydrostatic case. Absolute vertical accelerations along different depths. Water depth  $H = 1$ , dimensionless speed of sound  $\beta = 40$ .

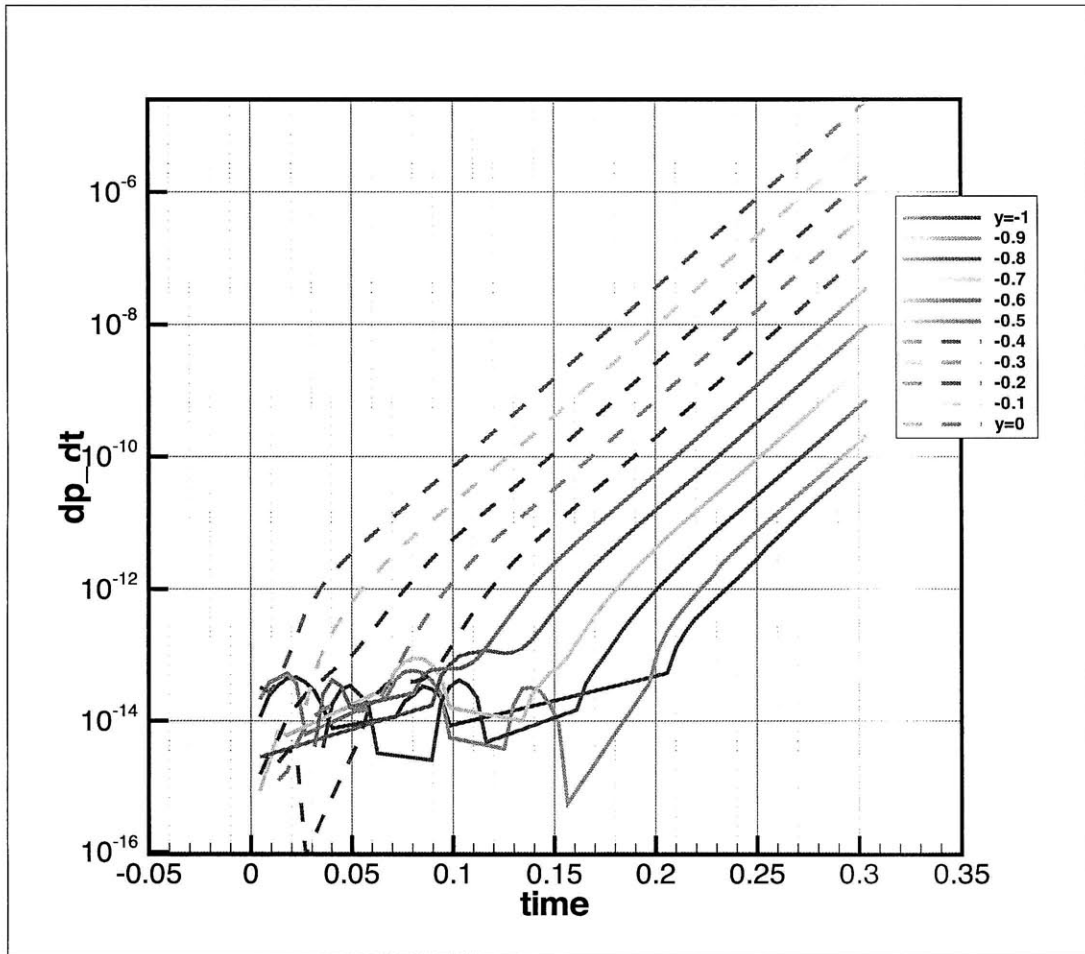


Figure 2-27: SPH simulation of a hydrostatic case. Absolute time rate of change of total pressure along different depths. Water depth  $H = 1$ , dimensionless speed of sound  $\beta = 40$ .

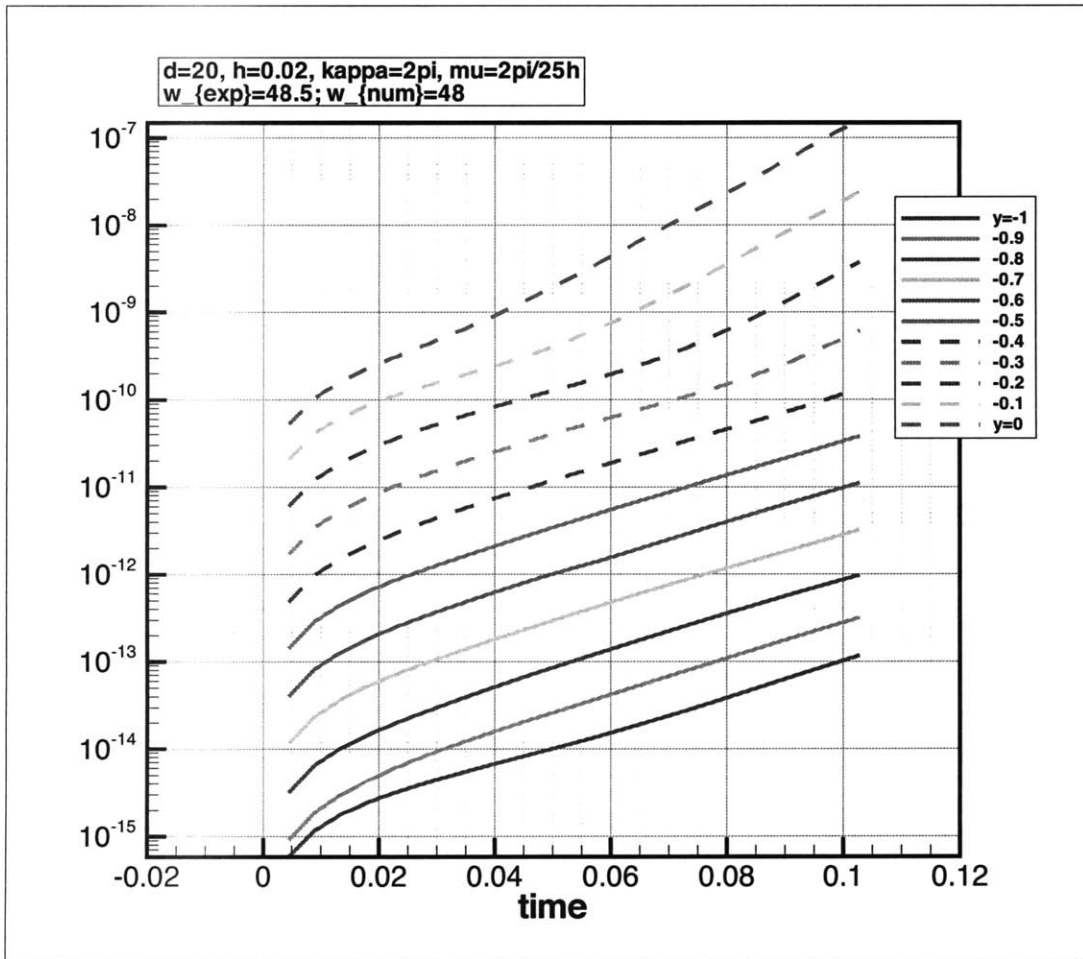


Figure 2-28: SPH simulation of a hydrostatic case. Growth of initial pressure perturbation  $p(\vec{x}, 0) = qe^{2\pi(ix + \frac{y}{25h})}$  along different depths. Simulation parameters  $c = 20$ ,  $h = 0.02$ . Expected growth rate  $\lambda_e = 48.5$ , obtained  $\lambda_o = 48$ .

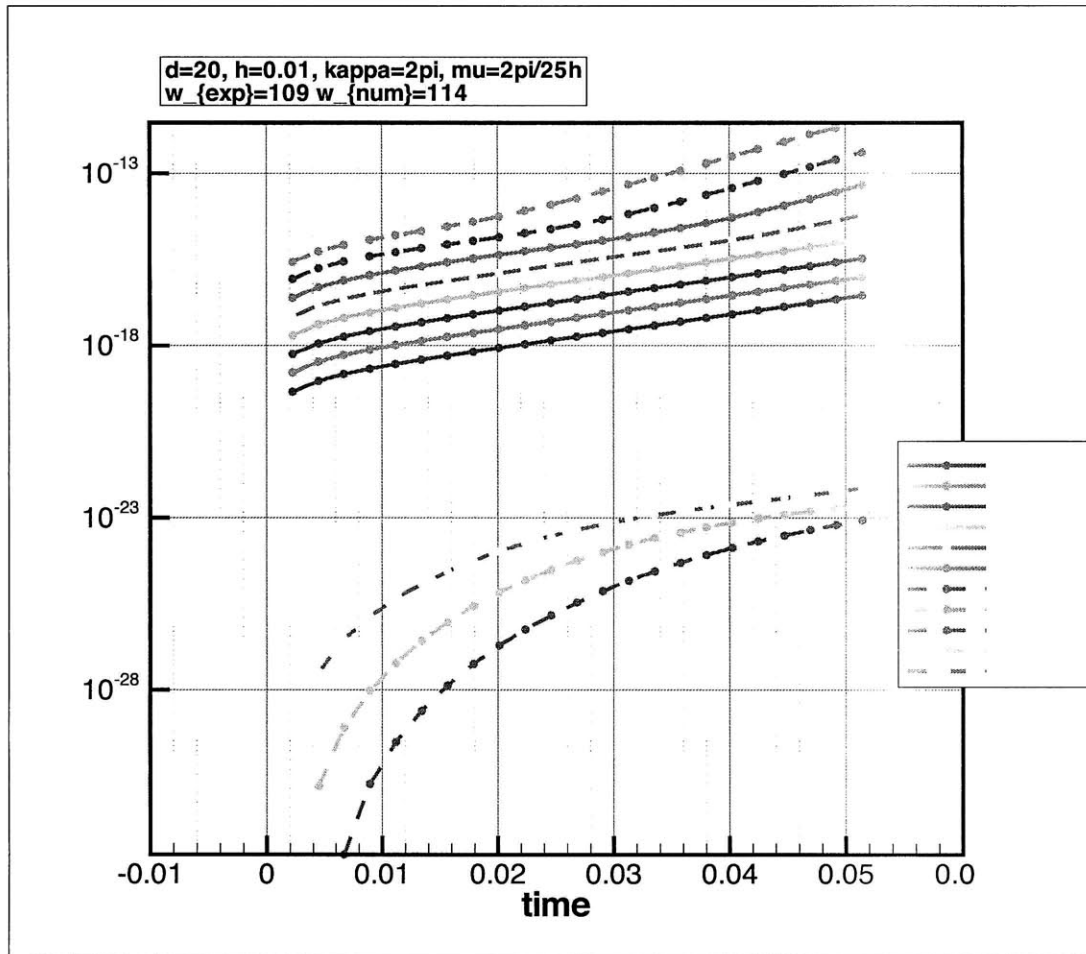


Figure 2-29: SPH simulation of a hydrostatic case. Growth of initial pressure perturbation  $p(\vec{x}, 0) = qe^{2\pi(ix + \frac{y}{25h})}$  along different depths. Simulation parameters  $c = 20$ ,  $h = 0.01$ . Expected growth rate  $\lambda_e = 109$ , obtained  $\lambda_o = 114$ .

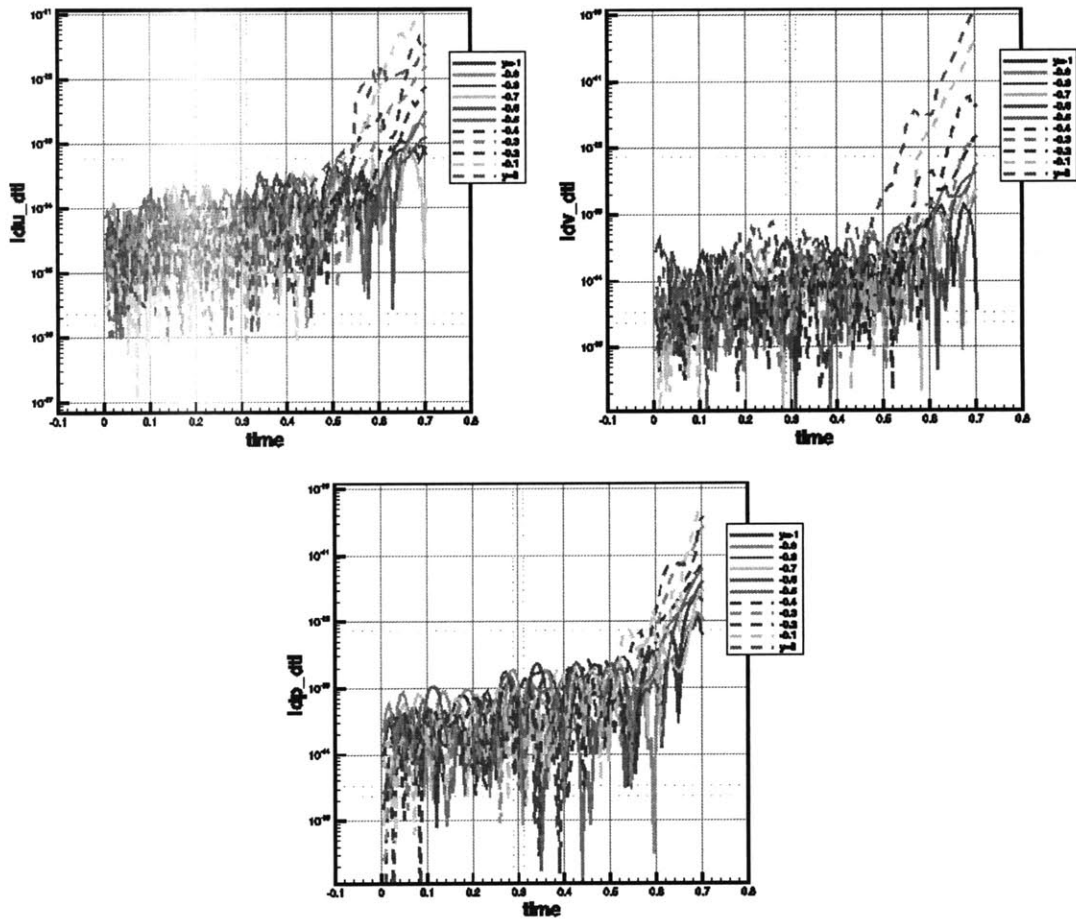


Figure 2-30: SPH simulation of a hydrostatic case, imposing zero-pressure free-surface fitting. Growth of absolute horizontal accelerations (top left), absolute vertical accelerations (top right) and dynamic pressure (bottom) at selected particles along a vertical cross section. Periodic horizontal boundary conditions and water depth  $H = 1$ .

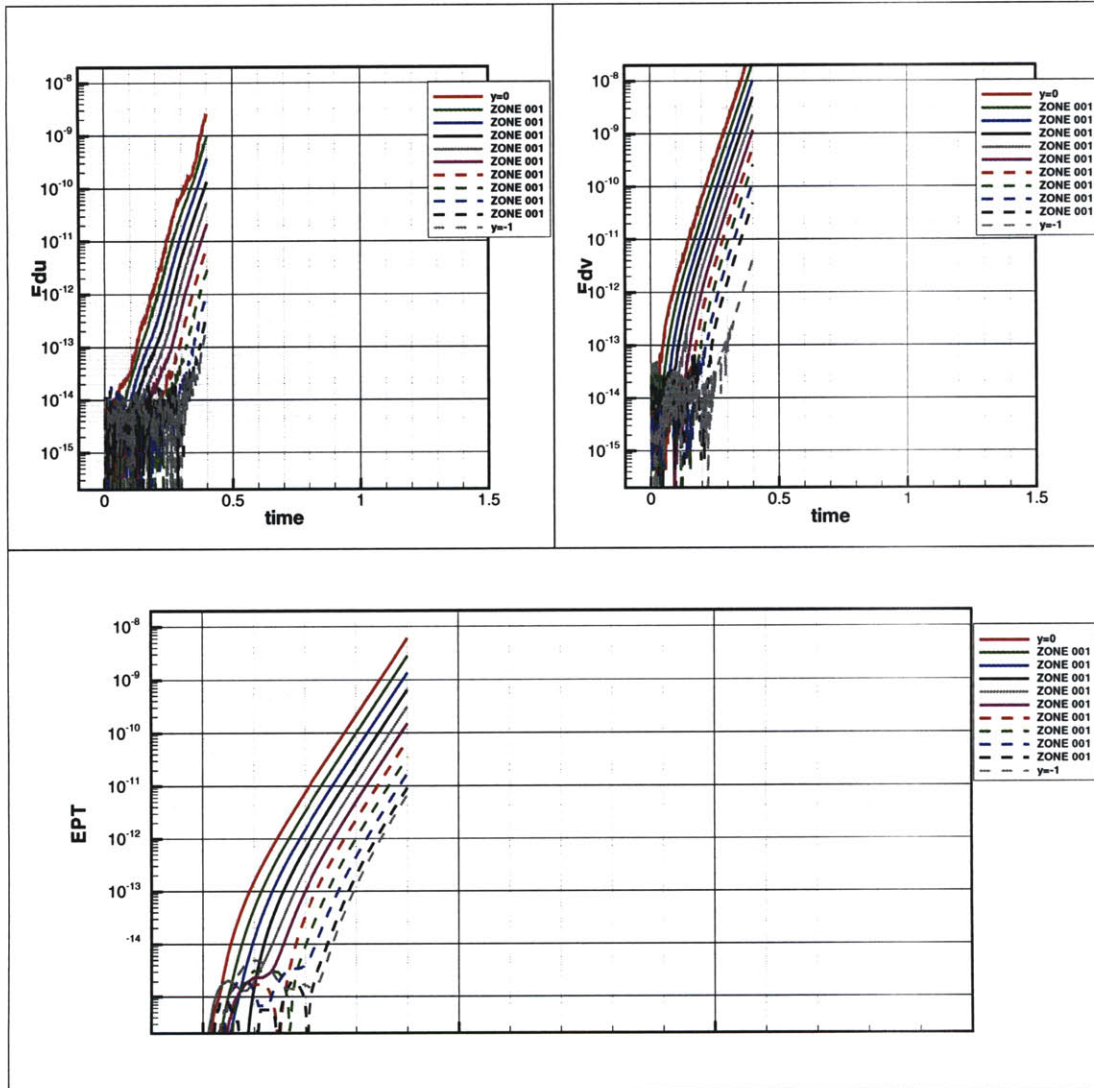


Figure 2-31: Simulation of a weakly compressible hydrostatic case. Computation of spatial derivatives with Moving Least Squares. Growth of absolute horizontal accelerations (top left), absolute vertical accelerations (top right) and dynamic pressure (bottom) at selected particles along a vertical cross section. Periodic horizontal boundary conditions and water depth  $H = 1$ .

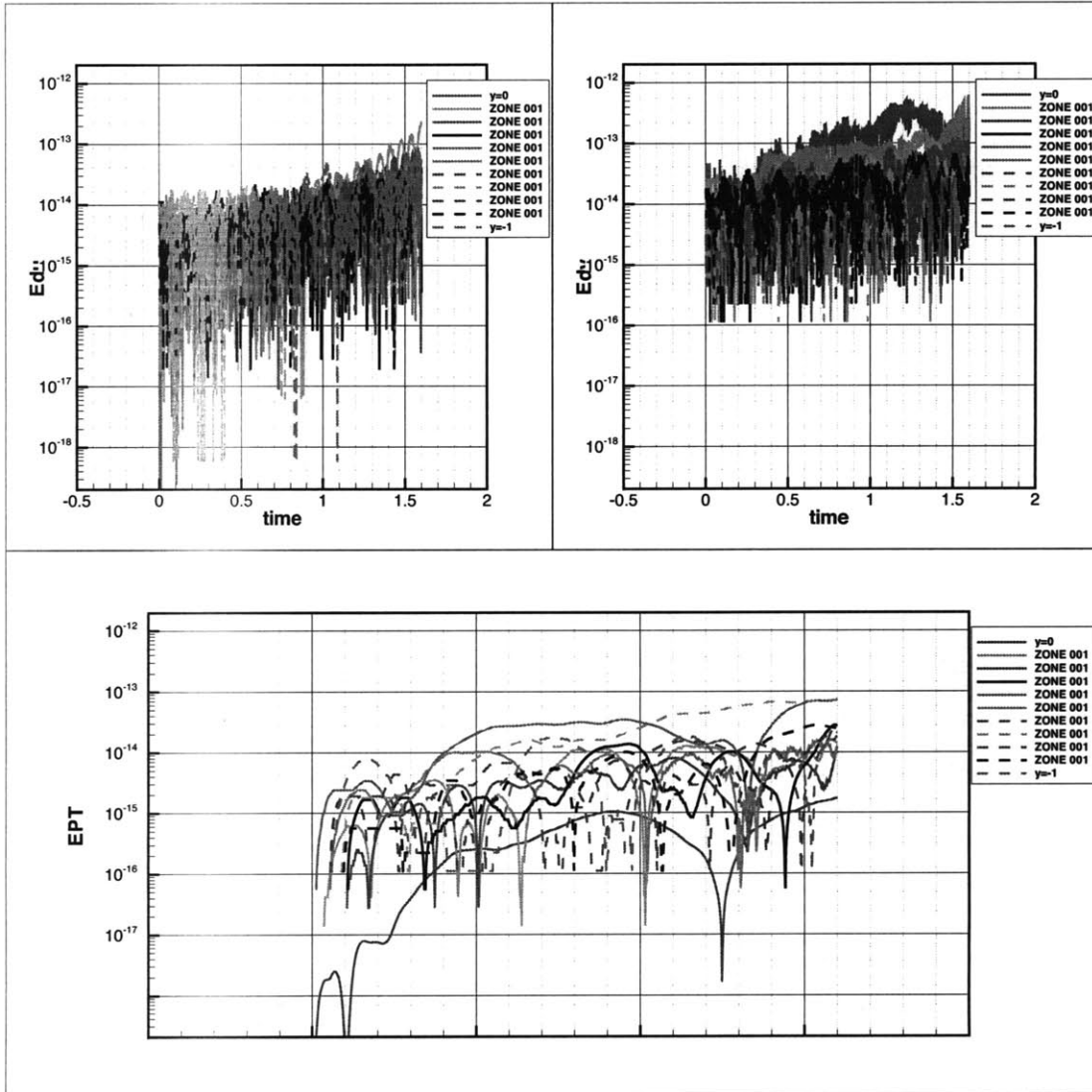


Figure 2-32: Simulation of a weakly compressible hydrostatic case. Computation of spatial derivatives with Moving Least Squares. Imposing zero-pressure free-surface fitting. Growth of absolute horizontal accelerations (top left), absolute vertical accelerations (top right) and dynamic pressure (bottom) at selected particles along a vertical cross section. Periodic horizontal boundary conditions and water depth  $H = 1$ .

### 2.6.3 Semi-discrete algorithm

This section examines the linear stability of the discrete in space, continuous in time algorithm. This analysis is essential in understanding the effects of the Kernel Interpolation alone in the stability behavior of the algorithm, and clearly distinguishes the effects of the temporal integration schemes. In section 2.6.2 it was shown that the initial hydrostatic density distribution de-stabilizes the system. In the literature the effect of gravity is neglected and the system is still found to exhibit a tensile instability [26, 44, 53]. To bridge the results, this section ignores gravity and performs the stability analysis for a zero base flow for two cases of (a) uniform density distribution and (b) a general, smooth but small density distribution. The results generalize the findings of section 2.6.2 and [26, 44, 53], showing that the semi-discrete scheme is unstable to *any* non-zero base density distribution with three main implications. First, it clarifies the misunderstanding that the SPH instability is due to the Kernel Interpolation [18, 53]. Second, it further enforces the finding that the hydrostatic density distribution needs to be taken into account in the analysis of the fully discrete scheme for the free-surface flows of interest. Thirdly, it justifies the usage of the semi-empirical treatments that periodically either re-initialize or smooth the density during an SPH simulation, essentially reducing base density gradients.

As in section 2.6.2 the analysis is performed in an infinite one-dimensional domain. The domain is discretized into  $N$  fluid particles of uniform spacing  $\delta x = h$ . The center of mass of particle  $a$  is given by  $\bar{x}_a = ah$  and its mass is  $m_a = \rho_f h \equiv m$ , where  $\rho_f$  is the unperturbed fluid density. A base flow solution at time  $t$  is assumed. Let the base flow velocity, pressure and density of particle  $a$  be  $\bar{u}_a$ ,  $\bar{P}_a$ , and  $\bar{\rho}_a$  respectively. The position and velocity of particle  $a$  satisfy the MA-SPH governing equations:

$$\dot{\bar{x}}_a = \bar{u}_a \quad (2.198)$$

$$\dot{\bar{u}}_a = - \sum_b m_b \left( \frac{\bar{P}_a}{\bar{\rho}_a^2} + \frac{\bar{P}_b}{\bar{\rho}_b^2} \right) W'_{ab} - g. \quad (2.199)$$

The density  $\bar{\rho}_a$  is given by either the direct or advanced computation:

$$\text{Direct: } \quad \bar{\rho}_a = \sum_b m_b W_{\bar{a}\bar{b}} \quad (2.200)$$

$$\text{Advanced: } \quad \dot{\bar{\rho}}_a = \sum_b m_b \bar{u}_{ab} W'_{\bar{a}\bar{b}}. \quad (2.201)$$

The pressure is determined by a constitutive Equation of State  $\bar{P}_a = \rho_f \frac{d^2}{d\gamma} \left[ \left( \frac{\bar{\rho}_a}{\rho_f} \right)^\gamma - 1 \right]$  and  $W_{\bar{a}\bar{b}} \equiv W(\bar{x}_a - \bar{x}_b)$  is given by the cubic B-Spline (2.111).

Next, following the linear von Neumann stability analysis outlined in section 2.6.1, infinitesimal perturbations  $y_a \ll h$ ,  $v_a \ll \bar{u}_a$ ,  $p_a \ll \bar{P}_a$  and  $\rho_a \ll \rho_f$  are superimposed to the base position, velocity, pressure and density respectively. Thus, the particle position, velocity, pressure and density are given by:

$$\begin{aligned} x_a &= \bar{x}_a + y_a \\ u_a &= \bar{u}_a + v_a \\ P_a &= \bar{P}_a + p_a \\ \rho_a &= \bar{\rho}_a + \varrho_a \end{aligned} \quad (2.202)$$

Further on, the perturbations are expressed in terms of normal modes:

$$\begin{aligned} y_a &= y(t) e^{ik\bar{x}_a} \\ v_a &= v(t) e^{ik\bar{x}_a} \\ \varrho_a &= \varrho(t) e^{ik\bar{x}_a} \end{aligned} \quad (2.203)$$

where  $k$  is the perturbation wave number.

Based on the previous assumptions, the kernel function evaluated at  $ab$ , can be written as:

$$\begin{aligned} W_{ab} &= W(x_a - x_b) = W((\bar{x}_a - \bar{x}_b) + (y_a - y_b)) \\ &\cong W(\bar{x}_a - \bar{x}_b) + (y_a - y_b) W'(\bar{x}_a - \bar{x}_b) + \text{h.o.t} \\ &= W_{\bar{a}\bar{b}} + y_{ab} W'_{\bar{a}\bar{b}} + \text{h.o.t} \end{aligned} \quad (2.204)$$

and in the same manner its first derivative becomes:

$$W'_{ab} = W'_{\bar{a}b} + y_{ab}W''_{\bar{a}b} + \text{h.o.t.} \quad (2.205)$$

Equations (2.200) and (2.201) show two different approaches for calculating the density. In the first, (2.200), the density is computed directly through Kernel Interpolation. In the second, (2.201), the time rate of change of the density is computed and the density is advanced in time. Both approaches are considered in the analysis, noting that in section 2.5.4 it is shown that both approaches are consistent with respect to the time step, provided the particles are sufficiently far away from the free-surface.

**Direct density formulation** The governing equations are (2.198), (2.199) and (2.200). First, the total solution is substituted into each one of the governing equations. Then the base flow is subtracted and finally the resulting equations are linearized with respect to the disturbances.

The governing equation for the position perturbations is obtained from (2.198):

$$\begin{aligned} \dot{x}_a &= u_a \rightarrow \\ \dot{\bar{x}}_a + \dot{y}_a &= \bar{u}_a + v_a \rightarrow \\ \dot{y}_a &= v_a. \end{aligned} \quad (2.206)$$

The governing equation for the density perturbations is obtained from (2.200):

$$\begin{aligned} \rho_a &= \sum_b m_b W_{ab} = m \sum_b (W_{\bar{a}b} + y_{ab}W'_{\bar{a}b}) \rightarrow \\ \bar{\rho}_a + \varrho_a &= m \sum_b W_{\bar{a}b} + m \sum_b y_{ab}W'_{\bar{a}b} \rightarrow \\ \varrho_a &= m \sum_b y_{ab}W'_{\bar{a}b} \xrightarrow{(28)} \\ \varrho_a &= \rho_f h y_a \left( (1 - e^{-ikh}) \frac{-1}{2h^2} + (1 - e^{ikh}) \frac{1}{2h^2} \right) \rightarrow \\ \varrho_a &= -i\rho_f \frac{\sin kh}{h} y_a. \end{aligned} \quad (2.207)$$

Next, the pressure term on the right hand side of the momentum equation (2.199) is simplified as follows:

$$\begin{aligned}
\frac{P_a}{\rho_a^2} &= \frac{c^2}{\rho_f \gamma} \left[ \left( \frac{\rho_a}{\rho_f} \right)^{\gamma-2} - \left( \frac{\rho_a}{\rho_f} \right)^{-2} \right] \rightarrow \\
&= \frac{c^2}{\rho_f \gamma} \left[ \left( \frac{\bar{\rho}_a + \varrho_a}{\rho_f} \right)^{\gamma-2} - \left( \frac{\bar{\rho}_a + \varrho_a}{\rho_f} \right)^{-2} \right] \rightarrow \\
&= \frac{c^2}{\rho_f \gamma} \left[ \left( \frac{\bar{\rho}_a}{\rho_f} \right)^{\gamma-2} \left( 1 + \frac{\varrho_a}{\rho_a} \right)^{\gamma-2} - \left( \frac{\bar{\rho}_a}{\rho_f} \right)^{-2} \left( 1 + \frac{\varrho_a}{\rho_a} \right)^{-2} \right] \xrightarrow{(27)} \\
&= \frac{c^2}{\rho_f \gamma} \left[ \left( \frac{\bar{\rho}_a}{\rho_f} \right)^{\gamma-2} \left( 1 + (\gamma-2) \frac{\varrho_a}{\rho_a} \right) - \left( \frac{\bar{\rho}_a}{\rho_f} \right)^{-2} \left( 1 - 2 \frac{\varrho_a}{\rho_a} \right) \right] \rightarrow \\
\frac{P_a}{\rho_a^2} &= \underbrace{\frac{c^2}{\rho_f \gamma} \left[ \left( \frac{\bar{\rho}_a}{\rho_f} \right)^{\gamma-2} - \left( \frac{\bar{\rho}_a}{\rho_f} \right)^{-2} \right]}_{A_a} + \\
&\quad + \underbrace{\frac{c^2}{\rho_f^2 \gamma} \left[ (\gamma-2) \left( \frac{\bar{\rho}_a}{\rho_f} \right)^{\gamma-3} + 2 \left( \frac{\bar{\rho}_a}{\rho_f} \right)^{-3} \right]}_{B_a} \varrho_a \tag{2.208}
\end{aligned}$$

Both  $A_a$  and  $B_a$  are considered to be sufficiently smooth such that both  $A_b \cong A_a + (x_b - x_a)A'_a$  and  $B_b \cong B_a + (x_b - x_a)B'_a$  are valid approximations for  $(x_b - x_a) \sim O(h)$ .

Finally, the momentum equation (2.199) is considered and the equation describing the velocity perturbations rate of change is determined:

$$\begin{aligned}
\dot{u}_a &= - \sum_b m_b \left( \frac{P_a}{\rho_a^2} + \frac{P_b}{\rho_b^2} \right) W'_{ab} - g \rightarrow \\
\dot{u}_a &= - \sum_b m_b (A_a + A_b + B_a \varrho_a + B_b \varrho_b) (W'_{ab} + y_{ab} W''_{ab}) - g \xrightarrow{(2.199)} \\
\dot{u}_a &= - \sum_b m_b (A_a + A_b) y_{ab} W''_{ab} - \sum_b m_b (B_a \varrho_a + B_b \varrho_b) W'_{ab} \xrightarrow{(2.207)} \\
\dot{u}_a &= - \sum_b m_b (A_a + A_b) y_{ab} W''_{ab} + i \sum_b m_b \rho_f \frac{\sin kh}{h} (B_a y_a + B_b y_b) W'_{ab} \tag{2.209}
\end{aligned}$$

Substituting (2.206), (2.207) into (2.209) obtains a single equation describing the

evolution of the position perturbations:

$$\begin{aligned}
\ddot{y}_a &= -m \left[ \sum_b (A_a + A_b) (1 - e^{ik(\bar{x}_b - \bar{x}_a)}) W''_{ab} \right] y_a \\
&\quad + i\rho_f^2 \sin kh \left[ \sum_b B_b e^{ik(\bar{x}_b - \bar{x}_a)} W'_{ab} \right] y_a \rightarrow \\
\ddot{y}_a &\equiv \Omega_a^2 y_a,
\end{aligned} \tag{2.210}$$

where  $\Omega_a^2$  is given by:

$$\Omega_a^2 = -m \left[ \sum_b (A_a + A_b) (1 - e^{ik(\bar{x}_b - \bar{x}_a)}) W''_{ab} \right] + i\rho_f^2 \sin kh \left[ \sum_b B_b e^{ik(\bar{x}_b - \bar{x}_a)} W'_{ab} \right]. \tag{2.211}$$

After some algebra, it can be shown that  $\Omega_a^2$  reduces to:

$$\begin{aligned}
\Omega_a^2 &= \frac{-\rho_f}{h^2} [8A_a(\sin kh/2)^2 + \rho_f B_a (\sin kh)^2] \\
&\quad + i\frac{\rho_f}{h} [2A'_a \sin kh + \rho_f B'_a \sin kh \cos kh].
\end{aligned} \tag{2.212}$$

Obviously  $\Omega_a^2$  depends only on  $c, \gamma, \rho_f, k, h$  and  $\bar{\rho}_a$  and does not depend on any of the perturbation quantities. Assuming that  $\bar{\rho}_a$  changes very slowly with respect to time relative to the perturbations, the linear stability analysis of the MA-SPH with direct density reduces to:

$$\ddot{y}_a = \Omega_a^2 y_a \rightarrow y(t) = y_a^0 e^{\pm\Omega_a t}. \tag{2.213}$$

The algorithm is therefore stable if  $\Omega_a$  is purely imaginary and unstable otherwise. Realizing that  $\Omega_a$  depends on the base flow density, we estimate  $\Omega_a$  for two cases for the base flow density (a) uniform and (b) smooth function of  $\bar{y}$ .

**Case a:** The initial assumption is that  $\bar{x}_a - \bar{x}_b = (a - b)h$ ,  $\bar{\rho}_a \equiv \sum m_b W_{ab} = \rho_f$  and therefore, upon substitution it is found that:

$$\begin{aligned} A_a &= 0 \\ A'_a &= 0 \\ B_a &= \frac{c^2}{\rho_f^2} \\ B'_a &= 0. \end{aligned}$$

Putting everything together obtains:

$$\Omega_a^2 = \left( ic \frac{\sin kh}{h} \right)^2. \quad (2.214)$$

The MA-SPH with direct density in this case is found to be stable. The frequency of the perturbations  $\omega_o$  is uniform. The dispersion relation of the perturbations is:

$$\omega_o = \Omega_a = c \frac{\sin kh}{h}. \quad (2.215)$$

**Case b:** The density  $\bar{\rho}_a$  can be written as a constant plus a small quantity  $\theta$ ,

$$\bar{\rho}_a \equiv \rho_f (1 + \theta_a). \quad (2.216)$$

From the previous discussion on the density, there exists small enough time  $t$  for which the following assumption holds:

$$\theta \ll \frac{y}{h} \ll 1. \quad (2.217)$$

In this case  $A_a$ ,  $B_a$  and their spatial derivatives, can be approximated by:

$$A_a = \frac{c^2}{\rho_f} \theta_a \quad (2.218)$$

$$A'_a = \frac{c^2}{\rho_f} \theta'_a \quad (2.219)$$

$$B_a = \frac{c^2}{\rho_f^2} (1 + (\gamma - 5)\theta_a) \quad (2.220)$$

$$B'_a = \frac{c^2}{\rho_f^2} (\gamma - 5)\theta'_a. \quad (2.221)$$

Putting everything together obtains  $\Omega_a^2$ :

$$\begin{aligned} \Omega_a^2 = & -c^2 \frac{\sin^2 kh}{h^2} \\ & -c^2 \left( 8 \frac{(\sin kh/2)^2}{h^2} + (\gamma - 5) \frac{\sin^2 kh}{h^2} \right) \theta_a \\ & + ic^2 \left( 2 \frac{\sin kh}{h} + (\gamma - 5) \frac{\sin kh \cos kh}{h} \right) \theta'_a. \end{aligned} \quad (2.222)$$

The first term in the right hand side of (2.222) is of order  $c^2/h^2$  while the other two terms are of order  $\theta_a c^2$ . Let  $\Omega_a$  be defined as:

$$\Omega_a^2 \equiv \omega_{0a}^2 + \omega_{1a}^2 \text{ where } \omega_{0a} \gg \omega_{1a}, \quad (2.223)$$

with

$$\begin{aligned} \omega_{0a}^2 &= -c^2 \frac{(\sin kh)^2}{h^2}, \text{ and} \\ \omega_{1a}^2 &= -c^2 \left( 8 \frac{(\sin kh/2)^2}{h^2} + (\gamma - 5) \frac{\sin^2 kh}{h^2} \right) \theta_a + ic^2 \left( 2 \frac{\sin kh}{h} + (\gamma - 5) \frac{\sin kh \cos kh}{h} \right) \theta'_a. \end{aligned}$$

By Taylor Series Expansion it can be shown that:

$$\Omega_a = \sqrt{\omega_{0a}^2 + \omega_{1a}^2} = \omega_{0a} \sqrt{1 + \left( \frac{\omega_{1a}}{\omega_{0a}} \right)^2} \cong \omega_{0a} \left( 1 + \frac{1}{2} \left( \frac{\omega_{1a}}{\omega_{0a}} \right)^2 \right).$$

Putting everything together, it is shown that  $\Omega_a$  is complex and the algorithm is not stable anymore. It is immediately evident that the growth rate is proportional to  $c$ . Therefore, if  $\bar{\rho}$  is non-uniform the algorithm is unstable. In particular, for a long wavelength approximation ( $kh \ll 1$ ) it can be shown that

$$\Omega_a \cong ick \left( 1 + \frac{\gamma - 3}{2} \theta_a \right) + \frac{\gamma - 3}{2} c \theta'_a. \quad (2.224)$$

The perturbations are therefore unstable with growth rate  $\frac{\gamma-3}{2}c\theta'_a$ . The growth rate increases linearly with  $\gamma$ ,  $c$  and  $\theta'_a$ . The following comments can be made. First, this result is in agreement with the results reduced for  $\bar{\rho}_a = \rho_f$ , which is just the limiting case of  $\theta_a = 0$ . Second, similar results are expected for different consistent kernels and different particle spacings, i.e., the algorithm is stable to leading order and instabilities are expected to be linearly proportional to  $d$  and  $\theta'_a$ . Third, the instability growth rate is independent of the perturbation wavenumber. This surprising result holds only under the assumption of infinitesimal  $\theta$ . Finally, if  $\theta'_a$  is kept minimal throughout the simulation then the initial growth rate of the instabilities will also be minimized. This is the basic empirical idea behind the two most common density re-initialization techniques [1, 48].

**Advanced density formulation** The governing equations are (2.198), (2.199) and (2.201). First, the total solution is substituted into each one of the governing equations. Then the base flow is subtracted and finally the resulting equations are linearized with respect to the disturbances. Following the same notation as the one used for the direct density formulation and following the same procedure, after some algebra, the linearized equations for the position, velocity and density perturbations

reduce to:

$$\dot{y}_a = v_a \quad (2.225)$$

$$\begin{aligned} \dot{v}_a &= -\rho_f \left( 8A_a \frac{(\sin kh/2)^2}{h^2} - i2A'_a \frac{\sin kh}{h} \right) y_a \\ &\quad - \rho_f \left( iB_a \frac{\sin kh}{h} + B'_a \cos kh \right) \varrho_a \end{aligned} \quad (2.226)$$

$$\dot{\varrho}_a = i2\rho_f \bar{u}'_a \frac{\sin kh}{h} y_a - i\rho_f \frac{\sin kh}{h} v_a = i\rho_f \frac{\sin kh}{h} (2y_a \bar{u}'_a - v_a). \quad (2.227)$$

For comparison with the direct density approach, note that the second term in (2.227) is simply the time derivative of (2.207), while the first term in (2.227) accounts for the base flow. Equations (2.225), (2.226) and (2.227) form a linear system, which in matrix form reads:

$$\begin{bmatrix} \dot{y} \\ \dot{v} \\ \dot{r} \end{bmatrix} = \begin{bmatrix} 0 & 1 & 0 \\ v_y & 0 & v_\varrho \\ \varrho_y & \varrho_v & 0 \end{bmatrix} \begin{bmatrix} y \\ v \\ r \end{bmatrix} \rightarrow \dot{X} = \mathcal{A}X, \quad (2.228)$$

where the following notation is used:

$$\begin{aligned} v_y &\equiv -\rho_f \left( 8A_a \frac{(\sin kh/2)^2}{h^2} - i2A'_a \frac{\sin kh}{h} \right) \\ v_\varrho &\equiv -\rho_f \left( iB_a \frac{\sin kh}{h} + B'_a \cos kh \right) \\ \varrho_y &\equiv i2\rho_f \bar{u}'_a \frac{\sin kh}{h} \\ \varrho_v &\equiv -i\rho_f \frac{\sin kh}{h}. \end{aligned} \quad (2.229)$$

Assuming that  $\mathcal{A}$  varies slowly in time compared to the perturbations, the solution to (2.228) is of the form  $X = X_o e^{\Omega t}$  where  $\Omega$  are the roots of the characteristic polynomial of the matrix  $\mathcal{A}$ , i.e.,

$$\Omega^3 - \Omega(\varrho_v v_\varrho + v_y) - \varrho_y v_\varrho = 0. \quad (2.230)$$

The algorithm is stable if  $\Omega_a$  is purely imaginary and unstable otherwise. Realizing that  $\Omega_a$  depends on the base flow density, we estimate  $\Omega_a$  for two cases for the base flow density (a) uniform and (b) smooth function of  $\bar{y}$ , just as was done for the direct density formulation.

**Case a:** By assumption it is  $\bar{x}_a - \bar{x}_b = (a - b)h$ ,  $\bar{\rho}_a \equiv \sum m_b W_{ab} = \rho_f$  and therefore upon substitution, it is found that:

$$\begin{aligned} A_a &= 0 \\ A'_a &= 0 \\ B_a &= \frac{c^2}{\rho_f^2} \\ B'_a &= 0. \end{aligned}$$

Further, the elements of matrix  $\mathcal{A}$  are found to be:

$$\begin{aligned} v_y &= 0 \\ v_e &= -i \frac{c^2 \sin kh}{\rho_f h} \end{aligned} \tag{2.231}$$

$$\begin{aligned} \varrho_y &= 0 \\ \varrho_v &= -i \rho_f \frac{\sin kh}{h}. \end{aligned} \tag{2.232}$$

Putting everything together obtains:

$$\Omega^3 = \Omega \left( ic \frac{\sin kh}{h} \right)^2 \rightarrow \begin{cases} \Omega_1 &= 0 \\ \Omega_{2,3}^2 &= \left( ic \frac{\sin kh}{h} \right)^2 \end{cases} \tag{2.233}$$

Therefore, the MA algorithm is stable if  $\bar{\rho} = \rho_f$ , for both the direct and advanced density formulations.

**Case b:** The density  $\bar{\rho}_a$  can be written as a constant plus a small quantity  $\theta$ ,

$$\bar{\rho}_a \equiv \rho_f (1 + \theta_a). \tag{2.234}$$

As in the direct density formulation, we assume that  $\theta \ll \frac{y}{h} \ll 1$ . In this case,  $A_a$ ,  $B_a$  and their spatial derivatives, can be approximated up by:

$$\begin{aligned} A_a &= \frac{c^2}{\rho_f} \theta_a \\ A'_a &= \frac{c^2}{\rho_f} \theta'_a \\ B_a &= \frac{c^2}{\rho_f^2} (1 + (\gamma - 5)\theta_a) \\ B'_a &= \frac{c^2}{\rho_f^2} (\gamma - 5)\theta'_a. \end{aligned}$$

Solving (2.230) for  $\Omega_a$  analytically is difficult, such that an approximate solution to  $\Omega$  will be given. First new notation is introduced and the elements of matrix  $\mathcal{A}$  are simplified according to:

$$\begin{aligned} v_y &= \epsilon V_y \\ v_\varrho &= -i \frac{c^2}{\rho_f} \frac{\sin kh}{h} + \epsilon V_r \\ \varrho_y &= \epsilon R_y \\ \varrho_v &= -i \rho_f \frac{\sin kh}{h} + \epsilon R_v, \end{aligned} \tag{2.235}$$

where the terms  $V_y$ ,  $V_r$ ,  $R_y$  and  $R_v$  denote the remaining terms that are of order  $\theta$  or  $\theta'$  and  $\epsilon$  is used to denote that the terms are small. Further,  $\Omega$  is defined as:

$$\Omega_a^3 \equiv \omega_{0a}^3 + \epsilon \omega_{1a}^3, \tag{2.236}$$

where again  $\epsilon$  is used to denote that  $\omega_{0a}^3 \gg \epsilon \omega_{1a}^3$ . By Taylor Series Expansion it can be shown that:

$$\Omega_a \cong \omega_{0a} \left( 1 + \frac{1}{3} \frac{\omega_{1a}^3}{\omega_{0a}^3} \right). \tag{2.237}$$

Putting everything together the characteristic polynomial for (2.230) reduces to:

$$\omega_{0a}^3 + \epsilon \omega_{1a}^3 - \omega_{0a} \left( 1 + \frac{\epsilon \omega_{1a}^3}{3 \omega_{0a}^3} \right) \left[ \left( ic \frac{\sin kh}{h} \right)^2 + \epsilon \vartheta \right] + i \epsilon R_y \frac{c^2}{\rho_f} \frac{\sin kh}{h} = 0, \tag{2.238}$$

where  $\vartheta \equiv i \left( R_v \frac{c^2 \sin kh}{\rho_f h} - V_r \rho_f \frac{\sin kh}{h} \right) + V_y$ . Equating same orders of  $\epsilon$  after some algebra, the equations for  $\omega_{0a}^3$ ,  $\omega_{1a}$  become:

$$\omega_{0a}^3 = \omega_{0a} \left( ic \frac{\sin kh}{h} \right)^2 \quad (2.239)$$

$$\omega_{1a}^3 = \frac{3}{2} \omega_{0a} (\vartheta - R_y). \quad (2.240)$$

It can be shown that  $\vartheta - R_y$  is given by:

$$\vartheta - R_y = \omega_{0a}^2 \left[ (\gamma - 3)\theta_a + i \left( 2 \frac{\bar{u}'_a}{ck} - (\gamma - 3) \frac{\theta'_a}{k} \right) \right]. \quad (2.241)$$

Therefore, from (2.239) and (2.239), it is:

$$\frac{\omega_{1a}^3}{\omega_{0a}^3} = \frac{3}{2} \left[ (\gamma - 3)\theta_a + i \left( 2 \frac{\bar{u}'_a}{ck} - (\gamma - 3) \frac{\theta'_a}{k} \right) \right]. \quad (2.242)$$

Substituting the last relation into (2.237) obtains:

$$\begin{aligned} \Omega_a &\cong \omega_{0a} \left[ 1 + \frac{(\gamma - 3)}{2} \theta_a + i \left( \frac{\bar{u}'_a}{ck} - \frac{(\gamma - 3)}{2} \frac{\theta'_a}{k} \right) \right] \rightarrow \\ &\cong ick \left( 1 + \frac{\gamma - 3}{2} \theta_a \right) + \left( \frac{(\gamma - 3)}{2} c \theta'_a - \bar{u}'_a \right). \end{aligned} \quad (2.243)$$

This means that  $\Omega_a$  is complex and the algorithm is again unstable with growth rate given by  $\pm \left( \frac{(\gamma - 3)}{2} c \theta'_a - \bar{u}'_a \right)$ . The following comments are made. First, the solution for uniform grid spacing is recovered for  $\theta_a \rightarrow 0$ . Second, for  $\bar{u}'_a = 0$  the perturbation growth rate for the MA-SPH with advance density is the same as the one for MA-SPH with direct density. Third, if  $\bar{u}'_a$  is maintained small through out the simulation then it can be deduced that  $\theta'_a$  will also be maintained small, and the perturbation growth rates will be small. Fourth, although no analysis has been performed for a two-dimensional case, if one was to be performed the last result would be expected to depend on  $\nabla \cdot \vec{u}$  and on  $\nabla \theta$ . Fifth, similarly to the direct density formulation, the perturbation growth rates do not depend on the perturbation wavenumber. Finally, if the base density gradient is non-zero then the semi-discrete algorithm is unstable

regardless which density formulation, direct or advanced, is employed, independently of the spatial discretization scheme. Therefore, periodic density re-initialization treatments [1, 48] essentially serve in reducing the density gradients and the corresponding unstable growth rates.

#### 2.6.4 Fully-discrete algorithm

Although the semi-discrete analysis is mathematically useful for the determination of the stability properties of the main algorithm, the results cannot be verified numerically, since any numerical simulation requires a temporal integration scheme. It is therefore of practical importance to study the stability properties of a fully-discrete scheme, i.e., both spatially and temporally. The temporal integration schemes considered here are Forward Euler, Predictor-Corrector, modified Predictor-Corrector and fourth order Runge-Kutta.

As in all the previous analysis a one-dimensional, initially uniform domain is assumed and both direct and advanced density formulations are considered. For the Forward Euler, the Predictor-Corrector, and the modified Predictor-Corrector the analysis is performed only for uniform base density distributions  $\bar{\rho}_a \equiv \rho_f$  for which the semi-discrete algorithm is stable, isolating the instability dependence on the temporal integration scheme and the Courant condition. For the fourth order Runge-Kutta both the uniform and hydrostatic base density distributions are considered, where it is recalled that the continuous and semi-discrete schemes are unstable in the presence of non-uniform base density distributions. The algebra in the stability analysis of the fully-discrete scheme with hydrostatic base density distribution is tedious. For this reason this stability analysis is performed only for the symplectic scheme, the fourth order Runge-Kutta, and can be straightforwardly extended to simpler, non-symplectic schemes.

**Direct density formulation** Based on the analysis of the semi-discrete algorithm, the linearized governing equations of the perturbations for the MA-SPH with direct

density are given by (2.206), and (2.209):

$$\begin{aligned}\dot{y} &= v \\ \dot{v} &= \left( ic \frac{\sin kh}{h} \right)^2 y.\end{aligned}$$

It is noted that the equations for  $y, v$  are decoupled from  $\rho$  when the direct density formulation is used. Denoting  $\phi \equiv \sin kh$  and  $\mu_c \equiv \delta t \frac{c}{h}$  the perturbation equations simplify to

$$\dot{y} = v \quad (2.244)$$

$$\dot{v} = -\frac{1}{\delta t^2} (\mu_c \phi)^2 y. \quad (2.245)$$

The stability properties of the fully-discrete schemes considered are obtained by substituting (2.244) and (2.245) into each one of the considered temporal integration schemes, i.e, Forward Euler, Predictor-Corrector, modified Predictor-Corrector, and fourth order Runge-Kutta.

For the case of Forward Euler the fully-discrete scheme can be written as:

$$y^{n+1} = y^n + \dot{y}^n \delta t \stackrel{(2.244)}{=} y^n + v^n \delta t \quad (2.246)$$

$$v^{n+1} = v^n + \dot{v}^n \delta t \stackrel{(2.245)}{=} v^n - \frac{1}{\delta t} (\mu_c \phi)^2 y^n + v^n. \quad (2.247)$$

In matrix form this is

$$\begin{bmatrix} y^{n+1} \\ v^{n+1} \end{bmatrix} = \begin{bmatrix} 1 & \delta t \\ -\frac{1}{\delta t} (\mu_c \phi)^2 & 1 \end{bmatrix} \begin{bmatrix} y^n \\ v^n \end{bmatrix} \rightarrow Y^{n+1} = \underbrace{A_{fe}}_{\text{Amplification matrix}} Y^n. \quad (2.248)$$

The algorithm is considered stable if the magnitude of all the eigenvalues  $|\lambda|$  of the corresponding amplification matrix  $A_{fe}$  are at most equal to one. For this matrix the eigenvalues are

$$|\lambda_{1,2}|^2 = 1 + (\mu_c \phi)^2 > 1. \quad (2.249)$$

Therefore, the MA-SPH with direct density formulation, uniform base density  $\rho_f$  and

Forward Euler temporal integration scheme is unconditionally unstable.

For the case of Predictor-Corrector the fully-discrete scheme can be written as:

$$y^p = y^n + \dot{y}^n \delta t \stackrel{(2.244)}{=} y^n + v^n \delta t \quad (2.250)$$

$$v^p = v^n + \dot{v}^n \delta t \stackrel{(2.245)}{=} -\frac{1}{\delta t} (\mu_c \phi)^2 y^n + v^n \quad (2.251)$$

$$y^{n+1} = y^n + (\dot{y}^n + \dot{y}^p) \frac{\delta t}{2} \stackrel{\dots}{=} \left(1 - \frac{(\mu_c \phi)^2}{2}\right) y^n + v^n \delta t \quad (2.252)$$

$$v^{n+1} = v^n + (\dot{v}^n + \dot{v}^p) \frac{\delta t}{2} \stackrel{\dots}{=} -\frac{1}{\delta t} (\mu_c \phi)^2 y^n + \left(1 - \frac{(\mu_c \phi)^2}{2}\right) v^n. \quad (2.253)$$

The corresponding amplification matrix  $A_{pc}$  becomes:

$$A_{pc} = \begin{bmatrix} 1 - \frac{(\mu_c \phi)^2}{2} & \delta t \\ -\frac{1}{\delta t} (\mu_c \phi)^2 & 1 - \frac{(\mu_c \phi)^2}{2} \end{bmatrix}, \quad (2.254)$$

with eigenvalues:

$$|\lambda_{1,2}|^2 = 1 + \frac{(\mu_c \phi)^4}{4} > 1. \quad (2.255)$$

Therefore, the fully-discrete MA-SPH with direct density formulation, uniform base density distribution  $\rho_f$  and Predictor-Corrector temporal integration scheme is unconditionally unstable.

For the case of the modified Predictor-Corrector the fully-discrete scheme can be written as:

$$y^{n+1} = y^n + \dot{y}^n \delta t + \dot{v}^n \frac{\delta t^2}{2} \stackrel{(2.245)}{\stackrel{(2.244)}{=}} \left(1 - \frac{(\mu_c \phi)^2}{2}\right) y^n + v^n \delta t \quad (2.256)$$

$$v^p = v^n + \dot{v}^n \delta t \stackrel{(2.245)}{=} -\frac{1}{\delta t} (\mu_c \phi)^2 y^n + v^n, \text{ and} \quad (2.257)$$

$$v^{n+1} = v^n + (\dot{v}^n + \dot{v}^{n+1}) \frac{\delta t}{2} \stackrel{\dots}{=} -\frac{1}{\delta t} (\mu_c \phi)^2 \left(1 - \frac{(\mu_c \phi)^2}{4}\right) y^n + \left(1 - \frac{(\mu_c \phi)^2}{4}\right) v^n \quad (2.258)$$

The corresponding amplification matrix  $A_{mpc}$  becomes:

$$A_{mpc} = \begin{bmatrix} 1 - \frac{(\mu_c \phi)^2}{2} & \delta t \\ -\frac{1}{\delta t} (\mu_c \phi)^2 \left(1 - \frac{(\mu_c \phi)^2}{4}\right) & 1 - \frac{(\mu_c \phi)^2}{2} \end{bmatrix}, \quad (2.259)$$

with eigenvalues  $|\lambda_{1,2}|^2 = 1$ , for  $0 < \mu_c \phi < 2 \rightarrow \mu_c < 2$ . Therefore, the fully-discrete MA-SPH with direct density formulation, uniform density distribution  $\rho_f$  and modified Predictor-Corrector temporal integration scheme is stable with Courant condition  $\mu_c < 2$ . This is a significantly larger Courant number compared to  $\mu_c < 0.3$  suggested in [3]. This is expected, since (a) the base density distribution in [3] is hydrostatic, i.e., the semi-discrete scheme is itself unstable and (b) a periodic density re-initialization is applied, i.e., the stability of the fully-discrete scheme is entirely different.

A final note for the modified Predictor-Corrector scheme is that the calculation of  $v^p$  is actually redundant and the scheme can be simplified to:

$$\begin{aligned} y_a^{n+1} &= y_a^n + v_a^n \delta t + (\dot{v}_a^n) \frac{\delta t^2}{2} \\ \rho_a^{n+1} &= \sum_b m_b W(y_a^{n+1} - y_b^{n+1}, h) \\ P^{n+1} &= \rho_f \frac{d^2}{\gamma} \left[ \left( \frac{\rho_a^{n+1}}{\rho_f} \right)^\gamma - 1 \right] \\ \dot{v}^{n+1} &= - \sum_b m_b \left( \frac{P_a^{n+1}}{\rho_a^{n+1}} + \frac{P_b^{n+1}}{\rho_b^{n+1}} \right) W'(y_a^{n+1} - y_b^{n+1}, h) \\ v^{n+1} &= v^n + (\dot{v}^n + \dot{v}^{n+1}) \frac{\delta t}{2}. \end{aligned}$$

Although this formulation requires two passings through the particles, it is found to be the most efficient scheme among the stable ones.

For the case of the fourth order Runge-Kutta scheme, after some algebra, the linearized perturbation equations lead to the following amplification matrix  $A_{rk4}$ :

$$A_{rk4} = \begin{bmatrix} 1 - \frac{(\mu_c \phi)^2}{2} + \frac{(\mu_c \phi)^4}{24} & \left(1 - \frac{(\mu_c \phi)^2}{6}\right) \delta t \\ -\frac{1}{\delta t} (\mu_c \phi)^2 \left(1 - \frac{(\mu_c \phi)^2}{6}\right) & 1 - \frac{(\mu_c \phi)^2}{2} + \frac{(\mu_c \phi)^4}{24} \end{bmatrix} \begin{bmatrix} y^n \\ v^n \end{bmatrix}. \quad (2.260)$$

For this temporal integration scheme, it can be shown that if  $\mu_c\phi < 2\sqrt{2}$ , the eigenvalues are:

$$|\lambda_{1,2}|^2 = 1 - \frac{(\mu_c\phi)^6}{72} + \frac{(\mu_c\phi)^8}{576} < 1. \quad (2.261)$$

Therefore, the MA-SPH with direct density formulation, uniform density distribution  $\rho_f$ , and fourth order Runge-Kutta temporal integration scheme is stable with Courant condition  $\mu_c < 2\sqrt{2}$ .

**Advanced density formulation** Based on the semi-discrete analysis, the linearized perturbation equations for the MA-SPH with advanced density formulation are (2.225), (2.231), and (2.232):

$$\dot{y} = v \quad (2.262)$$

$$\dot{v} = -i \frac{1}{\rho_f} \frac{c^2}{h} \phi \varrho \quad (2.263)$$

$$\dot{\varrho} = -i \frac{\rho_f}{h} \phi v. \quad (2.264)$$

The stability properties are obtained by substituting the above equations into each of the studied temporal integration schemes, i.e., Predictor-Corrector, modified Predictor-Corrector, and fourth order Runge-Kutta. The Forward Euler scheme is omitted since it was already shown in the direct density formulation to be in general the most unstable.

For the case of the Predictor-Corrector, the corresponding amplification matrix  $B_{pc}$  of the fully-discrete scheme is given by:

$$B_{pc} = \begin{bmatrix} 1 & \delta t & -i \frac{\delta t}{2} \frac{c}{\rho_f} \mu_c \phi \\ 0 & 1 - \frac{(\mu_c \phi)^2}{2} & -i \frac{c}{\rho_f} \mu_c \phi \\ 0 & -i \frac{\rho_f}{c} \mu_c \phi & 1 - \frac{(\mu_c \phi)^2}{2} \end{bmatrix}. \quad (2.265)$$

The eigenvalues  $|\lambda|$  of  $B_{pc}$  are:

$$|\lambda_{1,2,3}|^2 = \begin{cases} 1 \\ 1 + \frac{(\mu_c\phi)^4}{4} > 1 \end{cases}. \quad (2.266)$$

Therefore, the MA-SPH with advanced density formulation, uniform density distribution  $\rho_f$ , and Predictor-Corrector temporal integration scheme is unconditionally unstable.

For the case of the modified Predictor-Corrector, the corresponding amplification matrix  $B_{mpc}$  of the fully-discrete scheme is given by:

$$B_{mpc} = \begin{bmatrix} 1 & \delta t & -i\frac{\delta t}{2}\frac{c}{\rho_f}\mu_c\phi \\ 0 & 1 - \frac{(\mu_c\phi)^2}{2} & -i\frac{c}{\rho_f}\mu_c\phi \\ 0 & -i\frac{\rho_f}{c}\mu_c\phi & 1 - \frac{(\mu_c\phi)^2}{2} \end{bmatrix} = B_{pc}. \quad (2.267)$$

Since  $B_{mpc} = B_{pc}$ , the MA-SPH with advanced density with either Predictor-Corrector or modified Predictor-Corrector temporal integration scheme is unconditionally unstable with eigenvalues given by (2.266). In [3] a Courant condition of  $\mu_c < 0.3$  that is much smaller than the corresponding  $\mu_c = 2$  with the direct density is reported. This partly explains the difference.

For the case of the fourth order Runge-Kutta, the corresponding amplification matrix  $B_{rk4}$  of the fully-discrete scheme is given by:

$$B_{rk4} = \begin{bmatrix} 1 & \delta t \left(1 - \frac{(\mu_c\phi)^2}{6}\right) & -i\delta t\frac{c}{\rho_f}\mu_c\phi \left(\frac{1}{2} - \frac{(\mu_c\phi)^2}{24}\right) \\ 0 & 1 - \frac{(\mu_c\phi)^2}{2} + \frac{(\mu_c\phi)^4}{24} & -i\frac{c}{\rho_f}\mu_c\phi \left(1 - \frac{(\mu_c\phi)^2}{6}\right) \\ 0 & -i\frac{\rho_f}{c}\mu_c\phi \left(1 - \frac{(\mu_c\phi)^2}{6}\right) & 1 - \frac{(\mu_c\phi)^2}{2} + \frac{(\mu_c\phi)^4}{24} \end{bmatrix}. \quad (2.268)$$

After some algebra, the Courant condition for the MA-SPH with advanced density formulation, uniform density distribution  $\rho_f$ , and fourth order Runge-Kutta temporal integration scheme is found to be  $\mu_c < 2\sqrt{2}$ .

### 2.6.4.1 Advanced density formulation with hydrostatic base density distribution

Denoting the time step with  $\delta t$  and  $q^n \equiv q(t = n\delta t) = [\bar{x}^n, \bar{u}^n, \rho^n]$  the flow variable vector, the fourth order Runge-Kutta temporal integration reads

$$\begin{cases} q^{1/4} &= q^n + Q^n \frac{\delta t}{2} \\ q^{1/2} &= q^n + Q^{1/4} \frac{\delta t}{2} \\ q^{3/4} &= q^n + Q^{1/2} \delta t \\ q^{n+1} &= q^n + (Q^n + 2Q^{1/4} + 2Q^{1/2} + Q^{3/4}) \frac{\delta t}{6} \end{cases} \quad (2.269)$$

where  $Q^m = [\frac{d\bar{x}^n}{dt}, \frac{d\bar{u}^n}{dt}, \frac{d\rho^n}{dt}]$ . For the case of hydrostatic initial conditions, typically employed in the standard SPH dam-break benchmark [30], the base flow is assumed to be static, i.e.,  $\bar{u} = 0$ , and the density distribution is assumed to be hydrostatic, i.e.,  $\bar{\rho} = \rho_f(1 - 2\delta y)$ . The stability analysis is performed in the vertical direction and only for the acoustic modes.

The following infinitesimal perturbations are assumed  $y_a \ll h$  in the position,  $u_a \ll 1$  in the velocity, and  $r_a \ll 1$  in the density. Substituting the perturbation quantities into the governing equations, subtracting the hydrostatic base flow, substituting  $W'_{ab} = W'_{ab} + y_{ab}W''_{ab}$  i.e., hydrostatic, and finally assuming  $[y_a, u_a, r_a] = [y(t), u(t), r_a(t)]e^{iky_a}$  yields after some algebra the perturbation evolution equations:

$$\frac{dy}{dt} = u \quad (2.270)$$

$$\frac{du}{dt} = \underbrace{(1 - 2\delta\bar{y}_a)}_{\simeq 1} \left[ -8c^2 \frac{(\sin kh/2)^2}{h^2} y - ic^2 \frac{\sin kh}{h} r \right] \quad (2.271)$$

$$\frac{dr}{dt} = -i \frac{\sin kh}{h} u. \quad (2.272)$$

It is pointed out that the first term in the right hand side of (2.271) is due to the hydrostatic density distribution. Therefore, the hydrostatic density distribution couples the position to velocity and density perturbations. Substituting into (2.269)

obtains the following  $3 \times 3$  amplification matrix:

$$\left[ \begin{array}{cc}
 1 - 4\mu_c^2 s_2 + \frac{1}{3}(\mu_c^2 s_2)^2 + \frac{1}{3}\mu_c^4 s_2 s_1^2 & 1 - \frac{4}{3}\mu_c^2 s_2 + \frac{1}{6}(i\mu_c s_1)^2 \\
 8\mu_c^2 s_2(-1 + \frac{1}{3}\mu_c^2 s_2 - \frac{1}{6}(i\mu_c s_1)^2) & 1 - 4\mu_c^2 s_2^2 + \frac{8}{3}(\mu_c^2 s_2)^2 + \frac{2}{3}\mu_c^4 s_2 s_1^2 - \frac{1}{2}(\mu_c s_1)^2 + \frac{1}{24}(\mu_c s_1)^4 \\
 i8\mu_c^2 s_1 s_2(\frac{1}{2} - \frac{1}{3}\mu_c^2 s_2 - \frac{1}{24}(\mu_c s_1)^2) & -is_1(1 + \frac{1}{6}\mu_c^2 s_2 + \frac{1}{6}(\mu_c s_1)^2)
 \end{array} \right]$$

$$\left. \begin{array}{l}
 i\mu_c^2 s_1(-\frac{1}{2} - \frac{1}{24}(i\mu_c s_1)^2 + \frac{1}{3}\mu_c^2 s_2) \\
 i\mu_c^2 s_1(\frac{4}{3}\mu_c^2 s_2 - 1 - \frac{1}{6}(i\mu_c s_1)^2) \\
 1 - \frac{1}{2}(\mu_c s_1)^2 + \frac{1}{24}(\mu_c s_1)^4 - \frac{1}{3}\mu_c^4 s_2 s_1^2
 \end{array} \right] \quad (2.273)$$

where  $s_1 = \sin kh$ ,  $s_2 = (\sin kh/2)^2$  and  $\mu_c = \frac{c\delta t}{h}$ . It is easy to verify that the above matrix reduces to that of a uniform initial density distribution when  $s_2 = 0$ . The stability depends solely on  $\mu$  and  $kh$ . The largest eigenvalue of the amplification matrix is always greater than zero, therefore the system is unstable. However, for small enough  $\mu$  the growth rates are negligible. In Figure 2-33 the unstable growth rates are given as functions of  $kh$  for four different values of  $\mu$ .

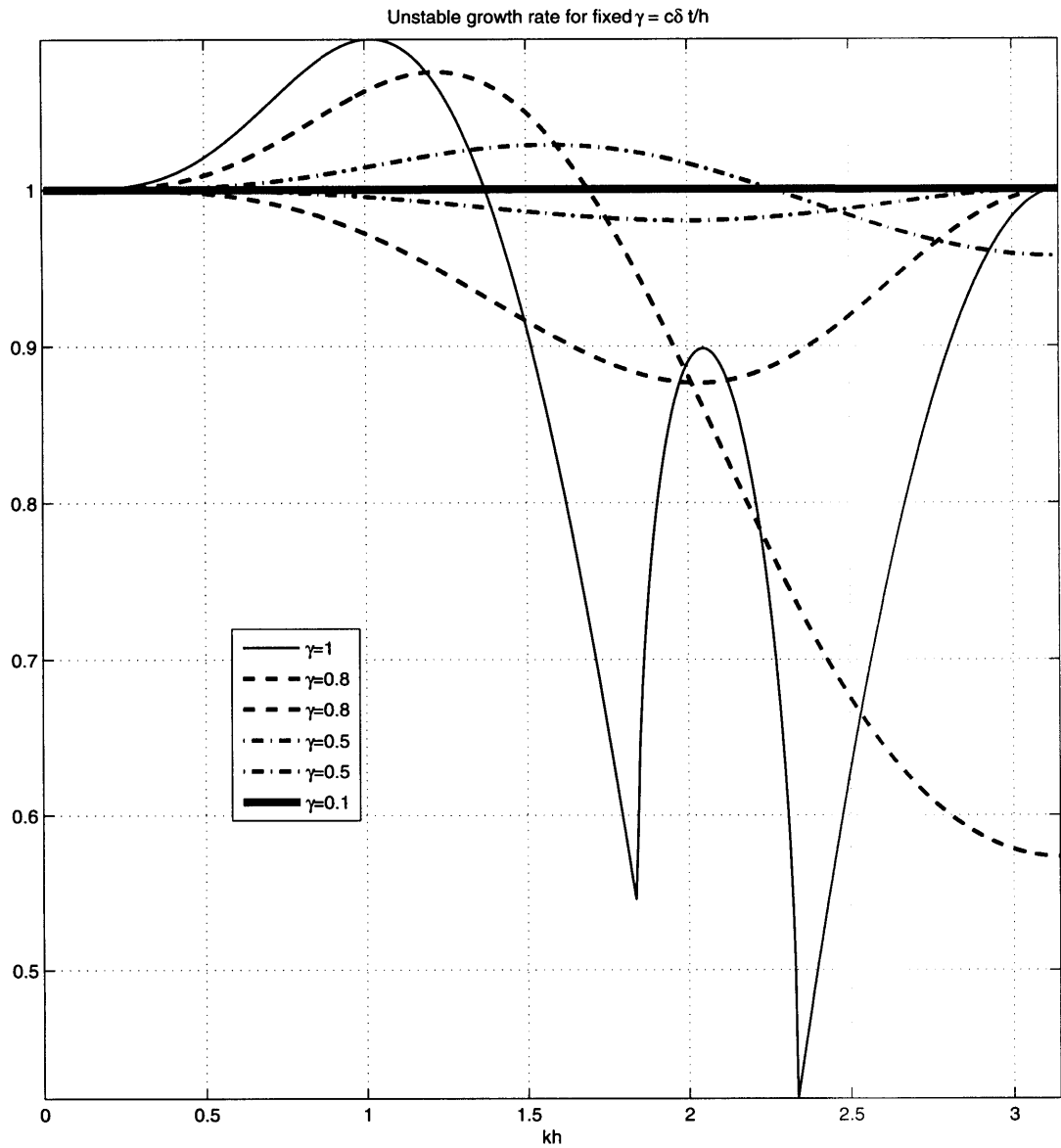


Figure 2-33: Unstable growth rates of the fully-discrete mSPH algorithm with fourth order Runge-Kutta as a function of the dimensionless perturbation wavenumber  $kh$ . Thin solid line  $\mu_c = 1$ , dashed line  $\mu_c = 0.8$ , dash-dot line  $\mu_c = 0.5$ , thick solid line  $\mu_c = 0.1$ .

### 2.6.5 Discussion on the linear stability of MA-SPH with advanced density formulation

The findings on the stability properties of the MA-SPH with advanced density formulation are summarized in the following Table 2.4, where two different cases are distinguished with respect to the perturbation properties.

In the first case, the perturbations are assumed to be depth decaying, as discussed in section 2.6.2 and in [43]. These modes are inherent to the CMA-SPH in the presence of a free-surface and are unconditionally unstable. The maximum unstable depth decaying wavenumbers  $\mu$  are of the order of  $O(1/h)$  and uniform along the bounded dimension, with large corresponding growth rates of order  $O(c\mu) \sim O(c/h)$ . Such modes are manifested in fixed simulation domains, for example, in the simulation of a hydrostatic case or a plane progressive wave. Since leading order depth decaying perturbations can be generated from the implicit free-surface boundary condition 2.5.6 and their growth rates are so large, the computational life of such simulations is significantly limited. It is also pointed out that these findings mean that the useful computational life is reduced when (a) the speed of sound is increased, (b) the spatial resolution is increased, i.e, the number of particles in the domain is increased, and (c) the Courant condition is reduced.

In the second case, the perturbations are assumed to be oscillatory. These modes are inherently unstable in the presence of non-uniform base density distributions but firstly, have significantly smaller growth rates compared to the depth decaying modes and secondly, their effects are manifested predominantly in the dynamics and not the kinematics. In summary, it is shown that (a) CMA-SPH and the semi-discrete MA-SPH are linearly stable in uniform base density distributions and unstable in the presence of non-uniform base density distributions, (b) the fully-discrete algorithm in uniform base density distribution can be either stable, with appropriate Courant condition, or unstable based on the employed temporal integration scheme, and (c) the fourth order Runge-Kutta is unstable in a hydrostatic base density distribution, with very small growth rates, Fig. 2-33, which depend on the Courant condition

and the dimensionless perturbation wavenumber  $kh$ . Such modes are dominant in evolving flow domains, such as the SPH dam-break benchmark. Even though they have leading-order initial amplitudes, generated by the spurious free-surface boundary condition, their growth rates are very small and their effects are limited to the dynamics, allowing for increased useful simulation lives.

This feature of MA-SPH, where the stability properties are strongly problem dependent, explains why SPH can be used successfully for the simulation of the most complex violent free-surface flows, such as the dam-break, and completely fail when employed for the simulation of the most trivial flows, such as a hydrostatic case.

Table 2.4: Summary of the findings of the linear stability analysis performed on MA-SPH with advanced density formulation. The analysis is performed for the continuous model, the semi-discrete algorithm and the fully-discrete algorithm with fourth order Runge-Kutta and Courant condition  $\mu_c = \frac{c\delta t}{h}$ . The base density distribution is given by  $\bar{\rho} = \rho_f(1 + \theta)$ . Three different values of  $\theta$  have been considered:  $\theta = 0$ ,  $\theta = -2\delta y$ , where  $\delta = \frac{g}{2c^2}$  and  $\theta \lll 1$ . Two different modes have been considered: depth decaying  $e^{\mu y}$  and acoustic  $e^{i\nu y}$ .

Mode	CMA-SPH		semi-discrete		fully-discrete	
	$\theta = 0$	$\theta = -2\delta y$	$\theta = 0$	$\theta \lll 1$	$\theta = 0$	$\theta = -2\delta y$
$e^{\mu y}$	$c\mu\sqrt{1 - \frac{2\delta}{\mu}}$	$c\mu\sqrt{1 + \frac{2\delta}{\mu}}$	$c\frac{\sinh \mu h}{h}$			
$e^{i\nu y}$	stable	$\frac{\delta}{\nu}$	stable	$O(c\theta')$	stable for $\mu_c \leq 2\sqrt{2}$	Fig. 2-33

## 2.7 Conclusions

Smoothed Particle Hydrodynamics (SPH) is a numerical simulation method for hydrodynamic flows. In SPH the flow domain is discretized into a finite number of fluid particles. Their equations of motion are obtained using a weakly compressible flow model. The spatial derivatives that appear in the equations of motion are computed through a meshless derivative computation technique defined as Kernel Interpolation (KI). Their positions are advanced in time from their equations of motion and an appropriate temporal integration scheme.

In this chapter, a main SPH algorithm (MA-SPH) is defined in section 2.2. A linear analysis is performed on the weak compressibility assumption in section 2.4, on the consistency of KI in section 2.5 and on the stability of MA-SPH in section 2.6. Although the analysis in each section is performed separately, it is also informed from the findings of the other two sections, as shown in Fig. 2-34.

First, the weakly compressible flow model is validated for free-surface gravity waves. The analysis shows that SPH can capture an incompressible solution with accuracy  $O(1/c^2)$  but also permits the generation of spurious (generated from numerical errors) and thus undesirable high frequency acoustic modes. Second, the consistency of the KI is investigated for uniform, smoothly advected, and random particle distributions inside the domain and near boundaries. It is shown that the KI in an SPH simulation is consistent inside the domain as long as velocity divergence is maintained small. However, KI imposes a fictitious free-surface dynamic boundary condition that is the main source of generation of the spurious acoustic modes. Finally, the stability analysis of the continuous, semi-discrete and fully-discrete schemes is performed, revealing that MA-SPH is an inherently unstable scheme in the presence of non-uniform density distributions.

This is the first unified analysis of the method and has enabled the classification of the sources of error in MA-SPH and the quantitative estimation of these errors. This improved understanding enables the further classification and analysis of the existing semi-empirical treatments, detailed in Chapter 3, and eventually highlights the way for the regularization of the method in Chapter 4.

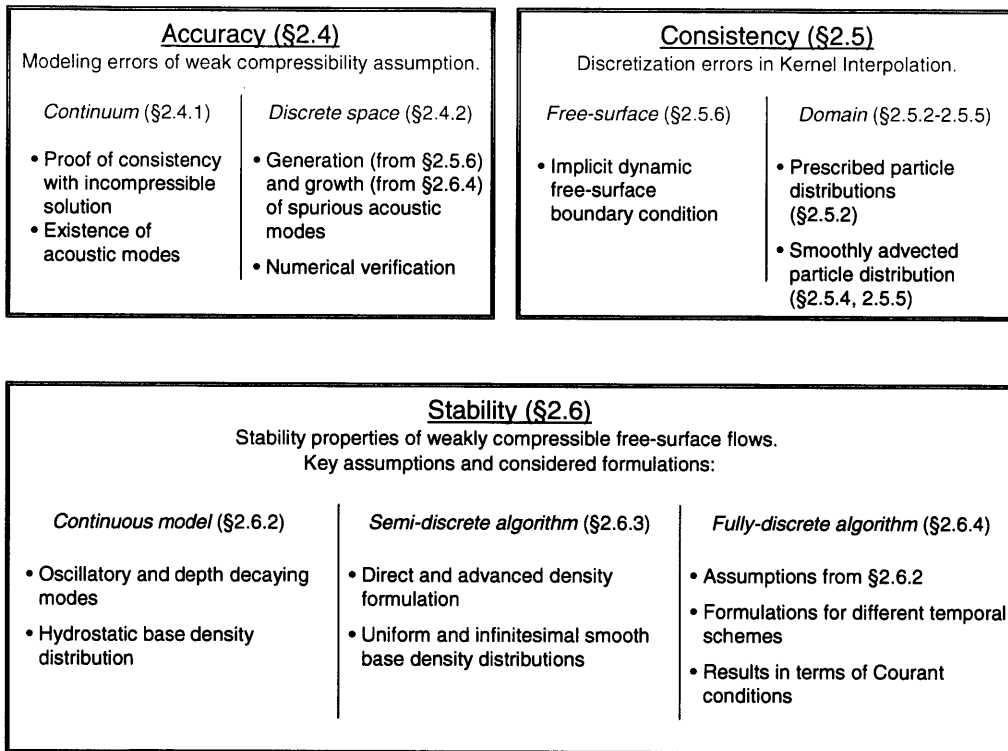


Figure 2-34: Summary of the analysis framework.



# Chapter 3

## Analysis of existing treatments for MA-SPH

### 3.1 Introduction

Chapter 2 detailed the accuracy, consistency, and stability issues associated with SPH for the simulation of free-surface flows. Due to the prior lack of a comprehensive analysis of the method, several semi-empirical treatments have been developed to address the aforementioned issues. These treatments introduce tunable parameters with unknown effects on the simulated physics even though their usefulness has not been appropriately justified. This chapter utilizes the knowledge gained from analysis in Chapter 2, for the understanding of selected existing treatments within the context of free-surface flows. The benefit of this analysis on the existing semi-empirical treatments is twofold. First, it either justifies the use of the treatment and provides a rationale for the choice of the associated tunable parameters, or it demonstrates that the benefits of the treatment are negligible and thus its usage is best avoided. Second, and most importantly, it leads the way towards the formulation of a modified SPH that rationally address the existing MA-SPH issues identified in Chapter 2.

The analysis is carried out in the following manner. First, the treatments are categorized as accuracy, consistency, and stability treatments, since in general, each treatment addresses essentially one of the above issues. Then, each treatment sepa-

rately is incorporated into MA-SPH. The resulting algorithm MA-SPH + treatment is analyzed within the framework of the treatment's usage. It is investigated whether and under what conditions the performance of the new algorithm MA-SPH + treatment is improved compared to the performance of MA-SPH. For example, assume treatment  $T_1$ , categorized as a stability treatment: stability analysis is performed on the algorithm  $\text{MA-SPH}_1 = \text{MA-SPH} + T_1$  and it is investigated under what conditions the stability properties of  $\text{MA-SPH}_1$  are improved compared to MA-SPH.

## 3.2 Accuracy treatments

As was discussed in detail in section 2.4, the weak compressibility assumption in MA-SPH for linear periodic deep-water free-surface gravity waves allows for a set of spurious high frequency oscillatory (HFO) solutions in addition to the incompressible-like solution. In particular, it was demonstrated that these HFO dominate the dynamics of the solution, i.e., pressure and accelerations, while temporally integrated quantities such as free-surface particle locations do not exhibit significant HFO. For this reason, the weakly compressible MA-SPH has been validated with experimental comparisons of free-surface elevations, in highly nonlinear and complex flows, but the corresponding dynamics have accuracy errors of the order of 100% [2]. Treatments attempting to remove the HFO from the MA-SPH pressure results are classified as accuracy treatments.

In general, the dynamics obtained by SPH are ignored, excluding applications related to fluid-structure interaction, [6, 13, 20, 39, 49]. For the cases that require knowledge of pressure values at specific locations, the results are simply post-processed to remove the HFO at the desired locations. The post-processing of the pressure involves either spatial averaging or temporal filtering. Therefore, the accuracy treatments considered in the following two subsections involve post-processing of the pressure results at desired locations with either temporal filtering or spatial averaging. Since the origins of the HFO as yet were not completely understood, the choices on the size of the averaging area or the cut-off frequency are empirical. The aim of the following

two subsections is merely to critique the empirical choices based on the findings of the analysis in Chapter 2.

It must be pointed out that there exist algorithms referenced as “incompressible SPH” or “implicit SPH” algorithms. One particular example is the moving particle semi-implicit method (MPS) [45] that requires the solution of a Poisson equation for the particle density. Although solving the Poisson equation could be viewed as a separate accuracy treatment this is not the case. First, it is by our definition that such algorithms are not considered in the present work as extensions to the standard MA-SPH but rather as different methods. Second, and most importantly, the algorithms are not free of the aforementioned HFO [32, 33, 34]. Moreover, it is believed that the source of the HFO is the same in MPS and in SPH and therefore, the pressure post-processing procedure typically applied in MPS is regarded as yet another SPH accuracy treatment.

### 3.2.1 Temporal filtering of pressure measurements

Post-processing temporal filtering implies the choice of a cut-off frequency through techniques such as Fourier filtering or temporal integration. To the best of the author’s knowledge, only the aforementioned two approaches are utilized in the literature.

For the case of the Fourier filtering, only the harmonic which coincides with the known excitation frequency is kept. This is particularly the case in the simulation of sloshing in anti-roll tanks [6, 49]. It is interesting to note that [6] reports that the HFO dominate the dynamic results, but not the particle locations. Therefore, filtering is applied to dynamic results only. The moments generated by the fluid in the tank with respect to time are computed as the summation of the moments of the momentum on the entire tank wall at each time step. A FFT is then performed and only the excitation harmonic is considered. The amplitude of this filtered result is within close agreement to the experimental results.

Filtering the excitation harmonic essentially obtains the leading order incompressible solution only, dropping leading order acoustic modes as well as higher order solutions. To construct a more general temporal filter, the findings of the analysis

in Chapter 2 are utilized. First, the dispersion relations for the acoustic modes obtained by the analysis in section 2.4 indicate that the acoustic modes have frequencies ranging from  $\omega_{\min} = c\frac{\pi}{2H}$  to  $\omega_{\max} = c\frac{\pi}{2h}$ , where  $c$  is the speed of sound.  $H$  is a characteristic water depth, and  $h$  is the kernel bandwidth. Second, the stability analysis of the fully-discrete scheme indicates that the most unstable acoustic mode has a wavelength  $\alpha(\mu)h$ , where  $\alpha(\mu) \sim O(5)$  is determined by the stability analysis and  $\mu$  is the Courant condition. Therefore, it is desirable to employ a low-pass filter that allows only frequencies lower than  $\omega = c\frac{\pi}{\alpha h}$ . Although a temporal filter is the most effective method to remove the HFO, it must be taken into account that it is still a local, post-processing approach, i.e., the unstable acoustic modes will have already affected the physics inside the domain.

Temporal integration of the pressure is also considered. Characteristic examples are detailed in simulations of green water on the ship deck with the Moving Particle Semi-implicit (MPS) numerical simulation method [32, 33, 34]. Although the method is referenced as incompressible, it exhibits HFO, the origins of which are believed to be the same as with SPH. Here the authors compare the time integral of particle pressure with experimental values, among other quantities. The time integrals of the particle pressure in these simulations underestimate the corresponding experimental values, but do not exhibit the HFO present in the particle pressure measurements, as expected. In such a case, if the pressure can be described as  $\sum_n P_n$ , where  $n = -1, 0, 1, \dots, m$  denotes the pressure amplitude of each frequency component with  $n = -1$  corresponding to the incompressible solution and  $n = m$  the cut-off frequency, then the temporal integration essentially obtains  $\sum_n \frac{1}{\omega_n} P_n$  and therefore is essentially attenuating the highest frequencies. The fact that temporal integration attenuates the higher frequencies is yet another expression of the statement that SPH obtains validated kinematics but not dynamics. To further remove the highest frequencies, the time step for the temporal integration of the pressure can be chosen larger than that corresponding to the cut-off frequency, i.e.,  $\delta t_p > 1/\omega_{\max}$ .

### 3.2.2 Spatial averaging of pressure measurements

In general, the most typical post-processing approach involves some sort of spatial averaging of the pressure either through KI or some other technique [20, 36]. It is noted that computation of forces on a structure as pressure integrals are considered as a particular case of pressure spatial averaging. In particular, in [13, 39] the three-dimensional wave impacts on tall structures are considered. The forces exerted on the structures are computed as the sum of the pressures at each structure particle along the height of the structures. HFO are not mentioned and the numerical and experimental results are in good agreement.

In [20] two-dimensional wedge water entries are considered. The local fluid force on the wedge is computed as the average pressure along a virtual sensor of length  $S_{\text{sensor}}$ . The pressures along this virtual sensor are computed from interpolated particle fluid pressures within a distance  $d \sim h$ . Results for various ratios of  $d/h$  are shown. The authors suggest a preferred range of  $d/h$  between 5 and 10, since HFO are still present for  $d/h = 2$  while for larger ratios the pressures are over-smoothed. This ratio “ $d/h$  between 5 and 10” is in very close agreement of the wavelength of the dominant unstable acoustic mode, computed in section 2.6.4.1.

A similar approach is seen in [36] in the context of sloshing. Again a virtual sensor area is considered and the pressure on this virtual sensor is computed from the interaction of fluid and ghost-boundary particles. Although, HFO are significant it is recorded that similar results were obtained with the method described in [20]. No reference is made however on the choice of the ratio  $d/h$ .

A simpler procedure is followed in [34, 32, 33] where green water on the ship deck is investigated through three-dimensional MPS numerical simulations. Experimental pressures on the deck are compared with numerical pressures averaged over 25 neighboring particles on deck. The authors report in [32] that “the spatial average reduces the pressure oscillation caused by the particle motion”. However, in [33] the same averaging does not reduce the oscillations, and the authors claim that in order “to restrain the pressure oscillations caused by the particle model, higher spatial

resolution is necessary in addition to post-processing such as time averaging and spatial averaging.” In the latter work the numerical pressures exceed the experimental values, contrary to the former work where the numerical results underestimate the experimental values.

These spatial filters rely on two assumptions. First that the spurious acoustic modes have wavelengths  $\simeq d$  and second that they can be decomposed into Fourier modes. However, as has been shown in detail in Chapter 2, neither assumption is valid. First, the wavelengths of the acoustic modes range from  $O(H)$ , the characteristic domain length, to  $O(h)$ , the characteristic discretization length. The wavelength corresponding to the most unstable mode depends on the Courant condition  $\mu_c$  and is of the order of  $5h$  for a typical  $\mu_c = 0.8$ , Figure 2-33, as determined from the stability analysis of the fully discrete advanced density scheme with fourth order Runge-Kutta and hydrostatic base density distribution. Second, the basis of the acoustic modes are not the Fourier functions. Therefore, the existing spatial averaging techniques cannot be effective. Within this context, an effective spatial filter has been developed in section 2.4.3. It is recalled that this spatial filter removes the HFO in the space domain through appropriately developed modal decomposition that involves integration of both horizontal and vertical velocities along the water depth. In short, spatial averaging filters aim solely at removing short wavelengths that are not necessarily acoustic modes, even though these modes are characterized by high frequencies. Therefore, there are no indications that simple, local, *post-processing* spatial averaging techniques can be used efficiently to remove the acoustic modes, in agreement with the above numerical observations. As will be discussed in Chapter 4, local spatial averaging is effective *during* the computation, as it dissipates the acoustic modes.

### 3.3 Consistency treatments

Section 2.5 detailed the consistency analysis of Kernel Interpolation (KI) for the numerical computation of derivatives on Lagrangian particles within an SPH simulation. First, the established results that KI is (a) consistent for unbounded uniform particle distributions [29], and (b) divergent near boundaries [52] were recapitulated in sections 2.5.2.1 and 2.5.2.3. The analysis is extended in section 2.5.5 to account for smooth advection of particles initially located on an unbounded uniform grid, which is the resulting particle motion in an SPH simulation, and consistency of KI within SPH was proven for the first time. The role of the density in the numerical consistency of KI was shown in section 2.5.4 for the first time. Finally, in section 2.5.6 the general statement that KI is divergent near the boundaries is expressed as a spurious dynamic free-surface boundary condition dependant on the free-surface slope.

The findings detailed in sections 2.5.4, 2.5.5 and 2.5.6 had not been known, associating the consistency of KI to uncertainties due to the discrepancy between the analytic findings, which indicated divergence, and the numerical findings, which showed consistency. This incomplete picture regarding the consistency of KI has lead to the usage of a number of consistency treatments. The consistency treatments investigated in the following two subsections are further categorized as (a) alternative derivative computation techniques, and (b) different discrete forms of the equations of motion. Alternative derivative computation techniques include but are not limited to Moving Least Squares and Corrected Kernels. Although these methods can be argued to be more accurate than KI they are also more expensive and, most importantly, less robust. The discrete forms of the equations of motion have been in general chosen on a case-to-case basis, ignoring the true effect of the density in the consistency of KI and the presence of boundaries.

#### 3.3.1 Alternative spatial derivative computation techniques

In section 2.5.5, the consistency of KI was proven even for the case of a non-uniform particle distribution. The two main assumptions are that the fluid particles have been

smoothly advected from an initial appropriate configuration and that the particle density is included in the summation.

However, partly because the consistency of KI in a non-uniform grid had not been established, and mainly because of the inconsistency of KI near boundaries, many alternative unstructured, discrete spatial derivative computation techniques are suggested in the literature such as MLS [35], Müller derivatives [48], the Element Free Galerking, RKPM, Particle in Cell, hp-clouds, techniques reviewed in [50].

To describe and analyze the general approach towards consistent discrete meshless differentiation techniques, assume a snapshot of a discrete particle field, where  $\vec{x}$  denotes location. Let  $q(\vec{x})$  denote a smooth field property known at discrete particle locations. Let  $\nabla q$  denote the unknown spatial gradient of  $q$ . The aim is to compute  $\nabla q$  at the location  $\vec{x}_a$ , i.e.,  $\nabla q_a \equiv \nabla q(\vec{x}_a)$  given the values of  $q$  at the discrete neighboring locations  $\vec{x}_b$ , i.e.,  $q_b \equiv q(\vec{x}_b)$ . Defining  $\vec{x}_{ba} \equiv \vec{x}_b - \vec{x}_a$ , by Taylor Series Expanding  $q_b$  about  $\vec{x}_a$  obtains:

$$q_b = \sum_{n=0}^{N-1} \frac{1}{n!} (\vec{x}_{ab} \cdot \nabla)^n q_a + O(|\vec{x}_{ab}|^N).$$

To demonstrate the approach for linear consistency let  $N = 2$ . The above reduces to:

$$q_b = q_a + \vec{x}_{ab} \cdot \nabla q_a + O(|\vec{x}_{ab}|^2)$$

Further, by subtracting  $q_a$  from  $q_b$ , multiplying with a weight function  $w_{ba} \equiv w(\vec{x}_{ba}; h)$  where  $h$  denoted the support, and summing over all  $b$  within the compact support of  $w$ , i.e.,  $|\vec{x}_{ba}| \leq h$ , it is:

$$\sum_b \vec{x}_{ab} w_{ba} \cdot \nabla q_a = \sum_b q_b w_{ba} + O(h^2) \quad (3.1)$$

A linear system  $A\mathbf{x} = \beta$  is formed to solve. The first term in the left hand side of (3.1) is the matrix  $A$ , the second term is the unknown vector  $\mathbf{x}$ , and the term in the

right hand side of (3.1) is the vector  $\beta$ . If  $A$  is non-singular, the solution is given by:

$$\nabla q_a = A^{-1} \sum_b q_{ba} w_{ba}. \quad (3.2)$$

The weight function  $w$  can either be the same as the kernels used in KI or their derivatives. However, as will be discussed, it is best for numerical issues if a simple hat function is used.

The alternative computation techniques are regarded as a panacea to the uncertainties raised by KI however, there are two main issues associated with their usage in MA-SPH. First, if there are not enough particles in all directions within the support of  $w$ , the matrix  $A$  is singular and the method fails. To alleviate this the size of  $A$ , and therefore the consistency of the method, is reduced [18]. Second, the momentum is not exactly conserved within the domain, i.e., the forces exerted from particle  $a_n$  to particle  $a_m$  are not identically opposite [21]. However, momentum is not exactly conserved with KI in the presence of a free-surface, either.

This section considers two examples of consistent derivative computation techniques, the Moving Least Squares (MLS) [35] and Müller derivative computation technique (Müller) [48], in one and two-dimensions respectively. The analysis is mainly demonstrative and by no means complete. However, the results obtained can be straightforwardly generalized, extended to other schemes, higher dimensions and advected grids.

### 3.3.1.1 MLS

The consistency and transforms of one-dimensional MLS interpolation and differentiation as defined in [35] are investigated. First, assume a one-dimensional, infinite, particle grid along the  $x$  axis. Without loss of generality, all analysis is performed about the origin. Let the position of the center of mass of particle  $b$  be denoted by  $x_b$ . Assume a sufficiently smooth function  $f(x)$  and let  $f_b \equiv f(x_b)$  and  $f \equiv f(0)$ . The

MLS interpolation is defined as:

$$\hat{f} = \sum_b \phi_b f_b = \sum_b \underbrace{q_o A^{-1}}_{\gamma} \underbrace{B_b f_b}_{\beta} \quad (3.3)$$

where  $q_o = [1, 0]^T$ ,  $A = qq^T$ ,  $q = [\sum_b w_b, \sum_b w_b x_b]^T$ ,  $\beta = [\sum_b w_b f_b, \sum_b w_b f_b x_b]^T$ . The weights  $w_b$  are typically computed from a known analytical function with compact support, such as the cubic B-Spline or a truncated Gaussian. Denoting the determinant of  $A$  with  $\Delta = \sum_b w_b \sum_b w_b x_b^2 - (\sum_b w_b x_b)^2$ , (3.3) reduces to:

$$\hat{f} = \frac{1}{\Delta} \left( \sum_b w_b f_b \sum_b w_b x_b^2 - \sum_b w_b x_b f_b \sum_b w_b x_b \right). \quad (3.4)$$

To determine the consistency of (3.4), the Taylor Series Expansion of  $f_b$  about the origin is considered, i.e.,  $f_b = f + x_b f' + \frac{x_b^2}{2} f'' + \text{h.o.t.}$  Substituting into (3.4), after some algebra, obtains:

$$\begin{aligned} \hat{f} = & f \frac{\overbrace{\sum_b w_b \sum_b w_b x_b^2 - \left( \sum_b w_b x_b \right)^2}^{\Delta}}{\Delta} + \\ & + \frac{f''}{2} \frac{\overbrace{\left( \sum_b w_b x_b^2 \right)^2 - \sum_b w_b x_b \sum_b w_b x_b^3}^{\delta}}{\Delta} \rightarrow \\ \hat{f} = & f + \frac{f''}{2} \frac{\delta}{\Delta}. \end{aligned} \quad (3.5)$$

First, it is observed that  $\frac{\delta}{\Delta} \sim O(h^2)$ . Second, it is found that on a regular grid of spacing  $h$  when  $w_b$  is obtained by an even function, then  $\sum_b w_b x_b = \sum_b w_b x_b^3 = 0$  and therefore  $\delta/\Delta$  reduces to:

$$\frac{\delta}{\Delta} = \frac{\sum_b w_b x_b^2}{\sum_b w_b}.$$

There is no apparent benefit in the MLS consistency in using any other  $w_b$  than a hat function, i.e. to define the support. Moreover, any other  $w_b$  increases the computational effort and numerical round-off errors. Therefore, it is strongly recommended that only a hat function is used with MLS. The consistency of the method for particles smoothly advected from a regular grid can be computed as in section 2.5.5, simply by substituting into  $\delta/\Delta$ . It must be noted though that even in random grids the method remains of order  $O(h^2)$ .

To determine the transforms associated to MLS expand the function  $f(x)$  in terms of normal modes  $f_b = f e^{\kappa x_b}$  where it is assumed that  $f \equiv f(0)$ . The wavenumber  $\kappa$  can be either imaginary,  $\kappa \rightarrow ik$ , or real,  $\kappa \rightarrow \mu$ . Substituting the above modal expansion into (3.4), after some algebra, the function interpolation transform is:

$$\tilde{f} = \frac{f}{\Delta} \left( \sum_b w_b x_b^2 \sum_b w_b e^{\kappa x_b} - \sum_b w_b x_b \sum_b w_b e^{\kappa x_b} x_b \right). \quad (3.6)$$

In a regular grid for  $w_b$  described by a hat function  $\sum_b w_b x_b = 0$ , the above further simplifies to:

$$\tilde{f} = f \frac{\sum_b e^{\kappa x_b}}{\sum_b 1}. \quad (3.7)$$

Further if  $-1 \leq b \leq 1$ , i.e., only two neighbors are considered in the summation then:

$$\begin{aligned} \tilde{f} &= f \frac{e^{-\kappa h} + 1 + e^{\kappa h}}{3} \\ &= f \left( 1 + \frac{e^{-\kappa h} - 2 + e^{\kappa h}}{3} \right) \\ &= f \left( 1 + \frac{(e^{\kappa h/2} - e^{-\kappa h/2})^2}{3} \right). \end{aligned}$$

For  $\kappa \rightarrow ik$  it is  $\tilde{f} = f - \frac{4}{3} \sin^2(kh/2)$ . For  $\kappa \rightarrow \mu$  it is  $\tilde{f} = f + \frac{4}{3} \sinh^2(\mu h/2)$ . For small  $|\kappa h| \rightarrow e^{\kappa h} \simeq \kappa h$  it is apparent that  $\hat{f} \simeq f(1 + \frac{\kappa^2}{3} h^2)$ .

The MLS differentiation is defined as:

$$\hat{f}' = \sum_b \phi_b f_b = \sum_b \underbrace{q_1 A^{-1}}_{\gamma} \underbrace{B_b f_b}_{\beta}, \quad (3.8)$$

where  $q_1 = [0, 1]^T$  and everything else is the same as with MLS interpolation, i.e.,  $A = qq^T$ ,  $q = [\sum_b w_b, \sum_b w_b x_b]^T$ ,  $\beta = [\sum_b w_b f_b, \sum_b w_b f_b x_b]^T$ . Denoting the determinant of  $A$  with  $\Delta = \sum_b w_b \sum_b w_b x_b^2 - (\sum_b w_b x_b)^2$ , (3.8) reduces to:

$$\hat{f}' = \frac{1}{\Delta} \left( \sum_b w_b f_b \sum_b w_b x_b - \sum_b w_b x_b f_b \sum_b w_b \right). \quad (3.9)$$

To determine the consistency of (3.9), the Taylor Series Expansion of  $f_b$  about the origin is considered, i.e.,  $f_b = f + x_b f' + \frac{x_b^2}{2} f'' + \text{h.o.t.}$  Substituting into (3.9), after some algebra, obtains:

$$\begin{aligned} \hat{f}' &= f' \frac{\overbrace{\sum_b w_b \sum_b w_b x_b^2 - \left( \sum_b w_b x_b \right)^2}^{\Delta}}{\Delta} + \\ &+ \frac{f''}{2} \frac{\overbrace{\sum_b w_b \sum_b w_b x_b^3 - \sum_b w_b x_b \sum_b w_b x_b^2}^{\delta_1}}{\Delta} \rightarrow \\ \hat{f}' &= f' + \frac{f''}{2} \frac{\delta_1}{\Delta}. \end{aligned} \quad (3.10)$$

First, it is observed that  $\frac{\delta_1}{\Delta} \sim O(h)$ . Second, it is found that on a regular grid of uniform spacing  $h$ , when  $w_b$  is even, it is  $\sum_b w_b x_b = \sum_b w_b x_b^3 = 0$  and therefore  $\delta_1/\Delta = 0$ , i.e., the method becomes order  $O(h^2)$ . It must be noted though, that even in random grids the method remains of order  $O(h)$ . Finally, there is no apparent benefit in terms of consistency in using any other  $w_b$  than a hat function. Finally, [35] points out that it is best to compute  $\gamma = q_i A^{-1}$  through an LU decomposition rather than inverting  $A$  to alleviate numerical issues due to poor conditioning of  $A$ .

To determine the transforms associated to derivatives using MLS. the function  $f(x)$  is expanded in terms of normal modes,  $f_b = f e^{\kappa x_b}$ , where it is assumed that  $f \equiv f(0)$ . The wavenumber  $\kappa$  can be either imaginary,  $\kappa \rightarrow ik$ , or real,  $\kappa \rightarrow \mu$ .

Substituting the above modal expansion into (3.9), after some algebra, obtains the function differentiation transform:

$$\tilde{f}' = \frac{f}{\Delta} \left( \sum_b w_b \sum_b w_b e^{\kappa x_b} x_b - \sum_b w_b x_b \sum_b w_b e^{\kappa x_b} \right). \quad (3.11)$$

In a regular grid for  $w_b$  described by a hat function  $\sum_b w_b x_b = 0$ , the above further simplifies to:

$$\tilde{f}' = f \frac{\sum_b x_b e^{\kappa x_b}}{\sum_b x_b^2}. \quad (3.12)$$

Further, if  $-1 \leq b \leq 1$ , i.e., only two neighbors are considered in the summation, it is:

$$\begin{aligned} \tilde{f}' &= f \frac{-he^{-\kappa h} + he^{\kappa h}}{2h^2} \\ &= f \frac{e^{\kappa h} - e^{-\kappa h}}{2h}. \end{aligned}$$

For  $\kappa \rightarrow ik$  it is  $\tilde{f}' = f \frac{i \sin kh}{h}$ . For  $\kappa \rightarrow \mu$  it is  $\tilde{f}' = f \frac{\sinh \mu h}{h}$ . For small  $|\kappa h| \rightarrow e^{\kappa h} \simeq \kappa h$  it is apparent that  $\tilde{f}' \simeq fk$ .

The major advantage of MLS is that it is at least of order  $O(h^2)$  for interpolation and  $O(h)$  for differentiation, even on highly distorted grids or in the presence of boundaries where KI diverges. The major disadvantage of MLS to KI is that MLS can become singular and is therefore less robust than KI.

### 3.3.1.2 Müller derivatives

The consistency and transforms of two-dimensional Müller derivatives as defined in [48] are investigated. First, assume the Cartesian coordinate system  $\vec{x} = [x, y]$  and a two-dimensional unbounded grid. Without loss of generality, all analysis is performed about the origin. Let the position of the center of mass of particle  $b$  be denoted by  $\vec{x}_b$ . Assume a sufficiently smooth function  $f(\vec{x})$  and let  $f_b \equiv f(\vec{x}_b)$  and  $f \equiv f(0)$ . The

Müller interpolation is defined as:

$$\hat{\nabla} f = \begin{bmatrix} \hat{f}_x \\ \hat{f}_y \end{bmatrix} = \begin{bmatrix} \sum_b w_b x_b^2 & \sum_b w_b x_b y_b \\ \sum_b w_b x_b y_b & \sum_b w_b y_b^2 \end{bmatrix}^{-1} \begin{bmatrix} \sum_b w_b x_b f_{b0} \\ \sum_b w_b y_b f_{b0} \end{bmatrix} \quad (3.13)$$

where  $f_{b0} = f_b - f$ ,  $f_x = \frac{\partial f}{\partial x}$ ,  $f_y = \frac{\partial f}{\partial y}$ , etc. Without loss of generality only the  $\hat{f}'_x$  is considered. Letting  $\Delta = \sum_b w_b x_b^2 \sum_b w_b y_b^2 - (\sum_b w_b x_b y_b)^2$ , (3.13) reduces to:

$$\hat{f}'_x = \frac{\sum_b w_b y_b^2 \sum_b w_b x_b f_{b0} - \sum_b w_b x_b y_b \sum_b w_b y_b f_{b0}}{\Delta}. \quad (3.14)$$

To determine the consistency of (3.14), the Taylor Series Expansion of  $f_{b0}$  about the origin is considered, i.e.,  $f_{b0} = f_b - f = x_b f_x + y_b f_y + \frac{x_b^2}{2} f_{xx} + x_b y_b f_{xy} + \frac{y_b^2}{2} f_{yy}$ . Substituting into (3.14), after some algebra, obtains:

$$\hat{f}'_x = f_x + f_{xx} \delta_{xx} + f_{xy} \delta_{xy} + f_{yy} \delta_{yy}, \quad (3.15)$$

where:

$$\begin{aligned} \delta_{xx} &= \frac{1}{2} \left( \sum_b w_b y_b^2 \sum_b w_b x_b^3 - \sum_b w_b x_b y_b \sum_b w_b x_b^2 y_b \right) \\ \delta_{xy} &= \frac{1}{2} \left( \sum_b w_b y_b^2 \sum_b w_b x_b^2 y_b - \sum_b w_b x_b y_b \sum_b w_b x_b y_b^2 \right) \\ \delta_{yy} &= \frac{1}{2} \left( \sum_b w_b y_b^2 \sum_b w_b x_b y_b^2 - \sum_b w_b x_b y_b \sum_b w_b y_b^3 \right) \end{aligned}$$

First, note that  $\delta/\Delta \sim O(h)$ . Second, on a uniform grid for  $w_b$  given by an even function it is  $\delta_{xx} = \delta_{xy} = \delta_{yy} = 0$ , thus the method becomes  $O(h^2)$ . Again, it is suggested that a hat function be used for  $w$ .

To determine the transforms associated to Müller derivatives, the function  $f(\vec{x})$  is expanded in terms of normal modes,  $f_b = f(0, y) e^{\kappa x_b}$ . The wavenumber  $\kappa$  can be either imaginary,  $\kappa \rightarrow ik$ , or real,  $\kappa \rightarrow \mu$ . Substituting the above modal expansion into (3.14) yields the function differentiation transform. For the case of a uniform grid of spacing  $\delta x = \delta y = h$ , with  $w_b$  given by a hat function of support  $h$ , after some

algebra, obtains:

$$\tilde{f}_x = f \frac{e^{\kappa h} - e^{-\kappa h}}{2h}.$$

For  $\kappa \rightarrow ik$  it is  $\tilde{f}' = f \frac{i \sin kh}{h}$ . For  $\kappa \rightarrow \mu$  it is  $\tilde{f}_x = f \frac{\sinh \mu h}{h}$ . For small  $|\kappa h| \rightarrow e^{\kappa h} \simeq \kappa h$  it is apparent that  $\tilde{f}_x \simeq f k$ .

The major advantage in computing derivatives using the Müller derivatives technique, instead of using the KI technique, is that the Müller derivatives are consistent at least up to order  $O(h)$  even on highly distorted grids or in the presence of boundaries where KI diverges. The major disadvantage in computing derivatives using the Müller derivatives technique is that the Müller derivatives can become singular. Therefore, the Müller derivatives less robust than KI.

Finally, comparing MLS and Müller derivatives, it is observed that while MLS can be used at any desired order of consistency, Müller derivatives are most efficient for first order consistency where the need for numerical matrix inversion is eliminated. Finally, regarding the choice of the weight function  $w_b$  for both MLS and Müller with respect to efficiency and numerical accuracy, it is recommended that a unit hat function with support of  $O(h)$  be used.

### 3.3.2 Different discrete forms of the equations of motion

In the literature there exists extensive reference on the formulation of the discrete inviscid equations of motion employed by MA-SPH [42]. The references can be collected into two different groups: those related to the formulation of the momentum equation and those related to the mass conservation. In general, formulations related to the momentum equation focus either on global momentum conservation, ignoring the presence of boundaries, or on the inclusion of the particle density. Formulations related to the mass conservation mainly address the inconsistency of KI near the free-surface.

### 3.3.2.1 Momentum equation

In addition to the two MA-SPH formulations for the inviscid momentum equation (2.12) and (2.15), the following consistent form is often employed in the literature [21, 42]:

$$\frac{d\vec{u}_a}{dt} = -\frac{1}{\rho_a} \sum_b (\pm P_a + P_b) \frac{m_b}{\rho_b} \nabla w_{ab} - g\hat{j} \quad (3.16)$$

Equation (3.16) is essentially (2.12) with the addition of the term  $A_p = \pm P_a \sum_b \frac{m_b}{\rho_b} \nabla w_{ab}$ . From the analysis on the consistency of KI in section 2.5.5, it is understood that inside a smoothly advected domain  $A_p$  should scale at most by  $h$ , i.e..  $A_p \sim O(h)$ . The term however is significant when the KI is incomplete. In particular, near the free-surface the computed acceleration, discussed in section 2.5.6, becomes:

$$\widehat{\frac{d\vec{u}}{dt}} = \left[ \begin{array}{c} -\frac{5}{6} \frac{P_{dx}}{\rho} \\ \frac{1}{2} \frac{P_d(1\pm 1) - hP_{dy}}{h\rho} - \frac{1}{2}g(1 + \frac{y}{h}) \end{array} \right] = \frac{d\vec{u}_a}{dt} + \left[ \begin{array}{c} \frac{1}{6} \frac{P_{dx}}{\rho} \\ \frac{1}{2} \frac{P_d(1\pm 1) + hP_{dy}}{h\rho} - \frac{1}{2}g(1 + \frac{y}{h}) \end{array} \right] \quad (3.17)$$

### 3.3.2.2 Mass conservation

For the case of the direct density formulation, alternatively to the standard form of the density equation (2.16), the particle density also appears in the literature [42] in the following forms:

$$\rho_a = \frac{\sum_b m_b W_{ab}}{\sum_b \frac{m_b}{\rho_b} W_{ab}} \quad (3.18)$$

Based on the findings of section 2.5.5, the form (3.18) introduces dissipation of the form  $\nabla^2 \rho$ , and improves the consistency near the free-surface.

For the case of the advanced density formulation, alternatively to the standard form of the conservation of mass (2.13), the time rate of density also appears in the literature [42] in the following forms:

$$\frac{d\rho_a}{dt} = -\rho_a \sum_b \frac{m_b}{\rho_b} \vec{u}_{ba} \cdot \nabla W_{ab} \quad (3.19)$$

$$\frac{d\rho_a}{dt} = -\sum_b m_b \vec{u}_{ba} \cdot \nabla W_{ab} \quad (3.20)$$

The main affect of the coefficient of  $\vec{u}_a$  is on the implementation of the free-surface dynamic boundary condition.

### 3.4 Stability treatments

The key issue in MA-SPH is that it is unstable. As has been discussed in detail in Chapter 2, there are three types of instabilities present in an MA-SPH simulation. The first, detailed in section 2.6.2, are depth-decaying wave components that occur under the continuous weak compressibility assumption in the presence of a free-surface [43]. These components are unconditionally unstable, have the largest growth rates, eventually dominate all long-term simulations and essentially determine the useful computational life. The second, detailed in section 2.6.2, are pure oscillatory components that are unstable in the presence of non-zero base density gradients. In the literature this type of instability is identified as tensile instability and is erroneously blamed on the spatial discretization [26, 40, 44, 50, 53]. For the violent free-surface flows of interest, where the base density gradient is hydrostatic, these components have in general growth rates inversely proportional to their wavenumbers, dominate the short-time solution and corrupt the dynamics. The third type, are instabilities introduced by the temporal integration scheme and depend, among other quantities, on the Courant condition  $\mu_c = \frac{\delta t c}{h}$ , where  $\delta t$  is the numerical time-stepping,  $c$  the speed of sound and  $h$  the kernel bandwidth.

Despite the prior lack of a conclusive stability analysis (as presented in Chapter 2), the majority of the existing SPH semi-empirical treatments essentially aimed towards the numerical stabilization, or regularization, of the method. The scope of this section 3.4 is threefold. First, it implicitly aims to justify the classification of certain treatments as stability treatments. Second, it sets guidelines for the analysis and evaluation of these treatments. Thirdly, and most importantly, it gains the appropriate insight to eventually propose a rational, numerical regularization of MA-SPH in Chapter 4. Therefore, it is *not* within the scope of this section 3.4 to present an in-depth analysis of the existing SPH treatments, as was the case for the main algorithm in Chapter 2. Instead, the theme is to give a brief analysis for each treatment under consideration followed by a discussion on the insight gained from its approach towards regularizing SPH.

Section 3.4 is structured as follows. First, in section 3.4.1, the rationale for the classification of stability treatments is stated and the framework of the analysis is described. Then, in sections 3.4.2 through 3.4.6 each stability treatment is considered separately for both the direct and advanced density formulations of the MA-SPH algorithm, either for the semi-discrete or fully-discrete algorithm.

### 3.4.1 Classification and framework

The existing stability analysis on SPH is limited to the tensile instability the source of which had been misleadingly identified as the KI [40, 44, 53], clarified in section 2.6.2. Therefore, even though a corresponding tensile instability treatment was proposed [26], the stability properties of MA-SPH for the simulation of free-surface flows remained unchanged [3, 26, 48], as expected. This led to the development of several semi-empirical stability treatments which generally have not been explicitly identified as stability treatments.

In a first general approach, treatments are classified as stability treatments when it is noted in the literature that their inclusion “stabilizes” or “regularizes the SPH simulations”. The stability treatments are collected into two groups. The first group, includes treatments that introduce a small term on the right hand side of the governing equations. The treatments considered here are: the artificial viscosity (AV) treatment [30, 3], the tensile instability (TI) treatment [26], the XSPH velocity treatment [24], and applying an initial dumping (ID) in the particle positions through the temporal integration scheme before starting the simulation [30]. The second group, includes density re-initialization schemes. The schemes considered in this second group are: the smoothed density re-initialization scheme [4] and the hydrostatic density re-initialization scheme [3].

Once the treatments have been classified, the framework for a unified stability analysis is sketched. First, the semi-discrete evolution equations for infinitesimal disturbances in MA-SPH for both direct and advanced density formulations are recapitulated, as in section 2.6.3. Then, the general approach for the first group of treatments is to incorporate treatment X (per se) into MA-SPH, formulate the am-

plification matrix  $A_X$  of either the semi-discrete or fully-discrete algorithm MA-SPH + X, and compute the amplitude of the corresponding eigenvalues  $|\lambda_X|$ .

As detailed in section 2.6.2, the most unstable conditions occur for flows independent of  $x$ . Therefore, the stability analysis is again performed in a one-dimensional problem, along the  $y$  axis, considering both depth decaying and purely oscillatory modes. The domain is discretized into  $N$  fluid particles of uniform spacing  $\delta y = h$ . The center of mass of particle  $a$  is given by  $\bar{y}_a = ah$  and its mass is  $m_a = \rho_f h \equiv m$ , where  $\rho_f$  is the unperturbed fluid density. Let  $c$  be the speed of sound in the fluid. A uniform base flow solution at time  $t$  is assumed, i.e., the base flow velocity, pressure and density of particle  $a$  are  $\bar{v}_a = 0$ ,  $\bar{P}_a = 0$ , and  $\bar{\rho}_a = \rho_f$  respectively. It is noted that although the tensile instability manifests itself in the presence of a non-zero base density gradient, the basic assumption henceforth is uniform base density distribution and gravity is neglected. Contradictory as though this might seem, recall that the scope of this paragraph is to perform a simple analysis on selected existing treatments, gain insight from the existing semi-empirical knowledge and propose a rational regularization based on the findings of the analysis. Therefore it is of interest to recognize the effects of a treatment on the unstable growth rates by performing the simplest analysis possible.

Next, following the linear von Neumann stability analysis outlined in section 2.6.1, infinitesimal perturbations  $y_a \ll h$ ,  $v_a$ ,  $p_a$  and  $\rho_a \ll \rho_f$  are superimposed to the base position, velocity, pressure and density respectively. Thus, the particle total position, velocity, pressure, and density are given by:

$$\begin{aligned} y_A &= \bar{y}_a + y_a \\ v_A &= v_a \\ P_A &= p_a \\ \rho_A &= \rho_f + \rho_a \end{aligned}$$

The total position and velocity of particle  $a$  satisfy the MA-SPH governing equations:

$$\dot{y}_A = v_A \quad (3.21)$$

$$\dot{v}_A = - \sum_b m_b \left( \frac{P_A}{\rho_A^2} + \frac{P_B}{\rho_B^2} \right) W'_{ab}. \quad (3.22)$$

The total density  $\rho_a$  is given by either the direct or advanced computation:

$$\text{Direct:} \quad \rho_a = \sum_b m_b W_{ab} \quad (3.23)$$

$$\text{Advanced:} \quad \dot{\rho}_a = \sum_b m_b v_{AB} W'_{ab}. \quad (3.24)$$

where the pressure is determined by a constitutive Equation of State

$$P_A = \rho_f \frac{d^2}{\gamma} \left[ \left( \frac{\rho_A}{\rho_f} \right)^\gamma - 1 \right]$$

and  $W_{ab} \equiv W(y_A - y_B)$  is the cubic B-Spline kernel (2.111). The kernel is expanded about  $\bar{y}_{ab}$  to obtain:

$$\begin{aligned} W_{ab} &= W(y_A - \tilde{y}_B) = W((\bar{y}_a - \bar{y}_b) + (y_a - y_b)) \\ &\cong W(\bar{y}_a - \bar{y}_b) + (y_a - y_b)W'(\bar{y}_a - \bar{y}_b) \\ &= W_{\bar{ab}} + y_{ab}W'_{\bar{ab}} \end{aligned}$$

In the same manner, the first derivative of the kernel is expanded about  $\bar{y}_{ab}$ :

$$W'_{ab} \cong W'_{\bar{ab}} + y_{ab}W''_{\bar{ab}}.$$

Next, the pressure term in the momentum equation (3.22) is expanded about 0, which, after some algebra, obtains to leading order:  $\frac{P_A}{\rho_A^2} = \frac{c^2}{\rho_f^2} \rho_a$ . Substituting the above into (3.21)-(3.24), subtracting the base flow and maintaining only linear terms with respect to the disturbances, after some algebra, obtains the governing equations

for the disturbances:

$$\frac{dy_a}{dt} = v_a \quad (3.25)$$

$$\frac{dv_a}{dt} = -\frac{c^2}{\rho_f^2} \sum_b m_b \varrho_b W'_{ab} \quad (3.26)$$

$$\rho_a = \sum_b m_b y_{ab} W'_{ab} \quad (3.27)$$

$$\frac{d\rho_a}{dt} = \sum_b m_b v_{ab} W'_{ab} \quad (3.28)$$

Next, the disturbances are expanded in terms of normal modes.

$$[y_a, v_a, \varrho_a] = [y(t), v(t), \varrho(t)] e^{\kappa \bar{y}_a}, \quad (3.29)$$

where  $\kappa$  is the wavenumber of the disturbance. Recalling that the flow is a simplification of a two-dimensional one, based on [43],  $\kappa$  can be either real ( $\kappa \rightarrow \mu$ ) or imaginary ( $\kappa \rightarrow ik$ ), therefore, both cases are considered. Substituting into (3.25) - (3.28) and defining  $r \equiv \varrho/\rho_f$ , obtains:

$$\frac{dy_a}{dt} = v_a \quad (3.30)$$

$$\frac{dv_a}{dt} = -c^2 h F r_a \quad (3.31)$$

$$r_a = -h F y_a \quad (3.32)$$

$$\frac{dr_a}{dt} = -h F v_a \quad (3.33)$$

where  $F \equiv \sum_b e^{\kappa \bar{y}_{ba}} W'_{ab}$ , is dependant on the shape of the kernel and on the wavenumber  $\kappa$ . In particular, for the cubic B-Spline,  $F$  becomes:

$$F = \begin{cases} i \frac{\sin kh}{h} & \text{for } \kappa = ik \text{ with } k \in \Re \\ \frac{\sinh \mu h}{h} & \text{for } \kappa = \mu \text{ with } \mu \in \Re \end{cases} \quad (3.34)$$

Table 3.1 summarizes the linearized MA-SPH evolution equations for infinitesimal disturbances in a uniform base flow. The evolution equations for the disturbances for

the direct density formulation reduce to:

$$\ddot{y} = c^2 F^2 y \rightarrow y \propto e^{\lambda t} \text{ where } \lambda = \pm \sqrt{c^2 F^2}.$$

For disturbances with imaginary wavenumbers (oscillatory) it is  $(cF)^2 < 0 \rightarrow \lambda$  is imaginary and thus the disturbances are stable. For disturbances with real wavenumbers (exponential) it is  $(cF)^2 > 0 \rightarrow \lambda$  is real and thus the disturbances are unstable. The aforementioned sign difference is the source of the inherent instability of the exponential modes, which are allowed in any finite domain.

Table 3.1: MA-SPH linearized evolution equations for infinitesimal disturbances. Both direct and advanced density algorithms are considered. The disturbances are expanded into both oscillatory and exponentially decaying modes. The base flow is assumed to be uniform, the particles are lying in a uniform grid of spacing  $h$  and their mass is  $m = \rho_f h$ .

Algorithm	General	SIN disturbance	EXP disturbance
Direct	$\dot{y} = v$ $\dot{v} = c^2(-F)^2 y$	$\dot{y} = v$ $\dot{v} = -c^2 \left(\frac{\sin kh}{h}\right)^2 y$	$\dot{y} = v$ $\dot{v} = c^2 \left(\frac{\sinh \mu h}{h}\right)^2 y$
Advanced	$\dot{y} = v$ $\dot{v} = -c^2 F r$ $\dot{r} = -F v$	$\dot{y} = v$ $\dot{v} = -i c^2 \frac{\sin kh}{h} r$ $\dot{r} = -i \frac{\sin kh}{h} v$	$\dot{y} = v$ $\dot{v} = -c^2 \frac{\sinh \mu h}{h} r$ $\dot{r} = -\frac{\sinh \mu h}{h} v$

From Table 3.1, the amplification matrix describing the evolution of the disturbances reduces to:

$$A_{ma} = \begin{bmatrix} 0 & 1 & 0 \\ 0 & 0 & -c^2 F \\ 0 & -F & 0 \end{bmatrix}$$

and the corresponding eigenvalues are  $\lambda_{ma} = (0, \pm \sqrt{c^2 F^2})$ , equal to the corresponding eigenvalues with the direct density formulation. It is pointed that the evolution equation for  $y$  can be neglected in the MA-SPH stability analysis for uniform base flow

and advanced density formulation. Finally, the analysis of each stability treatment under consideration reduces to formulating additional terms on the amplification matrix and computing the corresponding eigenvalues.

### 3.4.2 XSPH

In [24] the author suggests the particle positions are updated based on a smoothed velocity given by:

$$\frac{d\vec{x}_a}{dt} = \vec{u}_a + \tilde{\alpha} \underbrace{\sum_b (\vec{u}_b - \vec{u}_a) \frac{2m_b}{(\rho_a + \rho_b)} W_{ab}}_X.$$

Assuming a one-dimensional uniform base flow, and maintaining leading order terms with respect to the disturbances obtains the corresponding term  $\delta X$  for the one-dimensional disturbances:

$$\delta X \equiv h \sum_b (v_b - v_a) W_{ab}^-.$$

Substituting the modal expansion (3.29) and performing the summations on the regular grid for the cubic B-Spline, obtains for  $\delta X$ :

$$\delta X = h \left( \sum_b (e^{\kappa \bar{x}_{ba}} - 1) W_{ab}^- \right) v = \frac{(e^{\kappa h/2} - e^{-\kappa h/2})^2}{6} v = X_v v,$$

where

$$X_v = \begin{cases} -\frac{2}{3} \left( \sin \frac{\kappa h}{2} \right)^2 \leq 0 & \text{for } \kappa = ik \text{ with } k \in \Re \\ \frac{2}{3} \left( \sinh \frac{\mu h}{2} \right)^2 \geq 0 & \text{for } \kappa = \mu \text{ with } \mu \in \Re \end{cases} \quad (3.35)$$

**Direct density formulation** The evolution equation for  $y$  becomes  $\dot{y} = (1 + \bar{a} X_v) y$  and the corresponding growth rates for the MA-SPH + XSPH with direct density formulation are:

$$\lambda = \pm \sqrt{c^2 F^2 (1 + \bar{a} X_v)}.$$

For oscillatory disturbances with imaginary wavenumbers it is  $\lambda = \pm ic \frac{\sin kh}{h} \sqrt{1 + \bar{a} X_v}$ .

Therefore, to retain stability  $\bar{a}$  must be chosen so that  $1 - \bar{a} \frac{2}{3} \left(\sin \frac{kh}{2}\right)^2 \geq 0 \rightarrow \bar{a} \leq 1.5$ . For disturbances with real wavenumbers (exponential) the XSPH velocity increases the instability growth rate.

**Advanced density formulation** For the advanced density formulation, for a uniform base density distribution, the XSPH velocity does not affect the stability properties of the system.

It is concluded that XSPH does not seem to lead the way to a generalized stabilization of the method, in agreement with numerical observations [26, 3].

### 3.4.3 Initial dumping

In [30] it is suggested that the initial particle configuration is dumped out before the flow is initialized. This initial dumping is incorporated in the temporal integration scheme, and therefore, the initial dumping treatment is studied in the fully-discrete scheme exactly as described in [30]. In this case the assumptions of uniform base flow are exact.

**Direct density formulation** Let  $\zeta \equiv 1 + 0.5\Gamma\delta t > 1$ , where  $\Gamma$  is a tunable parameter. Given the values of  $y^n$ ,  $v^n$  at time step  $n$  and time step size  $\delta t$ , the evolution equations for the disturbances in the fully-discrete ID scheme are:

1. Predictor step

$$y^{n+p} = y^n + \frac{\delta t}{2} \dot{y}^n \quad (3.36)$$

$$v^{n+p} = \frac{1}{\zeta} \left( v^n + \frac{\delta t}{2} \dot{v}^n \right) \quad (3.37)$$

2. Corrector step

$$y^{n+1} = y^n + \delta t \dot{y}^{n+p} \quad (3.38)$$

$$v^{n+1} = \frac{2}{\zeta} \left( v^n + \frac{\delta t}{2} \dot{v}^{n+p} \right) - v^n \quad (3.39)$$

The values of  $\dot{y}$  and  $\dot{v}$  from Table 3.1 are substituted in (3.36) - (3.39). After some algebra, the amplification matrix  $A_{id}$  of fully discrete is obtained:

$$A_{id} = \begin{bmatrix} 1 + \frac{(\delta tdF)^2}{2\zeta} & \frac{\delta t}{\zeta} \\ \frac{(\delta tdF)^2}{\zeta \delta t} & \frac{2}{\zeta} - 1 + \frac{(\delta tdF)^2}{2\zeta} \end{bmatrix}$$

with  $F$  given by (3.34). The amplitudes of the corresponding eigenvalues  $\lambda_{1,2}$  of the amplification matrix are:

$$|\lambda_{1,2}| = \left| \frac{1 + \frac{1}{2}(\delta tdF)^2 \pm \sqrt{1 + (\delta tdF)^2 - 2\zeta + \zeta^2}}{\zeta} \right|$$

Figures 3-1 and 3-2 describe the maximum amplitude  $|\lambda| = \max|\lambda_1, \lambda_2|$  for  $\zeta = [1, 1.005, 1.025]$  as a function of the Courant condition  $\mu_c = \delta td/h$  for the sinusoidal disturbances, and as function of  $\mu^* = \delta td \sinh \mu h/h$  for the exponential disturbances respectively.

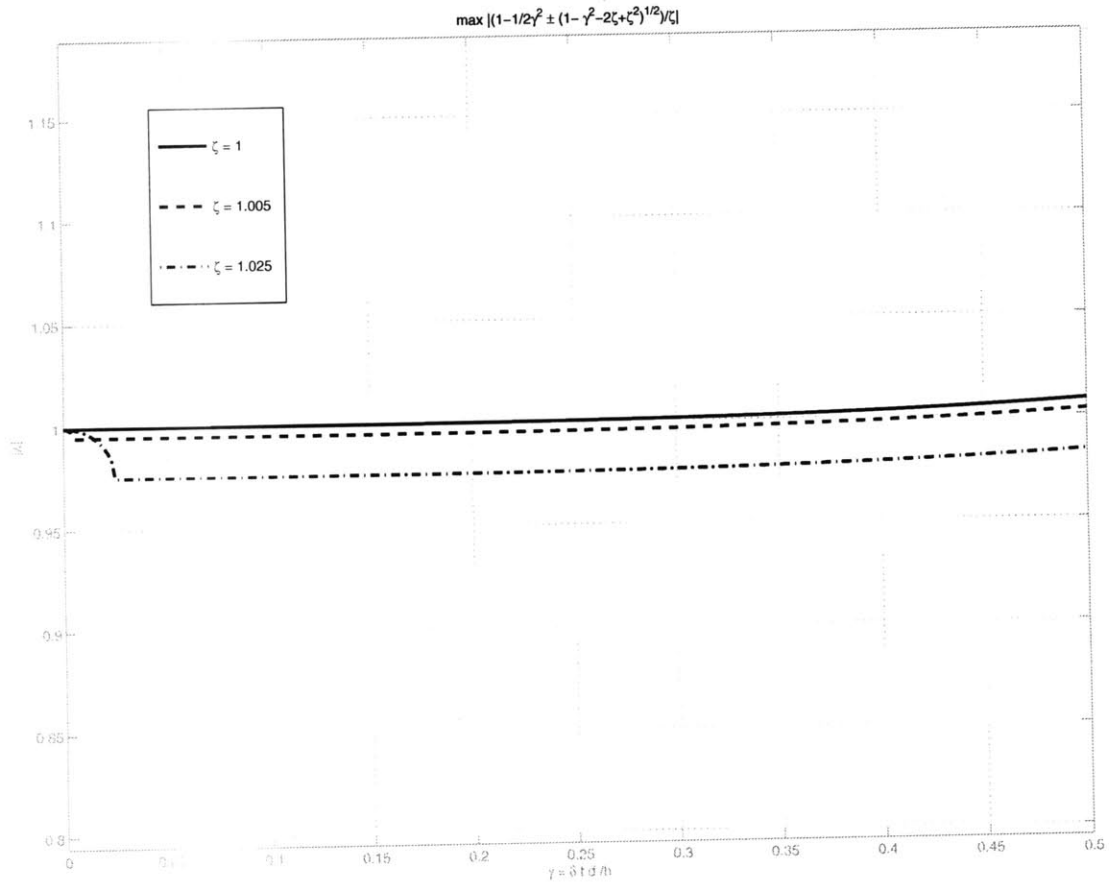


Figure 3-1: Maximum amplitude of the eigenvalues of the amplification matrix  $|\lambda| = \max |\lambda_1, \lambda_2|$  for MA-SPH with ID treatment and modified Predictor-Corrector temporal integration scheme. The amplitude of  $|\lambda|$  is given as function of the Courant condition  $\mu_c = \delta t d/h$  for three values of  $\zeta = 1 + 0.5\Gamma\delta t = [1, 1.005, 1.025]$ . Sinusoidal disturbances are assumed.

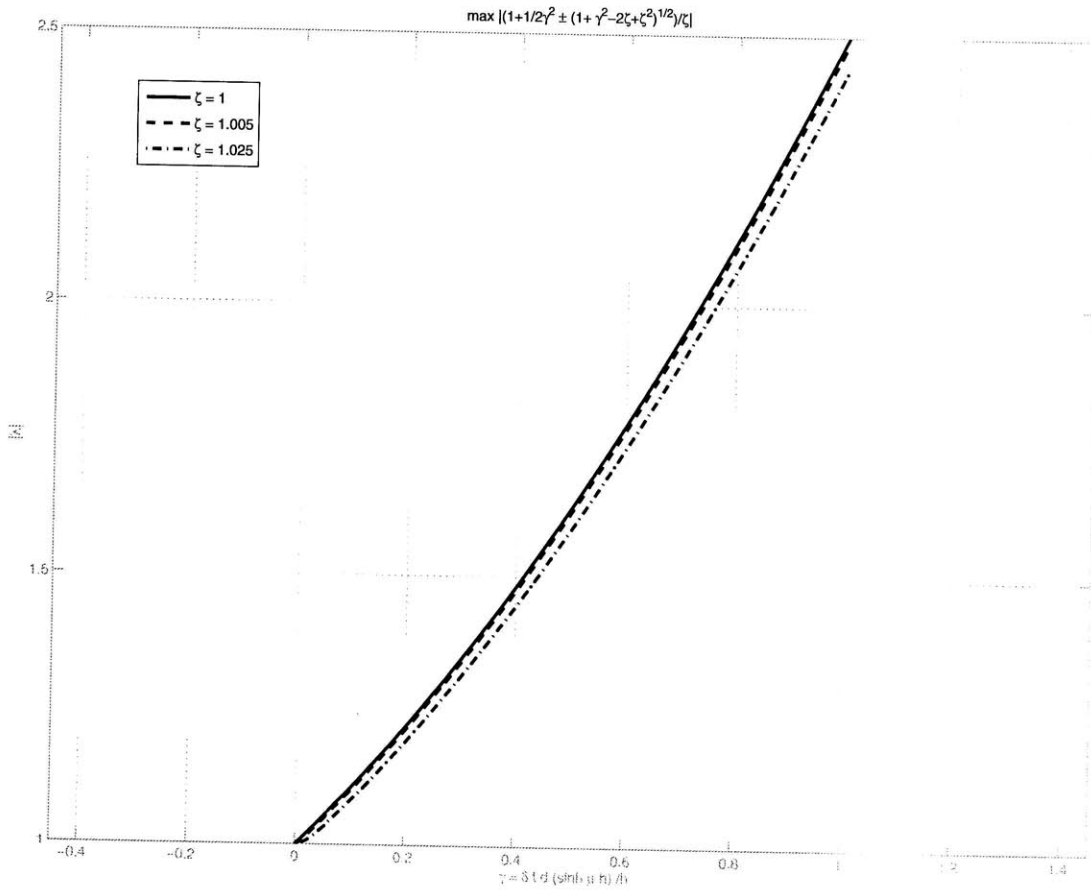


Figure 3-2: Maximum amplitude of the eigenvalues of the amplification matrix  $|\lambda| = \max |\lambda_1, \lambda_2|$  for MA-SPH with ID treatment and modified Predictor-Corrector temporal integration scheme. The amplitude of  $|\lambda|$  is given as function of  $\mu^* = \delta t d \sinh \mu h / h$  for three values of  $\zeta = 1 + 0.5\Gamma\delta t = [1, 1.005, 1.025]$ . Exponential disturbances are assumed.

**Advanced density formulation** Given the values of  $y^n$ ,  $v^n$ , and  $\rho^n$  at time step  $n$  and time step size  $\delta t$ , the evolution equations for the disturbances in the fully-discrete ID scheme are:

1. Predictor step

$$y^{n+p} = y^n + \frac{\delta t}{2} \dot{y}^n \quad (3.40)$$

$$v^{n+p} = \frac{1}{\zeta} \left( v^n + \frac{\delta t}{2} \dot{v}^n \right) \quad (3.41)$$

$$r^{n+p} = r^n + \frac{\delta t}{2} \dot{r}^n \quad (3.42)$$

2. Corrector step

$$y^{n+1} = y^n + \delta t \dot{y}^{n+p} \quad (3.43)$$

$$v^{n+1} = \frac{2}{\zeta} \left( v^n + \frac{\delta t}{2} \dot{v}^{n+p} \right) - v^n \quad (3.44)$$

$$r^{n+1} = r^n + \delta t \dot{r}^{n+p} \quad (3.45)$$

where, again,  $\zeta \equiv 1 + 0.5\Gamma\delta t > 1$ , and  $\Gamma$  is a tunable parameter.

It is noted that the evolution equation for  $y$  can be neglected in the stability analysis for uniform base flow and advanced density formulation. The values of  $\dot{v}$  and  $\dot{r}$  from Table 3.1 are substituted in (3.41), (3.42), (3.44), and (3.45). After some algebra, the amplification matrix  $A_{id,a}$  describing the evolution of the disturbances of the fully-discrete MA-SPH with advanced density formulation and ID treatment in a uniform base density distribution becomes:

$$A_{id,a} = \begin{bmatrix} \frac{2}{\zeta} - 1 + \frac{(\delta t dF)^2}{2\zeta} & -\frac{\delta t d^2 F}{\zeta} \\ -\frac{\delta t F}{\zeta} & 1 + \frac{(\delta t dF)^2}{2\zeta} \end{bmatrix}$$

with  $F$  given by (3.34). The amplitude of the corresponding eigenvalues  $\lambda_{1,2}$  of the amplification matrix  $A_{id,a}$  are:

$$|\lambda_{1,2}| = \left| \frac{1 + \frac{1}{2}(\delta t dF)^2 \pm \sqrt{1 + (\delta t dF)^2 - 2\zeta + \zeta^2}}{\zeta} \right|$$

which are the same with those obtained by the direct density formulation. This is expected, since the two formulations differ inside the domain only in the presence of non-zero base density gradients.

Summarizing, the initial dumping treatment for MA-SPH with both the direct and advanced density formulations in uniform base density distribution (a) increase the Courant condition, for sinusoidal disturbances and (b) reduces the instability growth rates for a given  $\mu_c$ , for exponential disturbances. This result indicates that the method can be regularized numerically through appropriate choice of numerical dumping.

### 3.4.4 Artificial viscosity

In [30] it is suggested that an artificial viscosity term (AV) is added to the right hand side of the momentum equation in which case the momentum equation becomes:

$$\frac{d\vec{u}}{dt} = - \sum_b m_b \left( \frac{P_a}{\rho_a^2} + \frac{P_b}{\rho_b^2} \right) \nabla W_{ab} - g\hat{j} - \underbrace{\sum_b m_b \Pi_{ab} \nabla W_{ab}}_{AV}$$

where

$$\Pi_{ab} = - \left( \frac{2\alpha dh}{\rho_a + \rho_b} \right) \frac{\vec{u}_{ab} \cdot \vec{x}_{ab}}{|\vec{x}_{ab}|^2 + \epsilon h^2} \text{ if } \vec{u}_{ab} \cdot \vec{x}_{ab} < 0; 0 \text{ else.} \quad (3.46)$$

Again, a one-dimensional, uniform particle distribution is considered. A uniform base flow is assumed, i.e.,  $\bar{\Pi}_{ab} = 0$ . Infinitesimal perturbations on the uniform base flow are assumed, described by (3.29). After dropping higher order terms with respect

to the perturbations the linear viscous term for the disturbances becomes:

$$\delta\Pi_{ab} = -\frac{\alpha dh}{\rho_f} \frac{v_{ab}\bar{y}_{ab}}{\bar{y}_{ab}^2} \text{ for } v_{ab}\bar{y}_{ab} < 0 \quad (3.47)$$

To further perform the summations in the KI for this non-continuous artificial viscosity term, the cubic B-Spline is employed and only sinusoidal disturbances are considered, i.e.,  $v = v(t)e^{ik\bar{y}}$ . In this case it is:

$$v_{ab}\bar{y}_{ab} = v_a \underbrace{(1 - e^{ik\bar{y}_{ba}})}_{\geq 0} (a - b)h$$

First, let  $v_a > 0$ . Then  $v_{ab}\bar{y}_{ab} < 0 \rightarrow \delta\Pi_{ab} \neq 0$  only for  $b > a$ . In this case, substituting (3.47) into  $\delta AV$  obtains:

$$\delta AV = -\sum_b m_b \delta\Pi_{ab} W'_{ab} \xrightarrow{b=a+1} -\alpha d \frac{1 - e^{ikh}}{2h} v_a \equiv G^* v_a, \text{ where } G^* < 0$$

Second, let  $v_a < 0$ . Then  $v_{ab}\bar{y}_{ab} < 0 \rightarrow \delta\Pi_{ab} \neq 0$  only for  $b < a$ . In this case, substituting (3.47) into  $\delta AV$  obtains:

$$\delta AV = -\sum_b m_b \delta\Pi_{ab} W'_{ab} \xrightarrow{b=a-1} \alpha d \frac{1 - e^{-ikh}}{2h} v_a \equiv G^{**} v_a, \text{ where } G^{**} > 0.$$

In either case the evolution equation for the velocity perturbations reduces to:

$$\dot{v} = -d^2 F r + G v \quad (3.48)$$

where  $F$  is given by (3.34) and, most importantly,  $\delta AV$  is proportional to  $v$ . This is in general the case, i.e., viscous terms add a quantity proportional to the velocity on the right hand side of the momentum equation. For this reason, in the stability analysis of the fully-discrete schemes it will be assumed that the viscous term is of the general form  $Gv$ . The amplification matrix  $A_{av}$  of the fully-discrete scheme is formulated and the amplitudes of the corresponding eigenvalues are determined with  $G$  as a parameter.

**Direct density formulation** Given the values of  $y^n, v^n$  at time step  $n$ , and time step size  $\delta t$  the evolution equations for the disturbances in the fully-discrete MA-SPH direct density formulation with AV scheme in uniform base density distribution are given by:

1. Predictor step

$$y^{n+p} = y^n + \frac{\delta t}{2} \dot{y}^n \quad (3.49)$$

$$v^{n+p} = v^n + \frac{\delta t}{2} \dot{v}^n \quad (3.50)$$

2. Corrector step

$$y^{n+1} = y^n + \delta t \dot{y}^{n+p} \quad (3.51)$$

$$v^{n+1} = v^n + \frac{\delta t}{2} \dot{v}^{n+p} \quad (3.52)$$

Substituting the values of  $\dot{y}$  and  $\dot{v}$  from Table 3.1 and (3.48) respectively, after some algebra, obtains the amplification matrix  $A_{av}$  of the fully discrete MA-SPH direct density formulation with AV scheme in uniform base density:

$$A_{av} = \begin{bmatrix} 1 + \frac{(\delta t dF)^2}{2} & \delta t \left(1 + \frac{\delta t G}{2}\right) \\ \frac{(\delta t dF)^2}{\delta t} \left(1 + \frac{\delta t G}{2}\right) & 1 + \frac{(\delta t dF)^2}{2} + \delta t G \left(1 + \frac{\delta t G}{2}\right) \end{bmatrix}$$

The amplitudes of the corresponding eigenvalues  $\lambda_{1,2}$  are:

$$|\lambda_{1,2}| = \left| \frac{1 - \frac{1}{2}(\delta t dF)^2 + \frac{1}{2}\bar{G} + \frac{1}{4}\bar{G}^2}{\pm \frac{1}{4}\sqrt{-16(\delta t dF)^2 + 4\bar{G}^2 - 16(\delta t dF)^2\bar{G} - 4(\delta t dF)^2\bar{G}^2 + 4\bar{G}^3 + \bar{G}^4}} \right|$$

where  $\bar{G} = \delta t G$ . It is  $\delta t dF \equiv \frac{\delta t d}{h} f_F(\kappa h) = \mu_c \underbrace{f_F(\kappa h)}_{O(1)}$  and  $\bar{G} = \alpha \frac{\delta t d}{h} f_G(\kappa h) = \alpha \mu_c \underbrace{f_G(\kappa h)}_{O(1)}$  with  $\alpha \ll 1$ . Dropping terms higher than  $\alpha^2$  and noting that the CFL

condition requires  $\mu_c < 1$  the above relation can be approximated by:

$$|\lambda_{1,2}| = \left| 1 - \frac{1}{2}\mu_c^2 \pm i\mu_c + \underbrace{\frac{1}{2}\alpha\mu_c f(e^{\kappa h})}_{AV} \right|$$

Given that  $f(e^{\kappa h}) = \pm \frac{1-e^{\mp i\kappa h}}{2h}$ , the amplitude of the eigenvalues simplifies to:

$$|\lambda_{1,2}|^2 = (1 - \frac{1}{2}\mu_c^2)^2 + \mu_c^2(1 \pm \frac{1}{2}\alpha\kappa)^2 \simeq 1 + \frac{1}{4}\mu_c^4 \pm \alpha\kappa\mu_c^2.$$

Therefore, there is no conclusive effect of the AV on the stability of the scheme.

**Advanced density formulation** Given the values of  $y^n$ ,  $v^n$  at time step  $n$ , and time step size  $\delta t$ . the evolution equations for the disturbances in the fully-discrete MA-SPH advanced density formulation with AV scheme in uniform density distribution are given by:

1. Predictor step

$$v^{n+p} = v^n + \frac{\delta t}{2}\dot{v}^n \quad (3.53)$$

$$r^{n+p} = r^n + \frac{\delta t}{2}\dot{r}^n \quad (3.54)$$

2. Corrector step

$$v^{n+1} = v^n + \delta t\dot{v}^{n+p} \quad (3.55)$$

$$r^{n+1} = r^n + \delta t\dot{r}^{n+p} \quad (3.56)$$

Substituting the values of  $\dot{y}$  and  $\dot{v}$  from Table 3.1 and (3.48) respectively, after some algebra, obtains the amplification matrix  $A_{av,a}$  of the fully discrete MA-SPH advanced density formulation with AV scheme in uniform density distribution:

$$A_{av,a} = \begin{bmatrix} 1 + \frac{(\delta t dF)^2}{2} + \delta t G \left(1 + \frac{\delta t G}{2}\right) & -\frac{(\delta t dF)^2}{\delta t} \left(1 + \frac{\delta t G}{2}\right) \\ -\delta t \left(1 + \frac{\delta t G}{2}\right) & 1 + \frac{(\delta t dF)^2}{2} \end{bmatrix} = A_{av}$$

Therefore, as expected, the advanced density formulation in this case behaves just like the direct density formulation under the assumption of uniform density distribution.

The conclusion is that the particular type of discontinuous artificial viscosity, which is introduced for shock capturing simulations [30], does not seem to have the potential to lead towards a general regularization of SPH.

### 3.4.5 Tensile instability treatment

In [26] it is suggested that negative pressures in the right hand side of the momentum equation are updated by multiplying them with a coefficient of the form  $1 - \epsilon f_{ab}$ , defined as a tensile instability treatment (TI). In particular if  $P_a, P_b < 0$  the momentum equation becomes:

$$\frac{d\vec{u}}{dt} = - \sum_b m_b (1 - \epsilon f_{ab}^n) \left( \frac{P_a}{\rho_a^2} + \frac{P_b}{\rho_b^2} \right) \nabla W_{ab} - g\hat{j}, \quad (3.57)$$

where  $\epsilon \sim O(0.1)$ ,  $n \sim O(4)$  and  $f_{ab} = \frac{W_{ab}}{W(h)}$ . It can be shown, after some algebra, that the evolution equation for the velocity disturbances are re-formulated as:

$$\dot{v} = - \underbrace{(d\sqrt{(1-\epsilon)})^2}_{d^*} Fr \quad (3.58)$$

where the cubic B-Spline has been employed. This means that the correction term simply reduces the effective speed of sound for the velocity perturbations.

Therefore, in the stability point of view the TI slightly reduces the unstable growth rates by reducing the effective speed of sound from  $d$  to  $d^* = d\sqrt{(1-\epsilon)}$  for both the direct and advanced density formulations for the case of uniform density distribution. As a results the instability growth rate has been slightly reduced compared to MA-SPH. In addition to that, the fact that the TI is not continuous (since it is applied only in the negative pressures) helps to ‘detune’ the instability in the domain. In the literature it is noted that the TI does not have any significant effects on the free-surface flows of interest [3, 26]. Therefore, similarly to the discontinuous AV treatment, the TI treatment does not seem to lead towards a general regularization

of SPH.

### 3.4.6 Density re-initialization schemes

In [1, 48] it is suggested that the density field is re-initialized periodically through a relation of the form:

$$\rho_a^* = \sum_b m_b w_{ab} \quad (3.59)$$

where  $m$  denotes particle mass and  $w_{ab}$  is an MLS coefficient of order either 1 or 2.

To perform an analysis of the effects of re-initializing the density with a relation of the form of (3.59), first a one-dimensional domain is assumed. Let  $y < 0$  denote the vertical axis pointing upwards,  $g$  the gravitational acceleration, and  $c$  the speed of sound. The domain is discretized into  $N$  fluid particles. The initial particle distribution is assumed to be uniform with spacing  $dy$ . Let  $W(x; h)$  denote the cubic B-Spline (2.111) with kernel bandwidth  $h = dy$ . Initially, each particle  $a$  is located at  $y_a^0 = ah$ , has density  $\rho_a^0$ , and mass  $m_a = \rho_a^0 h$ , which remains constant in time.

Two cases are distinguished. The first, is that the initial particle density and mass are uniform, i.e.,  $\rho_a^0 = \rho_f$  and  $m_a = \rho_f h$ . The second, is that the initial density and mass are hydrostatic, i.e.,  $\rho_a^0 = \rho_f(1 - 2\delta y_a^0)$  and  $m_a^0 = h\rho_f(1 - 2\delta y_a^0)$ , where  $\delta = \frac{g}{2c^2}$ . This last case is the typical initialization approach in the free-surface flows of interest [3, 30]. A smoothly advected grid is defined, as in section 2.5.3. Following the analysis for the density of smoothly advected particles detailed in sections 2.5.4, a later time  $t$  is assumed such that the particle is located at  $y_a$  and has density  $\rho_a = \rho_a^0(1 - \zeta'_a)$ , where  $\zeta$  is a measure of the velocity gradient.

Next, two separate approaches are distinguished based on the order of the interpolation scheme that appears in (3.59). In the first approach, the scheme employs a first order consistent interpolation and is referred to as smoothed density re-initialization scheme [48]. In the second approach, the scheme employs a second order consistent interpolation and is referred to as hydrostatic density re-initialization scheme [3]. Both schemes are considered for both approaches on the initial particle mass distribution, i.e., uniform and hydrostatic.

### 3.4.6.1 Smoothed density re-initialization scheme

When first order consistent interpolation is used, (3.59) reduces to:

$$\rho_a^* = \frac{\sum_b m_b W_{ab}}{\sum_b \frac{m_b}{\rho_b} W_{ab}} \quad (3.60)$$

First, the particle mass is considered to be uniform  $m_a = m = h\rho_f$  and the density  $\rho_a = \rho_f(1 - \zeta'_a)$ . From (2.152) from section 2.5.5 it is found that  $\sum_b m_b W_{ab} = \rho_a + \frac{h^2}{6}\rho_a''$  and  $\sum_b \frac{m_b}{\rho_b} W_{ab} = 1$ , omitting terms of order  $h^2\zeta^{(3)}, \zeta\zeta'$ . Therefore,

$$\rho_a^* \simeq \rho_a + \frac{h^2}{6}\rho_a'' \quad (3.61)$$

This means that the scheme is not reducing the developed density gradients that are the source of the tensile instability. Any stabilizing effects this scheme has are due to the introduced density dissipation, with a coefficient that depends on the shape of the kernel, the kernel bandwidth  $h$ , and the ratio of the initial particle spacing  $dy$  over  $h$ , i.e.,  $dy/h$ .

Second, the particle mass is considered to be hydrostatic  $m_a = h\rho_f(1 - 2\delta y_a^0)$ . In this case the density becomes  $\rho_a = \rho_f(1 - 2\delta y_a^0 - \zeta'_a)$ , with  $\zeta'_a \ll \delta y_a^0$ . From (2.152) from section 2.5.5, after some algebra, and omitting terms of order  $h^2, \zeta\zeta'$  obtains:

$$\rho_a^* \simeq \rho_a \quad (3.62)$$

Again, the scheme is essentially dissipating the density and not removing existing density gradients, i.e., it has no significant effects on the physics simulated. Finally, it is noted that the dissipation is introduced in a spirit compatible with the nature of SPH, i.e., robust and smooth.

### 3.4.6.2 Hydrostatic density re-initialization schemes

When a second order MLS scheme is employed, the interpolation in (3.59) from the consistent relation (3.5) becomes:

$$\rho_a^* = \frac{m_a}{h} + O(h^2) \quad (3.63)$$

where it is pointed out that  $m_a$  is the initial particle mass, and the particle density has no contribution.

First, the particle mass is considered to be uniform  $m_a = m = h\rho_f$ . In this case,

$$\rho_a^* = \rho_f + O(h^2),$$

i.e., the particle density is re-initialized to its initial uniform distribution. Therefore, the scheme essentially removes all density gradients to leading order. This stabilizes the scheme with respect to the tensile instability but also (a) has a significant effect on the physics: by re-initializing the pressure to a hydrostatic-like distribution, and (b) has only short-term effects on removing any perturbations, since those are re-generated from un-removed perturbations in the velocity field.

Second, the particle mass is considered to be hydrostatic  $m_a = h\rho_f(1 - 2\delta y_a^0)$ . In this case,

$$\rho_a^* = \rho_f(1 - 2\delta y_a^0) + O(h^2),$$

i.e., the particle density is re-initialized based on its initial hydrostatic distribution. The scheme essentially reduces the density gradients but is expected to significantly affect the simulated physics, mainly in the vertical direction.

Therefore, the hydrostatic density re-initialization scheme is shown to have significant implications on the simulated physics and on the numerical behavior of SPH. Desirable implications include: (a) that the pressure near the free-surface is re-initialized to zero if the free-surface particles have remained on the free-surface, i.e., enforces the physical free-surface dynamic boundary condition; and most importantly, (b) the system is stabilized, since as shown in section 2.6.3 the source of the tensile instabil-

ity are the non-zero base flow gradients. Undesirable implications include: (a) that the pressure field through the Equation of State is also re-initialized with either zero pressure, or some hydrostatic-like distribution; (b) that by altering the density the consistency of KI is reduced within the domain as detailed in section 2.5.5; and (c) when only the density is re-initialized the acoustic modes in the density field are immediately re-generated from the un-removed perturbations in the velocity field, i.e., the scheme proposed in [1] obtains images of a smooth pressure field only if the latter are taken right after the re-initialization.

Summarizing, two density re-initialization schemes were considered, the smooth and hydrostatic. The two schemes have significantly different effects. The smooth scheme introduces a small dissipation, while the hydrostatic scheme significantly affects the simulated physics with only short term stabilizing benefits. In considering a regularization scheme for SPH, only the smooth approach is therefore considered.

### 3.5 Conclusions

Selected existing semi-empirical treatments to MA-SPH have been considered. These were classified as accuracy, consistency and stability treatments. Brief analysis was performed on each of the selected treatments within the context of their usage to determine their usefulness and obtain insight towards the generalized improvement of the MA-SPH method. The following Table 3.2 summarizes the classification and findings of the analysis.

Table 3.2: Classification and summary of effects of selected existing semi-empirical treatments to MA-SPH.

Classification	Treatment	Comments
Accuracy (§ 3.2)	Pressure temporal filtering	Local, effective (§ 3.2.1)
	Pressure spatial filtering	Local, ineffective (§ 3.2.2)
Consistency (§ 3.3)	MLS	Higher order, not robust (§ 3.3.1.1)
	Müller	First order, not robust (§ 3.3.1.2)
Stability (§ 3.4)	XSPH	Reduces certain growth rates (§ 3.4.2)
	Artificial viscosity	Ineffective (§ 3.4.4)
	Initial dumping	Removes certain growth rates (§ 3.4.3)
	Tensile instability treatment	Reduces growth rates (§ 3.4.5)
	Smooth density re-initialization scheme	Introduces dissipation (§ 3.4.6.1)
	Hydrostatic density re-initialization scheme	Removes density gradients, affects physics (§ 3.4.6.1)



# Chapter 4

## Rational development of convergent SPH methods

### 4.1 Introduction

The SPH continuous main algorithm (CMA-SPH) assumes a weakly compressible flow. The flow is described by the Euler equation (2.1) for the momentum conservation  $d\vec{u}/dt$  and the mass conservation (2.2) for the density  $\rho$ . Closure is obtained by a constitutive Equation of State (EoS) that relates total pressure  $P$  and density fluctuations rather than solving the Poisson equation that is typical for most numerical simulations of incompressible, rotational flow models. The MA-SPH employs the Kernel Interpolation (KI) technique for the computation of spatial derivatives in discrete space.

Analysis of MA-SPH for free-surface flows in Chapter 2 has elucidated three key issues. First, the weak compressibility assumption permits the development of acoustic modes (section 2.4.1.4). Spurious acoustic modes are developed in the simulations from inconsistent numerical implementations of the initial and boundary conditions, round-off errors, instabilities and higher-order interactions (section 2.4.1.5). Second, the incompleteness of the KI near the free-surface produces a spurious, leading order, dynamic free-surface boundary condition that is a function of the shape of the free-surface (section 2.5.6). Third and most importantly, it is shown that three types of

instabilities may develop in an MA-SPH simulation: (i) inherent, unconditional instabilities of weakly compressible flows in semi-infinite domains with depth decaying profile (section 2.6.2), (ii) tensile instability present in flows with non-zero base density gradients (sections 2.6.2 and 2.6.3), and (iii) instabilities due to the numerical integration scheme that depend on the Courant condition and the base density distribution (section 2.6.4). Given the absence of a conclusive analysis of the method, several semi-empirical treatments have been developed. Analysis in Chapter 3 showed that these treatments can be classified as accuracy (removing spurious acoustic modes), consistency (addressing mainly the implementation of the free-surface boundary conditions) and stability treatments. While the analysis of selected treatments showed that they generally point in the right direction, they do not manage to sufficiently address key MA-SPH issues.

At this point, a note must be made regarding the advantages and disadvantages of KI, the standard MA-SPH approach for the computation of spatial derivatives detailed in section 2.2, versus alternative consistent, derivative computation techniques like MLS, described in section 3.3.1. The key disadvantages of KI are (a) that KI requires the density, which is field variable, to ensure consistency (section 2.5.5), (b) that the error in KI is coupled with the modeling error (section 2.5.5), and (c) that the inconsistent behavior of KI near the boundaries (section 2.5.2.3) imposes a spurious, leading order free-surface boundary condition, detailed in section 2.5.6. The major advantage of the KI technique is that it is robust even in highly non-linear complex flows. In contrast, the key advantages of Moving Least Squares (MLS) are (a) that they do not require any field variable to ensure consistency, (b) that the consistency error is determined and independent of the modeling error, and (c) that the error on the boundaries is of the same order as that within the domain. The major disadvantage of MLS is that for highly non-linear free-surfaces the method becomes singular and eventually fails, i.e., currently MLS is not equally robust with KI. As a consequence, each technique is best suited for different types of applications. KI is best used in highly non-linear, transient problems of short duration, such as the standard SPH dam-break benchmark, where the free-surface becomes highly com-

plex and the effect of the spurious dynamic free-surface boundary conditions is to primarily introduce spurious acoustic modes. Moving Least Squares is best used for problems involving free-surface of lower complexity, where the dynamic free-surface boundary condition significantly alters the solution, such as long-time solutions of plane periodic progressive waves.

As a first step, two different approaches can now be defined, based on the technique used for the computation of spatial derivatives. The first approach is a higher-order SPH (hSPH) scheme, using the artificial compressibility assumption and Moving Least Squares. A new instability removal and flow field re-initialization scheme is introduced that obtains the leading order incompressible solution. The second approach is a modified SPH (mSPH) scheme, based on the existing MA-SPH, that retains both the weak compressibility assumption and KI, removing all existing treatments. New, rational formulations are introduced that reduce the generation of spurious modes on the boundaries and numerically dissipate them.

These schemes are the rational outcome of the analysis on MA-SPH performed in Chapter 2, and the insight obtained from the analysis of the existing treatments in Chapter 3. The hSPH scheme is of higher-order and dissipative, but is currently limited to periodic domains. The mSPH scheme is first order, retains the simplicity and robustness of SPH, allows for larger time steps than SPH, removes the existing tuneable SPH parameters, and most importantly is dissipative.

Finally, a global, *a posteriori* error metric is defined to measure the stability of the simulation and is thus used as an appropriate indicator of the validity of the results.

## 4.2 A higher-order hSPH scheme with Moving Least Squares

The complete analysis of MA-SPH performed in Chapter 2, along with the insight obtained from the analysis of the existing treatments in Chapter 3, allowed the suggestion of a higher-order SPH (hSPH) scheme that (i) eliminates the density variable, (ii) projects the solution to an incompressible flow field, (iii) maintains the same consistency properties in the domain and on the boundaries, and most importantly (iv) is stable. However, currently hSPH can be used for the simulations of flows where the free-surface is not highly non-linear.

The hSPH starts from CMA-SPH, retaining the weak compressibility assumption and reformulates the governing equation to eliminate the density. It is realized that the weak compressibility assumption will introduce an acceptable error of order  $O(1/c^2)$ , where  $c$  is the artificial speed of sound, along with spurious acoustic modes linearly dependent on  $c$ . Given that hSPH is to be employed in periodic or fixed domains, the spurious, unstable depth decaying modes described in section 2.6.2 will be generated from inconsistent initial and boundary conditions and numerical noise, eventually dominate the flow and terminate the simulation.

The first step in hSPH is to minimize the generation of the spurious modes by removing inconsistencies between the governing equations and the boundary conditions. This is achieved by (i) linearizing the artificial Equation of State, (ii) reformulating the governing equations to capture the incompressible hydrostatic pressure, (iii) correcting the boundary conditions to account for hydrostatic pressure differences when mirroring the particles along the sea-bed (section 2.2.3), and (iv) increasing the consistency of the computation of the spatial derivatives on the free-surface with MLS. The dynamic free-surface boundary condition is imposed periodically through a periodic flow field re-initialization scheme.

The second step is to impose a periodic flow field re-initialization scheme. This scheme accomplishes two things: it removes the dominant depth-decaying unstable modes and it projects to an incompressible flow field. Numerical examples validate

hSPH, for the first time, for plane progressive waves with varying wave slopes and show convergence to the analytic solution.

### 4.2.1 Governing Equations

In section 2.4.1.2 it was shown that the CMA-SPH system of  $(\vec{u}, \rho, P)$  can be reduced to a simplified equivalent system of  $(\vec{u}, P)$ . If a consistent spatial differentiation scheme is employed, such as MLS described in section 3.3.1, then the numerical need for the inclusion of the density is removed and a reduced system of  $(\vec{u}, P)$  can be solved for. The resulting algorithm is not only more efficient (in that it eliminates one variable) but it is also conceptually clearer: the Lagrangian particles are advected by the Euler equations, an artificial equation is used for the pressure, and the fluid density is constant. The resulting algorithm is a non-iterative formulation of the well-established artificial compressibility method [10, 12, 22, 23].

This section first proposes the usage of a higher-order SPH (hSPH) algorithm that considers as variables only velocity and pressure. In hSPH the time rate of the velocity is computed through the incompressible Euler equation (4.19) and the time rate of pressure is computed from the mass conservation, where the time rate of density is substituted from the EoS. All density terms appearing in the governing equations are treated as constant and equal to the undisturbed fluid density  $\rho_f$ . Second, this section shows that the hSPH algorithm differs from CMA-SPH only in second order terms with respect to density fluctuations, which are typically even smaller than numerical differentiation errors (i.e.,  $O(\delta^2)$  vs.  $O(h^2)$ ), and therefore retains the  $O(\delta)$  consistency to the incompressible problem just as CMA-SPH. It is again noted that the scheme in discrete space must be coupled with a technique such as MLS for the computation of spatial derivatives.

Assume a two-dimensional Cartesian coordinate system  $\vec{x} = [x, y]$  and a two-dimensional fluid domain. Let  $c$  denote the speed of sound in the fluid,  $\rho_f$  the density of the undisturbed fluid, and  $-g\hat{j}$  the gravitational acceleration pointing downwards. Define  $\delta = \frac{g}{2c^2}$ . Let  $t > 0$  denote time and  $\vec{u}(\vec{x}, t)$ ,  $P(\vec{x}, t)$  denote the fluid velocity and pressure respectively. The hSPH weakly compressible flow in the above domain

is described by:

$$\frac{d\vec{u}}{dt} = -\nabla P^* - g\hat{j} \quad (4.1)$$

$$\frac{dP^*}{dt} = -c^2 \nabla \cdot \vec{u}, \quad (4.2)$$

where  $P^* = P/\rho_f$ . Equation (4.2) results from substituting the density rate of change appearing in the left hand side of the conservation of mass (4.36) with the linearized EoS (4.21) and the variable density  $\rho$  appearing on the right hand side with the constant density  $\rho_f$ . Alternatively, (4.2) can be viewed as an EoS that relates pressure changes to the velocity divergence.

Next, it is shown that hSPH and CMA-SPH are consistent up to leading order with respect to the density fluctuations, and therefore hSPH retains the  $O(\delta)$  consistency with the desired incompressible model. To prove this statement in the above two-dimensional fluid domain, let  $\rho(\vec{x}, t)$  denote the fluid density. Denoting with the subscripts  $c$  and  $h$  the equations describing the CMA-SPH and hSPH formulations respectively, the governing equations of the CMA-SPH are:

$$\frac{d\vec{u}_c}{dt} = -\frac{1}{\rho} \nabla P - g\hat{j} \quad (4.3)$$

$$\frac{d\rho_c}{dt} = -\rho \nabla \cdot \vec{u}. \quad (4.4)$$

Furthermore, define  $\rho \equiv \rho_f(1 + \varrho)$  where  $\varrho$  are the density fluctuations. By the weak compressibility assumption it is  $\varrho \ll 1$ . Substituting into the momentum equation (4.3) and employing the linearized EoS (4.21) obtains:

$$\begin{aligned} \frac{d\vec{u}_c}{dt} &= -\frac{1}{\rho_f(1 + \varrho)} c^2 \rho_f \nabla \varrho - g\hat{j} \\ &= -c^2 \frac{\nabla \varrho}{1 + \varrho} - g\hat{j}. \end{aligned} \quad (4.5)$$

By Taylor Series Expansion about  $\varrho \ll 1$ , it is  $(1 + \varrho)^{-1} \simeq 1 - \varrho$ , and therefore, the

momentum equation is approximated by:

$$\begin{aligned}
\frac{d\vec{u}_c}{dt} &= -c^2\nabla\varrho(1-\varrho) - g\hat{j} + O(\varrho^3) \\
&= -c^2\nabla\varrho - g\hat{j} + c^2\varrho\nabla\varrho + O(\varrho^3) \xrightarrow{\nabla P=c^2\rho_f\nabla\varrho} \\
&= -\frac{\nabla P}{\rho_f} - g\hat{j} + \frac{1}{2}\nabla\varrho^2 + O(\varrho^3) \\
&= \underbrace{-\frac{\nabla P}{\rho_f} - g\hat{j}}_{\frac{d\vec{u}_h}{dt}} + O(\varrho^2)
\end{aligned} \tag{4.6}$$

Substituting the EoS into the CMA-SPH conservation of mass (4.20) obtains:

$$\begin{aligned}
\frac{1}{c^2} \frac{dP_c}{dt} &= -\rho_f(1+\varrho) \overbrace{\nabla \cdot \vec{u}}^{O(\varrho)} = -\rho_f \nabla \cdot \vec{u} - \rho_f \varrho \nabla \cdot \vec{u} \rightarrow \\
\frac{dP_c}{dt} &= \underbrace{-c^2\rho_f \nabla \cdot \vec{u}}_{\rho_f \frac{dP^*}{dt}} - c^2\rho_f \varrho \underbrace{\nabla \cdot \vec{u}}_{O(\varrho^2)}.
\end{aligned} \tag{4.7}$$

Recalling that  $P^* = P/\rho_f$ , the schemes CMA-SPH and hSPH are shown to be consistent up to  $O(\varrho^2)$ . Therefore, hSPH remains consistent up to order  $O(\varrho)$  with the incompressible flow model.

Alternatively, the above result can be shown by letting  $\rho = \rho_f(1+\varrho)$  and observing that:

$$\begin{aligned}
dP &= c^2 d\rho = c^2 \rho_f d(1+\varrho) \rightarrow \\
\frac{\nabla P}{\rho} &= \frac{c^2 \rho_f \nabla(1+\varrho)}{\rho_f(1+\varrho)} = c^2 \nabla \ln(1+\varrho)
\end{aligned}$$

and

$$\frac{1}{\rho} \frac{d\rho}{dt} = \frac{1}{1+\varrho} \frac{d(1+\varrho)}{dt} = \frac{d \ln(1+\varrho)}{dt}.$$

Letting  $R = \ln(1 + \varrho)$  and substituting into (4.3) and (4.4) yields

$$\frac{d\vec{u}}{dt} = -c^2 \nabla R - g\hat{j} \quad (4.8)$$

$$\frac{dR}{dt} = -\nabla \cdot \vec{u}. \quad (4.9)$$

However it is,

$$\begin{aligned} dR &= d\ln(1 + \varrho) = \frac{d\varrho}{1 + \varrho} \xrightarrow{dP=c^2\rho_f d\varrho} \\ &= \frac{dP}{c^2\rho_f} \frac{1}{1 + \varrho} \xrightarrow{\text{TSE}} \\ dR &= \frac{dP}{c^2\rho_f} (1 - \varrho) = \frac{dP}{c^2\rho_f} - \underbrace{\varrho \frac{dP}{c^2\rho_f}}_{O(\varrho)}. \end{aligned} \quad (4.10)$$

Therefore, substituting  $dR$  with  $dP$  from the above, in (4.8) and (4.9) yields:

$$\frac{d\vec{u}}{dt} = -c^2 \frac{\nabla P}{\rho_f} - g\hat{j} + c^2 \underbrace{\varrho \frac{dP}{c^2\rho_f}}_{O(\varrho^2)} = -c^2 \nabla P^* - g\hat{j} + O(\varrho^2) \quad (4.11)$$

$$\frac{dP^*}{dt} = -c^2 \nabla \cdot \vec{u} + \frac{dP^*}{dt} \underbrace{\varrho \nabla \cdot \vec{u}}_{O(\varrho^2)} = c^2 \nabla \cdot \vec{u} + O(\varrho^2). \quad (4.12)$$

Finally, substituting  $\vec{u} = \nabla\Phi$  into (4.1) and (4.2), eliminating the pressure and linearizing similarly to [46], leads to the familiar governing equation for (2.21). In summary, hSPH is consistent to leading order to CMA-SPH, but is both conceptually and numerically simpler. However, hSPH can be discretized only with a method like MLS, and therefore is expected to be of higher-order than mSPH but less robust.

## 4.2.2 Spatial discretization

The spatial discretization employed in hSPH is the same as in MA-SPH, i.e., the evolution of a set of discrete fluid particles is followed in time. The flow is discretized into  $N \gg 1$  fluid particles with an average initial spacing  $O(h)$  that carry their own constant mass  $m_a$ , and field properties such as pressure  $P_a(t)$ , and velocity  $\vec{u}_a(t)$ .

MLS is employed for the computation of the spatial derivatives. MLS has known consistency behavior but is less robust than Kernel Interpolation, thus limiting the applications of hSPH to flows with smoother free-surface geometries.

For robustness the order of the MLS is chosen to be one, i.e., the basis function is  $[1, x, y]^T$ . The method is known to fail when there is insufficient number of neighbors, and thus  $A$  becomes singular. As a rule of thumb, the minimum number of neighbors  $N_{MLS}$  required in each direction is the same as the order of MLS. Therefore, if particle  $a$  has more neighbors than  $N_{MLS}$  then  $\hat{\nabla} P_a$  and  $\hat{\nabla} \cdot \vec{u}$  are computed using 1<sup>st</sup> order MLS. Otherwise, it is assumed that the particle is a free-surface particle and it is assumed that  $\hat{\nabla} P_a = 0$  and  $P_a = 0$ . In the numerical examples a value of  $N_{MLS} = 2$  was used. Evidently, both the criterion for the singularity of MLS as well as the value of  $N_{MLS}$  involve tuning. For example, the determinant or eigenvalues of  $A$  [47] could have been considered.

The MLS weights, are given by a unit hat function of compact support  $\alpha h$ . Small  $\alpha$  is sufficient but can reduce the number of neighbors below  $N_{MLS}$ . In the numerical examples a value of  $\alpha = 3$  was used. The MLS coefficients for particle  $a$ ,  $w_a$ , are obtained from a system of the form  $A w_a = q_1$ , as described in section 3.3.1, where, as suggested in [35], the matrix  $A$  is not inverted; instead, the coefficients  $w_a = A^{-1} q_1$  are computed by solving  $A w_a = q_1$ . Once the MLS coefficients  $w_a$  have been determined the pressure gradient and the velocity divergence are obtained from:

$$\nabla P_a = \sum_b P_b w_{a,b} \quad (4.13)$$

$$\nabla \cdot \vec{u}_a = \sum_b \vec{u}_b \cdot w_{a,b}. \quad (4.14)$$

When the hSPH approach is followed, the equations of motion for each particle  $a$

become:

$$\begin{aligned}\frac{d\vec{x}_a}{dt} &= \vec{u}_a \\ \frac{d\vec{u}_a}{dt} &= -\sum_b P_b^* w_{a,b} - \vec{g}\end{aligned}\quad (4.15)$$

$$\frac{dP_a^*}{dt} = -c^2 \sum_b \vec{u}_b \cdot w_{a,b}, \quad (4.16)$$

where  $P^* = P/\rho_f$ .

The boundary conditions and temporal integration scheme in hSPH are the same as those employed in mSPH, discussed in sections 4.3.3 and 4.3.5, respectively. The initial conditions for hSPH are simply the velocity and pressure of an incompressible, irrotational flow field. No information on the mass or density of the particles is required.

### 4.2.3 Regularization

All three MA-SPH, mSPH, and hSPH algorithms are inherently unstable, since they maintain the weak compressibility assumption. The unstable modes are either depth decaying, with growth rates of  $O(c)$ , or acoustic, with significantly smaller growth rates. The most crucial point is to realize that, as detailed in section 2.6.2, the dominant instabilities in the domains of application of hSPH are uniform in the horizontal direction, depth decaying modes.

Three approaches were considered, the first two were unsuccessful. The first unsuccessful approach involved varying the speed of sound and the kernel bandwidth in a random manner to de-tune the instability, extending the ideas of [43]. The reason that this form of regularization is not sufficient in hSPH is that, unlike the geophysical problems presented in [43], in the Lagrangian hydrodynamic simulations both the free-surface and particle distribution are varying significantly in time. The second unsuccessful approach involved imposing a zero pressure dynamic free-surface boundary condition, on particles initially on the free-surface. This approach significantly delayed the appearance and initial amplitude of the instability, but as expected does

not stabilize the method as it has no effects on the governing equations. The third successful approach was to periodically map the domain in a uniform grid and simply subtract the length averaged flow quantities at each depth. The effectiveness of the method was verified in the simulation of plane progressive waves.

Once the dominant instability has been removed, the entire flow field is re-initialized based on the modal decomposition described in section 2.4.3. The horizontal Fourier modes of the velocity components are computed at each depth and the field is reconstructed from filtering the incompressible components of those modes from the reconstruction equation (2.103).

Two re-initialization criteria were considered: the first involved a random, fixed re-initialization, while the second examined the growth rate of the global vertical velocity  $V(t) = \sum_{\mathcal{V}} v d\mathcal{V}$ . The field was re-initialized when  $V(t) \geq \alpha kA$ .

#### 4.2.4 Non-dimensionalization

The following scales are introduced:

$$\begin{aligned}(\vec{x}, h) &= L(\vec{x}', h') \\ \vec{u} &= \sqrt{gL}\vec{u}' \\ P &= \rho_f g L P' \\ \rho &= \rho_f \rho' \\ t &= \sqrt{\frac{L}{g}} t'\end{aligned}$$

where  $L$  is a problem dependent characteristic domain dimension,  $g$  the gravitational acceleration,  $\rho_f$  the undisturbed fluid density, and  $h$  the average initial particle spacing. The non-dimensional form of the governing equations reduces to:

$$\frac{d\vec{u}'}{dt'} = -\nabla' P' - \hat{j} \quad (4.17)$$

$$\frac{dP'}{dt'} = -\beta \nabla' \cdot \vec{u}'. \quad (4.18)$$

The non-dimensional parameter  $\beta$  is defined as  $\beta = \frac{c^2}{gL} = \frac{1}{2\delta L}$ , where by assumption it is  $\beta \ll 1$ . Finally, the numerical time step becomes:

$$\delta t = \mu \frac{h}{c} \rightarrow \delta t' = \mu \frac{h'}{\sqrt{\beta}}$$

where  $\mu = 1$  is the Courant condition.

#### 4.2.5 Numerical simulations of deep-water Airy waves with hSPH

The hSPH method is validated for deep-water plane progressive gravity waves of varying steepness. Figures 4-2, 4-3 and 4-5 compare the kinematics and dynamics of hSPH with and without periodic re-initialization every 15 time steps. Figures 4-7, 4-9 and 4-10 validate the kinematics and dynamics of hSPH, re-constructed when  $\int_{\mathcal{V}} v \geq \frac{kA}{20\pi}$ . Figures 4-11 - 4-15 demonstrate convergence with respect to  $h$  for the velocities, pressure and accelerations. Finally, Figures 4-16 and 4-17 show the free-surface elevation for waves of steepness  $kA = [0.006, 0.25]$  respectively.

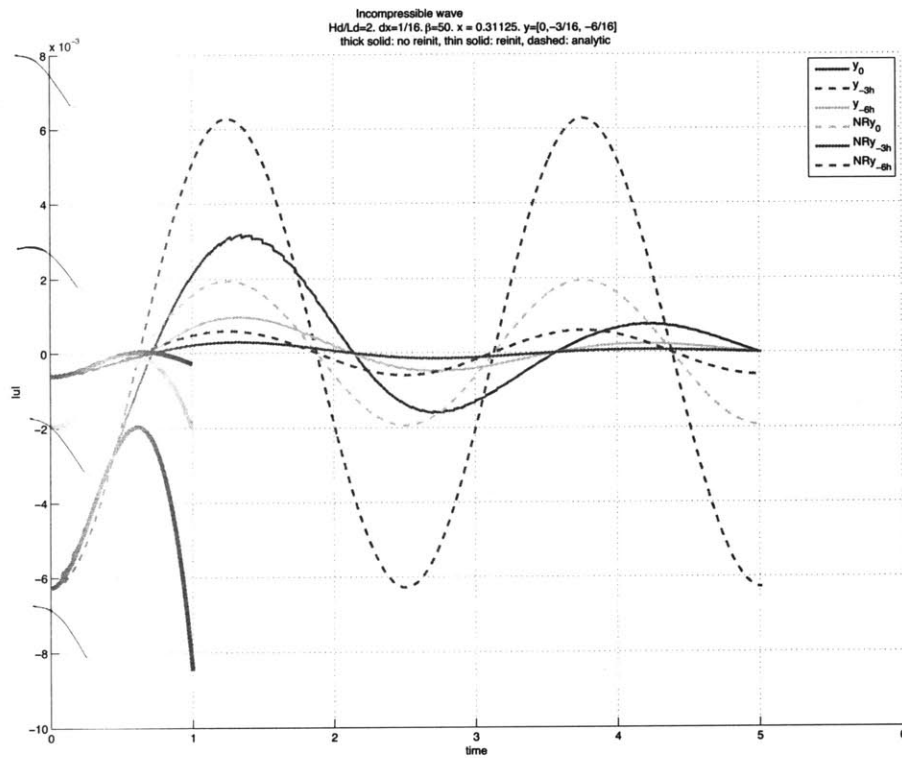


Figure 4-1: Horizontal velocity at depths  $[0, -h]$  for  $h = 1/16$ . Dashed line theory, thin solid line hSPH method with re-initialization with instability removal and flow field reconstruction every 15 time steps, thick solid line hSPH without re-initialization.

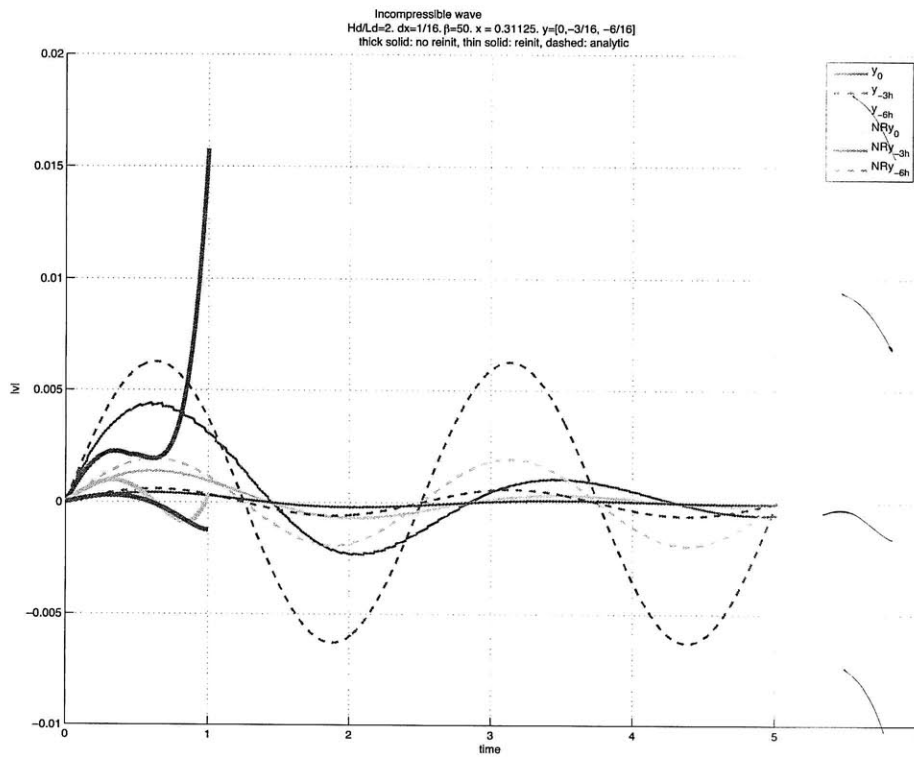


Figure 4-2: Vertical velocity at depths  $[0, -h]$  for  $h = 1/16$ . Dashed line theory, thin solid line hSPH method with re-initialization with instability removal and flow field reconstruction every 15 time steps, thick solid line hSPH without instability removal.

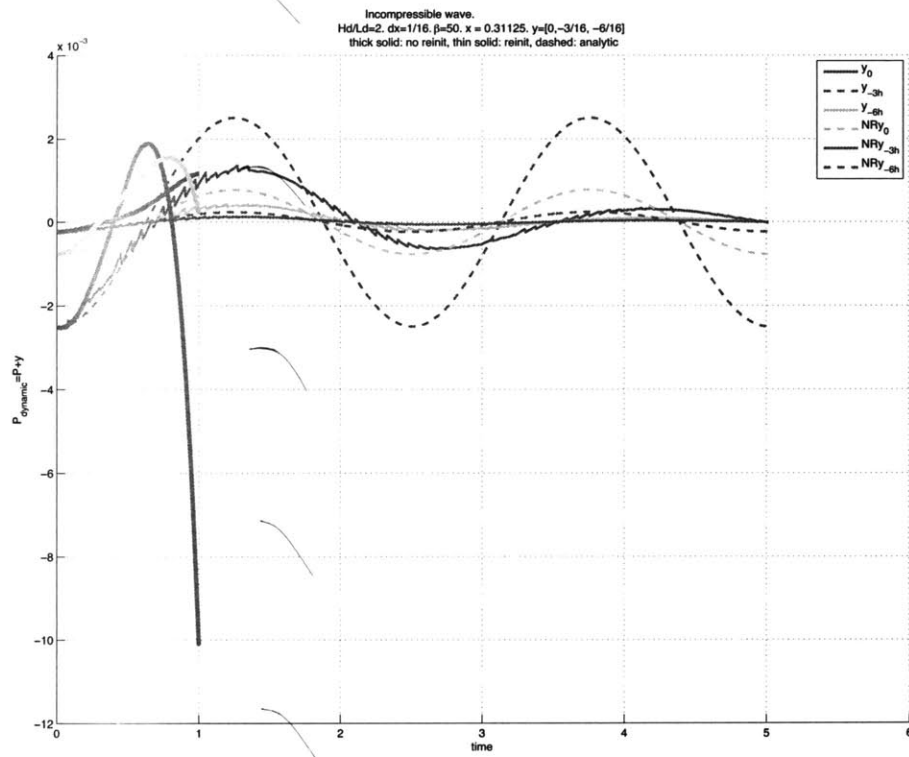


Figure 4-3: Pressure at depths  $[0, -h]$  for  $h = 1/16$ . Dashed line theory, thin solid line hSPH method with re-initialization with instability removal and flow field reconstruction every 15 time steps, thick solid line hSPH without instability removal.

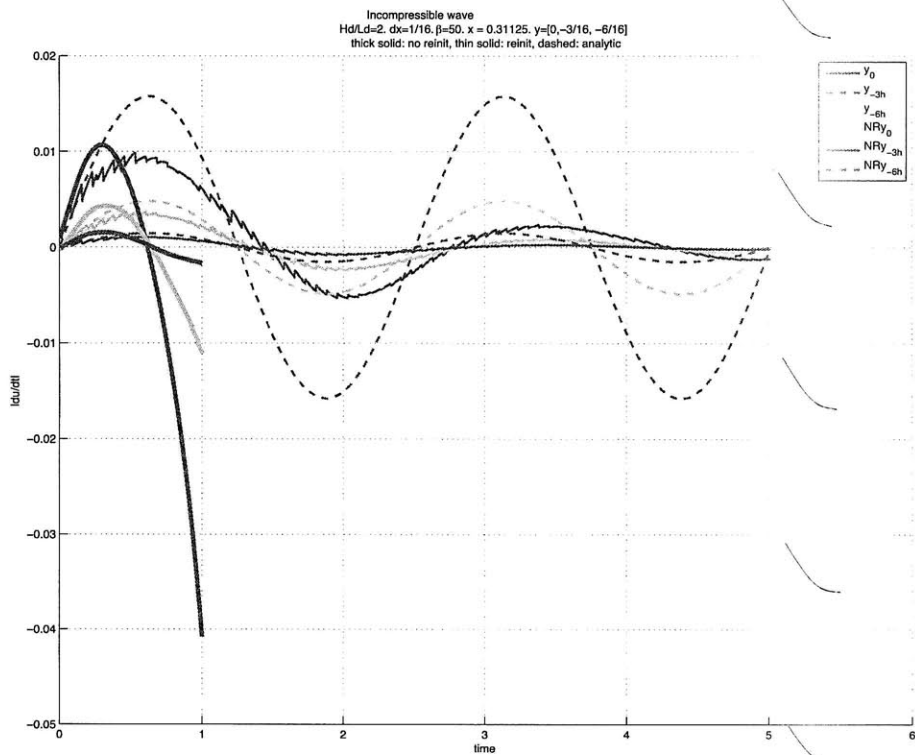


Figure 4-4: Horizontal accelerations at depths  $[0, -h]$  for  $h = 1/16$ . Dashed line theory, thin solid line hSPH method with re-initialization with instability removal and flow field reconstruction every 15 time steps, thick solid line hSPH without instability removal.

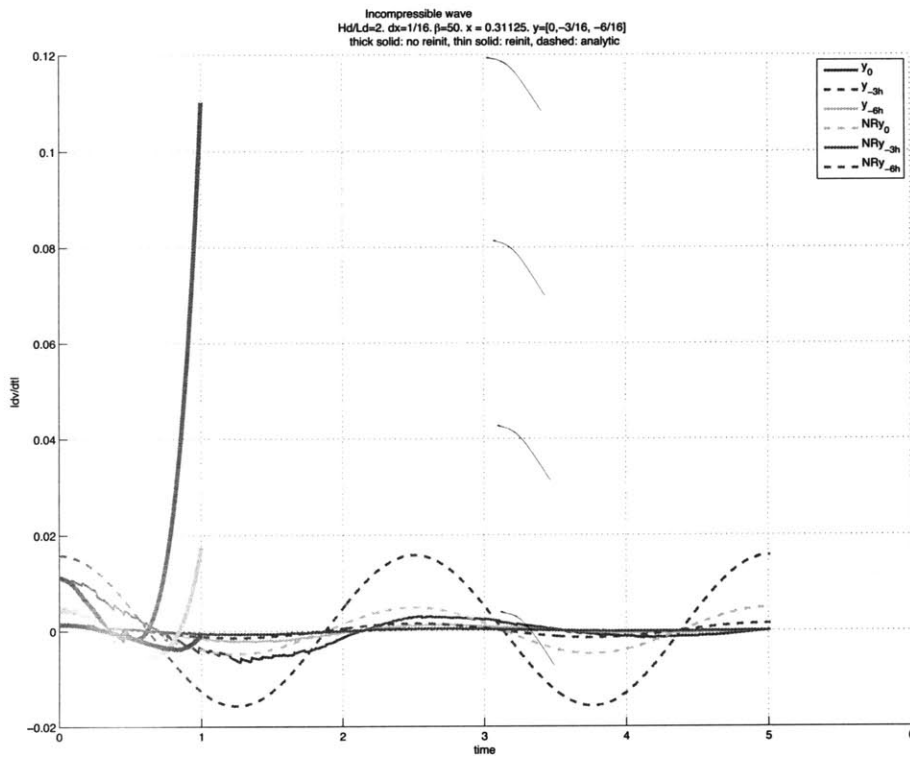


Figure 4-5: Vertical accelerations at depths  $[0, -h]$  for  $h = 1/16$ . Dashed line theory, thin solid line hSPH method with re-initialization with instability removal and flow field reconstruction every 15 time steps, thick solid hSPH without instability removal.

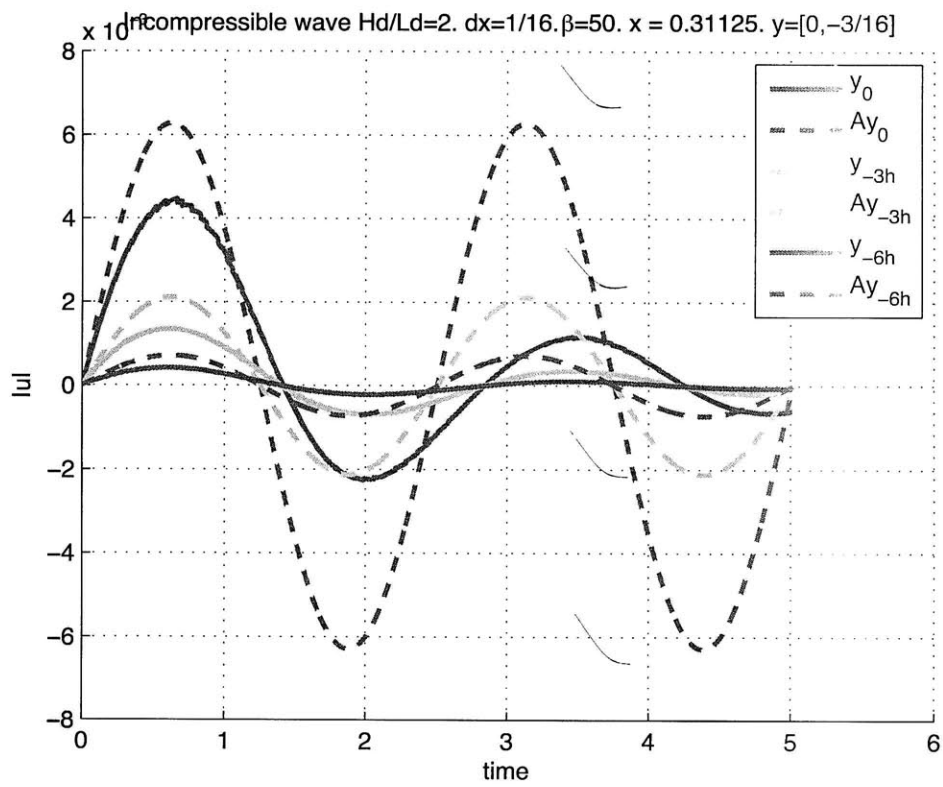


Figure 4-6: Horizontal velocity at depths  $[0, -3h, -6h]$  for  $h = 1/16$ . Dashed line theory, solid line hSPH method with re-initialization with instability removal and flow field reconstruction when  $\int_{\mathcal{V}} v \geq a_{\ell}/10$ .

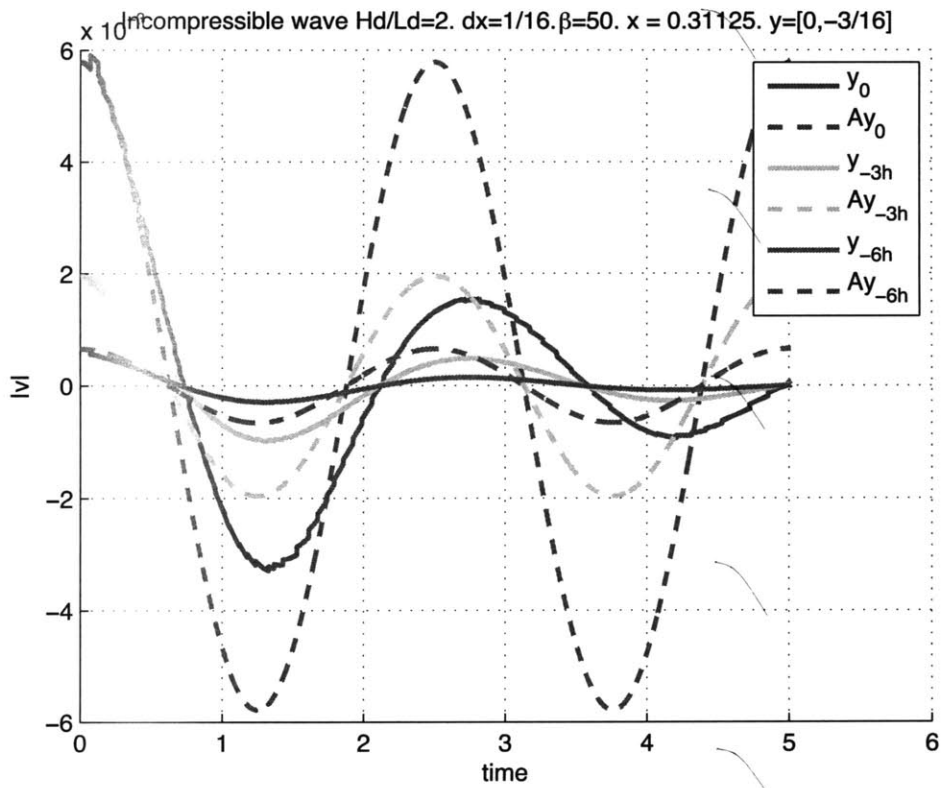


Figure 4-7: Vertical velocity at depths  $[0, -3h, -6h]$  for  $h = 1/16$ . Dashed line theory, solid line hSPH method with re-initialization with instability removal and flow field reconstruction when  $\int_V v \geq a_\epsilon/10$ .

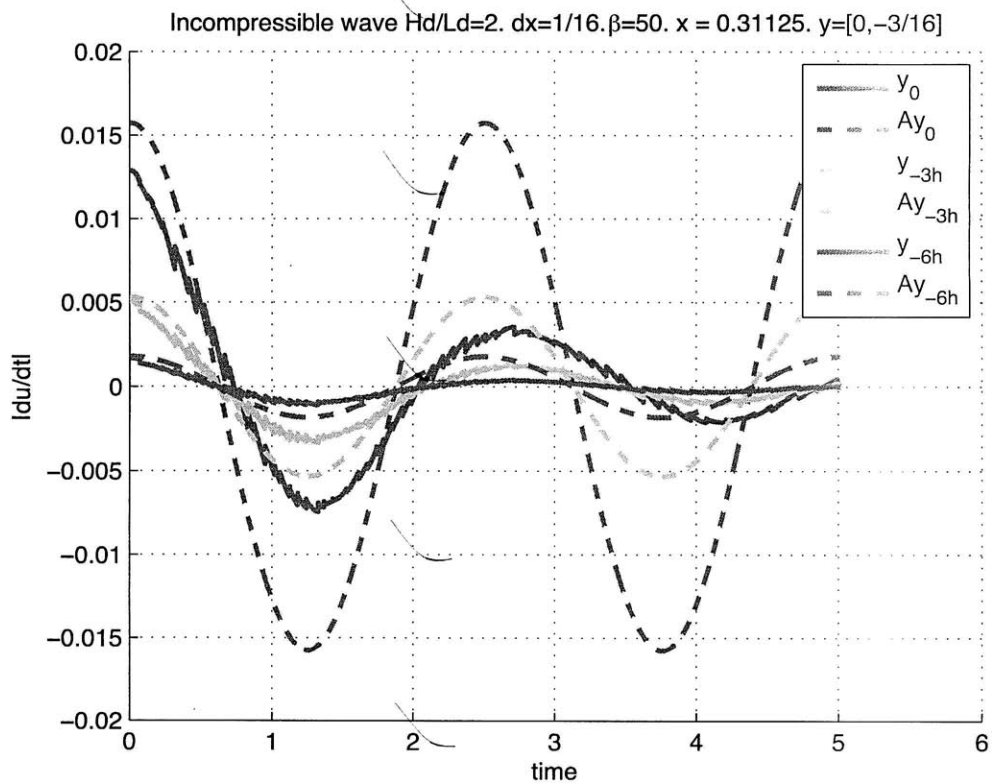


Figure 4-8: Horizontal accelerations at depths  $[0, -3h, -6h]$  for  $h = 1/16$ . Dashed line theory, solid line hSPH method with re-initialization with instability removal and flow field reconstruction when  $\int_V v \geq a_\ell/10$ .

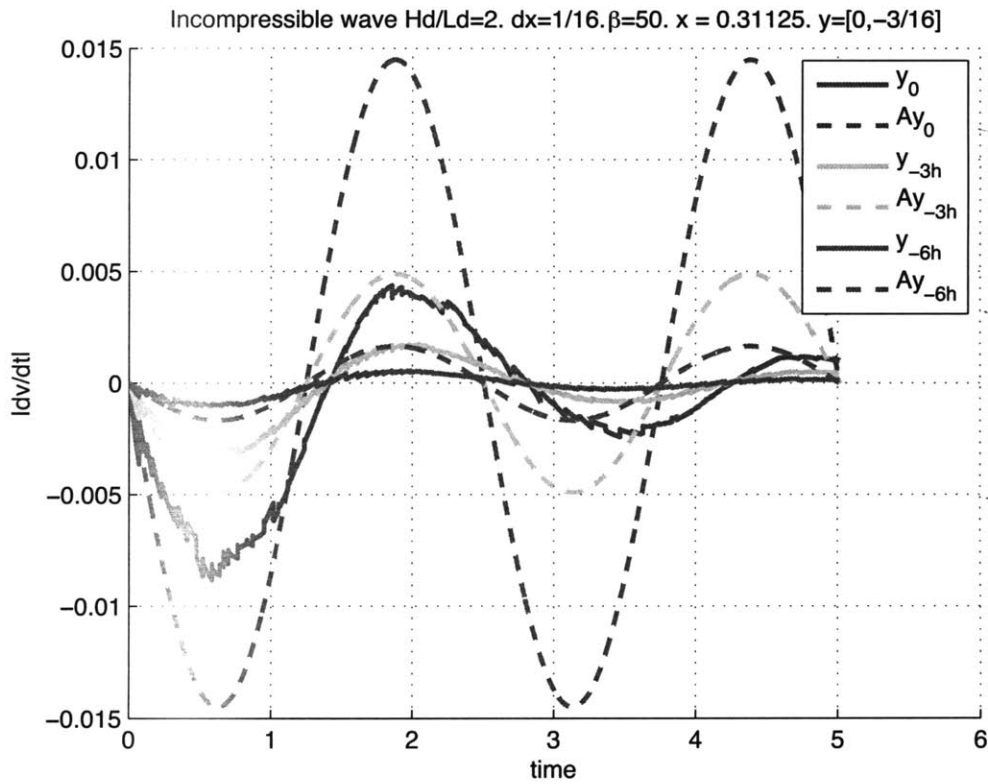


Figure 4-9: Vertical accelerations at depths  $[0, -3h, -6h]$  for  $h = 1/16$ . Dashed line theory, solid line hSPH method with re-initialization with instability removal and flow field reconstruction when  $\int_{\mathcal{V}} v \geq a_{\epsilon}/10$ .

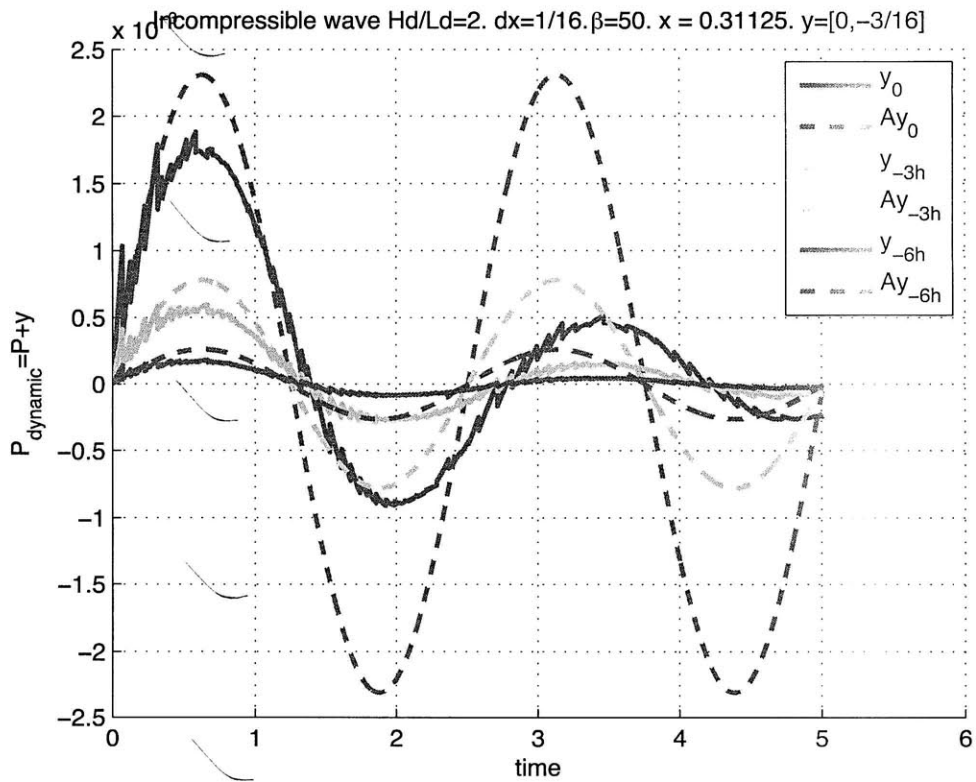


Figure 4-10: Time rate of pressure change at depths  $[0, -3h, -6h]$  for  $h = 1/16$ . Dashed line theory, solid line hSPH method with re-initialization with instability removal and flow field reconstruction when  $\int_{\mathcal{V}} v \geq a_{\ell}/10$ .

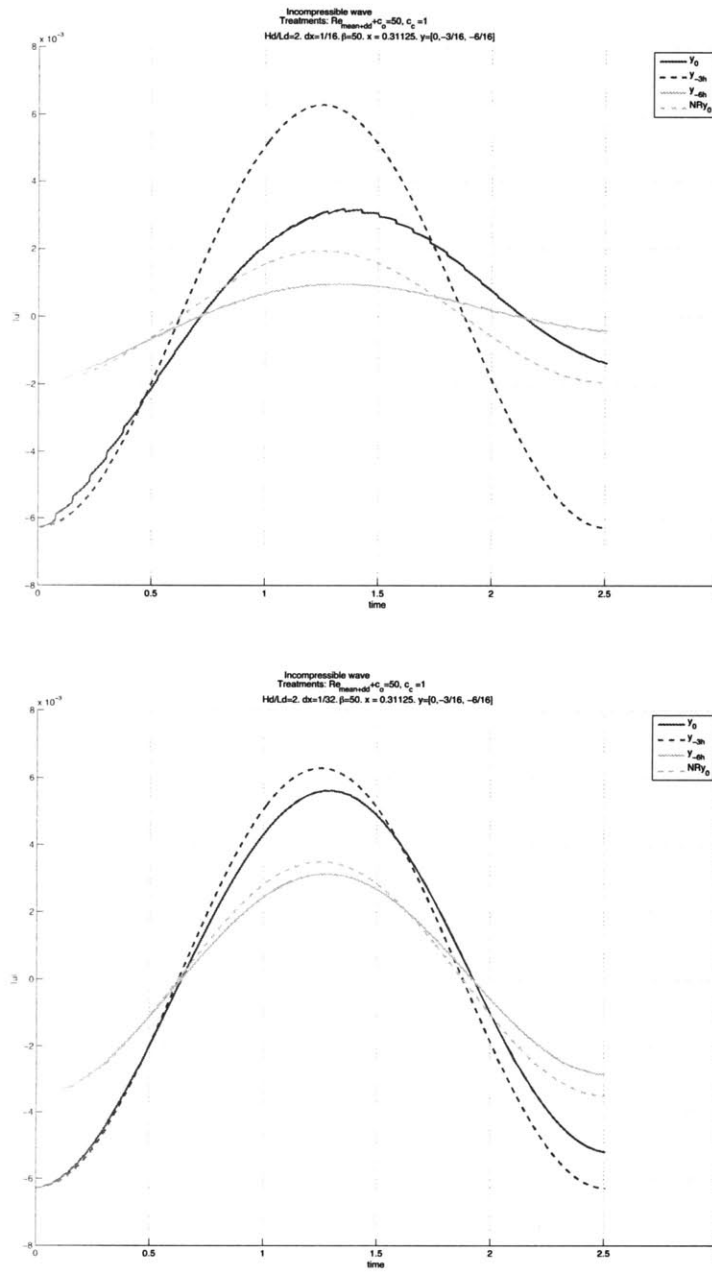


Figure 4-11: Simulation of an Airy wave with hSPH method with re-initialization with instability removal and flow field reconstruction every 15 time steps. Horizontal velocity at depths  $[0, -h]$  for  $h = 1/16$  (top) and  $h = 1/32$  (bottom).

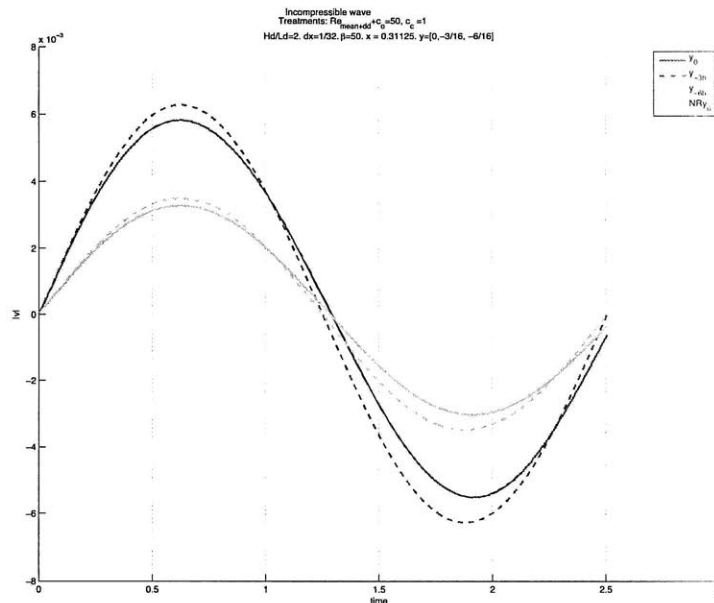
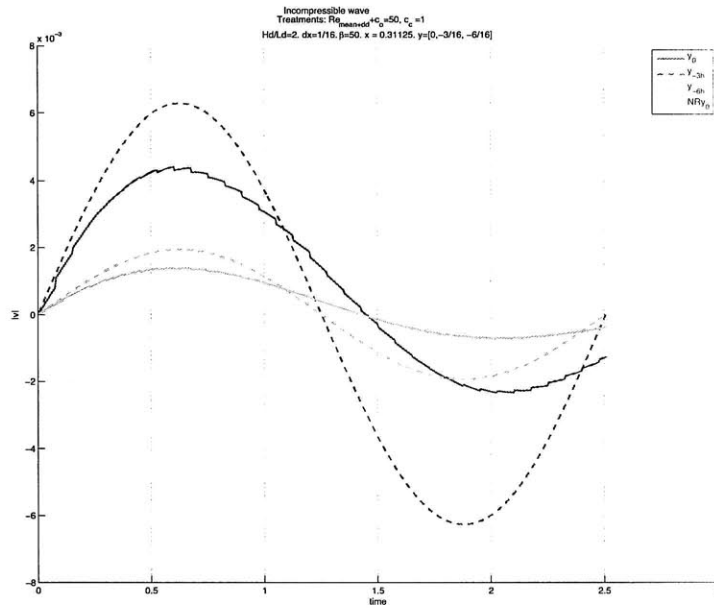


Figure 4-12: Simulation of an Airy wave with hSPH method with re-initialization with instability removal and flow field reconstruction every 15 time steps. Vertical velocity at depths  $[0, -h]$  for  $h = 1/16$  (top) and  $h = 1/32$  (bottom).

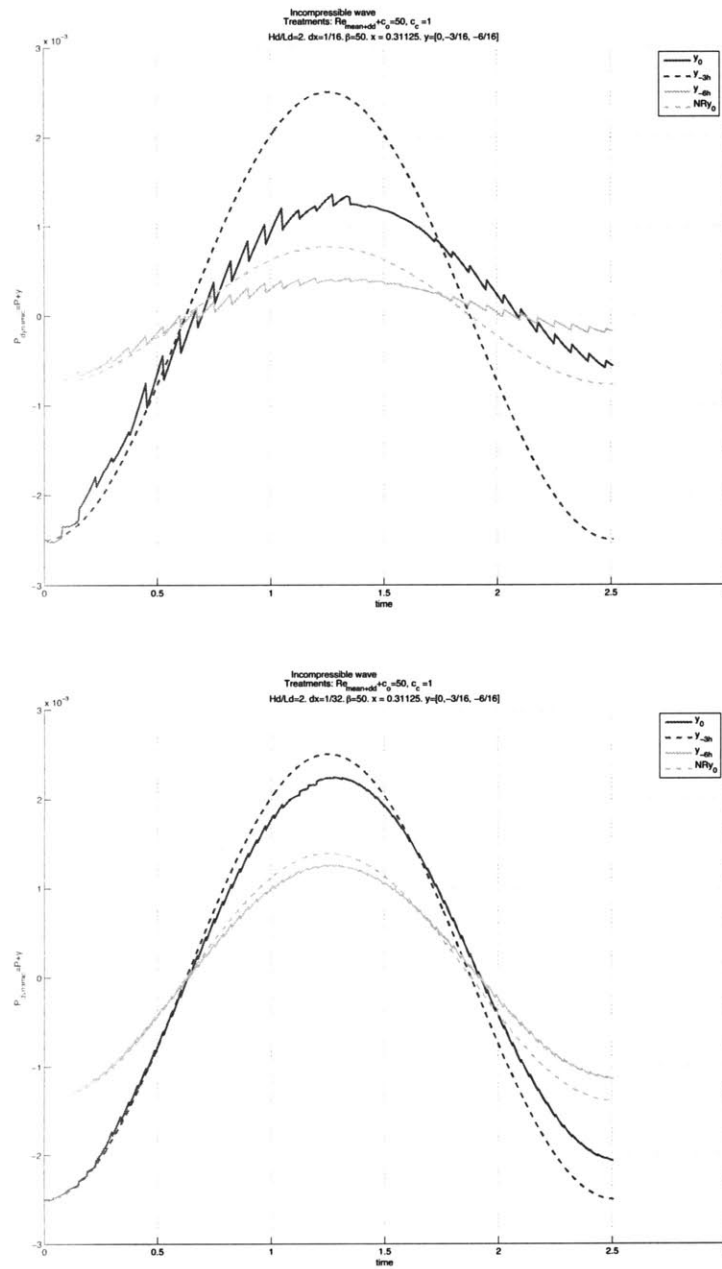


Figure 4-13: Simulation of an Airy wave with hSPH method with re-initialization with instability removal and flow field reconstruction every 15 time steps. Dynamic pressure at depths  $[0, -h]$  for  $h = 1/16$  (top) and  $h = 1/32$  (bottom).

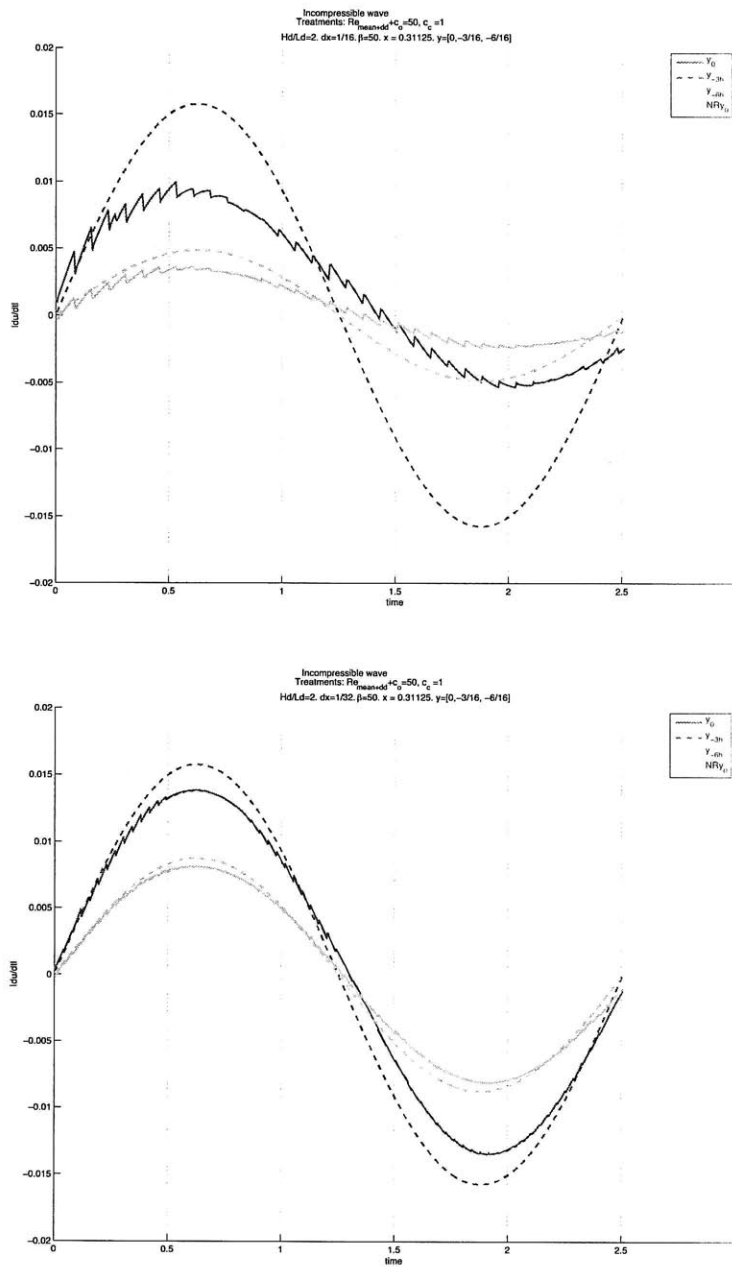


Figure 4-14: Simulation of an Airy wave with hSPH method with re-initialization with instability removal and flow field reconstruction every 15 time steps. Horizontal acceleration at depths  $[0, -h]$  for  $h = 1/16$  (top) and  $h = 1/32$  (bottom).

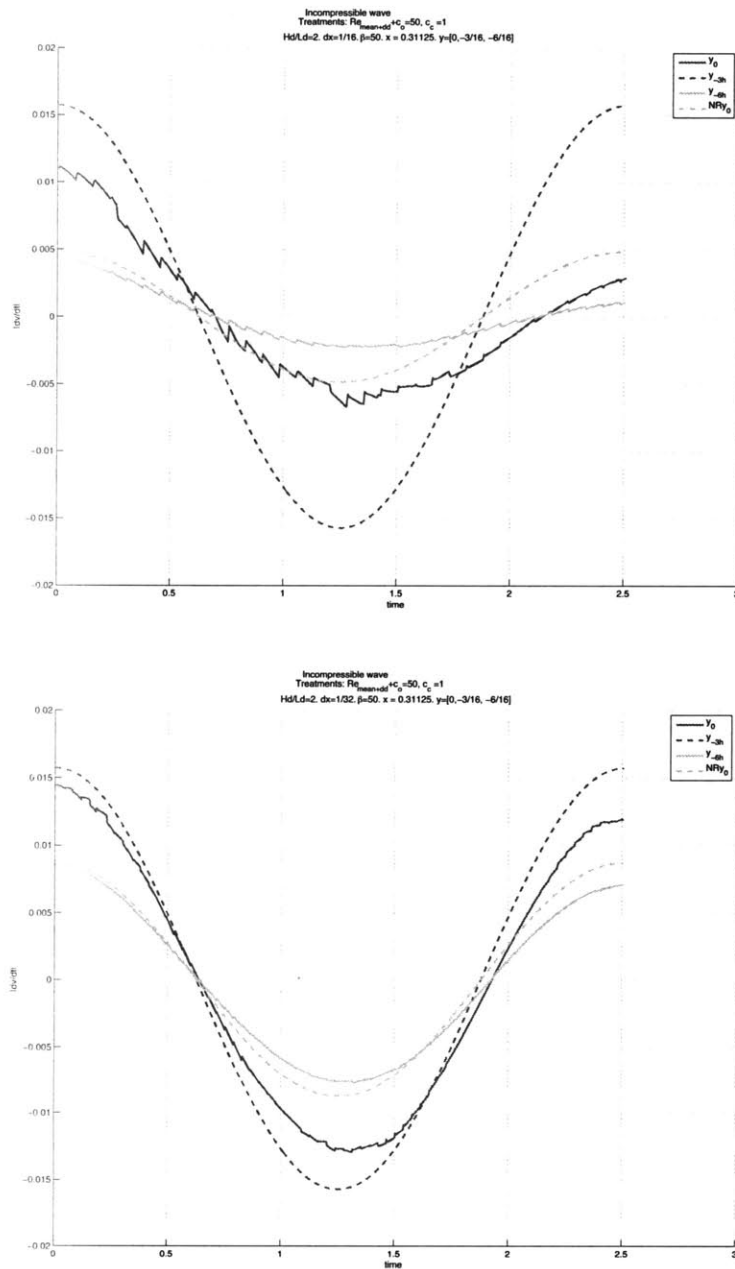


Figure 4-15: Simulation of an Airy wave with hSPH method with re-initialization with instability removal and flow field reconstruction every 15 time steps. Vertical acceleration at depths  $[0, -h]$  for  $h = 1/16$  (top) and  $h = 1/32$  (bottom).

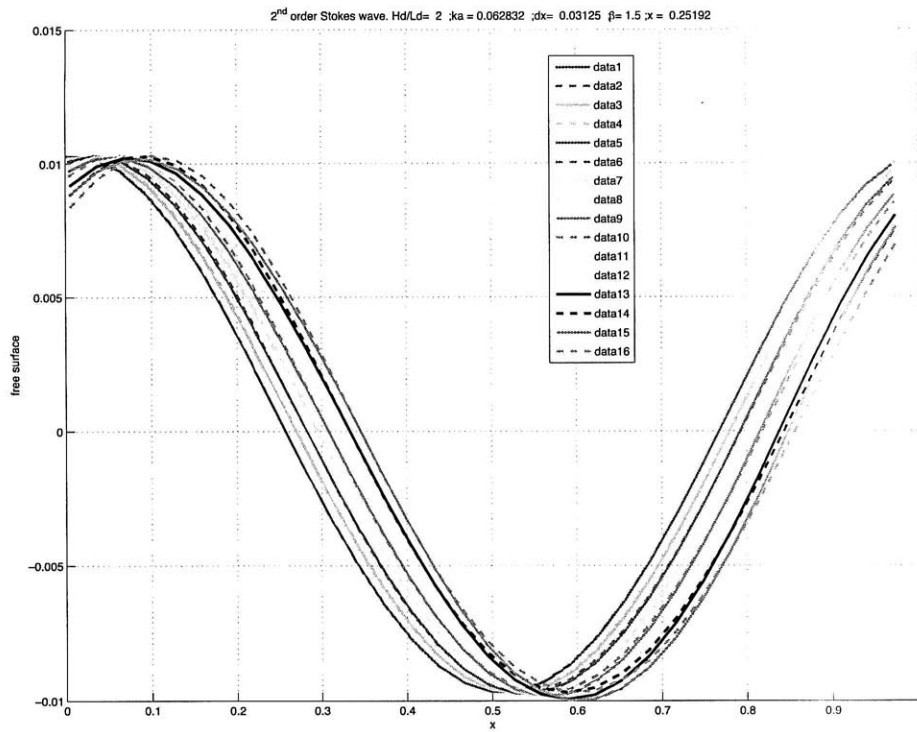


Figure 4-16: Free-surface evolution of a plane progressive wave with steepness  $kA = 0.06$ . comparison between linear theory (solid line) and hSPH method with re-initialization with instability removal and flow field reconstruction every 15 time steps (dashed line).

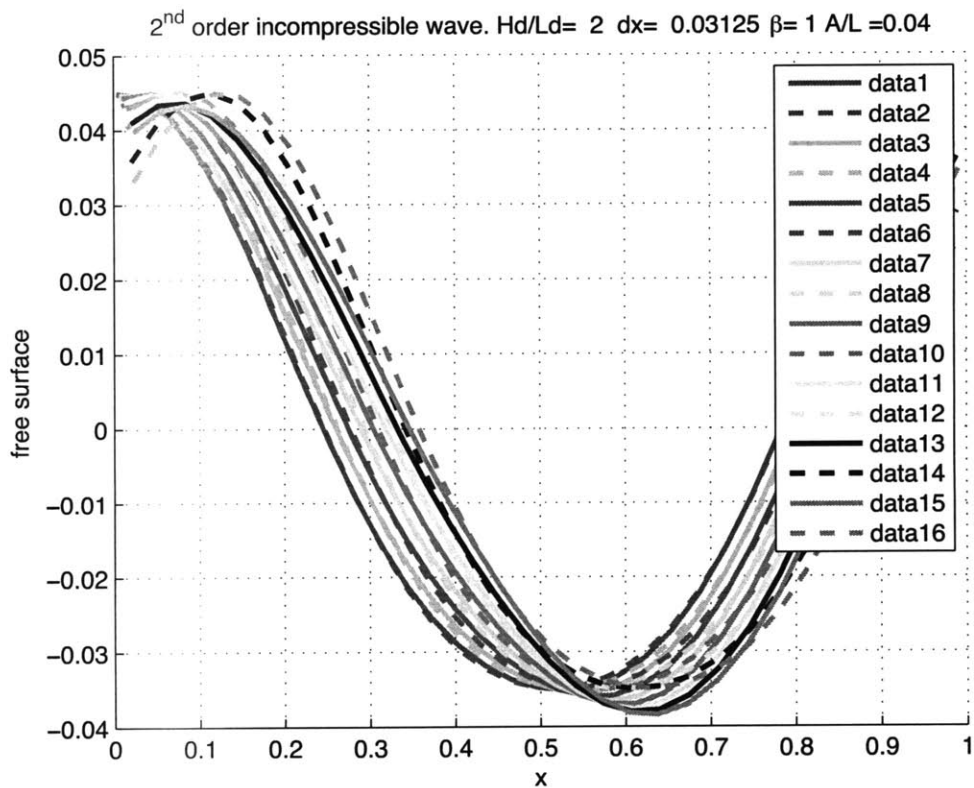


Figure 4-17: Free-surface evolution of a plane progressive wave with steepness  $kA = 0.25$ . comparison between linear theory (solid line) and hSPH method with re-initialization with instability removal and flow field reconstruction every 15 time steps (dashed line).

### 4.3 A stable modified SPH, mSPH, scheme with Kernel Interpolation

The complete analysis of MA-SPH performed in Chapter 2, along with the insight obtained from the analysis of the existing treatments in Chapter 3, allowed the suggestion of a modified SPH scheme that (i) retains the simplicity and robustness of SPH, (ii) allows for larger time steps than SPH, (iii) removes the existing tuneable SPH parameters, and most importantly (iv) is stable with known convergence properties.

The modified SPH scheme (mSPH) starts from MA-SPH, retaining the weak compressibility assumption. It is realized that the weak compressibility assumption will introduce an acceptable error of order  $O(1/c^2)$ , where  $c$  is the artificial speed of sound, along with spurious acoustic modes linearly dependent on  $c$ . The acoustic modes are generated predominantly by inconsistent initial and boundary conditions and secondarily by numerical noise. In SPH, these modes eventually dominate the dynamics, due to numerical instabilities.

The first step in mSPH is to minimize the generation of the acoustic modes by removing inconsistencies between the governing equations and the boundary conditions. This is achieved by (i) linearizing the artificial Equation of State, (ii) reformulating the governing equations to capture the incompressible hydrostatic pressure, and (iii) correcting the boundary conditions to account for hydrostatic pressure differences when mirroring the particles along the sea-bed (section 2.2.3). It is pointed out that no consistency treatment is introduced to remove the artificial dynamic free-surface boundary condition discussed in section 2.5.6.

The second step is to enforce the invaluable stability, realizing that the form of the dominant instability is problem dependent. Within the context of mSPH, for the flows of interest, the dominant unstable modes are purely oscillatory due to the base hydrostatic density distribution. These modes are generated predominantly near the free-surface from the incomplete Kernel Interpolation. We suggest and verify their removal employing a higher-order temporal integration scheme coupled with a periodic smoothing of the entire flow field, introducing known dissipation.

### 4.3.1 Governing Equations

The continuous governing equations in mSPH are the incompressible Euler equation for the momentum and the conservation of mass for the density:

$$\frac{d\vec{u}}{dt} = -\frac{1}{\rho_f} \nabla P - \vec{g} \quad (4.19)$$

$$\frac{d\rho}{dt} = -\rho \nabla \cdot \vec{u}. \quad (4.20)$$

Closure is obtained by a linear, artificial Equation of State for the computation of the pressure  $P$ :

$$dP = c^2 d\rho. \quad (4.21)$$

The rationale in formulating the governing equations in mSPH has as follows: starting from CMA-SPH, we linearize the Equation of State and then modify the momentum equation to model the incompressible hydrostatic distribution. Finally, an additional dynamic pressure formulation is suggested.

**Equation of State** Typical SPH simulations employ a Tait Equation of State of the form  $P = \frac{c^2}{\gamma} \rho_f \left[ \left( \frac{\rho}{\rho_f} \right)^\gamma - 1 \right]$ , where  $\gamma$  is the compressibility ratio, with typical value  $\gamma = 7$  and  $\rho_f$  the undisturbed fluid density. As shown in section 2.2.1, this EoS is equivalent to leading order, with respect to density fluctuations, to the linear EoS (4.21). To reduce the artificial higher-order effects introduced from an already artificial EoS, the linear formulation (4.21) is always employed in mSPH.

**Momentum equation** The momentum equation in SPH is the typical compressible Euler equation:

$$\frac{d\vec{u}}{dt} = -\frac{1}{\rho} \nabla P - \vec{g}, \quad (4.22)$$

where the density appearing in the right hand side is variable and satisfies the conservation of mass. Letting  $\rho_h(y)$  denote a hydrostatic density distribution, the hydro-

static pressure  $P_h(y)$  is defined so that it satisfies:

$$-\frac{1}{\rho_h} \frac{dP_h}{dy} - g = 0. \quad (4.23)$$

Therefore, for the MA-SPH weakly compressible flow, the hydrostatic pressure profile will depend on the form of the EoS. In particular for the linear EoS, substituting  $dP_h = c^2 d\rho_h$  obtains:

$$\frac{d \ln \rho_h}{dy} = -\frac{g}{c^2} \int_{-y}^0 \rho_h = \rho_f e^{-gy/c^2}. \quad (4.24)$$

Letting  $\delta = \frac{g}{2c^2}$ , and by Taylor Series Expansion about  $\delta = 0$ , this hydrostatic density distribution is approximately

$$\rho_h = \rho_f(1 - 2\delta y) + O(\delta^2), \quad (4.25)$$

while the hydrostatic pressure distribution becomes:

$$P_h = \rho_f c^2 (e^{-2\delta y} - 1) = -\rho_f g y (1 - \delta y) + O(\delta^2). \quad (4.26)$$

Alternatively, if the momentum equation was the incompressible Euler equation (4.19), where the density appearing in the right hand side is constant and given by the unperturbed fluid density, the hydrostatic pressure does not depend on the choice of the EoS, and is given by the incompressible hydrostatic distribution:

$$P_h = -\rho_f g y. \quad (4.27)$$

However, the density dependence on the EoS remains. For the linear EoS (4.21) the hydrostatic density distribution is:

$$\rho_h = \rho_f(1 - 2\delta y). \quad (4.28)$$

Furthermore, it is shown that (4.22) and (4.19) are consistent up to  $O(\delta^2)$ , which

is the order of consistency of CMA-SPH with the incompressible model, section 2.4. Assume a two-dimensional fluid domain and let  $\rho(\vec{x}, t) = \rho_f(1 + \varrho(\vec{x}, t))$  denote the fluid density. By the weak compressibility assumption it is  $\varrho \ll 1$ . Denoting with the subscripts  $c$  and  $m$  the momentum equations (4.22) and (4.19) of CMA-SPH and mSPH respectively, Equation (4.22) becomes:

$$\begin{aligned} \frac{d\vec{u}_c}{dt} &= -\frac{1}{\rho_f(1+\varrho)}\nabla P - g\hat{j} \xrightarrow{\text{EoS}} \\ &= -\frac{1}{\rho_f(1+\varrho)}c^2\rho_f\nabla\varrho - g\hat{j} \\ &= -c^2\frac{\nabla\varrho}{1+\varrho} - g\hat{j}. \end{aligned} \quad (4.29)$$

By Taylor Series Expansion of the term  $(1 + \varrho)^{-1}$  about  $\varrho = 0$  and substituting again the EoS, obtains:

$$\begin{aligned} \frac{d\vec{u}_c}{dt} &= -c^2\nabla\varrho(1-\varrho) - g\hat{j} + O(\varrho^3) \\ &= -c^2\nabla\varrho - g\hat{j} + c^2\varrho\nabla\varrho + O(\varrho^3) \xrightarrow{\text{EoS}} \\ &= -\frac{\nabla P}{\rho_f} - g\hat{j} + \frac{1}{2}\nabla\varrho^2 + O(\varrho^3) \\ &= \underbrace{-\frac{\nabla P}{\rho_f} - g\hat{j} + O(\varrho^2)}_{\frac{d\vec{u}_m}{dt}} \rightarrow \end{aligned} \quad (4.30)$$

$$\frac{d\vec{u}_c}{dt} = \frac{d\vec{u}_m}{dt} + O(\varrho^2) \quad (4.31)$$

The two formulations of the Euler equation are thus equal to leading-order with respect to density fluctuations. Therefore, to avoid artificial higher-order effects and to get the hydrostatic pressure equal to the incompressible solution, mSPH employs the incompressible Euler equation (4.19).

In summary, the governing equations for mSPH are the incompressible Euler momentum equation (4.19) and the conservation of mass (4.20). The pressure is obtained by a linear EoS (4.21).

**Dynamic pressure formulation** Alternatively, a dynamic pressure formulation is suggested, which so far has only been validated for the simulation of a hydrostatic case. It is noted that even though such validation seems trivial, MA-SPH cannot be used for the simulation of a hydrostatic case for a long time because of the inherent instabilities in the method (section 2.6.5).

First, the total pressure is decomposed into a dynamic and hydrostatic component:

$$P = P_d + P_h = P_d - \rho_f g y. \quad (4.32)$$

Substituting (4.32) into the Euler equation (4.19) obtains:

$$\frac{d\vec{u}}{dt} = -\frac{1}{\rho_f} \nabla P_d. \quad (4.33)$$

Similarly, the EoS is reformulated in terms of the dynamic pressure:

$$\begin{aligned} dP &= c^2 d\rho \rightarrow \\ dP_d + dP_h &= c^2 d\rho \rightarrow \\ dP_d &= c^2 d\rho + \rho_f g dy. \end{aligned} \quad (4.34)$$

Putting everything together, the mSPH dynamic pressure formulation reads:

$$\frac{d\vec{u}}{dt} = -\frac{1}{\rho_f} \nabla P_d \quad (4.35)$$

$$\frac{d\rho}{dt} = -\rho \nabla \cdot \vec{u}. \quad (4.36)$$

with the dynamic pressure obtained from (4.34).

Lastly, a discussion on the choice of the artificial speed of sound  $c$ . As shown in section 2.4.1.3, accuracy with respect to the desired incompressible requires choosing a large speed of sound  $c$ . Inversely, efficiency, stability (section 2.6.2) and accuracy with respect to the spurious acoustic modes (section 2.4.1.4) require smaller values of  $c$ . Provided that the method is appropriately stabilized and the spurious acoustic

modes are removed, the choice of the speed of sound is based on balancing between efficiency and accuracy requirements, which set a lower acceptable limit on  $c$ . This lower limit is determined as the minimum value of  $c > \max(10U, c_o)$ , where  $U = |\vec{u}_a(t)|_{\max}$  to ensure subsonic behavior and  $\delta_o = \frac{g}{2c_o^2}$  that satisfies  $\delta_o H < 1 + \frac{2\delta_o^2}{\kappa^2 - \delta_o^2}$  to ensure a single incompressible-like solution, section 2.4.1.3.

### 4.3.2 Spatial discretization

The spatial discretization employed in mSPH is the same as in MA-SPH, i.e., the evolution of a set of discrete fluid particles is followed in time. The flow is discretized into  $N \gg 1$  fluid particles with an average initial spacing  $O(h)$  that carry their own constant mass  $m_a$ , and field properties such as density  $\rho_a(t)$ , pressure  $P_a(t)$ , and velocity  $\vec{u}_a(t)$ .

In order to evolve the governing equations (4.19) and (4.20) in time, the pressure gradient  $\nabla P|_a$  and the velocity divergence  $\nabla \cdot \vec{u}|_a$  need to be obtained on the location of each Lagrangian particle (collocation point). This is achieved without any underlying grid, using Kernel Interpolation. Letting  $W(\vec{x}; h)$  denote the cubic B-Spline (2.111), it is:

$$\nabla P_a = \sum_b P_b \frac{m_b}{\rho_b} \nabla W_{ba} = \sum_b (P_a + P_b) \frac{m_b}{\rho_b} \nabla W_{ba} \quad (4.37)$$

$$\nabla \cdot \vec{u}_a = \sum_b \frac{m_b}{\rho_b} \vec{u}_b \cdot \nabla W_{ba} = \sum_b \frac{m_b}{\rho_b} (\vec{u}_b - \vec{u}_a) \cdot \nabla W_{ba}, \quad (4.38)$$

where the relations  $\sum_b \frac{m_b}{\rho_b} P_a \nabla W_{ba} = 0(h^2)$ , and  $\sum_b \frac{m_b}{\rho_b} \vec{u}_a \cdot \nabla W_{ba} = 0(h^2)$ , from section 2.5.5 have been used.

When the standard SPH approach is followed, the equations of motion for each

particle  $a$  become

$$\frac{d\vec{x}_a}{dt} = \vec{u}_a \quad (4.39)$$

$$\frac{d\vec{u}_a}{dt} = -\frac{1}{\rho_f} \sum_b (P_a + P_b) \frac{m_b}{\rho_b} \nabla W_{ba} - \vec{g} \quad (4.40)$$

$$\frac{d\rho_a}{dt} = \rho_a \sum_b \frac{m_b}{\rho_b} (\vec{u}_a - \vec{u}_b) \cdot \nabla W_{ba}, \quad (4.41)$$

with the pressure given by the linearized EoS (4.21).

It is noted that the inclusion of the terms  $P_a$ , and  $\vec{u}_a$  in momentum equations and mass equations respectively, affects mainly the implementation of the free-surface dynamics boundary condition. As discussed in section 2.5.6, Kernel Interpolation implicitly imposes a leading order spurious dynamic free-surface boundary condition, such that  $\frac{d\vec{u}_{fs}}{dt} = -\alpha \frac{P_{fs}}{\rho h} \nabla \eta - \hat{g}$ , with  $\eta = \eta(x, t)$  denoting the free-surface elevation. This spurious boundary condition generates spurious acoustic modes, dominant in the dynamics, in an area close to the free-surface. To conserve the robustness of MA-SPH, the approach is to allow for the development of the latter modes in mSPH and remove them, imposing a numerical, known, appropriate dissipation.

### 4.3.3 Boundary conditions

The desired boundary conditions are: (i) the no flux on impermeable boundaries  $\vec{u} \cdot \hat{n} = 0$ , where  $\hat{n}$  denotes the surface boundary normal, (ii) the zero pressure  $P(x, y = \eta, t) = 0$  dynamic free-surface boundary condition, and (iii) the continuity of the free-surface  $\dot{y}_{fs} = \frac{d\eta(x, t)}{dt}$  kinematic free-surface boundary condition.

In mSPH the sole boundary condition explicitly implemented is no-flux on the impermeable boundaries, i.e.,  $\vec{u}_a \cdot \hat{n}_{ib} \rightarrow 0$  as  $a \rightarrow \partial_{ib}$  and  $\hat{n}_{ib}$  denote the surface boundary normal. In practice this is achieved with ghost particles, mirrored with respect to the boundary [3], to satisfy the no-flux boundary condition. Particular care is taken to account for the hydrostatic pressure difference, i.e., the fluid and ghost particles have equal dynamic pressure so that  $d\vec{u}_a/dt \cdot \hat{n}_{ib} \rightarrow 0$  as  $a \rightarrow \partial_{ib}$ .

Only flat impermeable boundaries are considered. For example, let  $a$  be a fluid

particle at a distance  $dy$  from the sea-bed  $y = -H$  with  $\vec{x}_a, \vec{u}_a, \rho_a$ . Then if  $dy \leq \alpha h$ ,  $\alpha \sim O(5)$ , the particle is mirrored perpendicularly to the boundary and a ghost particle  $a^*$  is created with:

$$x_{a^*} = x_a, y_{a^*} = -H - dy, \quad (4.42)$$

$$u_{a^*} = u_a, v_{a^*} = -v_a, \text{ and} \quad (4.43)$$

$$\rho_{a^*} = \rho_a + \rho_f \frac{g}{c^2} (y_a - y_{a^*}). \quad (4.44)$$

It is noted for completeness that if the sea-bed is located at  $y = -H$ , the last row of fluid particles must be created at a distance  $h/2$  from the boundary, i.e.,  $y = -H + h/2$ . to obtain symmetry.

The kinematic free-surface boundary condition is satisfied automatically in mSPH as in all Lagrangian methods:

$$\frac{dy_a}{dt} = \frac{d\eta}{dt} \text{ for } a \in \partial_{\text{fs}}. \quad (4.45)$$

#### 4.3.4 Hydrostatic initial conditions

The initial conditions need to be consistent with the governing equations and the boundary conditions. If the flow has an initial hydrostatic component it must be incorporated into the initial density distribution as well as the initial particle mass for Kernel Interpolation.

As an example, the standard SPH benchmark dam-break where the flow is initialized as hydrostatic is considered. The particles are initially placed along a uniform, two-dimensional grid of spacing  $h$ . Denoting with  $H$  a reference height for the hydro-

static pressure, the initial flow properties of particle  $a$  are:

$$\vec{x}_a = [a_x h, a_y h], \quad (4.46)$$

$$\vec{u}_a = 0, \quad (4.47)$$

$$\rho_a = \rho_f (1 + 2\delta(H - a_y h)), \text{ and} \quad (4.48)$$

$$m_a = \rho_a h^2. \quad (4.49)$$

These hydrostatic initial conditions are consistent with the mSPH governing equations (4.40) and (4.41) with the pressure obtained from (4.21). Inconsistent initial conditions will simply generate spurious acoustic modes.

### 4.3.5 Temporal integration

The fourth order Runge-Kutta scheme is employed for the temporal integration of the governing equations. Denoting the time step with  $\delta t$  and  $q^n \equiv q(t = n\delta t) = [\bar{x}^n, \bar{u}^n, \rho^n]$ , the flow variable vector, the temporal integration reads:

$$\begin{cases} q^{1/4} &= q^n + \dot{q}^n \frac{\delta t}{2} \\ q^{1/2} &= q^n + \dot{q}^{1/4} \frac{\delta t}{2} \\ q^{3/4} &= q^n + \dot{q}^{1/2} \delta t \\ q^{n+1} &= q^n + (\dot{q}^n + 2\dot{q}^{1/4} + 2\dot{q}^{1/2} + \dot{q}^{3/4}) \frac{\delta t}{6} \end{cases} \quad (4.50)$$

where  $\dot{q}^m$  denotes the time rate of the flow field variables at time  $t = m\delta t$ , given by the appropriate semi-discrete governing equations. The time step is  $\delta t = \mu_c \frac{h}{c}$ , where  $\mu_c$  is the Courant condition.

The one-dimensional, linear stability analysis performed in section 2.6.4 for the acoustic modes on the standard SPH fully-discrete scheme with advanced density formulation and hydrostatic based density distribution, determined that, as expected, the scheme is unstable. The unstable growth rates are given in Figure 2-33 in section 2.6.4, as functions of the non-dimensional wavenumbers of the acoustic modes for

different Courant conditions  $\mu_c$ , showing that the growth rates reduce as  $\mu_c$  reduces. The Courant conditions considered for the numerical simulations were  $\mu_c = 0.8$  and  $\mu_c = 0.5$ .

### 4.3.6 Regularization

The described mSPH scheme is inherently unstable, just as SPH. Both algorithms are unstable in depth decaying modes, with large growth rates of  $O(c)$  and in acoustic modes, but with significantly smaller growth rates. The most crucial point is to realize that the dominant instability in SPH simulations is problem dependent. Immediately two cases are distinguished based on the domain geometry. In the first case, periodic or fixed boundaries are distinguished, where the dominant instability is depth decaying that leads to blow-up. Examples of this case include long-time hydrostatic simulations and plane progressive waves. In the second case, time-evolving boundaries are distinguished, where the dominant instability is acoustic and the unstable growth rates are significantly lower, affecting mainly the dynamics. A characteristic example of this case is the standard SPH dam-break benchmark. The above distinctions between the instabilities and the flow characteristics explain (a) why SPH could not be used for any long-time simulations and (b) why SPH can obtain validated kinematics, yet noisy dynamical results for the dam-break case.

Since it has already been determined that mSPH is to be employed for flows similar to the dam-break, mSPH is to be stabilized for the acoustic modes. From the findings on the analysis on the existing stability treatments in Chapter 3, it is realized that the most efficient stability treatments include some form of dissipation. Therefore, mSPH proceeds towards this same path, realizing that for the dissipation to be efficient it must be applied to the *entire* field. We chose to apply a periodic smoothing employing the Shephard functions. Namely, every  $n$  time steps the field

is updated based on:

$$\vec{u}_a^s = \frac{\sum_b \frac{m_b}{\rho_b} \vec{u}_b W_{ab}}{\sum_b \frac{m_b}{\rho_b} W_{ab}} \quad (4.51)$$

$$\rho_a^s = \frac{\sum_b m_b W_{ab}}{\sum_b \frac{m_b}{\rho_b} W_{ab}}. \quad (4.52)$$

From section 2.5.5, taking into account that the density has been smoothly advected, the dissipation for a cubic B-Spline and  $dx = h$  is found to be:

$$\begin{aligned} f_a^s &= \frac{\sum_b \frac{m_b}{\rho_b} \vec{u}_b W_{ab}}{\sum_b \frac{m_b}{\rho_b} W_{ab}} \rightarrow \\ &\simeq \frac{f_a + f_a'' \frac{h^2}{6} + f_a t u''' \frac{h^2}{6}}{1 + t u''' \frac{h^2}{6}} \rightarrow \\ f_a^s &\simeq f_a + f_a'' \frac{h^2}{6} + \text{h.o.t.} \end{aligned} \quad (4.53)$$

The coefficient  $h^2/6$  of the dissipation depends on the choice of kernel and the kernel bandwidth. Therefore, this dissipation is enforced every  $n$  time steps. To suppress the acoustic modes  $e^{ikh}$  it suffices to have:

$$\lambda^n \left(1 - \frac{(kh)^2}{6}\right) < 1 \quad (4.54)$$

where  $\lambda$  is the growth rate determined from the stability analysis of the fully-discrete scheme in Figure 2-33, section 2.6.4. It is evident that  $n$  depends essentially on the Courant condition  $\mu$ . Choosing appropriate  $\mu$  with  $\mu = 1 + \epsilon$  such that  $\epsilon \ll 1 \rightarrow \lambda^n \simeq 1 + n\epsilon$ , it is determined that  $n$  must satisfy:

$$n < \left(\frac{1}{\lambda - 1}\right) \frac{1}{1 - \frac{(kh)^2}{6}}. \quad (4.55)$$

Figure 4-18 shows the minimum number of time steps required to apply smoothing in order to achieve stability for three different values of the Courant number  $\mu_c$ . Although not shown (to maintain a reasonable scale for the other curves) for  $\mu_c = 0.1$  it is  $n \sim O(10^3)$ . This form of dissipation also removes the need for a variable time

step used in current SPH applications that often becomes so restrictive that stops the simulation.

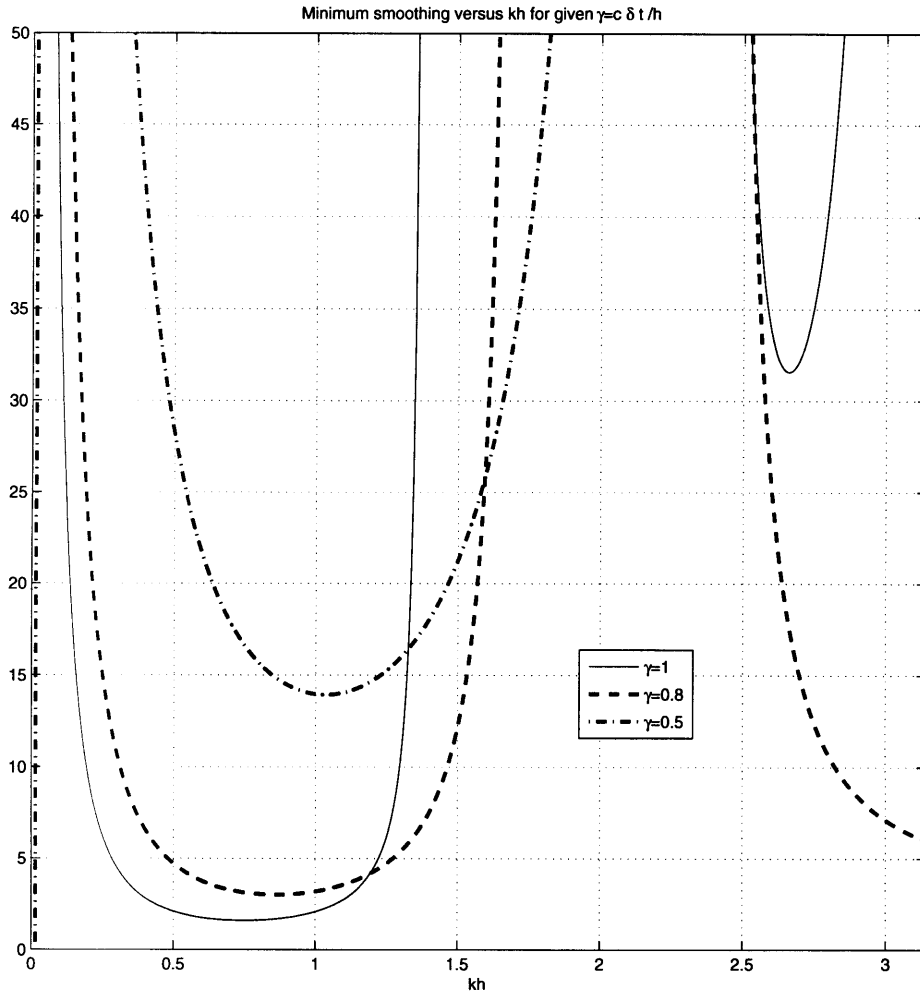


Figure 4-18: Minimum number of time steps for smoothing to achieve stability. Thin solid line  $\mu_c = 1$ , dashed line  $\mu_c = 0.8$ , dash-dot line  $\mu_c = 0.5$ .

### 4.3.7 An *a posteriori* error metric

The analysis described in the previous section 4.3.6 for choosing the smoothing period  $n$  is most accurate for the first time steps where there is no base flow and the density

has a hydrostatic distribution. For the free-surface flows this is always a valid approximation, since the leading order density is hydrostatic. However, a global measure  $Q(t)$  that indicates the growth of the acoustic modes in the flow is also proposed:

$$Q(t) = \sum \left| \frac{d\vec{u}}{dt} \right|^2. \quad (4.56)$$

Realizing that the dominant instability is problem dependent and that the acoustic modes are predominant in the accelerations,  $Q$  provides an efficient *a posteriori* measure for the magnitude of the oscillations, through time FFT, as well as for the instability growth rate.

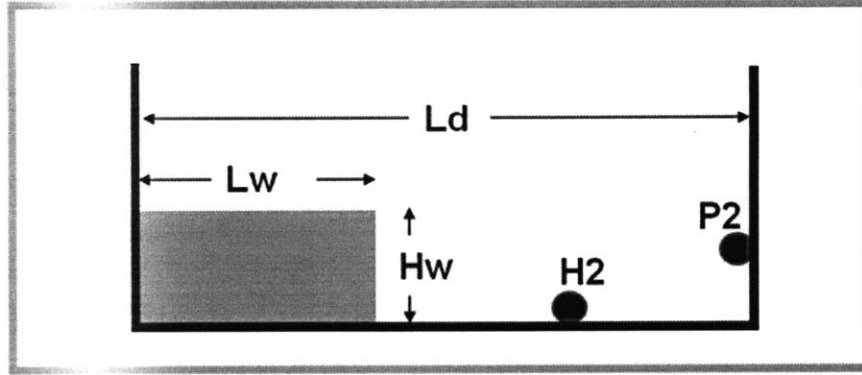


Figure 4-19: Initial conditions for the standard SPH dam-break benchmark, described in [55]. The kernel bandwidth is  $h = 0.025m$ , the particle spacing is  $dx = 0.75h$ . The domain dimensions are  $L_d = 5.36m$ ,  $L_w = 1.2m$ , and  $H_w = 0.6m$ .

### 4.3.8 Numerical simulation of standard SPH dam-break benchmark with mSPH

The standard SPH dam-break benchmark, described in [55] with initial configuration given in Fig. 4-20 has been used for comparisons between MA-SPH, MA-SPH with selected fixes and mSPH.

The following figures 4-20- 4-44 compare time evolving snapshots of the horizontal and vertical velocities, horizontal and vertical accelerations and pressure field for MA-SPH with MLS density re-initialization, i.e., hydrostatic re-initialization, mSPH with no smoothing, which is essentially SPH with consistent initial and boundary conditions, and mSPH with smoothing every  $n = 5$  time steps. The artificial speed of sound is  $c = 26.46m/s$ , the kernel bandwidth is  $h = 0.025$ , the particle spacing is  $dx = 0.75h$  and the Courant condition  $\mu_c = 0.8$  for all simulations. Noting that in all the all three simulations have identical physical and numerical parameters and all the level contours are identical, the figures clearly demonstrate (i) the dominance of the high frequency oscillations in the pressure field and even more so in the accelerations for MA-SPH with MLS density re-initialization and mSPH without smoothing, as predicted from the analysis, (ii) the improved stability of mSPH, and (iii) the unphysical effects of the MLS density re-initialization in the shape of the free-surface.

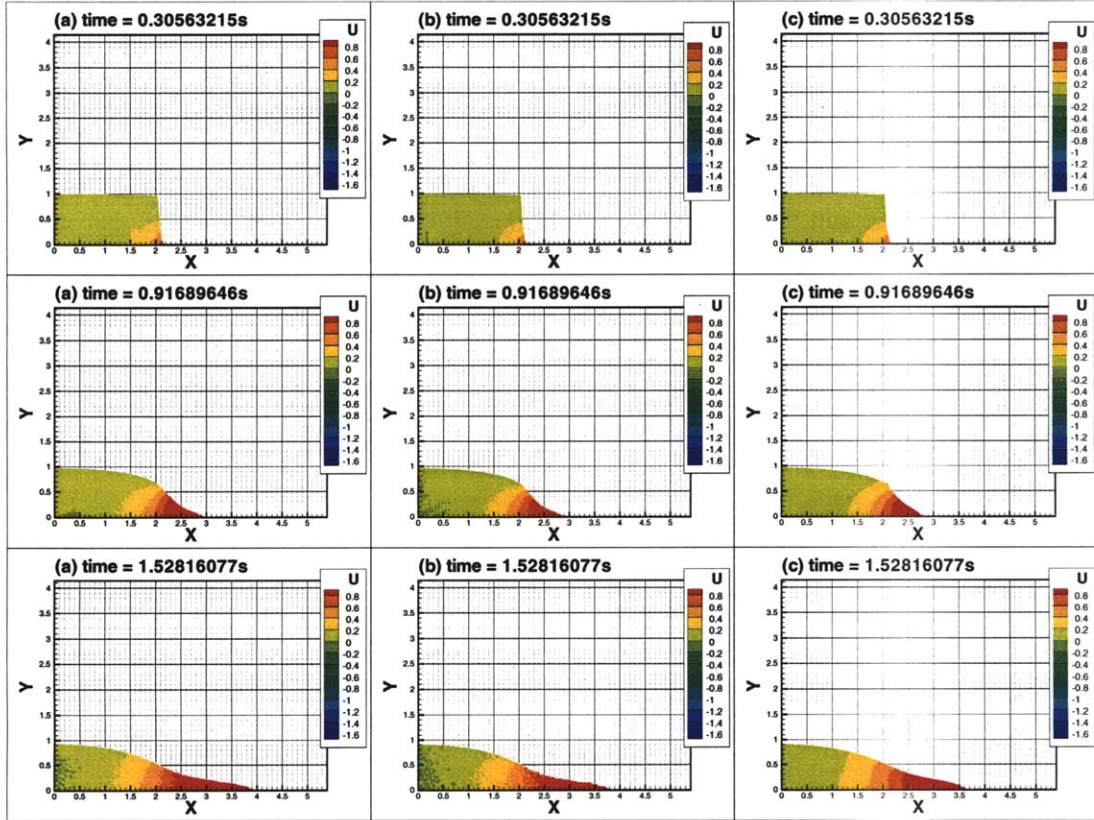


Figure 4-20: In color. Comparison of time evolving snapshots of the horizontal velocity field of (a) MA-SPH MLS density re-initialization, (b) mSPH with no smoothing, and (c) mSPH with smoothing every  $n = 5$  time steps. The artificial speed of sound is  $c = 26.46m/s$ , the kernel bandwidth is  $h = 0.025$ , the particle spacing is  $dx = 0.75h$  and the Courant condition  $\mu_c = 0.8$  for all simulations. Time increases from top to bottom. It is emphasized that all three simulations are initialized with the same initial conditions, employ identical spatial and temporal discretization parameters, the contour levels use the same coloring schemes, *no* filtering or post-processing has been employed in any of the results, and finally no other treatments have been employed other than those described.

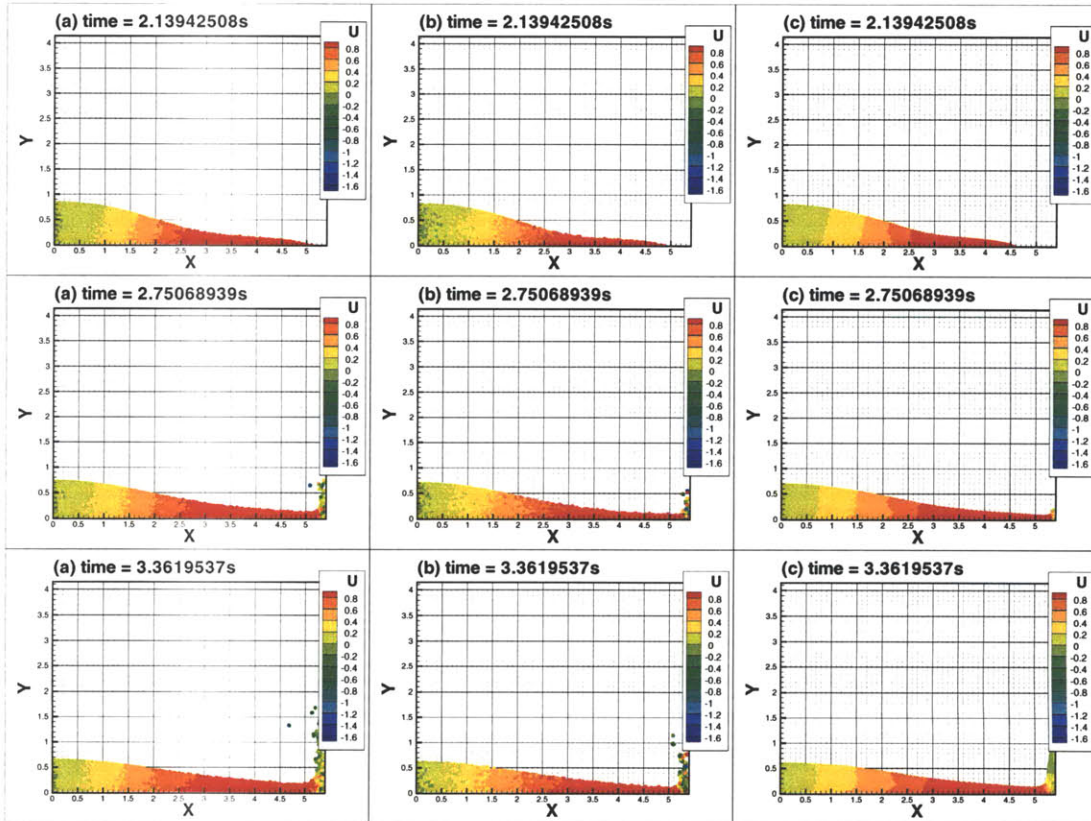


Figure 4-21: In color. Comparison of time evolving snapshots of the horizontal velocity field of (a) MA-SPH MLS density re-initialization, (b) mSPH with no smoothing, and (c) mSPH with smoothing every  $n = 5$  time steps. The artificial speed of sound is  $c = 26.46m/s$ , the kernel bandwidth is  $h = 0.025$ , the particle spacing is  $dx = 0.75h$  and the Courant condition  $\mu_c = 0.8$  for all simulations. Time increases from top to bottom. It is emphasized that all three simulations are initialized with the same initial conditions, employ identical spatial and temporal discretization parameters, the contour levels use the same coloring schemes, *no* filtering or post-processing has been employed in any of the results, and finally no other treatments have been employed other than those described.

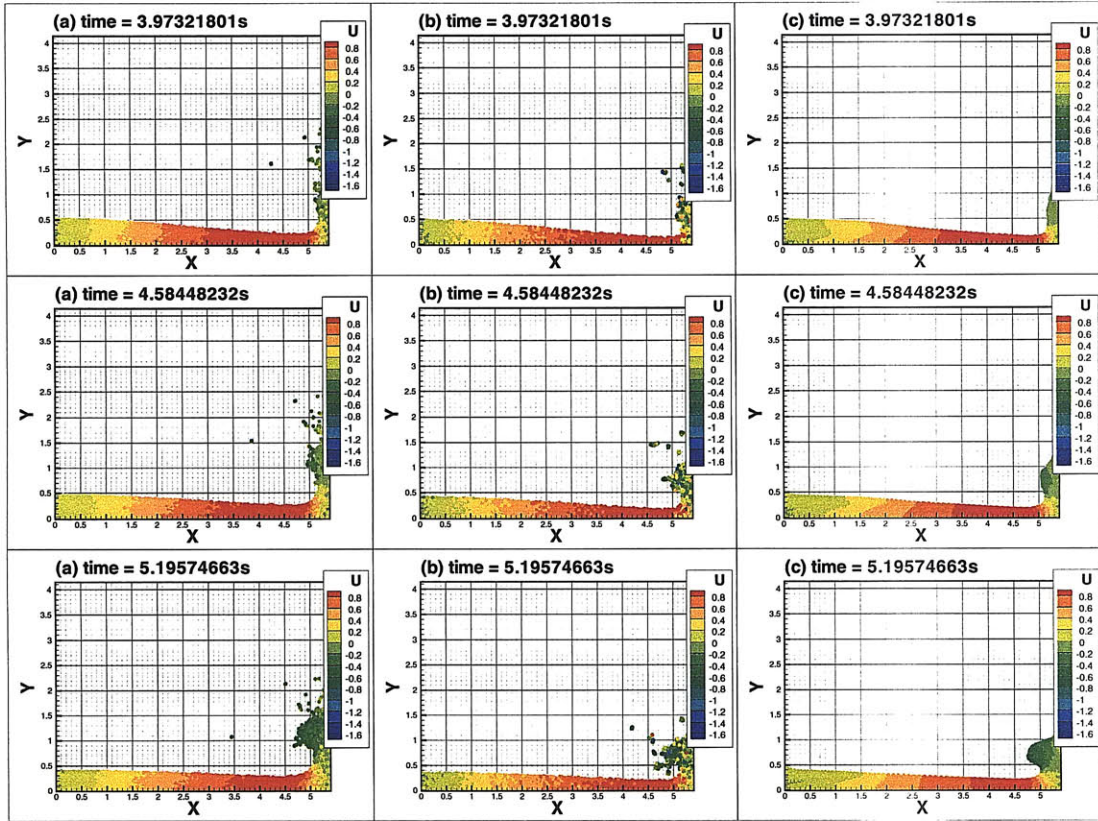


Figure 4-22: In color. Comparison of time evolving snapshots of the horizontal velocity field of (a) MA-SPH MLS density re-initialization, (b) mSPH with no smoothing, and (c) mSPH with smoothing every  $n = 5$  time steps. The artificial speed of sound is  $c = 26.46m/s$ , the kernel bandwidth is  $h = 0.025$ , the particle spacing is  $dx = 0.75h$  and the Courant condition  $\mu_c = 0.8$  for all simulations. Time increases from top to bottom. It is emphasized that all three simulations are initialized with the same initial conditions, employ identical spatial and temporal discretization parameters, the contour levels use the same coloring schemes, *no* filtering or post-processing has been employed in any of the results, and finally no other treatments have been employed other than those described.

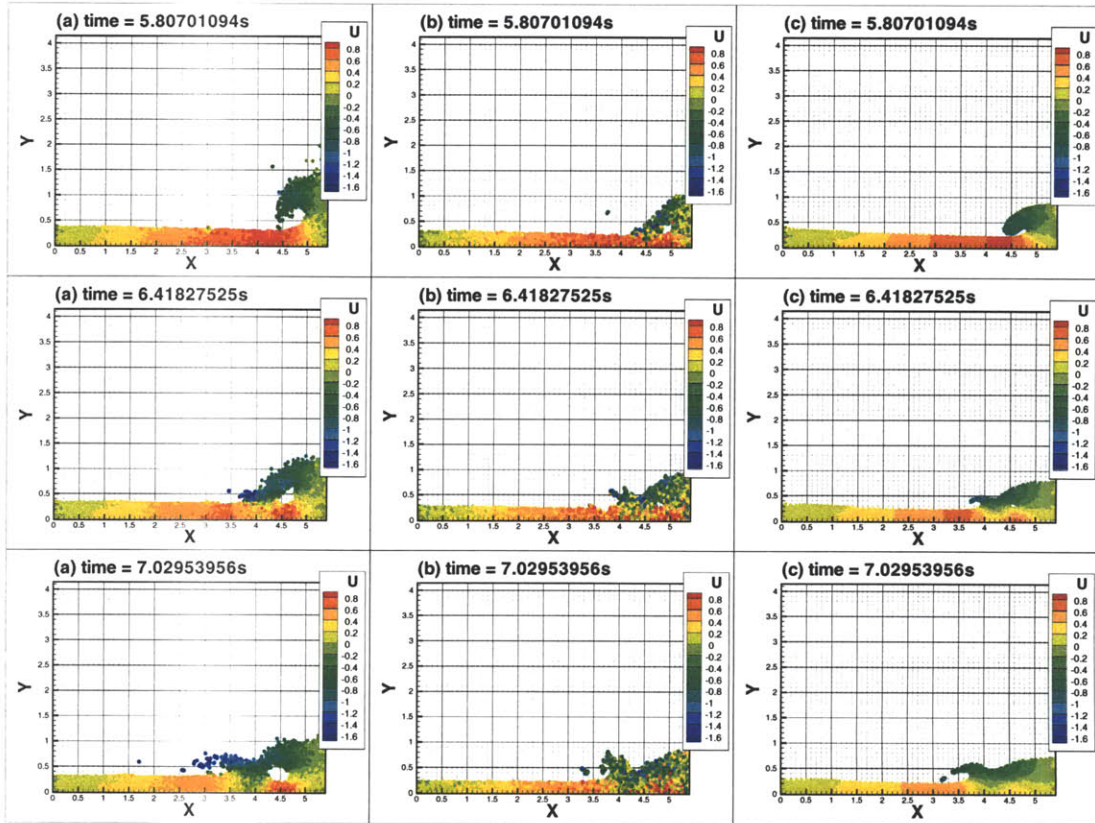


Figure 4-23: In color. Comparison of time evolving snapshots of the horizontal velocity field of (a) MA-SPH MLS density re-initialization, (b) mSPH with no smoothing, and (c) mSPH with smoothing every  $n = 5$  time steps. The artificial speed of sound is  $c = 26.46m/s$ , the kernel bandwidth is  $h = 0.025$ , the particle spacing is  $dx = 0.75h$  and the Courant condition  $\mu_c = 0.8$  for all simulations. Time increases from top to bottom. It is emphasized that all three simulations are initialized with the same initial conditions, employ identical spatial and temporal discretization parameters, the contour levels use the same coloring schemes, *no* filtering or post-processing has been employed in any of the results, and finally no other treatments have been employed other than those described.

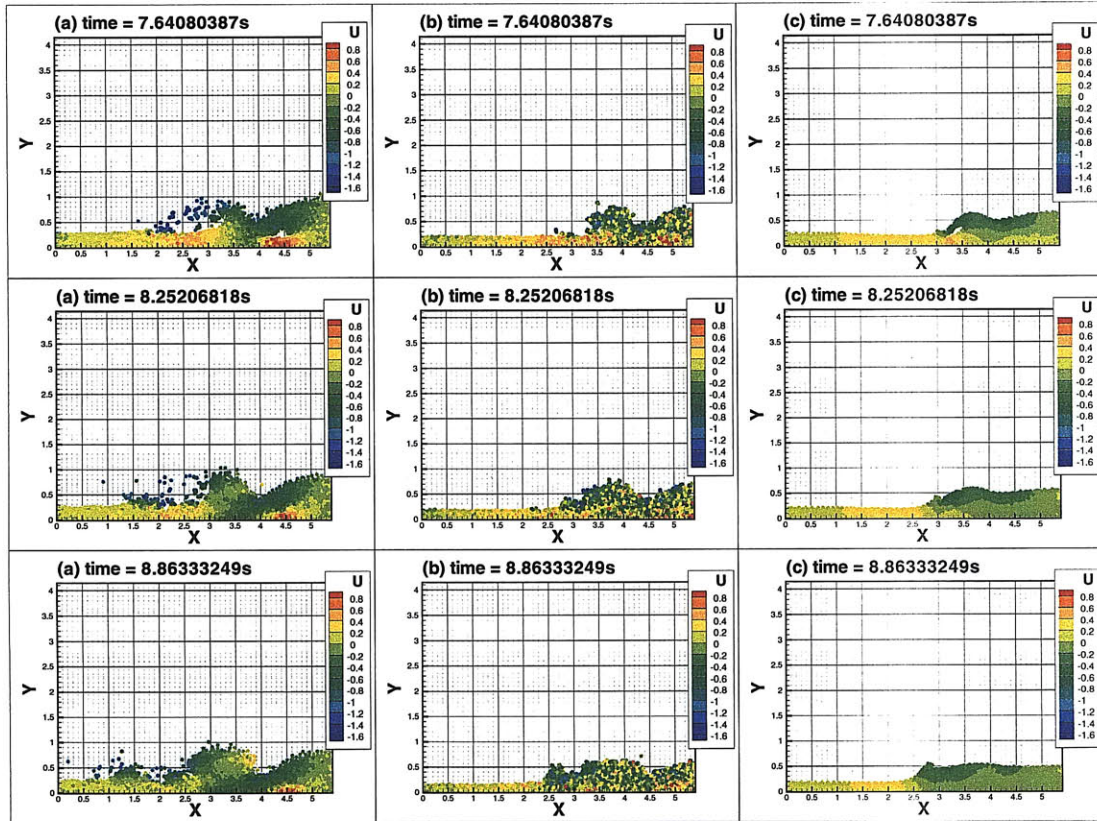


Figure 4-24: In color. Comparison of time evolving snapshots of the horizontal velocity field of (a) MA-SPH MLS density re-initialization, (b) mSPH with no smoothing, and (c) mSPH with smoothing every  $n = 5$  time steps. The artificial speed of sound is  $c = 26.46m/s$ , the kernel bandwidth is  $h = 0.025$ , the particle spacing is  $dx = 0.75h$  and the Courant condition  $\mu_c = 0.8$  for all simulations. Time increases from top to bottom. It is emphasized that all three simulations are initialized with the same initial conditions, employ identical spatial and temporal discretization parameters, the contour levels use the same coloring schemes, *no* filtering or post-processing has been employed in any of the results, and finally no other treatments have been employed other than those described.

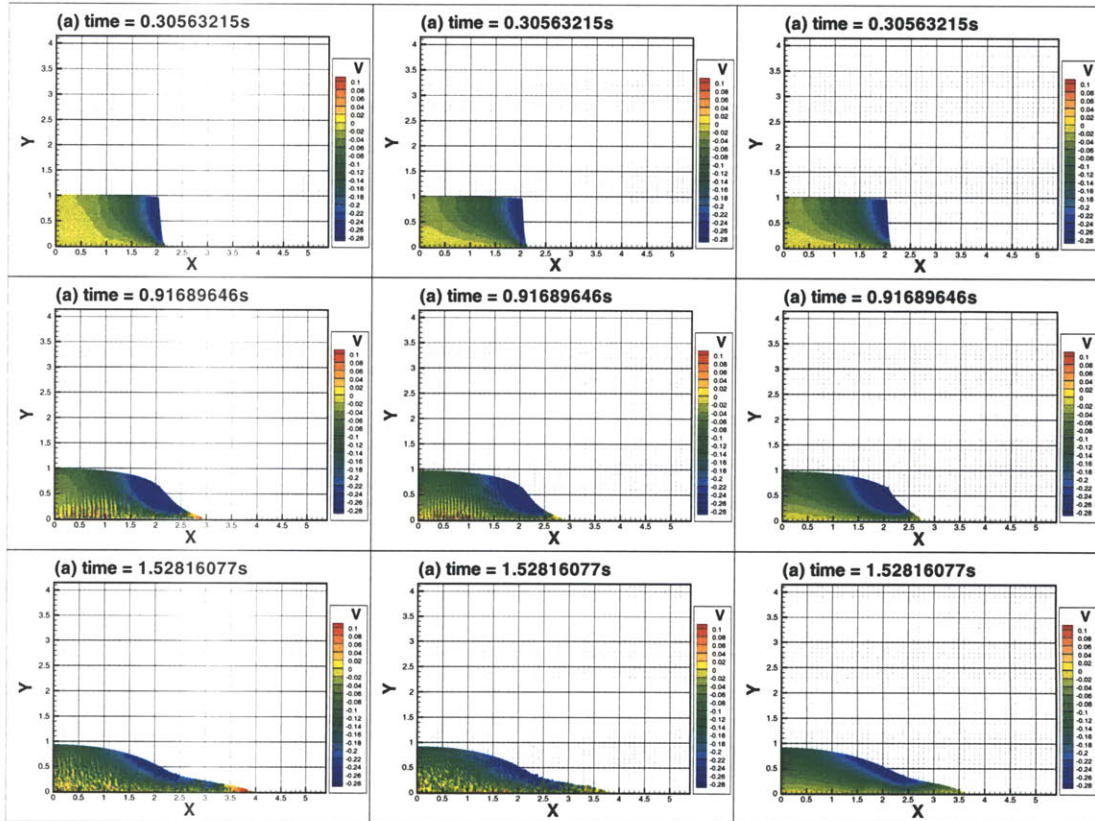


Figure 4-25: In color. Comparison of time evolving snapshots of the vertical velocity field of (left column) MA-SPH MLS density re-initialization, (middle column) mSPH with no smoothing, and (right column) mSPH with smoothing every  $n = 5$  time steps. The artificial speed of sound is  $c = 26.46m/s$ , the kernel bandwidth is  $h = 0.025$ , the particle spacing is  $dx = 0.75h$  and the Courant condition  $\mu_c = 0.8$  for all simulations. Time increases from top to bottom. It is emphasized that all three simulations are initialized with the same initial conditions, employ identical spatial and temporal discretization parameters, the contour levels use the same coloring schemes, *no* filtering or post-processing has been employed in any of the results, and finally no other treatments have been employed other than those described.

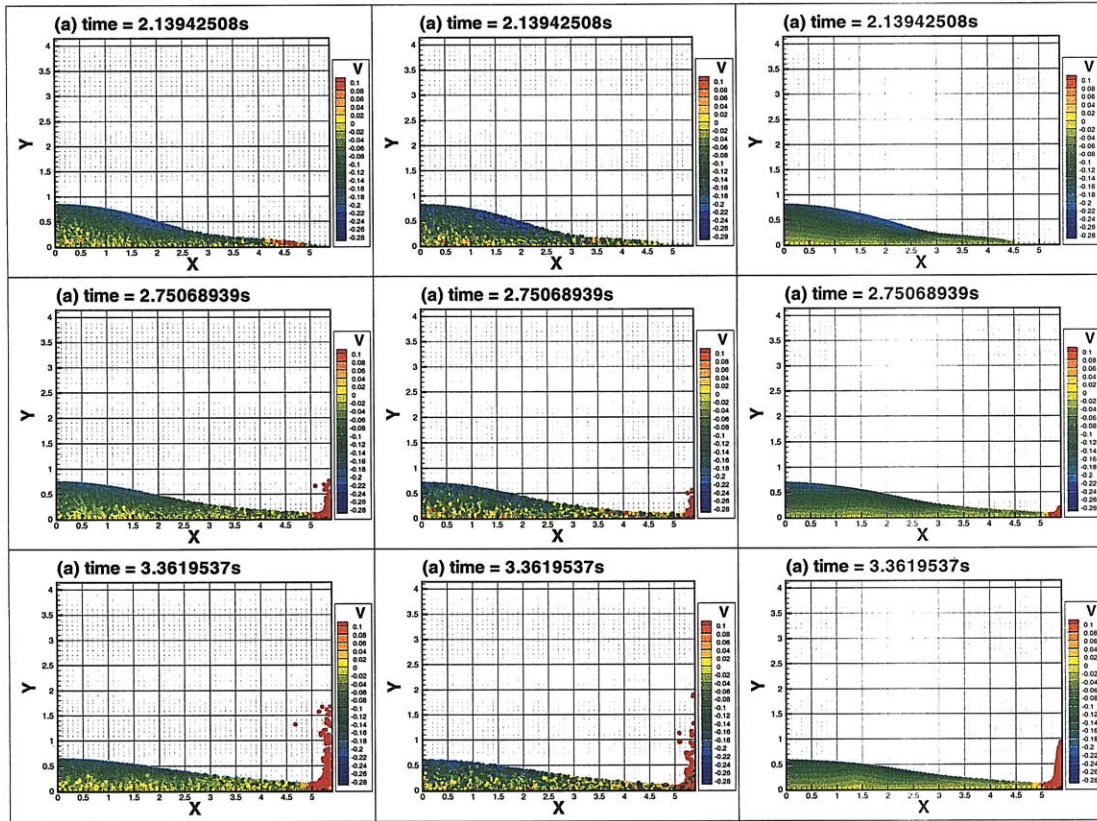


Figure 4-26: In color. Comparison of time evolving snapshots of the vertical velocity field of (left column) MA-SPH MLS density re-initialization, (middle column) mSPH with no smoothing, and (right column) mSPH with smoothing every  $n = 5$  time steps. The artificial speed of sound is  $c = 26.46m/s$ , the kernel bandwidth is  $h = 0.025$ , the particle spacing is  $dx = 0.75h$  and the Courant condition  $\mu_c = 0.8$  for all simulations. Time increases from top to bottom. It is emphasized that all three simulations are initialized with the same initial conditions, employ identical spatial and temporal discretization parameters, the contour levels use the same coloring schemes, *no* filtering or post-processing has been employed in any of the results, and finally no other treatments have been employed other than those described.

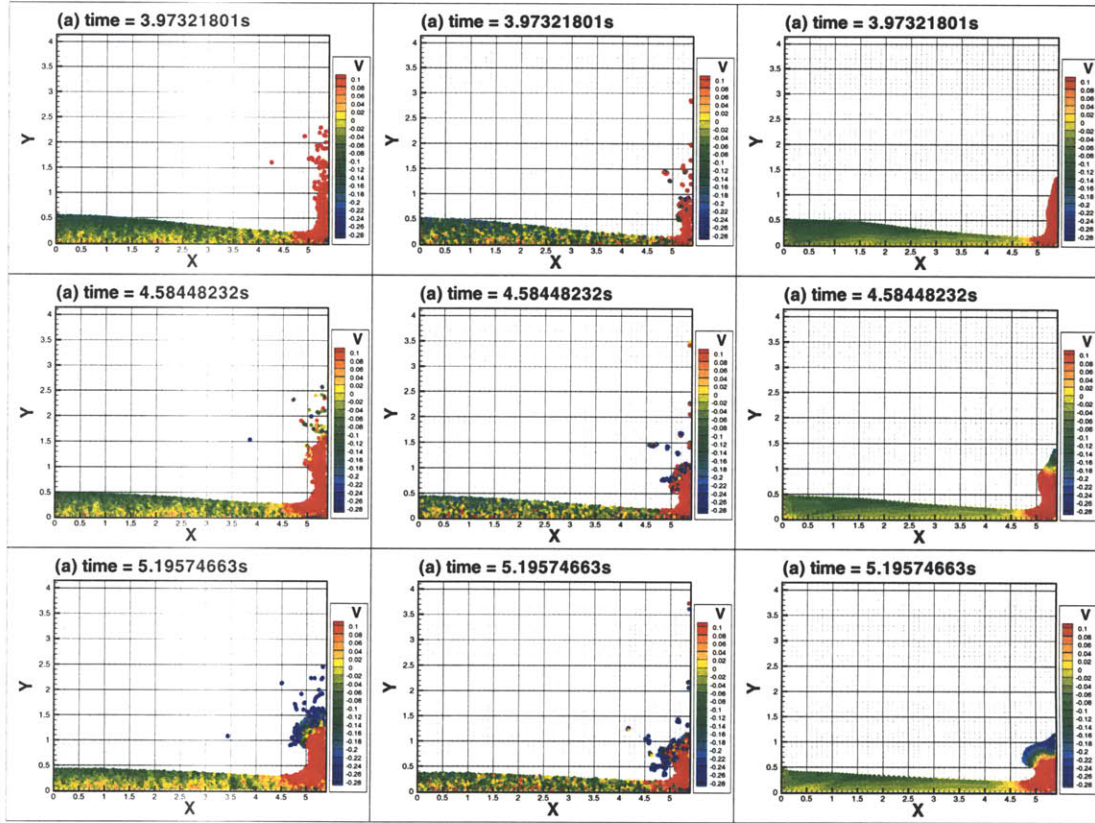


Figure 4-27: In color. Comparison of time evolving snapshots of the vertical velocity field of (left column) MA-SPH MLS density re-initialization, (middle column) mSPH with no smoothing, and (right column) mSPH with smoothing every  $n = 5$  time steps. The artificial speed of sound is  $c = 26.46m/s$ , the kernel bandwidth is  $h = 0.025$ , the particle spacing is  $dx = 0.75h$  and the Courant condition  $\mu_c = 0.8$  for all simulations. Time increases from top to bottom. It is emphasized that all three simulations are initialized with the same initial conditions, employ identical spatial and temporal discretization parameters, the contour levels use the same coloring schemes, *no* filtering or post-processing has been employed in any of the results, and finally no other treatments have been employed other than those described.

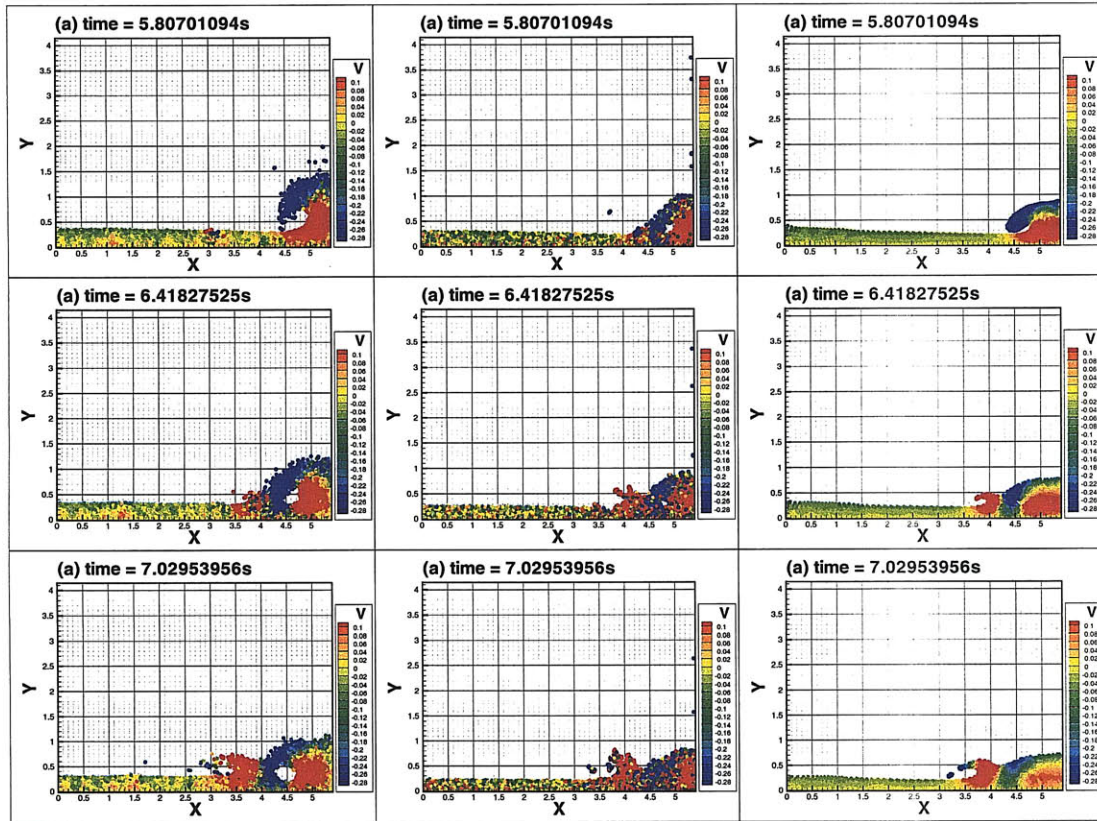


Figure 4-28: In color. Comparison of time evolving snapshots of the vertical velocity field of (left column) MA-SPH MLS density re-initialization, (middle column) mSPH with no smoothing, and (right column) mSPH with smoothing every  $n = 5$  time steps. The artificial speed of sound is  $c = 26.46m/s$ , the kernel bandwidth is  $h = 0.025$ , the particle spacing is  $dx = 0.75h$  and the Courant condition  $\mu_c = 0.8$  for all simulations. Time increases from top to bottom. It is emphasized that all three simulations are initialized with the same initial conditions, employ identical spatial and temporal discretization parameters, the contour levels use the same coloring schemes, *no* filtering or post-processing has been employed in any of the results, and finally no other treatments have been employed other than those described.

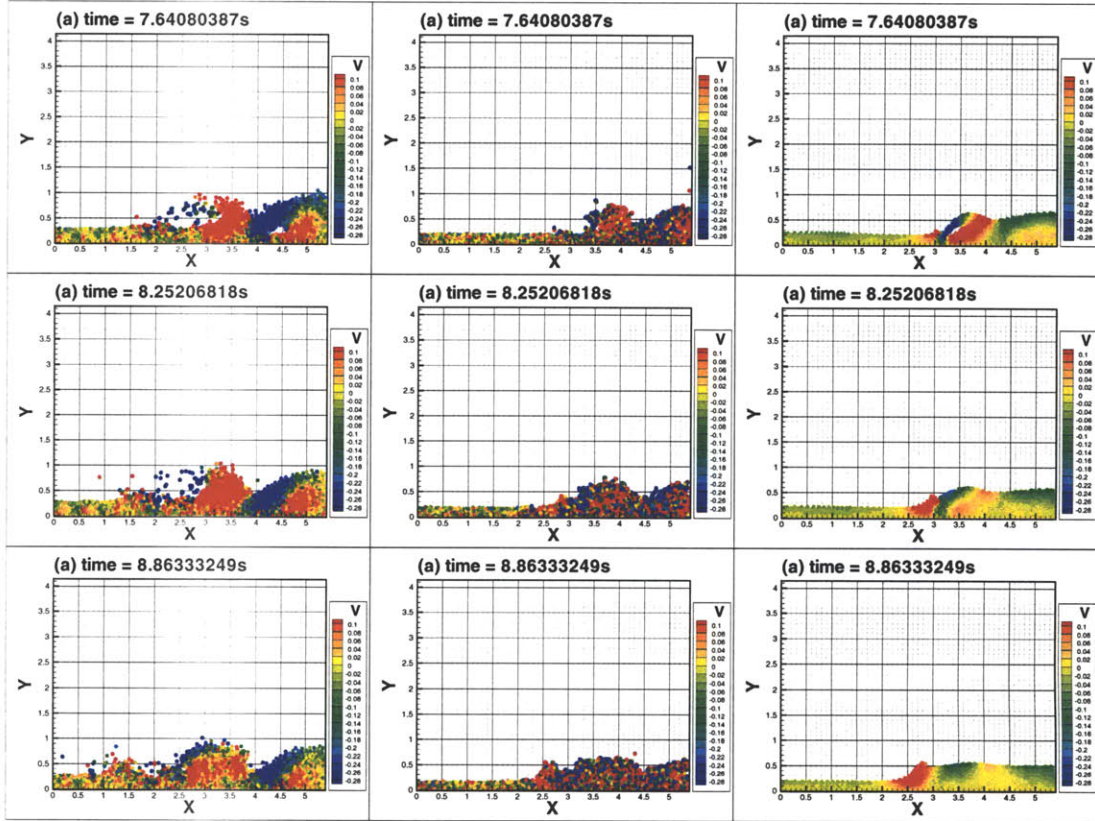


Figure 4-29: In color. Comparison of time evolving snapshots of the vertical velocity field of (left column) MA-SPH MLS density re-initialization, (middle column) mSPH with no smoothing, and (right column) mSPH with smoothing every  $n = 5$  time steps. The artificial speed of sound is  $c = 26.46m/s$ , the kernel bandwidth is  $h = 0.025$ , the particle spacing is  $dx = 0.75h$  and the Courant condition  $\mu_c = 0.8$  for all simulations. Time increases from top to bottom. It is emphasized that all three simulations are initialized with the same initial conditions, employ identical spatial and temporal discretization parameters, the contour levels use the same coloring schemes, *no* filtering or post-processing has been employed in any of the results, and finally no other treatments have been employed other than those described.

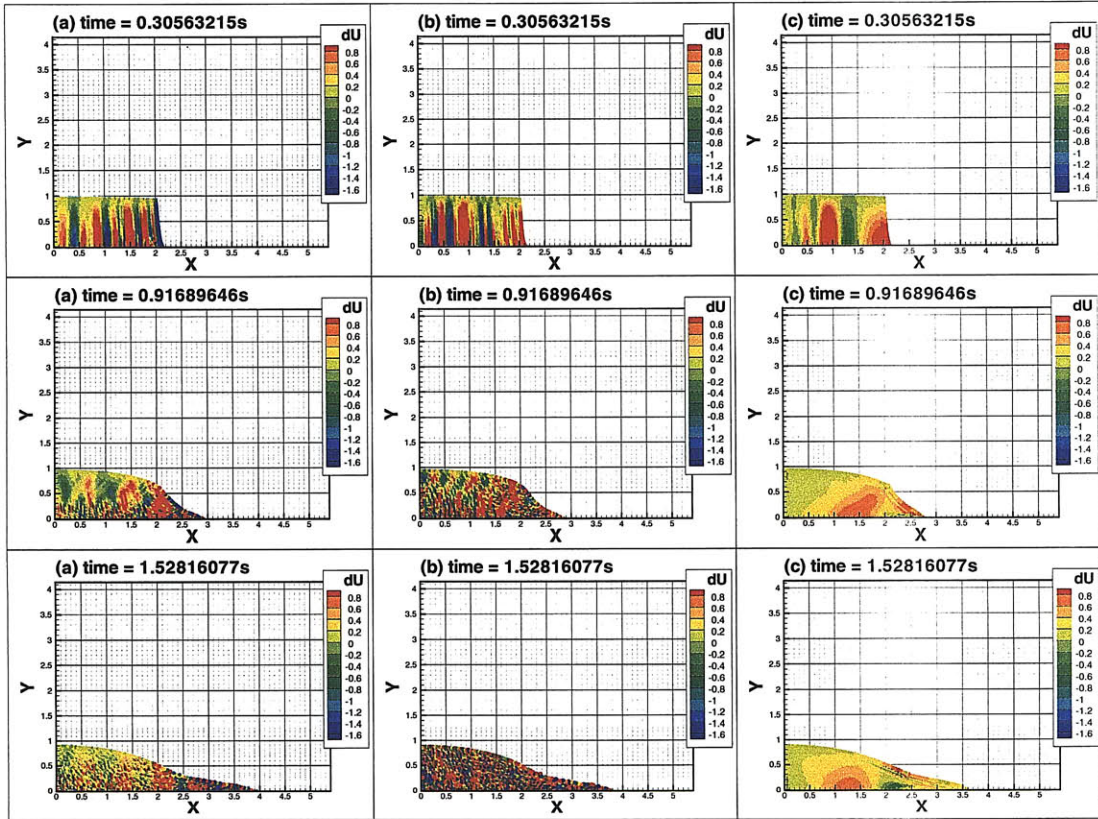


Figure 4-30: In color. Comparison of time evolving snapshots of the horizontal accelerations of (a) MA-SPH with MLS density re-initialization, (b) mSPH with no smoothing, and (c) mSPH with smoothing every  $n = 5$  time steps. The artificial speed of sound is  $c = 26.46m/s$ , the kernel bandwidth is  $h = 0.025$ , the particle spacing is  $dx = 0.75h$  and the Courant condition  $\mu_c = 0.8$  for all simulations. Time increases from top to bottom. It is emphasized that all three simulations are initialized with the same initial conditions, employ identical spatial and temporal discretization parameters, the contour levels use the same coloring schemes, *no* filtering or post-processing has been employed in any of the results, and finally no other treatments have been employed other than those described.

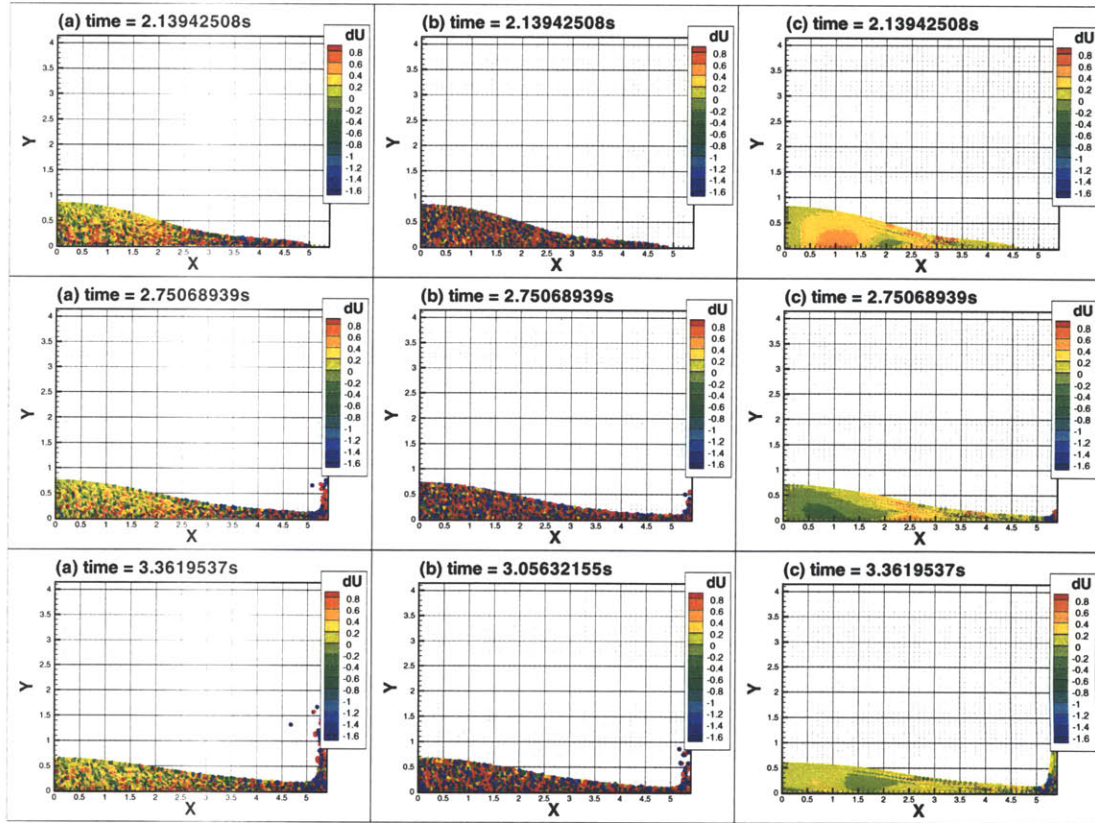


Figure 4-31: In color. Comparison of time evolving snapshots of the horizontal accelerations of (a) MA-SPH with MLS density re-initialization, (b) mSPH with no smoothing, and (c) mSPH with smoothing every  $n = 5$  time steps. The artificial speed of sound is  $c = 26.46m/s$ , the kernel bandwidth is  $h = 0.025$ , the particle spacing is  $dx = 0.75h$  and the Courant condition  $\mu_c = 0.8$  for all simulations. Time increases from top to bottom. It is emphasized that all three simulations are initialized with the same initial conditions, employ identical spatial and temporal discretization parameters, the contour levels use the same coloring schemes, *no* filtering or post-processing has been employed in any of the results, and finally no other treatments have been employed other than those described.

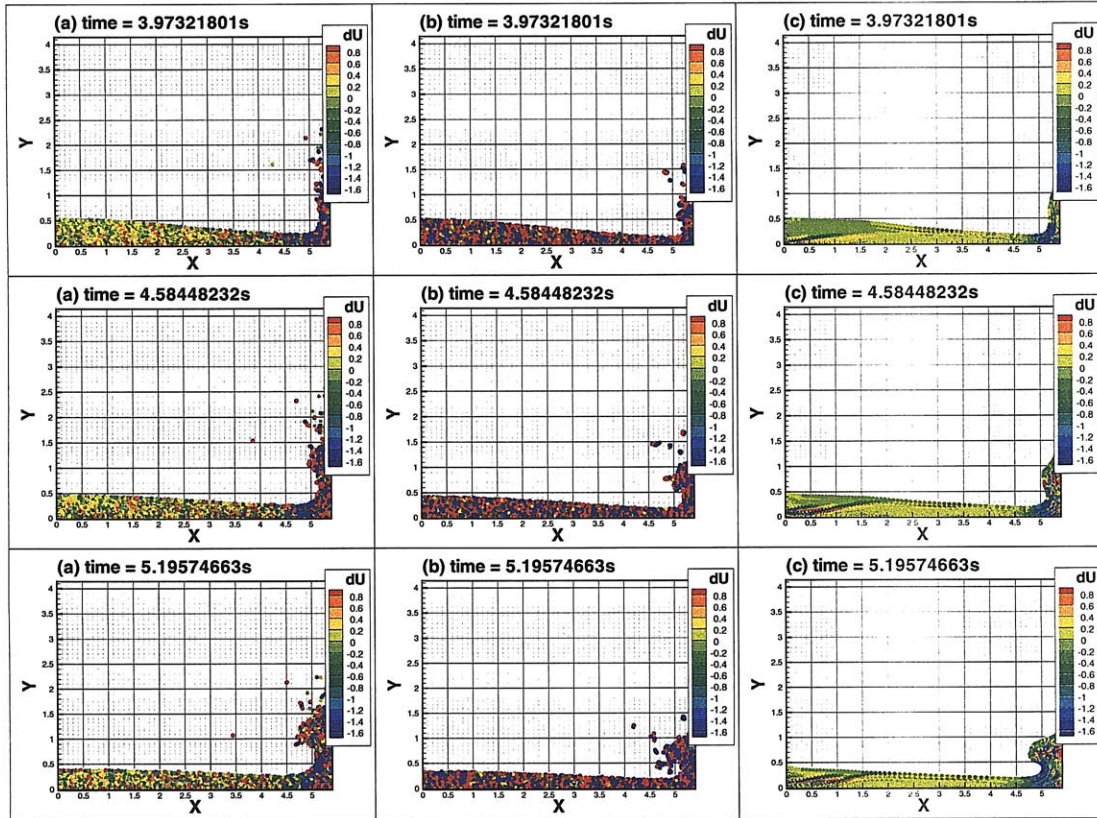


Figure 4-32: In color. Comparison of time evolving snapshots of the horizontal accelerations of (a) MA-SPH with MLS density re-initialization, (b) mSPH with no smoothing, and (c) mSPH with smoothing every  $n = 5$  time steps. The artificial speed of sound is  $c = 26.46m/s$ , the kernel bandwidth is  $h = 0.025$ , the particle spacing is  $dx = 0.75h$  and the Courant condition  $\mu_c = 0.8$  for all simulations. Time increases from top to bottom. It is emphasized that all three simulations are initialized with the same initial conditions, employ identical spatial and temporal discretization parameters, the contour levels use the same coloring schemes, *no* filtering or post-processing has been employed in any of the results, and finally no other treatments have been employed other than those described.

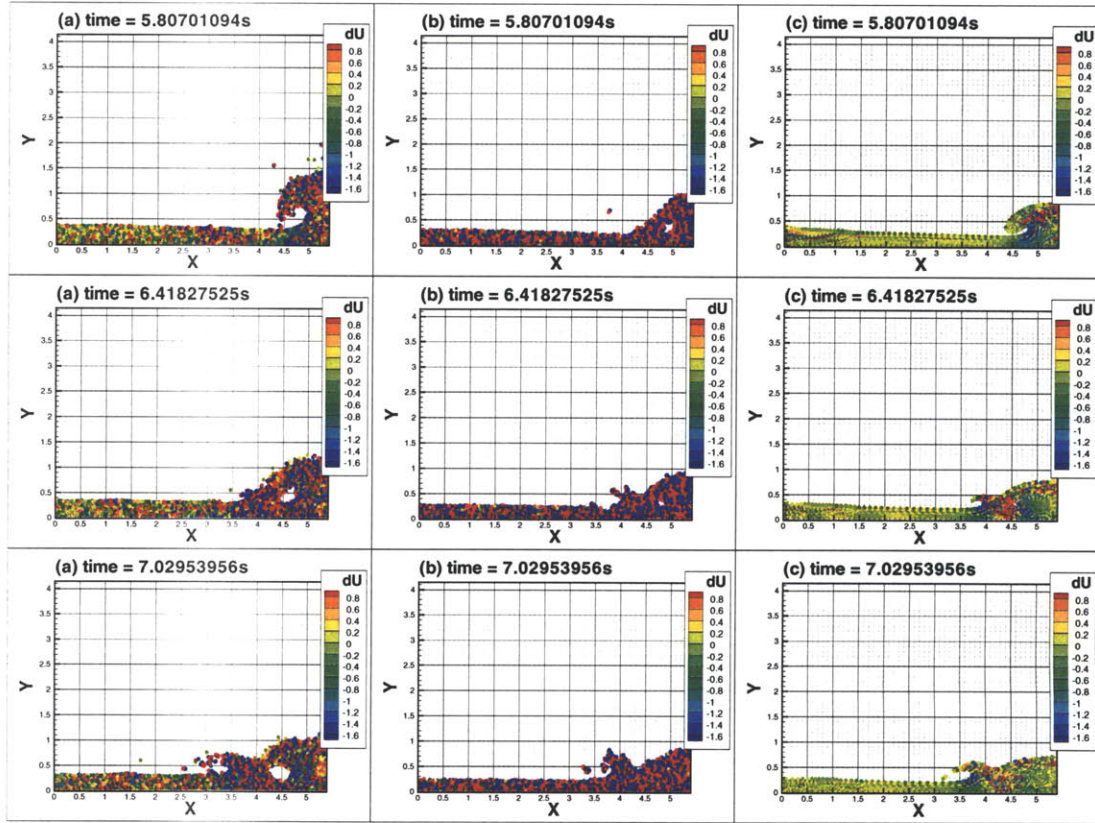


Figure 4-33: In color. Comparison of time evolving snapshots of the horizontal accelerations of (a) MA-SPH with MLS density re-initialization, (b) mSPH with no smoothing, and (c) mSPH with smoothing every  $n = 5$  time steps. The artificial speed of sound is  $c = 26.46m/s$ , the kernel bandwidth is  $h = 0.025$ , the particle spacing is  $dx = 0.75h$  and the Courant condition  $\mu_c = 0.8$  for all simulations. Time increases from top to bottom. It is emphasized that all three simulations are initialized with the same initial conditions, employ identical spatial and temporal discretization parameters, the contour levels use the same coloring schemes, *no* filtering or post-processing has been employed in any of the results, and finally no other treatments have been employed other than those described.

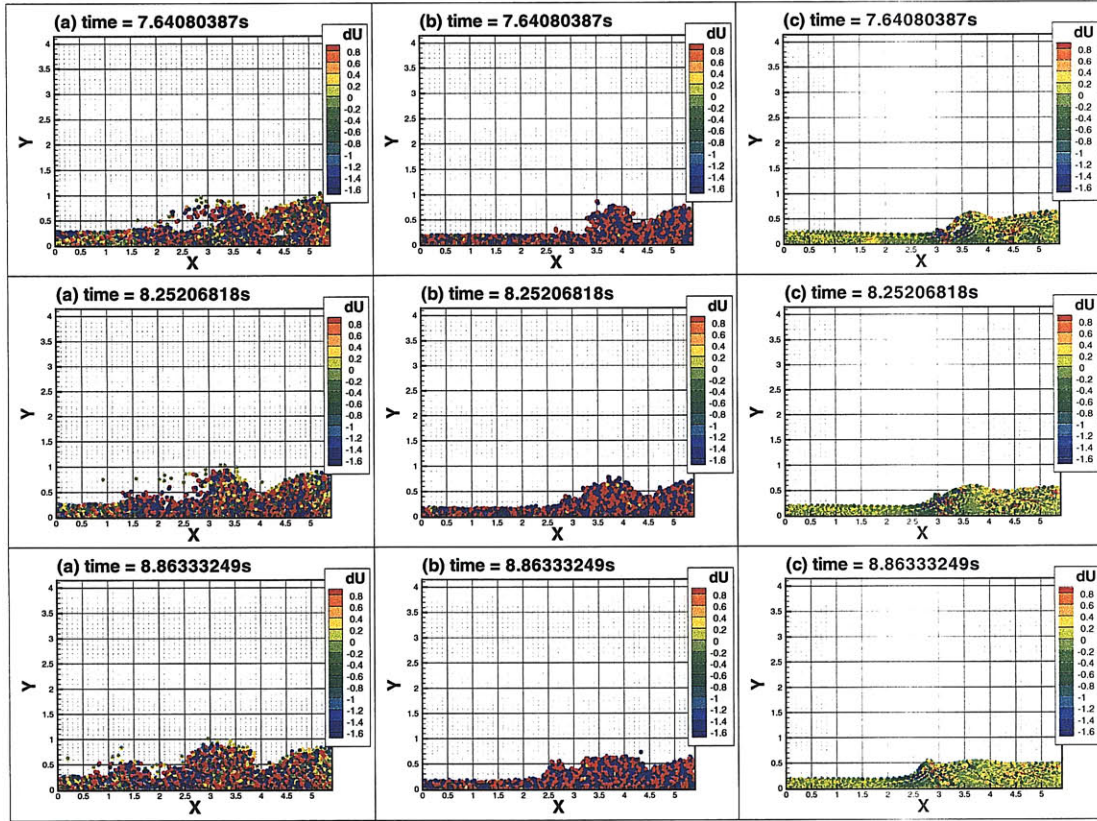


Figure 4-34: In color. Comparison of time evolving snapshots of the horizontal accelerations of (a) MA-SPH with MLS density re-initialization, (b) mSPH with no smoothing, and (c) mSPH with smoothing every  $n = 5$  time steps. The artificial speed of sound is  $c = 26.46m/s$ , the kernel bandwidth is  $h = 0.025$ , the particle spacing is  $dx = 0.75h$  and the Courant condition  $\mu_c = 0.8$  for all simulations. Time increases from top to bottom. It is emphasized that all three simulations are initialized with the same initial conditions, employ identical spatial and temporal discretization parameters, the contour levels use the same coloring schemes, *no* filtering or post-processing has been employed in any of the results, and finally no other treatments have been employed other than those described.

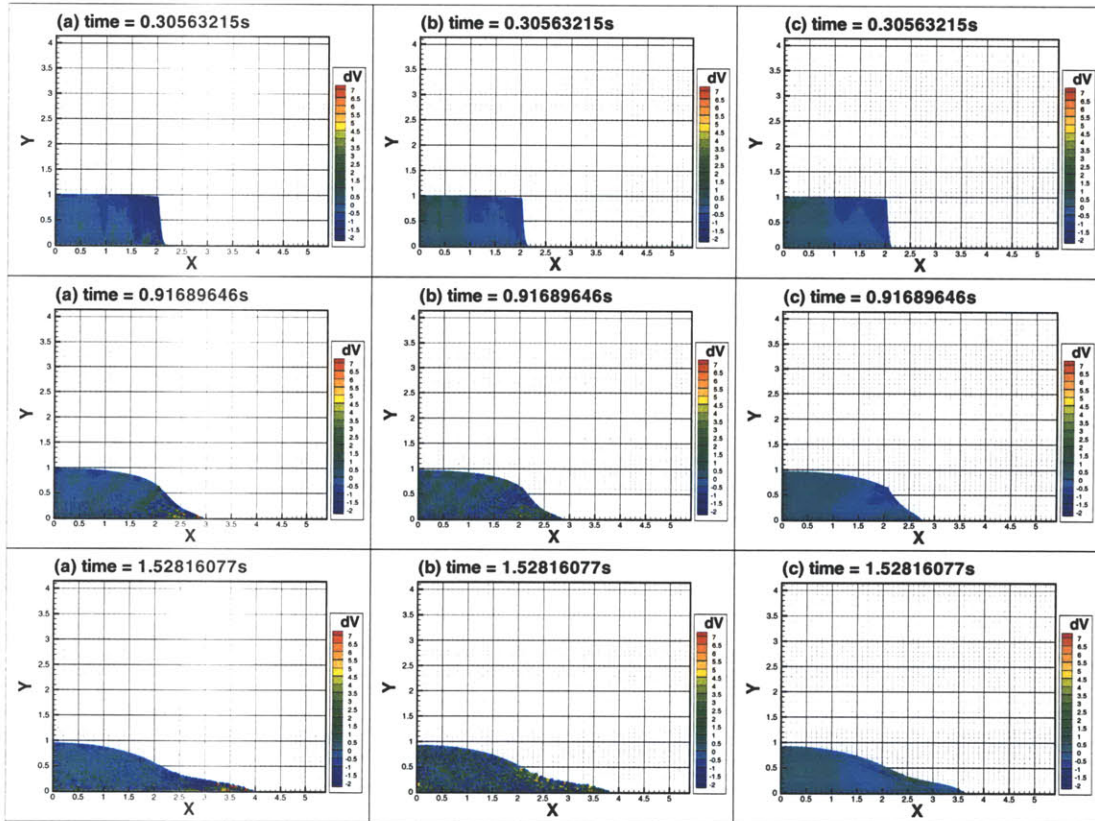


Figure 4-35: In color. Comparison of time evolving snapshots of the vertical accelerations of (a) MA-SPH with MLS density re-initialization, (b) mSPH with no smoothing, and (c) mSPH with smoothing every  $n = 5$  time steps. The artificial speed of sound is  $c = 26.46m/s$ , the kernel bandwidth is  $h = 0.025$ , the particle spacing is  $dx = 0.75h$  and the Courant condition  $\mu_c = 0.8$  for all simulations. Time increases from top to bottom. It is emphasized that all three simulations are initialized with the same initial conditions, employ identical spatial and temporal discretization parameters, the contour levels use the same coloring schemes, *no* filtering or post-processing has been employed in any of the results, and finally no other treatments have been employed other than those described.

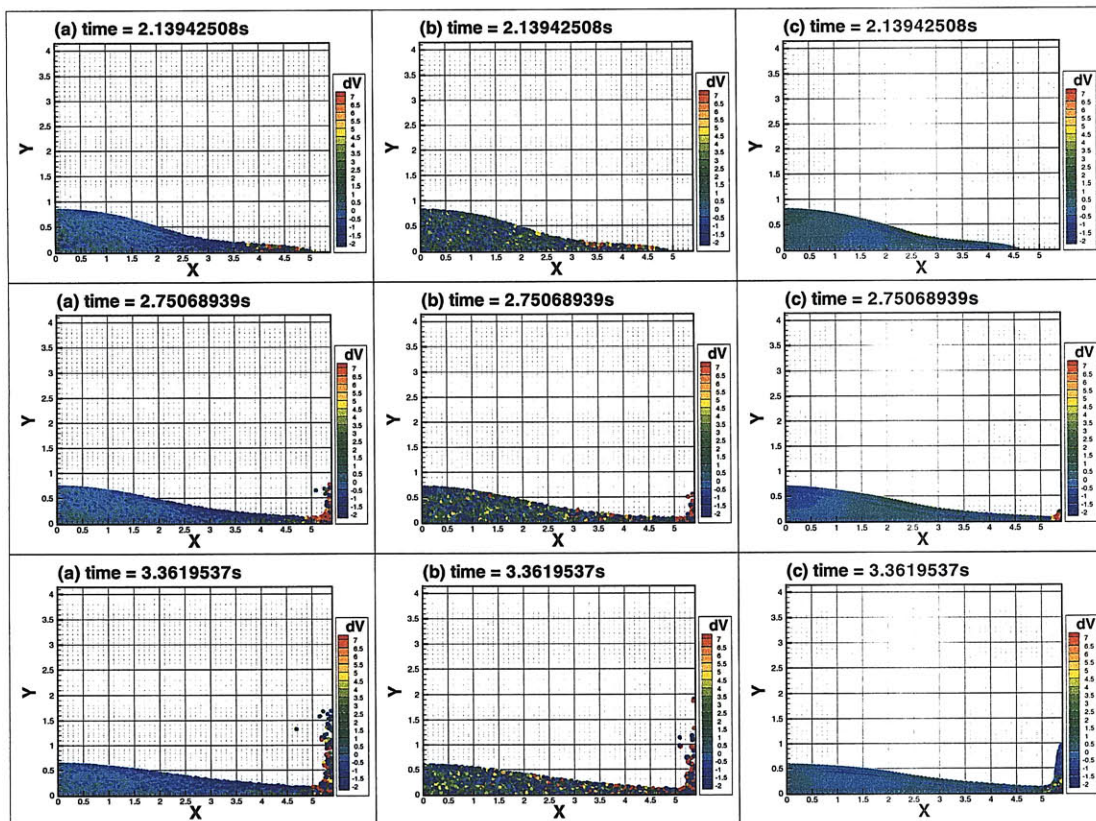


Figure 4-36: In color. Comparison of time evolving snapshots of the vertical accelerations of (a) MA-SPH with MLS density re-initialization, (b) mSPH with no smoothing, and (c) mSPH with smoothing every  $n = 5$  time steps. The artificial speed of sound is  $c = 26.46m/s$ , the kernel bandwidth is  $h = 0.025$ , the particle spacing is  $dx = 0.75h$  and the Courant condition  $\mu_c = 0.8$  for all simulations. Time increases from top to bottom. It is emphasized that all three simulations are initialized with the same initial conditions, employ identical spatial and temporal discretization parameters, the contour levels use the same coloring schemes, *no* filtering or post-processing has been employed in any of the results, and finally no other treatments have been employed other than those described.

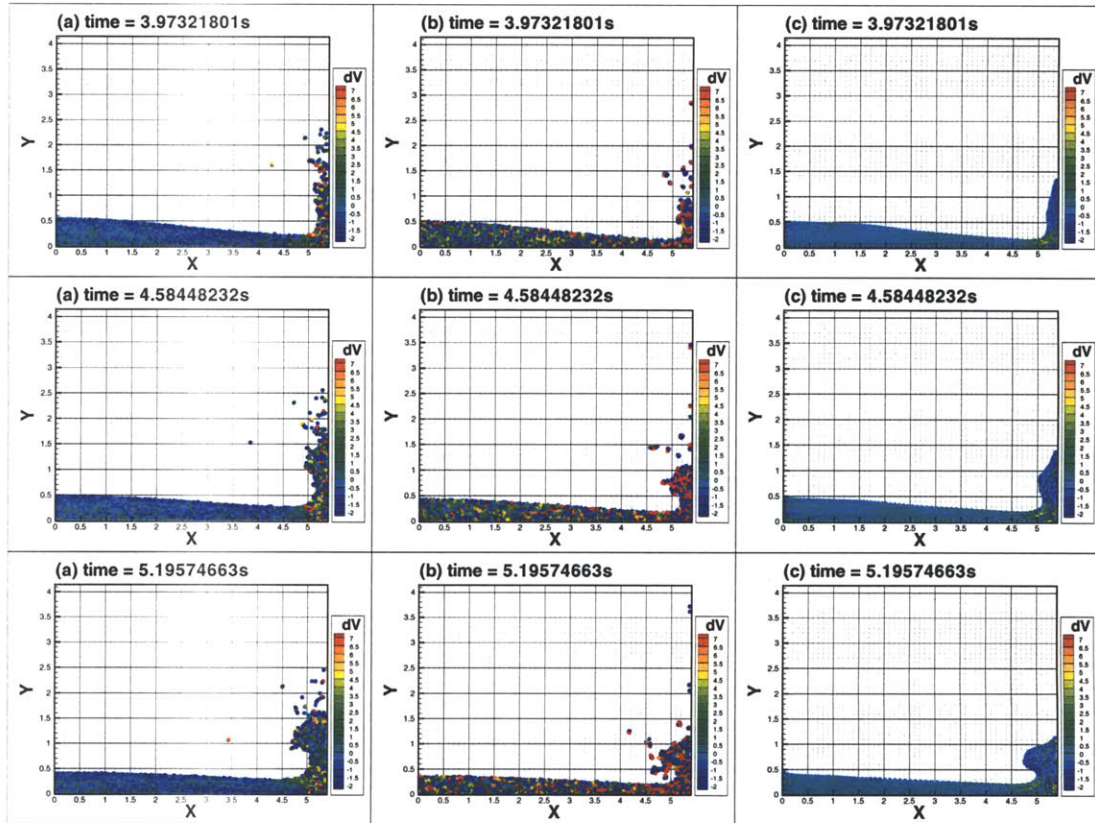


Figure 4-37: In color. Comparison of time evolving snapshots of the vertical accelerations of (a) MA-SPH with MLS density re-initialization, (b) mSPH with no smoothing, and (c) mSPH with smoothing every  $n = 5$  time steps. The artificial speed of sound is  $c = 26.46\text{m/s}$ , the kernel bandwidth is  $h = 0.025$ , the particle spacing is  $dx = 0.75h$  and the Courant condition  $\mu_c = 0.8$  for all simulations. Time increases from top to bottom. It is emphasized that all three simulations are initialized with the same initial conditions, employ identical spatial and temporal discretization parameters, the contour levels use the same coloring schemes, *no* filtering or post-processing has been employed in any of the results, and finally no other treatments have been employed other than those described.

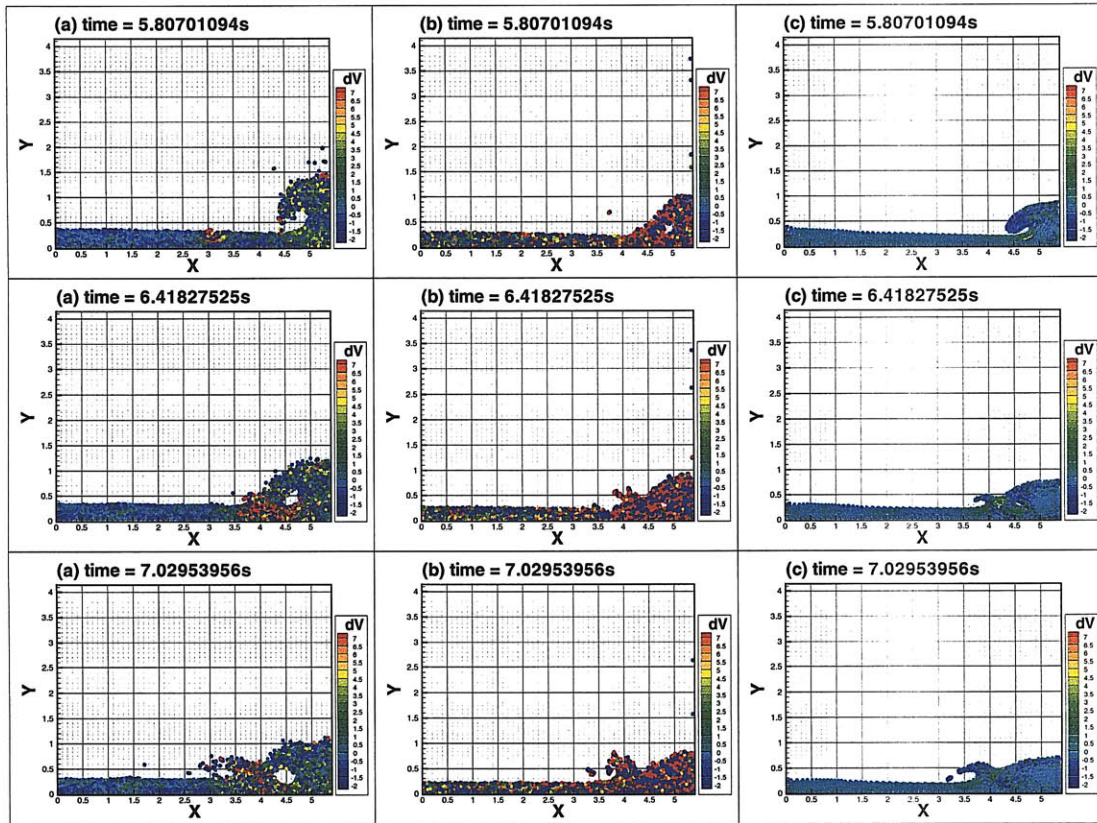


Figure 4-38: In color. Comparison of time evolving snapshots of the vertical accelerations of (a) MA-SPH with MLS density re-initialization, (b) mSPH with no smoothing, and (c) mSPH with smoothing every  $n = 5$  time steps. The artificial speed of sound is  $c = 26.46m/s$ , the kernel bandwidth is  $h = 0.025$ , the particle spacing is  $dx = 0.75h$  and the Courant condition  $\mu_c = 0.8$  for all simulations. Time increases from top to bottom. It is emphasized that all three simulations are initialized with the same initial conditions, employ identical spatial and temporal discretization parameters, the contour levels use the same coloring schemes, *no* filtering or post-processing has been employed in any of the results, and finally no other treatments have been employed other than those described.

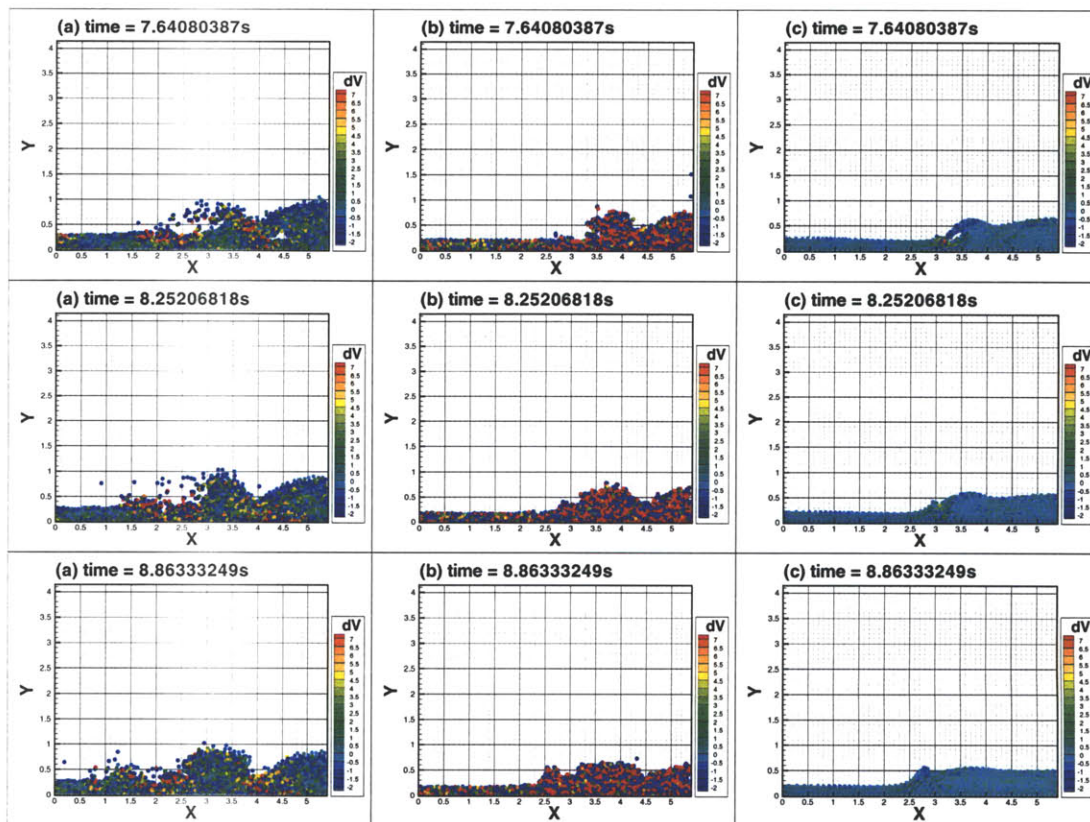


Figure 4-39: In color. Comparison of time evolving snapshots of the vertical accelerations of (a) MA-SPH with MLS density re-initialization, (b) mSPH with no smoothing, and (c) mSPH with smoothing every  $n = 5$  time steps. The artificial speed of sound is  $c = 26.46m/s$ , the kernel bandwidth is  $h = 0.025$ , the particle spacing is  $dx = 0.75h$  and the Courant condition  $\mu_c = 0.8$  for all simulations. Time increases from top to bottom. It is emphasized that all three simulations are initialized with the same initial conditions, employ identical spatial and temporal discretization parameters, the contour levels use the same coloring schemes, *no* filtering or post-processing has been employed in any of the results, and finally no other treatments have been employed other than those described.

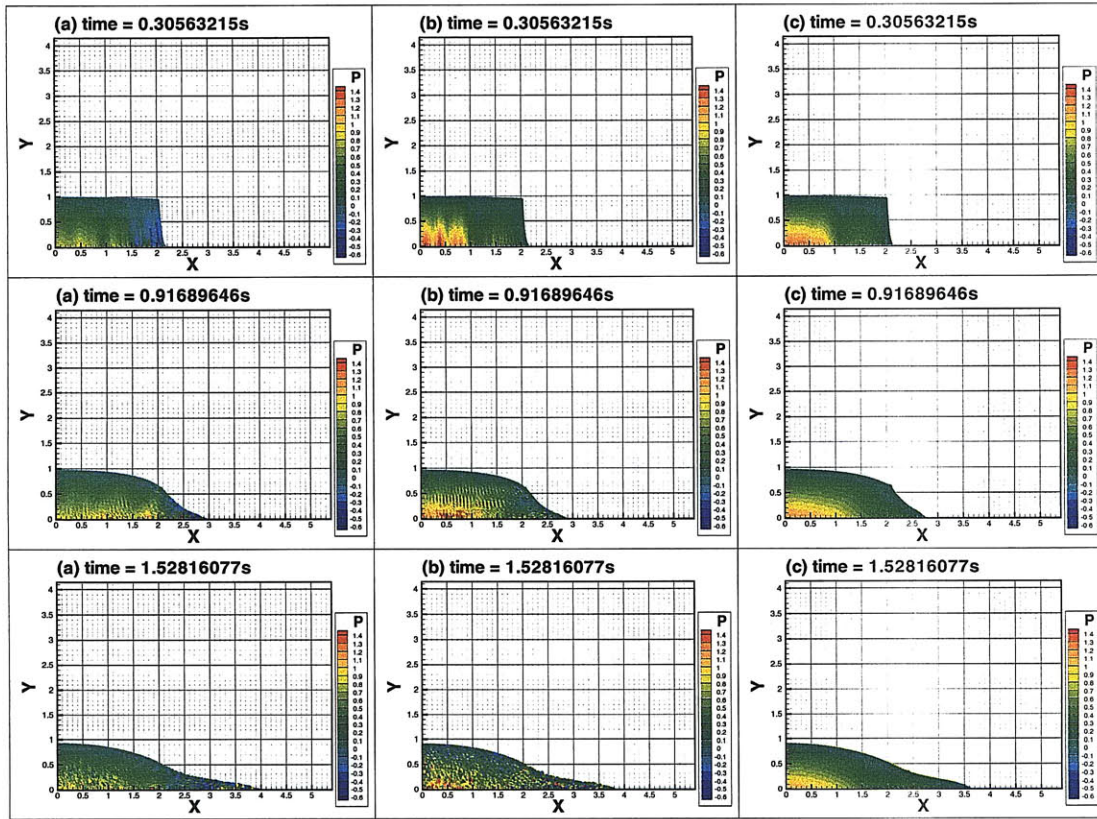


Figure 4-40: In color. Comparison of time evolving snapshots of the pressure field of (a) MA-SPH with MLS density re-initialization, (b) mSPH with no smoothing, and (c) mSPH with smoothing every  $n = 5$  time steps. The artificial speed of sound is  $c = 26.46m/s$ , the kernel bandwidth is  $h = 0.025$ , the particle spacing is  $dx = 0.75h$  and the Courant condition  $\mu_c = 0.8$  for all simulations. Time increases from top to bottom. It is emphasized that all three simulations are initialized with the same initial conditions, employ identical spatial and temporal discretization parameters, the contour levels use the same coloring schemes, *no* filtering or post-processing has been employed in any of the results, and finally no other treatments have been employed other than those described.

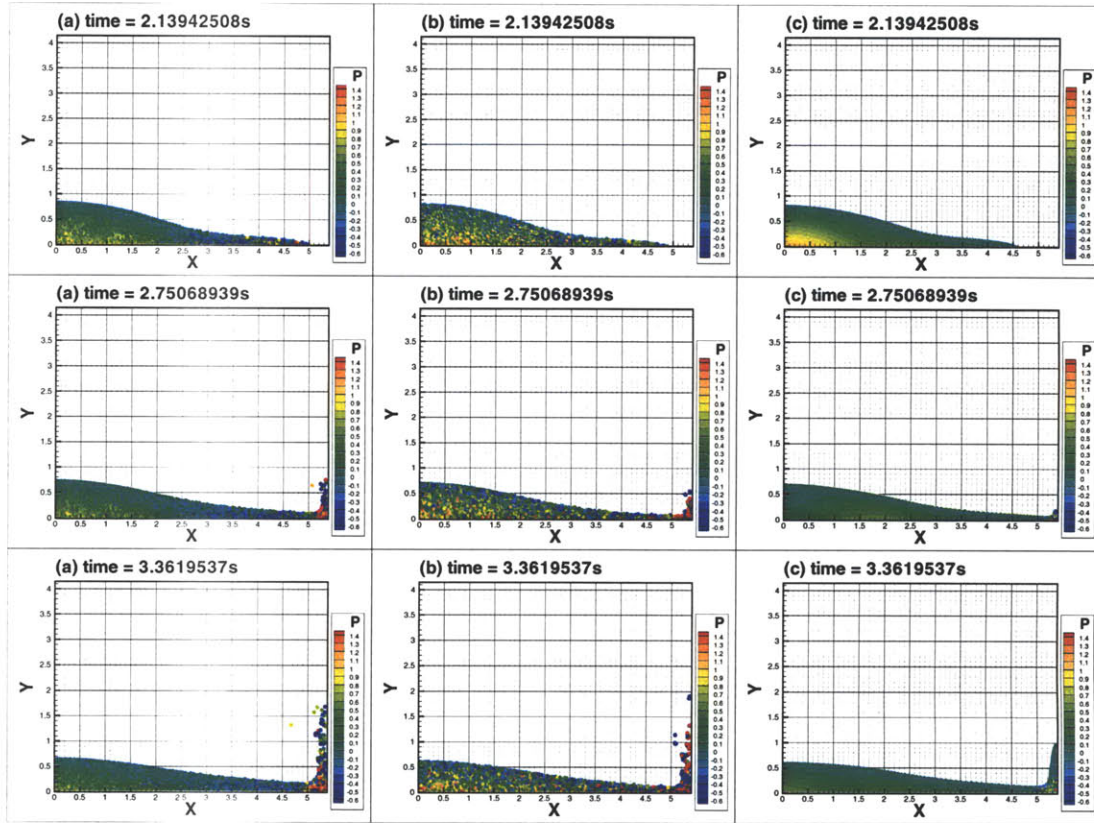


Figure 4-41: In color. Comparison of time evolving snapshots of the pressure field of (a) MA-SPH with MLS density re-initialization, (b) mSPH with no smoothing, and (c) mSPH with smoothing every  $n = 5$  time steps. The artificial speed of sound is  $c = 26.46m/s$ , the kernel bandwidth is  $h = 0.025$ , the particle spacing is  $dx = 0.75h$  and the Courant condition  $\mu_c = 0.8$  for all simulations. Time increases from top to bottom. It is emphasized that all three simulations are initialized with the same initial conditions, employ identical spatial and temporal discretization parameters, the contour levels use the same coloring schemes, *no* filtering or post-processing has been employed in any of the results, and finally no other treatments have been employed other than those described.

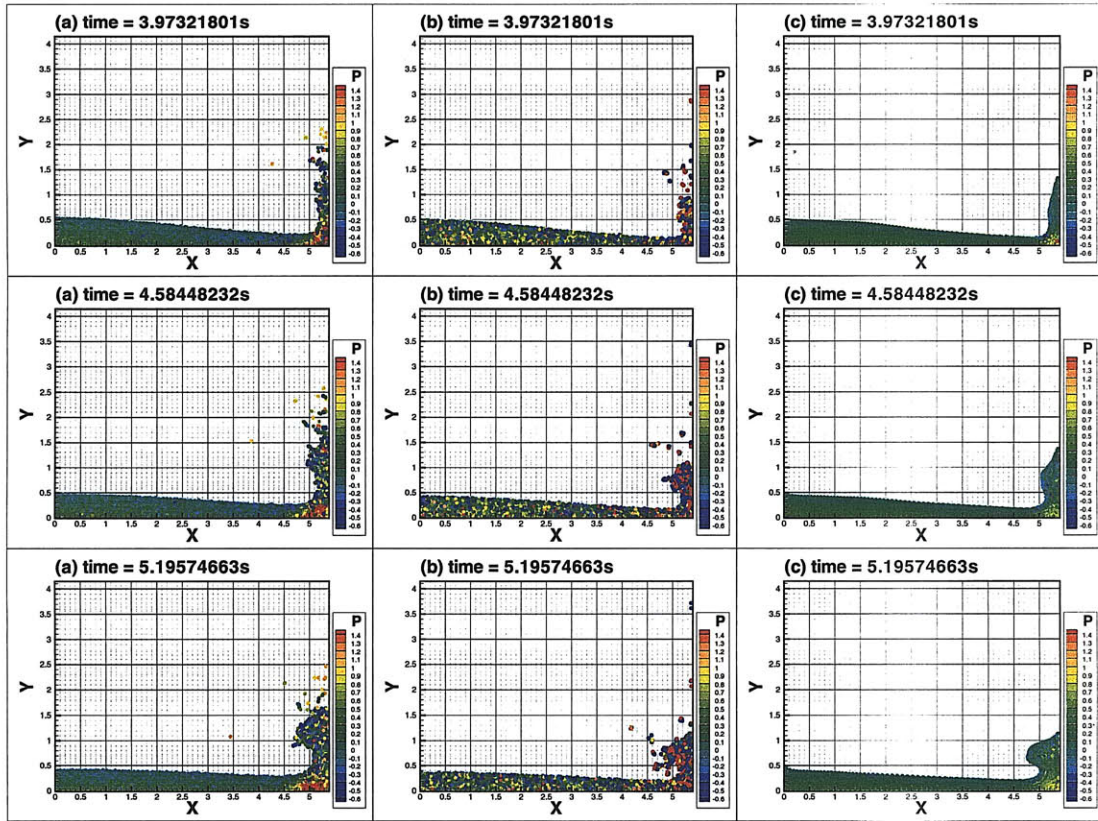


Figure 4-42: In color. Comparison of time evolving snapshots of the pressure field of (a) MA-SPH with MLS density re-initialization, (b) mSPH with no smoothing, and (c) mSPH with smoothing every  $n = 5$  time steps. The artificial speed of sound is  $c = 26.46m/s$ , the kernel bandwidth is  $h = 0.025$ , the particle spacing is  $dx = 0.75h$  and the Courant condition  $\mu_c = 0.8$  for all simulations. Time increases from top to bottom. It is emphasized that all three simulations are initialized with the same initial conditions, employ identical spatial and temporal discretization parameters, the contour levels use the same coloring schemes, *no* filtering or post-processing has been employed in any of the results, and finally no other treatments have been employed other than those described.

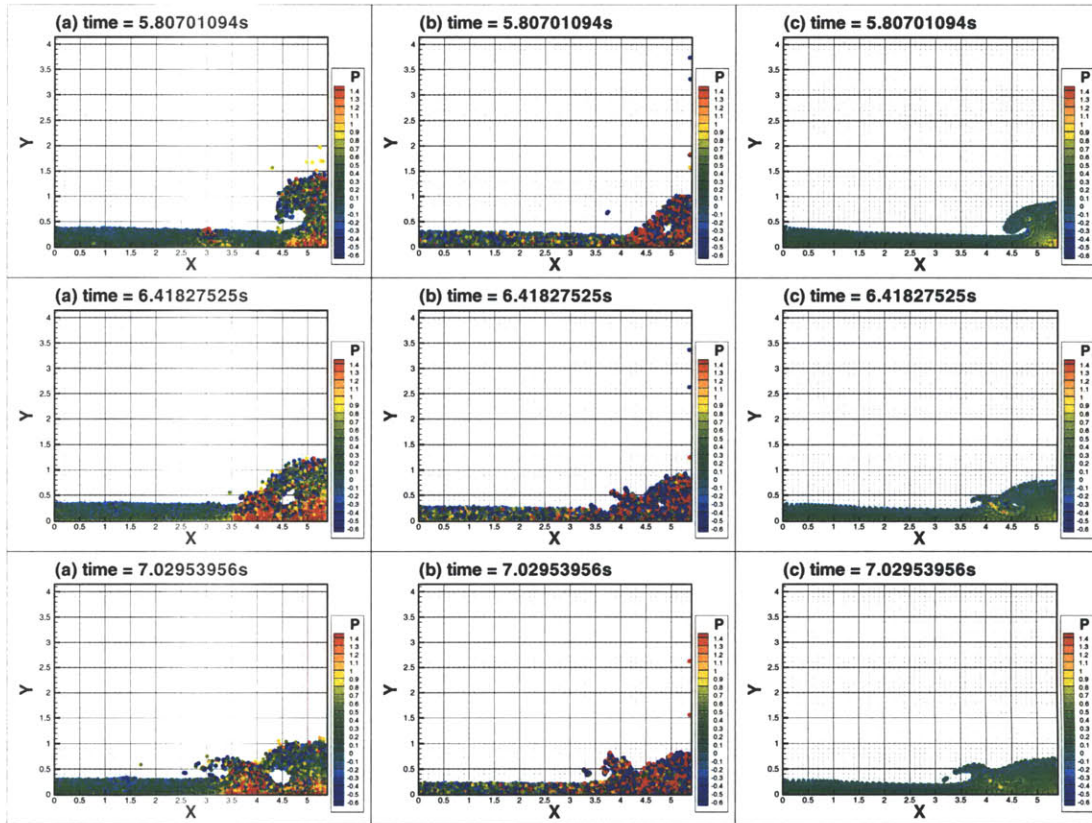


Figure 4-43: In color. Comparison of time evolving snapshots of the pressure field of (a) MA-SPH with MLS density re-initialization, (b) mSPH with no smoothing, and (c) mSPH with smoothing every  $n = 5$  time steps. The artificial speed of sound is  $c = 26.46m/s$ , the kernel bandwidth is  $h = 0.025$ , the particle spacing is  $dx = 0.75h$  and the Courant condition  $\mu_c = 0.8$  for all simulations. Time increases from top to bottom. It is emphasized that all three simulations are initialized with the same initial conditions, employ identical spatial and temporal discretization parameters, the contour levels use the same coloring schemes, *no* filtering or post-processing has been employed in any of the results, and finally no other treatments have been employed other than those described.

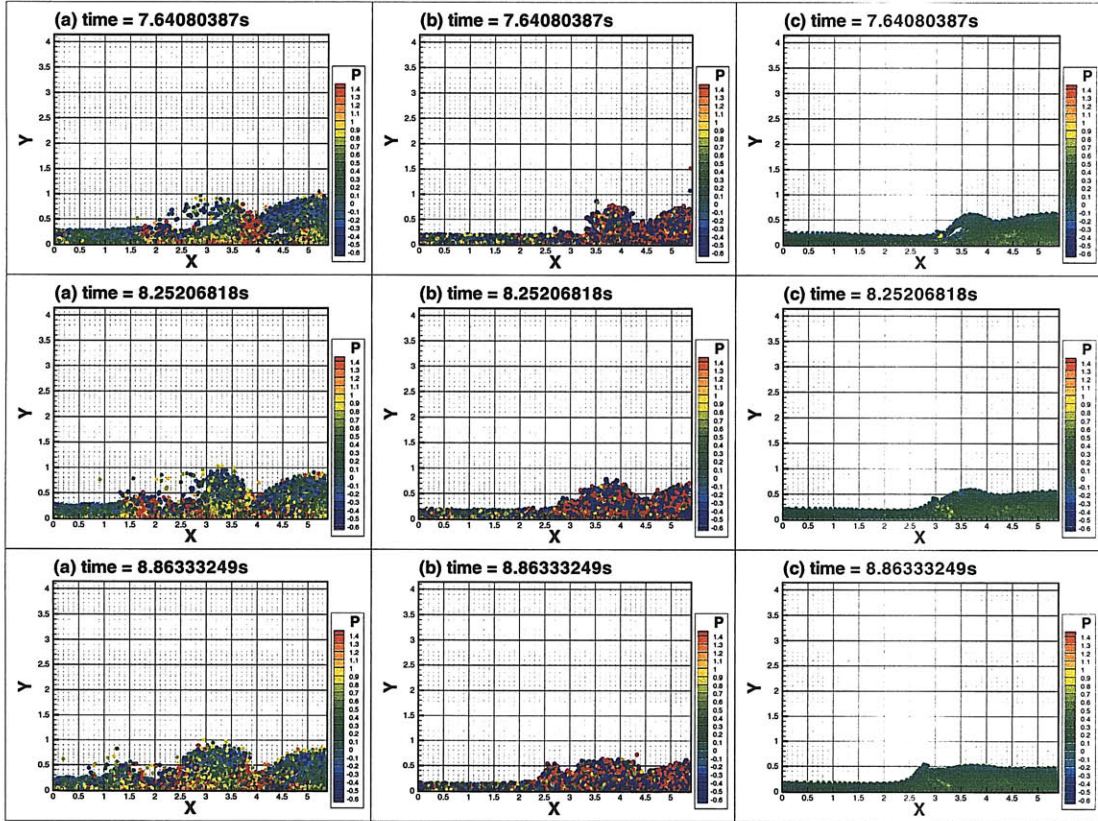


Figure 4-44: In color. Comparison of time evolving snapshots of the pressure field of (a) MA-SPH with MLS density re-initialization, (b) mSPH with no smoothing, and (c) mSPH with smoothing every  $n = 5$  time steps. The artificial speed of sound is  $c = 26.46m/s$ , the kernel bandwidth is  $h = 0.025$ , the particle spacing is  $dx = 0.75h$  and the Courant condition  $\mu_c = 0.8$  for all simulations. Time increases from top to bottom. It is emphasized that all three simulations are initialized with the same initial conditions, employ identical spatial and temporal discretization parameters, the contour levels use the same coloring schemes, *no* filtering or post-processing has been employed in any of the results, and finally no other treatments have been employed other than those described.

Figure 4-45 compares the effect of smoothing on the global error metric  $Q(t)$  without smoothing, and with smoothing every  $n$  time steps for a given Courant condition  $\mu = 0.8$ . From the analysis it is expected that for  $\mu$  the optimal value of the re-initialization period is  $n = 5$ . It is shown that indeed the value of  $Q(t)$  for the combination  $\mu = 0.8, n = 5$  is significantly dissipated.

Figures 4-46, 4-46, 4-47 validate the free-surface elevation and *unfiltered* wall impact pressures of the standard SPH dam-break benchmark with experimental results of [55] without smoothing and with smoothing every  $n$  time steps for a constant Courant condition  $\mu = 0.8$ . From the analysis it is expected that for  $\mu$  the optimal value of the re-initialization period is  $n = 5$ . It is shown that for the combination  $\mu = 0.8, n = 5$  the experimental data and mSPH simulation results are in the best agreement. For  $n > 5$  the pressures are overestimated, while for  $n < 5$  the system is over-dissipated.

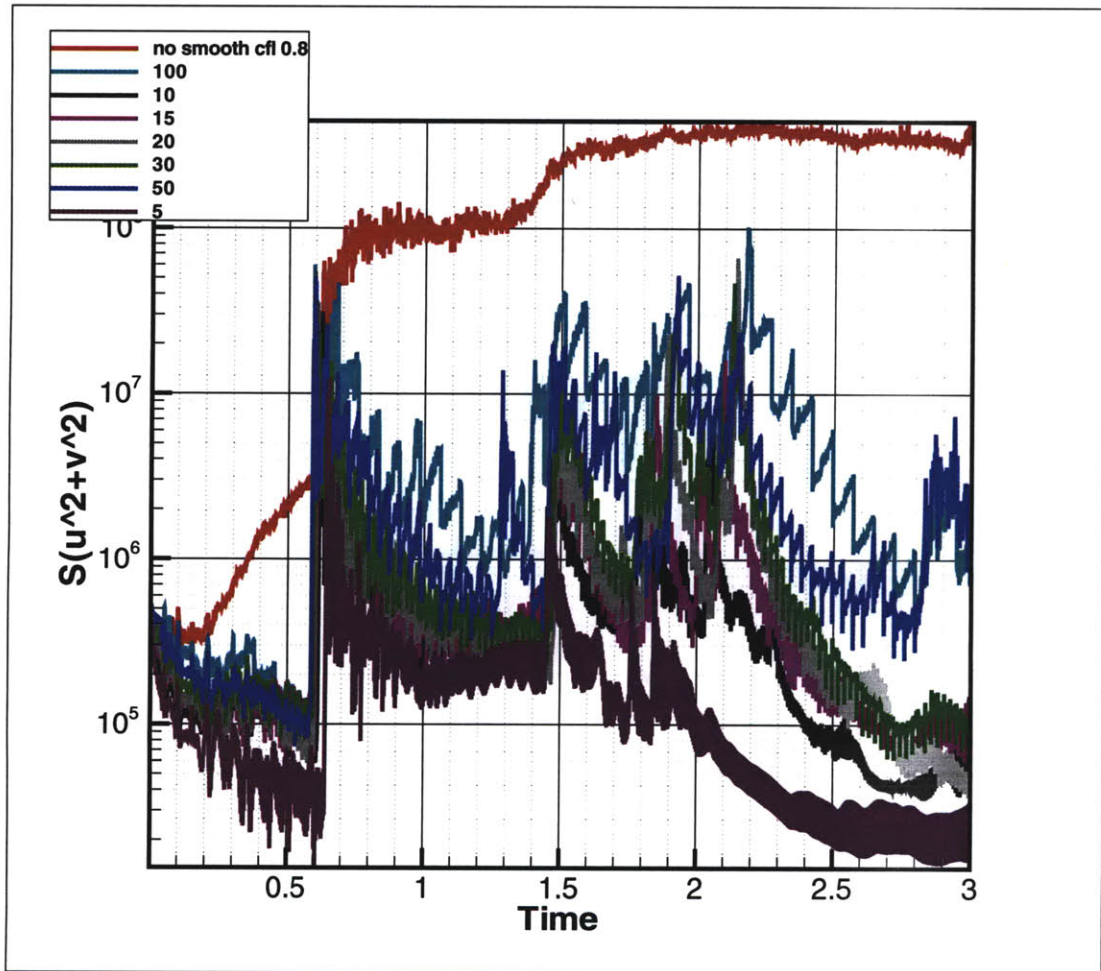


Figure 4-45: Comparisons of the evolution of  $Q(t)$  in an mSPH dam-break simulation without smoothing (red line) and with smoothing every  $n$  time steps for a constant Courant condition  $\mu = 0.8$  for all simulations. Smoothing periods  $n = [5, 10, 15, 20, 30, 50, 100]$ .

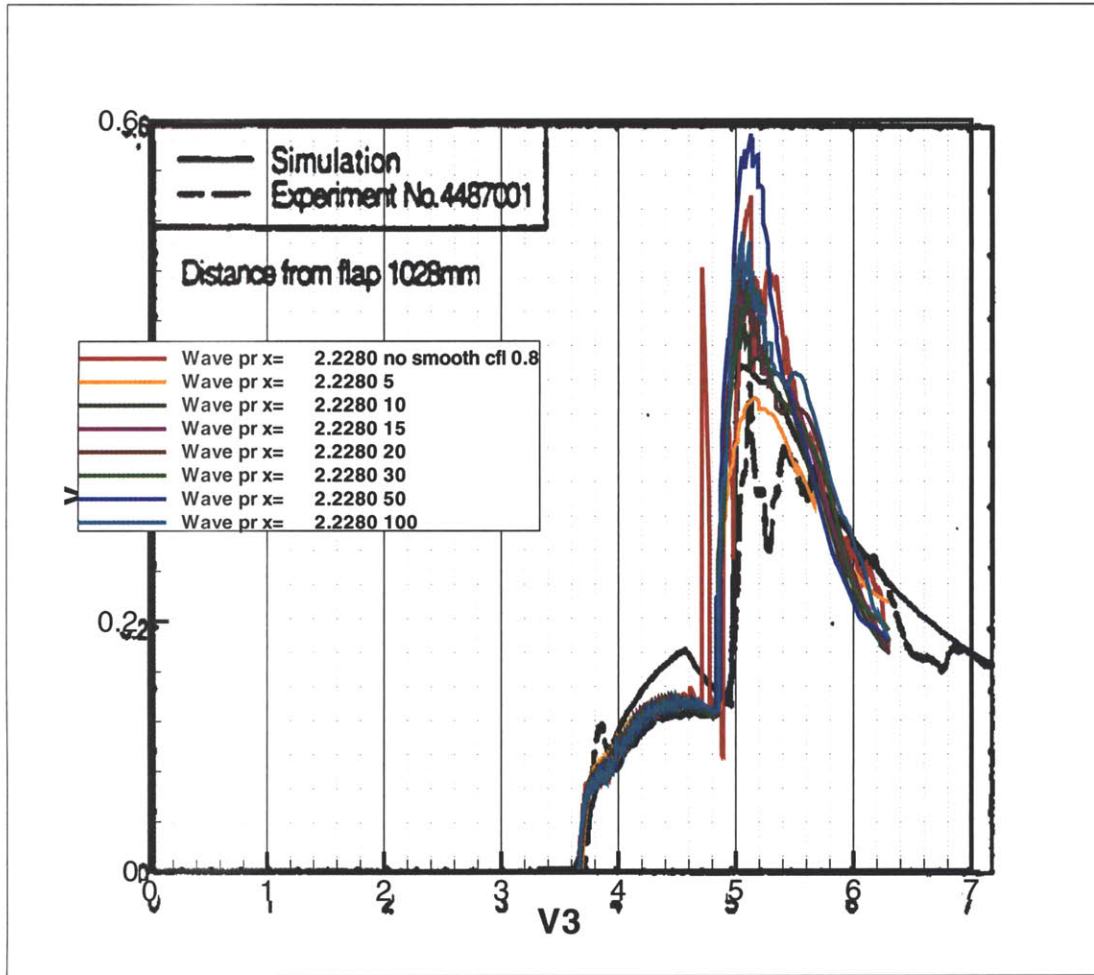


Figure 4-46: Comparison of free-surface elevation of the standard SPH dam-break benchmark with experimental results of [55] (black line) and mSPH simulation results without smoothing (red line) and with smoothing every  $n$  time steps for a constant Courant condition  $\mu = 0.8$  for all simulations. Smoothing periods  $n = [0, 5, 10, 15, 20, 30, 50, 100]$ .

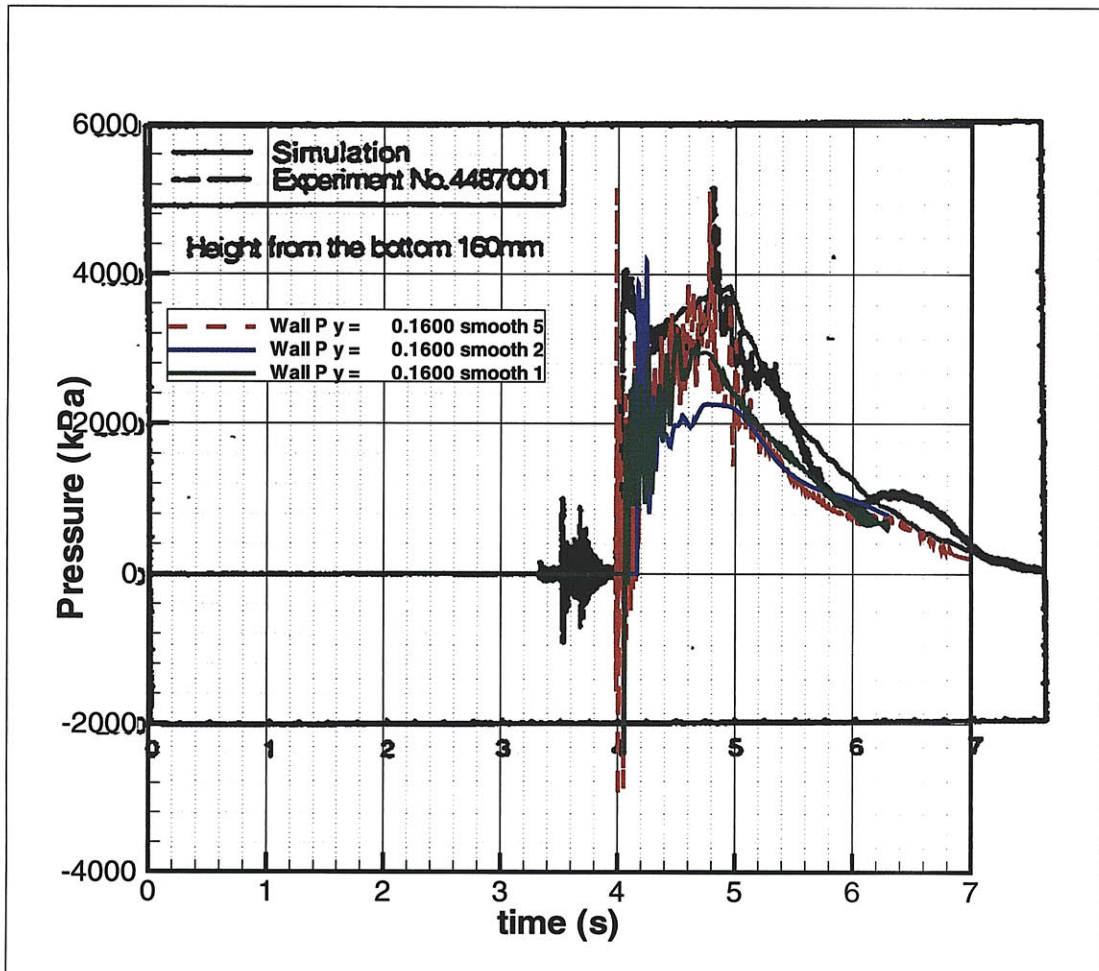


Figure 4-47: Comparison of *unfiltered* wall impact pressures of the standard SPH dam-break benchmark with experimental results of [55] (black line) and mSPH simulation results with smoothing every  $n$  time steps for a constant Courant condition  $\mu = 0.8$  for all simulations. Smoothing periods  $n = [1, 2, 5]$ .

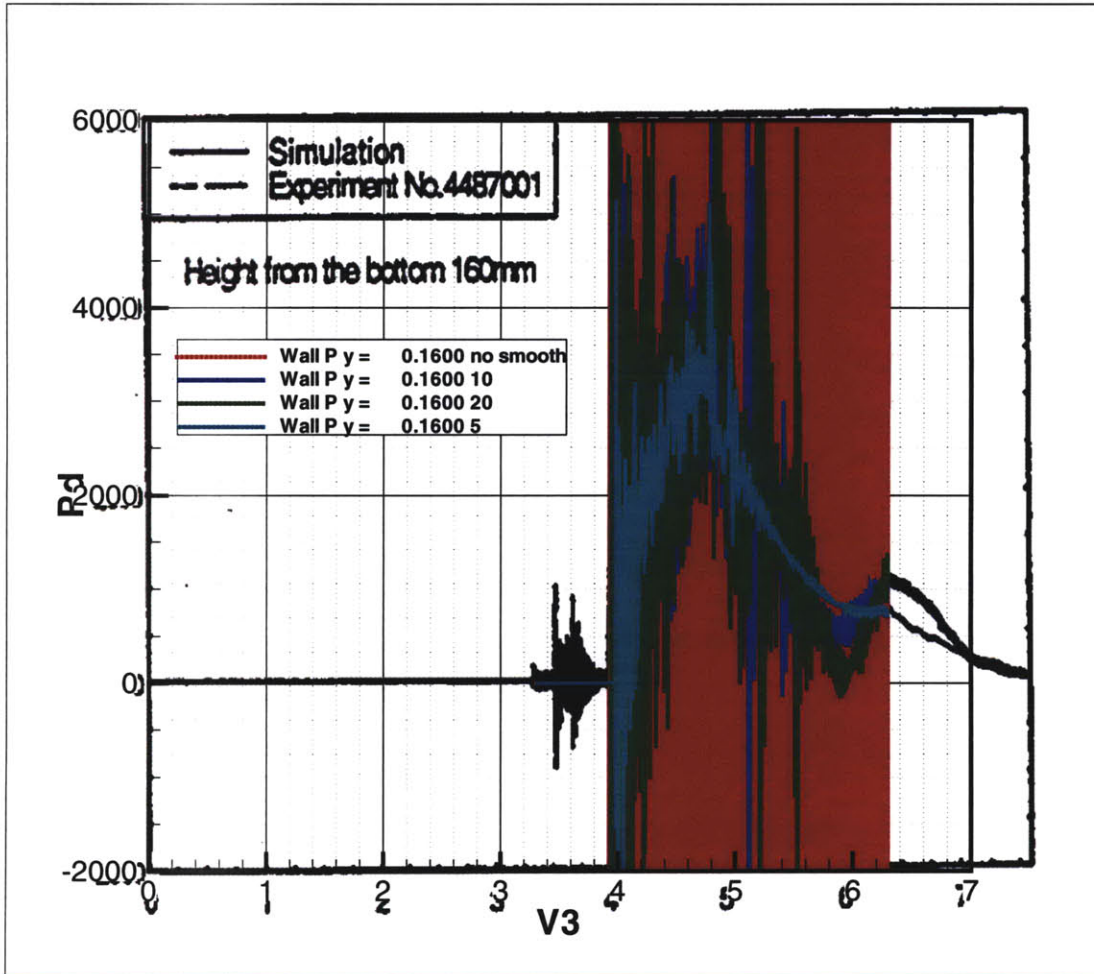


Figure 4-48: Comparison of *unfiltered* wall impact pressures of the standard SPH dam-break benchmark with experimental results of [55] (black line) and mSPH simulation results without smoothing (red line) and with smoothing every  $n$  time steps for a constant Courant condition  $\mu = 0.8$  for all simulations. Smoothing periods  $n = [0, 5, 10, 20]$ . It is pointed out that the mSPH simulation results without smoothing (red line) seem like a solid line due to the significant HFO of amplitude  $6 \cdot 10^4$  (not shown).

## 4.4 Discussion

Two approaches in modifying MA-SPH have been suggested based on the technique used for the computation of spatial derivatives. The first is a higher-order SPH, hSPH scheme that employs Moving Least Squares. The second is a modified SPH, mSPH scheme that employs the standard SPH Kernel Interpolation derivative computation technique. This section discusses issues and further developments for each approach.

In choosing the mSPH approach, it must be pointed out that the scheme will remain of low-order, bounded by the Kernel Interpolation consistency within the domain. Further improvements include: (a) increasing the consistency near the free-surface, but within the Kernel Interpolation framework, (b) regularizing for depth decaying modes, and (c) improving the accuracy by projecting onto an incompressible solution.

An approach towards increasing the consistency is sketched here. In section 2.5.5 it was determined that when the Kernel Interpolation technique is employed for the evaluation of spatial derivatives the inclusion of either the direct or advanced particle density is required to ensure numerical consistency. Based on this finding a split-density scheme can be introduced, in which the density is decomposed into two parts according to:

$$\rho = (\rho_0 - \rho_f) + \underbrace{\rho_f + \rho_{adv}}_{\rho_{KI}}.$$

The total density  $\rho$  is used in the EoS, while the density  $\rho_{KI}$  is used for the computation of the derivatives with Kernel Interpolation. This decomposition can improve the consistency of the Kernel Interpolation, particularly close to the free-surface, without altering the simulated physics.

To formulate the governing equations, the time rate of change of the EoS is considered and  $d\rho/dt$  is substituted from the conservation of mass (4.20) obtaining the time rate of change of the pressure:

$$\frac{dP}{dt} = c^2 \frac{d\rho_0}{dt} - c^2 \rho \nabla \cdot \vec{u}. \quad (4.57)$$

In particular, for an initial hydrostatic density distribution  $\rho_0 = \rho_f(1 - 2\delta y)$  the governing equations for the split-density scheme are still described by (4.19) and (4.36), but the EoS is replaced by:

$$\frac{dP}{dt} = \underbrace{-\rho_f g v}_{\text{hydrostatic}} \underbrace{-c^2 \rho \nabla \cdot \vec{u}}_{\text{hydrodynamic}}, \quad (4.58)$$

where  $v = dy/dt$  has been used. Introducing the intermediate density variable  $\rho_{KI}$ , the density is integrated in time based on:

$$\rho_{KI} = \rho_f + \int \frac{d\rho}{dt} dt \quad (4.59)$$

$$\rho = \underbrace{(\rho_0 - \rho_f)}_{-2\delta\rho_f y} + \rho_{KI}. \quad (4.60)$$

This split-advanced density formulation can improve the consistency near the free-surface by adjusting the  $\rho_{KI}$  without affecting the physics.

Improving the accuracy of mSPH by projecting into an incompressible flow field with an iterative artificial compressibility method is also suggested. However, it is realized that such scheme will only affect accuracy, but neither stability or consistency.

In choosing the hSPH approach it must be realized that robustness is currently the main issue. The strength of hSPH is the periodic instability removal and incompressible flow-field re-initialization scheme. However, this re-initialization requires mapping onto a regular grid and detection of the free-surface. Despite recent developments on mapping SPH flows onto regular grids [47], this is a limitation of the most attractive feature of SPH, i.e., it is entirely meshless. For completeness both approaches have been described, but it must be pointed out that hSPH will require improvements before it can be employed in the highly non-linear flows of interest.

## 4.5 Conclusions

Detailed analysis of MA-SPH in Chapter 2, and insight gained from the effects of the existing semi-empirical treatments in Chapter 3, allowed us to obtain a very clear understanding of the SPH method for free-surface flows and propose rational modifications to address the current key SPH issues. Two approaches are highlighted based on the technique employed for the computation of spatial derivatives. The first is a higher-order SPH scheme, hSPH, that employs Moving Least Squares for the computation of spatial derivatives. The second is a modified SPH scheme, mSPH, that employs Kernel Interpolation for the computation of spatial derivatives. Both schemes have different advantages and disadvantages.

The mSPH scheme is a  $O(N)$ , first-order method like SPH but (i) removes the tuneable semi-empirical treatments currently associated with SPH, (ii) retains the robustness of SPH, with increased efficiency since it allows for constant time-steps, (iii) has a simpler algorithm than SPH, and (iv) most importantly, is stable. Therefore, mSPH can be used to obtain fast, convergent dynamics of violent free-surface flows that most other numerical methods cannot simulate.

The hSPH scheme is a  $O(N)$  method and retains the weak compressibility assumption like SPH but (i) is second-order, (ii) periodically projects the flow onto an incompressible solution and (iii) is stable. However, the applicability of hSPH is currently limited to periodic domains.

# Chapter 5

## Conclusions

### 5.1 Thesis contributions

Smoothed Particle Hydrodynamics (SPH) is a mature meshless Lagrangian particle method that first appeared in 1977 in [5, 7] for the simulation of unbounded astrophysical flows. The SPH algorithm is very attractive in that it is simple, efficient with operation count  $O(N)$ , and highly parallelizable. In addition, it is robust and obtains ‘pretty pictures’, i.e., it qualitatively captures the kinematics of complex, highly non-linear flows. For these reasons, SPH has found applications in violent flows across different disciplines including shock capturing, die-casting, explosions, magnetohydrodynamics, and granular flow, to name a few.

SPH was first extended to free-surface hydrodynamic flows in [30]. It is used to simulate transient, highly non-linear flows, with complex, multi-scaled free-surfaces that can be multiply connected (such as the standard SPH dam-break benchmark) where most other methods fail. Typically, the simulated free-surfaces compare well with experiments, while dynamic quantities are plagued by spurious, large amplitude, high frequency oscillations rendering the dynamics practically unusable without filtering.

Despite the method’s attractiveness and increasing popularity (SPHERIC 2006-2010), the method cannot be validated for a simple hydrostatic case [21]. There exists no conclusive numerical analysis with uncertainties on the method’s accuracy, e.g.,

[2], and consistency, e.g., [25], and the simulations are unstable [53]. To address these issues and uncertainties, several tunable semi-empirical treatments have been developed, following the approach of [30]. As a consequence the present State-of-the-Art SPH, SPHysics, for applications in free-surface hydrodynamics [1, 48]. includes many tunable semi-empirical treatments which further add to the uncertainty currently associated with the method.

This thesis has three objectives. First, to perform an analytical and numerical investigation of the SPH method for free-surface flows, focusing primarily on understanding the physics captured and the numerical behavior through a detailed analysis. Second, to develop a rationale on analyzing the existing semi-empirical treatments of the State-of-the-Art SPH, elucidate their benefits, and where applicable provide guidelines on their usage. Third, and based on the findings of the analysis, to develop rational, and convergent SPH methods that obtain validated dynamics retaining the simplicity, robustness, and efficiency of the existing SPH.

All three objectives are met. We perform for the first time a unified, quantitative error analysis of the SPH method. We identify and analyze the weak spurious high frequency oscillations that dominate the dynamics. We demonstrate consistency of the method away from the free-surface, a major source of uncertainty in SPH. We further identify and verify the stability behavior of the method with the corresponding growth rates. We extend the analysis to the existing semi-empirical SPH treatments by classifying them with respect to accuracy, consistency, or stability. We demonstrate that in general the ad-hoc treatments point to the right direction, but insufficiently. Based on the findings of the analysis, we develop a modified SPH scheme for the dynamics of violent free-surface flows that maintains the robustness and simplicity of SPH, but in addition has known consistency, stability, and dissipative properties and has significantly reduced spurious solutions.

Specifically, in Chapter 2 we perform a quantitative, unified analysis of the numerical method and the physics it captures. In section 2.2 we introduce the notion of a main SPH algorithm and in section 2.3 we justify and sketch the framework of the analysis. In section 2.4 we assess the weak compressibility assumption within

the context of linear, free-surface waves based on the validated analysis of [8, 46] in continuous space. It is determined that the method converges to the desired incompressible solution as the artificial speed of sound increases but in addition permits high frequency acoustic modes. It is realized that these modes in a discrete numerical simulation are generated predominantly by numerical inconsistencies and are therefore spurious and undesired, shedding light on the origins of the spurious solutions that plague the SPH dynamics. In section 2.5 we investigate the consistency properties of Kernel Interpolation. We account for the motion of the fluid particles and show the numerical significance of the density in maintaining the consistency of the Kernel Interpolation technique. We further investigate the behavior of Kernel Interpolation on the free-surface and determine the artificial dynamic free-surface boundary condition imposed as a function of the free-surface slope. Lastly, in section 2.6 we assess the method's stability properties in the continuous, semi-discrete, and fully-discrete formulations. We determine that three type of instabilities are manifested in an SPH simulation. The first are depth decaying, allowed in the presence of a free-surface. The second are purely oscillatory that appear in the presence of non-zero base density gradients. The third are introduced by the numerical temporal integration scheme and depend on the Courant condition, and these are the ones actually observed in a numerical simulation.

In Chapter 3 we extend the analysis to address the effects of different empirical SPH treatments introduced in the literature. We classify these respectively as accuracy, consistency, or stability treatments. These treatments are further analyzed within the context of the issue they address, characterizing their effectiveness. This analysis, based on the existing empirical knowledge, sheds light on the rationale behind each treatment and guides us towards the rational development of convergent SPH methods in Chapter 4.

Finally, in Chapter 4 we propose the rational development of convergent SPH methods that maintain key features of SPH, significantly reduce spurious errors present in current SPH implementations, obtain validated dynamics, and have known consistency and stability behaviors.

This thesis is among the first to provide a unified systematic analysis of the SPH method, shedding insight into the many proposed variations and treatments, and informs and guides new rational improvements to the method. This work lays the foundation for the development of SPH as a valuable engineering tool in the study of violent free-surface flows.

## 5.2 Perspectives on the SPH approach

SPH is simple, robust, efficient and can be used for the simulation of the most difficult free-surface problems. However, the method has very limited credibility in the scientific community due to the lack of analysis, its semi-empirical nature and the presence of large high frequency oscillations predominant in the dynamics.

In some ways, the extension of SPH for free-surface hydrodynamic flows with the weak compressibility assumption presented in [30] is ingenious, in that it essentially demonstrates that once we are in the discrete space and accept any discretization errors (provided we know their behavior) it is legitimate to accept modeling errors as well (provided we know their behavior). Once the modeling and discretization errors are understood, the method's credibility is restored, since understanding the behavior of such errors is the essence of numerical analysis. In that sense, SPH should be regarded as a pioneer in the field of computational fluid dynamics.

The success of Kernel Interpolation within SPH can be regarded as a surprising bonus. If Kernel Interpolation did not *happen* to have the consistency properties it has, SPH would have never met such success.

Inversely, the issues in SPH could have been avoided, if [30] had not directed towards a semi-empirical approach. To make matters worse, the method's robustness allowed for literally random initial and boundary conditions, which are decomposed into unstable acoustic modes. To stabilize the method numerous tunable semi-empirical treatments are employed, some of which do indeed reduce the acoustic growth rates but others only affect the simulated physics. In the end, the kinematic simulations results are qualitatively correct, but the dynamics are plagued by large amplitude high

frequency oscillations and it is impossible to distinguish between the real physics and the artificial physics introduced from the treatments rendering the simulations results unreliable.

In summary, as long as the limitations on the accuracy of the method are understood, it is not the method itself, but rather the approach in using SPH that diminished its credibility.

Finally, it is noted that the analysis of SPH, even though very simple in the mathematical sense, has been challenging and interesting in a unique way. In a first step the analysis requires to distinguish between the three different sources of error, namely the modeling error, the consistency error due to the Kernel Interpolation, and finally errors due to instabilities. Next, it must be realized that these three sources of error interact. In other words, the analysis has to be performed iteratively. In a first step the sources of error are classified and identified, while in the next steps the quantitative error estimates are updated by taking into account the coupling between the different approximations. For example, the weak compressibility assumption behaves differently in the continuum and in the discrete space since it is highly affected by the spurious boundary conditions imposed by the Kernel Interpolation (section 2.4.1.5). In turn, the consistency of the Kernel Interpolation depends on the flow properties inside the domain (section 2.5.5) and on the shape of the free-surface, close to the free-surface (section 2.5.6). Lastly, the stability properties of the scheme are significantly affected not only by the temporal integration scheme and the associated Courant condition (section 2.6.4), but also by the base density distribution, which for the flows of interest should be regarded as hydrostatic (sections 2.6.2 and 2.6.4.1), and finally by the shape of the domain (section 2.6.5), rendering the useful simulation life strongly problem-dependent: in the worst case scenario it deteriorates very fast and in the best case scenario obtains spurious dynamics.

### 5.3 Future work

Four different areas of future work can be identified. The first area of future work is related to extending the analysis of SPH for free-surface flows specifically. The immediate extension is to obtain a quantitative understanding of the effects of the implicit dynamic free-surface boundary condition due to the incomplete Kernel Interpolation near the free-surface in both the continuum and discrete space. In the continuum the primary interest is to understand the long-time effects of the implicit dynamic free-surface boundary condition. One approach to achieve this is to incorporate the implicit dynamic free-surface boundary condition into the continuous problem of linear plane progressive waves and seek for the solution. The eigenmodes will not be affected, by employing a non-zero boundary condition, but the solution might eventually become entirely acoustic. In the discrete space the main interest is to compute the wavenumbers and initial amplitudes of the spurious acoustic modes. One way to achieve this is by decomposing the results of the consistency analysis in 2.5.6 into incompressible and acoustic modes, with the modal decomposition developed in 2.4.3.

It is also of interest to extend the stability analysis of the semi-discrete scheme within the context of free-surface flows, in addition to the present results for a general infinitesimal base density distribution, and analyze the dispersion properties of the method accounting for gravity, in addition to the general analysis in [44].

The inclusion of viscosity is considered as an extension of the analysis of SPH, since currently it is not known how to obtain second spatial derivatives in an equally robust manner as with first derivatives. In that sense inclusion of turbulence models should also be considered as an analysis extension.

The second area of future work includes algorithmic extensions, such as increasing the order of accuracy of mSPH both inside the domain as well as near the free-surface, by differentiating between the numerical requirement on the density for the consistency of Kernel Interpolation and the density employed in the Equation of State to obtain the pressure. Finally, increase in the accuracy of mSPH could be achieved by projecting into a divergence-free space, as in hSPH, but with a periodic

pseudo-compressibility approach.

The third area of future work is related to extending current SPH applications in mSPH, such as parallelizing, addition of different phase particles, inclusion of different boundary geometries, extension to three dimensions.

Lastly, the fourth area of future work involves coupling with accurate larger scale models, where SPH will be used as the meso-scale method to simulate the areas of high non-linearity and multiply connected free-surfaces. This area of future work can be regarded as the most complex and ultimately of the greatest engineering importance.

# Bibliography

- [1] Colagrossi A. *A meshless Lagrangian method for free-surface and interface flows with fragmentation*. PhD thesis, Universita di Roma La Sapienza. 2004.
- [2] Colagrossi A., Le Touze D., and Colicchio G. Characteristic aspects for SPH solutions for free-surface problems: Source and possible solutions of high frequency numerical oscillations of local loads. In *1st SPHERIC Workshop, Rome, Italy, 2006*.
- [3] Colagrossi A. and Landrini M. Numerical simulation of interfacial flows by SPH. *Journal of Computational Physics*, 2003.
- [4] Dalrymple R. A. and Rogers B. D. Numerical modeling of water waves with the SPH method. *Coastal engineering*, 53, 2005.
- [5] Gingold R. A. and Monaghan J. J. Smoothed Particle Hydrodynamics: Theory and application to non-spherical stars. *Monthly Notices of the Royal Astronomical Society*, 181, 1977.
- [6] Iglesias A.S., Rojas L.P., and Rodriguez R.Z. Simulation of anti-roll tanks and sloshing type problems with Smoothed Particle Hydrodynamics. *Ocean Engineering*, 31, 2004.
- [7] Lucy L. B. A numerical approach to testing of fission hypothesis. *The Astronomical journal*, 82, 1977.
- [8] Pidduck F. B. On the propagation of a disturbance in a fluid under gravity. *Proceedings of the Royal Society of London. Series A, Containing papers of a Mathematical and Physical Character*, 83, 1910.
- [9] Pidduck F. B. The wave-problem of Cauchy and Poisson for finite depth and slightly compressible fluid. *Proceedings of the Royal Society of London. Series A, Containing papers of a Mathematical and Physical Character*. 86, 1912.
- [10] Chang J. L. C and Kwak D. On the method of pseudo compressibility for numerically solving incompressible flows. In *AIAA pap 84-0252 Reno, NV, 1984*.
- [11] Mei C. C. *The applied dynamics of ocean surface waves*. World Scientific, 1989.

- [12] Kwak D., Chang J. L. C., Shanks S., and Chakravarthy S. An incompressible Navier-Stokes solver in three-dimensional curvilinear coordinate systems using primitive variables. In *AIAA pap 84-0253 Reno, NV*, 1984.
- [13] Le Touze D., Colagrossi A., and Colicchio G. Ghost technique for squared angles applied to the solution of benchmarks 1 and 2. In *1st SPHERIC Workshop Rome, Italy*, 2006.
- [14] Molteni D. and Colagrossi A. A simple procedure to improve the pressure evaluation in hydrodynamic context using the SPH. *Computer Physics Communications*, 180. 2009.
- [15] Molteni D., Colagrossi A., and Colicchio G. On the use of an alternative water state equation in SPH. In *2nd SPHERIC Workshop, Madrid, Spain*, 2007.
- [16] Zhou D., Chan E.S., and Melville W. K. Wave impact pressures on vertical cylinders. *Applied Ocean Research*, 13, 1991.
- [17] Fulk D.A. *A numerical analysis of Smoothed Particle Hydrodynamics*. PhD thesis, Air Force Institute of Technology, 1994.
- [18] Dilts G. Moving Least Squares Particle Hydrodynamics I. Consistency and stability. *International Journal for Numerical Methods in Engineering*, 44, 1999.
- [19] Oger G., Doring M., Alessandrini B., and Ferrant P. 3D Wave resistance simulations using Smoothed Particle Hydrodynamics. In *26th Symposium on Naval Hydrodynamics - Rome, Italy*, 2006.
- [20] Oger G., Doring M., Alessandrini B., and Ferrant P. Two-dimensional SPH simulations of wedge water entries. *Journal of Computational Physics*, 213, 2006.
- [21] Oger G., Doring M., Alessandrini B., and Ferrant P. An improved SPH method: Towards higher order convergence. *Journal of Computational Physics*, 225, 2007.
- [22] Chung T. J. *Computational Fluid Dynamics*, chapter 11. Cambridge University Press, 2002.
- [23] Chung T. J. *Computational Fluid Dynamics*, chapter 12. Cambridge University Press, 2002.
- [24] Monaghan J. J. On the problem of penetration in particle methods. *Journal of Computational Physics*, 82, 1989.
- [25] Monaghan J. J. Smoothed Particle Hydrodynamics. *Annual Review of Astronomy and Astrophysics*, 30, 1992.
- [26] Monaghan J. J. SPH without a tensile instability. *Journal of Computational Physics*, 159, 2000.

- [27] Monaghan J. J. Smoothed Particle Hydrodynamics. *Reports on Progress in Physics*, 68, 2005.
- [28] Rapp R. J. and Malville W. K. Laboratory measurements of deep-water breaking waves. *Philosophical Transactions of the Royal Society of London. Series A, Mathematical and Physical Sciences*, 331, 1990.
- [29] Schoenberg I. J. *Cardinal Spline Interpolation*. SIAM, Philadelphia, 1973.
- [30] Monaghan J.J. Simulating free surface flows with SPH. *Journal of Computational Physics*, 110, 1994.
- [31] Melville W. K. The role of surface-wave breaking in air-sea interaction. *Annual Review Fluid Mechanics*, 28, 1996.
- [32] Shibata K. and Koshizuka S. Numerical analysis of shipping water impact on a deck using a particle method. *Ocean Engineering*, 34, 2007.
- [33] Shibata K., Koshizuka S., and Tanizawa K. Three-dimensional numerical analysis of shipping water onto a moving ship using a particle method. *Journal of Marine Science and Technology*, 14, 2009.
- [34] Shibata K., Koshizuka S., Tanizawa K., and Oka Y. A three-dimensional numerical analysis code for shipping water on deck using a particle method. In *Proceedings of HT-FED'04 2004 ASME Heat Transfer/Fluids Engineering Summer Conference Charlotte, North Carolina, USA*, 2004.
- [35] Liew K.M., Huang Y.Q., and Reddy J.N. Analysis of general shaped thin plates by the moving least-squares differential quadrature method. *Finite Elements in Analysis and Design*, 2004.
- [36] Delorme L., Colagrossi A., Souto-Iglesias A., Zamora-Rodriguez R., and Botia-Vera E. A set of canonical problems in sloshing, Part I: Pressure field in forced roll - comparisson between experimental results and SPH. *Ocean Engineering*, 36, 2009.
- [37] Libersky L., Petschek A., Carney T., Hipp J., and Allahdadi F. High strain Lagrangian hydrodynamics. *Journal of Computational Physics*. 109, 1993.
- [38] Sir H. Lamb. *Hydrodynamics*. Dover Publications, 6th Edition. 1993.
- [39] Gomez-Gesteira M. and Dalrymple R. A. Using a three-dimensional Smoothed Particle Hydrodynamics method for wave impact on a tall structure. *Journal of Waterway, Port, Coastal and Ocean Engineering*, 130, 2004.
- [40] Morris J. P. *Analysis of Smoothed Particle Hydrodynamics with applications*. PhD thesis, Monash University, 1996.
- [41] Morris J. P., Fox P. J., and Zhu Y. Modeling low Reynolds number incompressible flows. *Journal of Computational Physics*, 136, 1997.

- [42] Liu G. R. and Liu M. B. *Smoothed Particle Hydrodynamics A meshfree particle method*. World Scientific, 2003.
- [43] Stacey R. New finite-difference methods for free-surfaces with a stability analysis. *Bulletin of the Seismological Society of America*, 84, 1994.
- [44] Balsara D. S. von Neumann stability analysis of Smoothed Particle Hydrodynamics - suggestions for optimal algorithms. *Journal of Computational Physics*, 121, 1995.
- [45] Koshizuka S. and Oka Y. Moving-particle semi-implicit method for fragmentation of incompressible fluid. *Nuclear Science and Engineering*, 123, 1996.
- [46] Longuet-Higgins M. S. A theory on the origin of microseisms. *Philosophical Transactions of the Royal Society of London. Series A, Mathematical and Physical Sciences*, 243, 1950.
- [47] Marrone S., Colagrossi A., Le Touze D., and Graziani G. Fast free-surface detection and level-set function definition in SPH solvers. *Journal of Computational Physics*, 2010 (in press).
- [48] Narayanaswamy Muthukumar S. *A hybrid Boussinesq-SPH wave propagation model with applications to forced waves in rectangular tanks*. PhD thesis, The Johns Hopkins University, 2008.
- [49] Souto-Iglesias A., Delorme L., Perez Rojas L., and Abril-Perez S. Liquid moment amplitude assessment in sloshing type problems with Smooth Particle Hydrodynamics. *Ocean Engineering*, 33, 2006.
- [50] Belytschko T., Guo Y., Liu W. K., and Xiao S. P. A unified stability analysis of meshless particle methods. *International Journal for Numerical Methods in Engineering*, 48, 2000.
- [51] Belytschko T., Krongauz Y., Organ D., Fleming M., and Krysl P. Meshless methods: an overview and recent developments. *Computer Methods in Applied Mechanics and Engineering*, 139, 1996.
- [52] Belytschko T., Krongauz Y., Dolbow J., and Gerlach C. On the completeness of meshfree particle methods. *International Journal for Numerical Methods in Engineering*, 1998.
- [53] Swegle J. W., Hicks D. L., and Attaway S. W. Smoothed Particle Hydrodynamics stability analysis. *Journal of Computational Physics*, 116, 1995.
- [54] Whipple F. J. W. and Lee A. W. Notes on the theory of microseisms. *Monthly notices of the Royal Astronomical Society. Geophysical Supplement*, 3, 1935.
- [55] Zhou Z.Q., De Kat J.O., and Buchner B. A nonlinear 3-D approach to simulate green water dynamics on deck. In *Proceedings of 7th International Conference in Numerical Ship Hydrodynamics, Nantes, 1999*.